

DESIGN AND CHARACTERIZATION OF MEANDER LINE SLOW WAVE STRUCTURES FOR W-BAND SPACE TRAVELING WAVE TUBES

Juan M. Socuéllamos

A thesis submitted to Lancaster University
for the degree of Doctor of Philosophy



Lancaster, United Kingdom
April 2021

Declaration

I declare that this thesis is my own work and has not been submitted in substantially the same form for the award of a higher degree elsewhere.

Acknowledgement

I would like to express my deepest gratitude to my supervisors at Lancaster University, Prof. Claudio Paoloni and Dr. Rosa Letizia, for their expert guidance, constant support and understanding during the research and writing of this thesis. I would also like to thank my workmates there, specially Rupa Basu and Laxma R. Billa, for their friendship, wise advice and making this research more enjoyable.

I am profoundly grateful to my supervisor at the European Space Agency, Mr. Roberto Dionisio, for supporting this research, giving me the opportunity to work with him and sharing his deep knowledge and valuable experience with me. Not to mention the excellent colleagues that I had the opportunity to meet at ESTEC and made my time there truly unforgettable.

Last but not least, my wholeheartedly appreciation to my family and friends for their love, support and encouragement that made possible a successful completion of the PhD.

Abstract

Satellite communication systems are nowadays facing the growing demand of different services such as internet, streaming or teleconferencing that consume a lot of resources and exhaust the available links. Increasing the frequency band of operation is becoming ever-more necessary to cope with the challenges of the future communication services.

The exploitation of W-band frequencies (71-86 GHz) may offer many benefits for satellite communications. The wide band channel and high data rate permits to transmit and receive more information at higher velocities. The reduced size of the components decreases the weight of payload and the mission cost. To overcome the huge atmospheric attenuation at W-band, traveling wave tubes (TWTs) are the only solution to provide enough power to feed the link between satellites and ground stations.

The amplification in a TWT is based on the interaction between an electromagnetic wave and an electron beam in such a way that, under specific circumstances, the electron beam is able to transfer part of its energy to the wave and amplify the signal. The main component of a TWT is the slow wave structure (SWS), whose role consists of slowing down the radiofrequency signal to a phase velocity comparable to that of the electrons in the electron beam in order to get amplification. Microwave TWTs are mostly based on helix SWSs. Going up in frequency to millimetre waves implies a reduction of the wavelength and, consequently, of the dimensions of the SWS. The helix is particularly affected by this reduction, making its manufacture unfeasible at W-band.

New SWSs have been then recently investigated as an alternative to the helix. One of them is the meander line SWS which, in its standard form, consists of a dielectric substrate where a serpentine-shaped metallization has been patterned. Compared to other SWSs at W-band, meander lines are potentially capable of offering very good performance while lowering the beam voltage and enhancing the interaction impedance, providing higher efficiency and reducing the size and weight of the TWT. This is particularly important for space applications, where saving power and reducing the mass on spacecraft has direct implications for the final system and launch costs per satellite. Given the simplicity and straightforward fabrication of the meander line, this kind of SWSs are also adequate for low-cost and high volume production. Thanks to its many benefits, the meander line is seen as a very

promising SWS for a new generation of low-cost, lightweight and compact TWTs for the establishment of future cost-effective satellite communication networks.

This thesis will dedicate the first chapter (Ch. 1) to a brief summary of the history and evolution of the TWT and its role as power amplifier for satellite communications and, in particular, at W-band. The working principle and main components of the TWT will be described as well as the requirements for space applications. Special emphasis will be put on the SWS and the different options available at W-band.

The second chapter (Ch. 2) will focus on the description of the characteristics and properties of the meander line SWS and will go through an extensive literature review to become familiarized with this kind of SWS and the different coupling transitions between the meander line and a rectangular waveguide. The main microfabrication techniques needed for manufacturing meander line SWSs will be also briefly explained.

The thesis will continue with the analysis and design of novel planar (Ch. 3) and three-dimensional (Ch. 4) meander line SWSs. From a thorough analysis of the most optimum material of the substrate, configuration of the metallization and geometry of the electron beam, two new planar meander line SWSs will be proposed to interact with a sheet electron beam and improve the performance of conventional meander lines. Other two novel three-dimensional meander line SWSs will be discussed for more efficient and higher-output-power TWTs using a cylindrical electron beam.

Phase velocity and interaction impedance are two of the most important parameters for characterizing TWTs. Ch. 5 will present an experimental method to compute the phase velocity based on the measurement of the phase delay of the same meander line SWS with two different lengths as well as a novel theoretical model to experimentally determine the interaction impedance from measurements of the same perturbed and unperturbed meander line SWS.

The thesis will conclude with the experimental validation of the theoretical models developed for measuring the phase velocity and the interaction impedance from the characterization of four different planar meander line SWSs that have been tested at Ka-band (Ch. 6).

Contents

List of Tables	xiii
List of Figures	xv
1 The traveling wave tube for satellite communications	1
1.1 Wireless communications	1
1.2 Satellite communications	3
1.3 Satellite communications at W-band	4
1.4 Traveling wave tubes	6
1.4.1 Beam-wave interaction	7
1.4.2 Electron beam dynamics	10
1.4.3 Main slow wave structure parameters	13
1.5 Space traveling wave tubes	16
1.6 Traveling wave tubes and slow wave structures at W-band	17
1.7 Summary	21
2 The meander line as slow wave structure for traveling wave tubes	23
2.1 Meander line slow wave structures	23
2.1.1 Dispersion	24
2.1.2 Interaction impedance	26
2.1.3 S-parameters	26
2.1.4 Meander line topologies	27
2.1.5 Phase velocity tapering	33
2.1.6 Double-substrate and 3D meander lines	34
2.1.7 Modifications on the substrate	38
2.1.8 Attenuators on meander lines	40
2.2 Meander line - Waveguide transitions	41
2.3 Microfabrication techniques	43
2.3.1 Sputtering	44
2.3.2 Lithography	44
2.3.3 Electroplating	45
2.3.4 Etching	46
2.3.5 LIGA (Lithography, Electroplating and Molding)	46

2.4	Summary	46
3	Analysis and design of novel planar meander line slow wave structures	49
3.1	Effect of the dimensions and material of the substrate	49
3.2	Effect of the dimensions of the metallization	53
3.3	Beam geometry analysis	56
3.3.1	Cylindrical beam	57
3.3.2	Sheet beam	60
3.4	Designs at W-band: Standard meander line (SML)	64
3.5	Designs at W-band: Standard meander line with round corners (SMLR)	66
3.6	Designs at W-band: New meander line 1 (NML1)	67
3.7	Designs at W-band: New meander line 2 (NML2)	68
3.8	W-band housing	69
3.9	Results and comparison of SML, SMLR, NML1 and NML2	71
3.10	Designs at Ka-band: Soft substrate	74
3.11	Designs at Ka-band: Alumina substrate	77
3.12	Ka-band housing	80
3.13	Other meander line structures	81
3.14	Summary	84
4	Analysis and design of novel three-dimensional meander line slow wave structures	87
4.1	Pillared meander line (PML)	88
4.2	3D meander line (3DML)	90
4.3	Cylindrical beam interaction analysis	93
4.4	Fabrication	95
4.5	Summary	96
5	Development of theoretical models for the experimental determination of phase velocity and interaction impedance of meander line slow wave structures	97
5.1	Calculation of the phase velocity	98
5.2	Determination of the interaction impedance	98
5.2.1	Derivation of the coefficients $G_{jk,z}$, $G_{jk,x}$ and $G_{jk,y}$	103
5.2.2	Derivation of the parameters Y_i , B_i , X_{jk} and k_{jk}	105
5.3	Summary	108
6	Characterization of planar meander line slow wave structures at Ka-band	109
6.1	Meander lines on soft substrate	109
6.1.1	Fabrication	109
6.1.2	S-parameters	114
6.1.3	Phase velocity	116
6.1.4	Interaction impedance	116

6.2	Meander lines on alumina substrate	118
6.2.1	S-parameters	119
6.2.2	Phase velocity	122
6.2.3	Interaction impedance	123
6.3	Summary	125
7	Conclusions and future work	127
	Bibliography	131
A	Derivation of the parameters X_{jk} and k_{jk} for NML1 and NML2	139
B	Interaction impedance computational codes	145
C	Publications	165

List of Tables

1.2.1	Microwave bands of frequencies [11].	4
1.5.1	TWTs on space missions.	17
3.1.1	Properties of the substrate materials.	50
3.1.2	Starting dimensions of the standard meander line for the parametric sweeps.	51
3.3.1	Performance of a cylindrical electron beam with two different radius when interacting with the standard meander line topology at W-band.	60
3.3.2	Performance of a sheet electron beam with different lengths and fixed $h_b = 143 \mu\text{m}$ and $d_b = 50 \mu\text{m}$	64
3.3.3	Performance of a sheet electron beam with different heights and fixed $l_b = 286 \mu\text{m}$ and $d_b = 50 \mu\text{m}$	64
3.3.4	Performance of a sheet electron beam at different distances to the meander line and fixed $l_b = 286 \mu\text{m}$ and $h_b = 143 \mu\text{m}$	64
3.4.1	Final dimensions of the standard meander line.	65
3.4.2	Dimensions of the coupling probe of the standard meander line.	65
3.5.1	Final dimensions of SMLR.	66
3.5.2	Dimensions of the coupling probe of SMLR.	67
3.6.1	Final dimensions of NML1.	68
3.6.2	Dimensions of the coupling probe of NML1.	68
3.7.1	Final dimensions of NML2.	69
3.7.2	Dimensions of the coupling probe of NML2.	69
3.8.1	Dimensions of the 20- and 40-period housing at W-band.	71
3.9.1	Dimensions of the sheet beam and the hot parameters used for the four meander lines at W-band.	72
3.10.1	Dimensions of SML and NML1 using RT/duroid 6002 laminates at Ka-band.	75
3.10.2	Dimensions of the coupling probe for SML and NML1 using RT/duroid 6002 substrate at Ka-band.	76
3.11.1	Dimensions of SML, SMLR, NML1 and NML2 on alumina substrate at Ka-band.	78
3.11.2	Dimensions of the coupling probe for SML, SMLR, NML1 and NML2 using alumina substrate at Ka-band.	78

3.12.1	Dimensions of the 20- and 40-period housing at Ka-band.	81
4.1.1	Dimensions of the pillared meander line at W-band.	89
4.1.2	Dimensions of the coupling probe of the pillared meander line at W-band.	90
4.2.1	Dimensions of the 3D meander line at W-band.	91
4.2.2	Dimensions of the coupling probe of the 3D meander line at W-band.	92
6.1.1	Results of the mechanical measurement of SML and comparison with the designed dimensions.	113
6.1.2	Results of the mechanical measurement of NML1 and comparison with the designed dimensions.	114

List of Figures

1.2.1	Free space path loss for different frequencies and distance of the link.	3
1.3.1	Total atmospheric attenuation per kilometre composed of the gas, clouds and rain attenuations. A temperature of 293 K, pressure of 1 atm and water vapor density of 7.5 g/m^3 is considered for computing the gas attenuation. The attenuation of the signal propagating through clouds is assumed with the typical cloud liquid water density of 0.5 g/m^3 . The rain attenuation is calculated for a light-moderate rainfall of 2.5 mm/h.	5
1.4.1	Schematic of a traveling wave tube.	7
1.4.2	Solutions of Eq. 1.4.3. a) Slow forward wave with growing amplitude, b) slow forward wave with decaying amplitude, c) fast forward wave with constant amplitude and d) fast backward wave with constant amplitude [21].	9
1.4.3	Illustration of the growing wave and the electron beam bunching. . .	11
1.4.4	Space charge force on a cylindrical and a sheet electron beam.	12
1.4.5	Variation of the wave phase velocity with frequency for a given SWS and beam line.	14
1.4.6	Incident and reflected signals in a 2-port system.	15
1.5.1	Percentage of TWT and SSP amplifiers on satellites for different frequency bands [24].	16
1.6.1	Schematic of a folded waveguide slow wave structure [38].	18
1.6.2	Picture of the FWSWS TWT built in [45].	19
1.6.3	3D model of the staggered double van SWS [48].	19
1.6.4	Unit cell of the double corrugated waveguide [49].	20
1.6.5	Schematic of the H-plane and E-plane loaded SWS [50].	21
2.1.1	Model of a conventional meander line slow wave structure.	24
2.1.2	Electromagnetic field lines of the quasi-TEM mode of the meander line.	24
2.1.3	Variation of the wave phase velocity with frequency for meander lines and a beam line.	25
2.1.4	Brillouin diagram of meander lines representing the first three modes and a beam line.	26
2.1.5	Typical transmission and reflection coefficients in meander line SWSs.	27

2.1.6	Drawing of the V-shaped meander line SWS [52].	28
2.1.7	Model of the rombus meander line SWS [53].	28
2.1.8	Model of the U-shaped meander line SWS [54].	29
2.1.9	Model of the S-shaped meander line SWS [55].	29
2.1.10	Schematic of the Ω -shaped meander line SWS [56].	30
2.1.11	Schematic of the ring-shaped meander line SWS [57].	30
2.1.12	Schematic of the ring bar shaped meander line SWS [58].	31
2.1.13	Model of the ladder meander lines [59].	31
2.1.14	Fabricated V-shaped meander line SWS at Ka-band [60].	32
2.1.15	Novel fabricated meander line SWS at V-band [61].	33
2.1.16	Model of the phase velocity tapered meander line [64].	34
2.1.17	Model of double V-shaped meander line [66].	35
2.1.18	3D view of the folded frame meander slow wave structure [67].	35
2.1.19	3D view of a single period of the double meander with channels [69].	36
2.1.20	Perspective view of the 3D meander structure [72].	37
2.1.21	Schematic of the symmetric folded meander line [74].	38
2.1.22	Model of the winding meander line [75].	39
2.1.23	Model of the embedded meander line [78].	40
2.1.24	Design of the meander line with the absorption structure on the bottom side [80].	41
2.2.1	Configuration of a meander line-waveguide transition by using a ridged waveguide.	42
2.2.2	Configuration of a meander line-waveguide transition by means of a slot on the ground plane of the meander line. a) Lateral and b) bottom view of the coupler.	42
2.2.3	Two configurations of the meander line extended into the waveguide by means of coupling probes. a) The substrate faces the propagation direction of the waveguide and b) the substrate is parallel to the propagation direction.	43
2.3.1	Schematic of a sputter deposition process.	44
2.3.2	Typical photolithography steps. The substrate is coated with the photoresist, then the mask is exposed to create the desired design after developing the photoresist.	45
2.3.3	Setup of an electroplating process.	45
3.1.1	Schematic and dimensions of the standard meander line (SML) used as a reference.	50
3.1.2	a) Results for the phase velocity and b) the interaction impedance for different substrate materials.	52
3.1.3	a) Results for the phase velocity and b) the interaction impedance after sweeping the parameter l_s	52
3.1.4	a) Results for the phase velocity and b) the interaction impedance after sweeping the parameter t_s	53

3.2.1	a) Results for the phase velocity and b) the interaction impedance after sweeping the parameter l_m	54
3.2.2	a) Results for the phase velocity and b) the interaction impedance after sweeping the parameter t_m	54
3.2.3	a) Results for the phase velocity and b) the interaction impedance after sweeping the parameters w and s while keeping a fixed p	55
3.2.4	a) Results for the phase velocity and b) the interaction impedance after sweeping the parameters w and p while keeping a fixed s	55
3.2.5	a) Results for the phase velocity and b) the interaction impedance after sweeping the parameters p and s while keeping a fixed w	56
3.3.1	y -plane axial view of the longitudinal electric field component of the standard meander line.	57
3.3.2	x -plane axial view of the longitudinal electric field component of the standard meander line.	57
3.3.3	z -plane longitudinal view at half pitch of the longitudinal electric field component of the standard meander line with a) superimposed cylindrical beam and b) sheet beam contours.	57
3.3.4	Schematic of a cylindrical electron beam on top of the meander line.	58
3.3.5	Lateral view of the cylindrical electron beam bunching.	58
3.3.6	Longitudinal cross section of the cylindrical electron beam for different distances along the meander line. a) at the beginning of the interaction b) at 1/3 of the full line length c) at 2/3 of the full line length and d) at the end of the interaction.	59
3.3.7	Interaction impedance over the cylindrical beam area with radius 100 μm	59
3.3.8	Gain and output power of the standard meander line at W-band using a cylindrical electron beam.	60
3.3.9	Schematic of a sheet electron beam on top of the meander line and parameters to be analysed.	61
3.3.10	Longitudinal cross section of the sheet electron beam with aspect ratio 4:1 for different distances along the meander line. a) at the beginning of the interaction b) at 1/3 of the full line length c) at 2/3 of the full line length and d) at the end of the interaction.	61
3.3.11	Longitudinal cross section of the cylindrical electron beam with aspect ratio 2:1 for different distances along the meander line. a) at the beginning of the interaction b) at 1/3 of the full line length c) at 2/3 of the full line length and d) at the end of the interaction.	62
3.3.12	Lateral view of the sheet electron beam bunching.	62
3.3.13	Interaction impedance over the sheet beam area.	63
3.4.1	Schematic and dimensions of the standard meander line (SML).	65
3.4.2	Schematic and parameters of the coupling probe of the standard meander line.	65
3.5.1	Schematic and dimensions of SMLR.	66

3.5.2	Schematic and parameters of the coupling probe of SMLR.	67
3.6.1	Schematic and dimensions of NML1.	67
3.6.2	Schematic and parameters of the coupling probe of NML1.	68
3.7.1	Schematic and dimensions of NML2.	69
3.7.2	Schematic and parameters of the coupling probe of NML2.	69
3.8.1	Final design of the 20-period housing at W-band.	70
3.8.2	Final design of both parts of the 20-period housing at W-band. a) Bottom part and b) top part.	71
3.9.1	a) Dispersion and b) interaction impedance curves of the four meander lines at W-band.	72
3.9.2	S-parameters of SML, SMLR, NML1 and NML2 for 20 and 40 periods length at W-band. a) SML 20 periods, b) SML 40 periods, c) SMLR 20 periods, d) SMLR 40 periods, e) NML1 20 periods, f) NML1 40 periods, g) NML2 20 periods and h) NML2 40 periods.	73
3.9.3	Comparison of the gain and output power of the four designed meander lines.	74
3.10.1	a) Normalized phase velocity and b) interaction impedance of SML and NML1 on RT6002 substrate at Ka-band.	75
3.10.2	Schematic and parameters of the coupling probe of SML using RT6002 substrate at Ka-band.	76
3.10.3	Schematic and parameters of the coupling probe of NML1 using RT6002 substrate at Ka-band.	76
3.10.4	S-parameters of SML and NML1 using RT/duroid 6002 substrate for 20 and 40 periods length. a) SML 20 periods, b) SML 40 periods, c) NML1 20 periods and d) NML1 40 periods.	77
3.11.1	a) Phase velocity and b) interaction impedance of the four meander lines at Ka-band.	78
3.11.2	S-parameters of SML, SMLR, NML1 and NML2 using alumina substrate for 20 and 40 periods length. a) SML 20 periods, b) SML 40 periods, c) SMLR 20 periods, d) SMLR 40 periods, e) NML1 20 periods, f) NML1 40 periods, g) NML2 20 periods and h) NML2 40 periods.	79
3.12.1	Final design of the 40-period housing at Ka-band.	80
3.12.2	Final design of both parts of the 40-period housing at Ka-band. a) Bottom part and b) top part.	80
3.13.1	Design of some novel alternative meander lines. a) SML and b), c), d) novel designs.	81
3.13.2	Phase velocity and interaction impedance of the designs in Fig. 3.13.1.	82
3.13.3	Design of the double meander line with a) the top meander facing the bottom meander with the same orientation and b) with the top meander rotated by 180°.	82
3.13.4	Phase velocity and interaction impedance of double meander lines.	83

3.13.5	Design of the meander line with a) channel b) pedestal and c) no metallization below the substrate.	83
3.13.6	Phase velocity and interaction impedance of the meander lines with different channels underneath the substrate.	84
4.0.1	a) Design of the pillared meander line and b) design of the 3D meander line.	87
4.1.1	Dimensions of the pillared meander line at W-band.	88
4.1.2	Dispersion and interaction impedance for the pillared meander line at W-band.	89
4.1.3	Schematic and parameters of the coupling probe of the pillared meander line.	89
4.1.4	S-parameters of the pillared meander line at W-band.	90
4.1.5	Gain and output power of the pillared meander line at W-band.	90
4.2.1	Schematic of the 3D meander line with the top substrate hidden and parameters.	91
4.2.2	Dispersion and interaction impedance for the 3D meander line designed at W-band.	92
4.2.3	Schematic and parameters of the coupling probe of the 3D meander line.	92
4.2.4	Scattering parameters for the 3D meander line. The transmission coefficient is plotted in green while the reflection coefficient is the red curve.	93
4.2.5	Gain and output power for the 3D meander line at W-band.	93
4.3.1	Lateral view of the longitudinal electric field profile of the pillared meander line and the 3D meander line.	94
4.3.2	Lateral view of the beam energy modulation of the pillared meander line and the 3D meander line.	94
4.4.1	Process flow of the fabrication of the meander line with pillars.	95
4.4.2	Fabrication of the 3D meander line.	95
5.2.1	xy -plane view of the two regions of the meander line to be analyzed. t is the thickness of the substrate, a is the length of the substrate and b is the height of the perfect conductor cavity.	100
5.2.2	xz -plane view of the standard meander line. There are five and three regions along the z and x axis, respectively. s is the distance between two consecutive strips, w is the strip width, p is the pitch length, a is the length of the substrate and l is the length of the metallization.	100
5.2.3	3D view of the three regions to be analysed including the perturbation.	101
5.2.4	xz -plane view of the SML. There are five and three regions along the z and x axis. s is the distance between two consecutive strips, w is the strip width, p is the pitch length, a is the length of the substrate and l is the length of the metallization.	106

6.1.1	Hot plate (1), spinner (2) and mask aligner (3) used during the fabrication of SML and NML1 on RT6002 substrates.	110
6.1.2	The four different mask designed for the fabrication. 1- 20 periods of SML, 2- 20 periods of NML1, 3- 40 periods of SML and 4- 40 periods of NML1.	111
6.1.3	a) Example of the 20 period NML1 after developing the photoresist and b) view under the microscope	111
6.1.4	Fabricated 20 period SML after the etching process.	112
6.1.5	Fabricated meander lines and aluminium holder for 20 periods.	112
6.1.6	Schematic of the designed SML with the probe termination. The parameters w_r , w_l , w_t and w_b make reference to the average right, left, top and bottom width of the strip for a single period, respectively. The parameter c characterizes the average width of the partially etched copper that remains next to every strip. The parameter s is then the average distance between this partially etched copper and not directly between two consecutive strips.	113
6.1.7	Schematic of the designed NML with the probe termination.	114
6.1.8	Experimental setup for the measurement of the S-parameters.	115
6.1.9	Experimental and simulated S-parameters for the RT6002 laminate. a) SML 20 periods, b) SML 40 periods, c) NML1 20 periods and d) NML1 40 periods	115
6.1.10	Simulated and experimental results for the normalized phase velocity using Eq. 5.1.1 for the calculation.	116
6.1.11	Comparison of the results obtained by the proposed theoretical model using Eq. 5.2.15 and the CST simulation.	117
6.1.12	Comparison of the experimental interaction impedance for different values of the permittivity of the perturbing dielectric rod.	117
6.1.13	Comparison of the experimental interaction impedance accounting for a deviation in the original position of the perturbing rod a) vertically or b) horizontally.	118
6.2.1	20 periods and the coupling terminations of the four different meander line topologies manufactured for the experiment.	119
6.2.2	a) 20 period housing used for the measurements and b) bottom half of the housing with one of the meander lines placed inside.	119
6.2.3	S-parameters of the SML, SMLR and NML1 for 20 and 40 periods length. The solid lines represent the measurement results while the dashed lines represent the simulations. a) SML 20 periods, b) SML 40 periods, c) SMLR 20 periods, d) SMLR 40 periods, e) NML1 20 periods and f) NML1 40 periods.	120

6.2.4	S-parameters of NML2 for 20 and 40 periods length. The solid lines represent the measurement results while the dashed lines represent the simulations. a) NML2 20 periods, b) NML2 40 periods, c) NML2 20 periods with the substrate in the simulation moved horizontally and d) NML2 40 periods with the substrate in the simulation moved horizontally.	121
6.2.5	Measurement of S_{12} for the four different meander line topologies. . .	121
6.2.6	Comparison of the phase velocity measurements with the simulation curves. a) SML, b) SMLR, c) NML1 and d) NML2.	122
6.2.7	Measured phase velocity curves for the four meander line topologies.	123
6.2.8	a) Bottom half of the housing with the perturbation introduced on top of the meander line and b) detail of the perturbation.	123
6.2.9	Comparison of the interaction impedance measurements with the simulation curves. a) SML, b) SMLR, c) NML1 and d) NML2	124
6.2.10	Measured interaction impedance curves for the four meander line topologies.	125
A.0.1	xz -plane view of the first new meander line. There are seven and three regions along the z and x axis, respectively. s is the distance between two consecutive strips, w is the strip width, p is the pitch length, a is the length of the substrate and l is the length of the metallization. . . .	139
A.0.2	xz -plane view of the second new meander line. There are nine and four regions along the z and x coordinates, respectively. s is the distance between two consecutive strips, w is the strip width, p is the pitch length, a is the length of the substrate and l is the length of the metallization.	142

1. The traveling wave tube for satellite communications

This first chapter aims to highlight the importance of the traveling wave tube in space communications and the necessity to find novel slow wave structures for the development of a new generation of millimetre-wave space TWTs. From the birth of wireless communications to the modern satellite communication networks, the first part of this introduction will go through the main developments that made TWTs to be the predominant power amplifier for space telecommunication services and scientific and research missions. The working principle and main components of the TWT, specially the SWS, will be described. The necessity of investigating novel SWSs for the development of higher-frequency TWTs that can cope with the increasing demand of telecommunication services will be stated.

1.1 Wireless communications

Wireless communications are nowadays of fundamental importance for the everyday life of all of us. Broadcasting data for radio or television, establishing internet links mostly everywhere, location and navigation services or even remote control systems in our homes, are just a few examples of the powerful and widespread wireless technology. These systems, that currently form an indispensable part in our routines and behaviour, seem to be quite recent, but the actual fact is that wireless communications did not become so massively extended until the second half of the XX century.

The history of wireless communications started long ago in the last years of the XIX century when the physicist H. R. Hertz first observed experimentally the propagation of electromagnetic waves through air [1]. It took twenty years for this phenomenon to be experimentally demonstrated after it had been theoretically formulated by the prominent physicist and mathematician J. C. Maxwell earlier in 1865 [2].

The recent advances in the field allowed the inventor G. Marconi to build one of the first radio transmitters and realize a transatlantic emission by the beginning of the new century, in 1901, without requiring the use of the, by then, predominant

submarine telegraph cables.

By that time, wireless communications already faced several problems to successfully transmit data from transmitter to receiver. The curvature of the Earth's surface limited a direct connection between two long-range stations. The communications were also very sensitive to weather conditions.

To overcome the attenuation due to the free-space path loss and bad weather, wireless signals were already amplified by the first practical vacuum tube created in 1906, the triode [3]. To compensate for the Earth's curvature, different stations were deployed between the transmitter and the receiver acting as relays that repeated the signal to ensure a correct transmission.

With the expansion and increased popularity of telephone communications and the beginning of the first television emissions during the 1920s-1930s, it was made necessary to send larger quantities of information, requiring wireless signals with higher frequencies and wider bands.

During those years, short-range transmissions were done by radio waves from stations directly to the customer. But to provide television over countries, sending the programs to every station was necessary and, by that time, there were two consolidated means of propagation: cables or wireless signals. In the first years of the 1950s, cable transmissions were still the oldest and most preferred option to allow telephone calls and television programs. However, these lines were only able to transmit hundreds of calls and just one single television program per cable. The cable system had not been designed to cope with the huge amount of information required for television broadcasting. Increasing the capacity by deploying more cables seemed quite expensive and the first successful wireless television transmission in the United Kingdom established with triodes as amplifiers looked very promising [4].

This motivated the use of vacuum amplifiers for wireless transmissions instead of using cables. After the discovery and development of the traveling wave tube in the early 1940s through the 1950s, these novel vacuum tubes meant a huge leap to telecommunications thanks to their high power and larger bandwidth ideal for sending huge amounts of information over long-range transmissions. The first commercial microwave radio-relay system using TWTs was functioning in 1952 to send television programs between England and Scotland [5]. France and Japan followed the United Kingdom, and developed their wireless system during the first half of the 1950s. The United States also incorporated the use of wireless transmission shortly after, but it was not until the second half of the 1950s that the triodes were replaced by TWTs. The TWT started to become massively accepted and used, which boosted the development of radio-relays systems for television around the world between the 1950s and the 1980s. The next step was to send those relays in outer space.

1.2 Satellite communications

Back in the 1940s, a few papers analysed the feasibility of using the Moon as passive reflector to achieve transcontinental communication [6], leading later to the first signals sent and received through space [7]. This concept was difficult to implement because of several inconveniences: in addition to the Moon not being visible for most of the day, a lot of power was attenuated due to the long Earth-Moon distance and the small fraction of energy reflected by the Moon's surface. This made television transmissions unfeasible, and the signal delay also complicated telephone conversations. The Moon was not the perfect relay but it suggested the idea of using the same approach with closer reflectors. In 1955, J. R. Pierce submitted the first work on using artificial satellites for orbital radio-relays [8]. Rather than considering satellites at the GeoSynchronous Orbit (GSO) for full visibility and permanent link with ground stations, he assessed the feasibility of using Low Earth Orbit (LEO) satellites for transoceanic communications in order to benefit from the smaller attenuation (see Fig. 1.2.1). The permanent connection would be ensured by the use of a number of lighter and more compact satellites that would form a so-called satellite constellation. The idea was already established and it started to shape up with the launch of the first man-made objects into space.

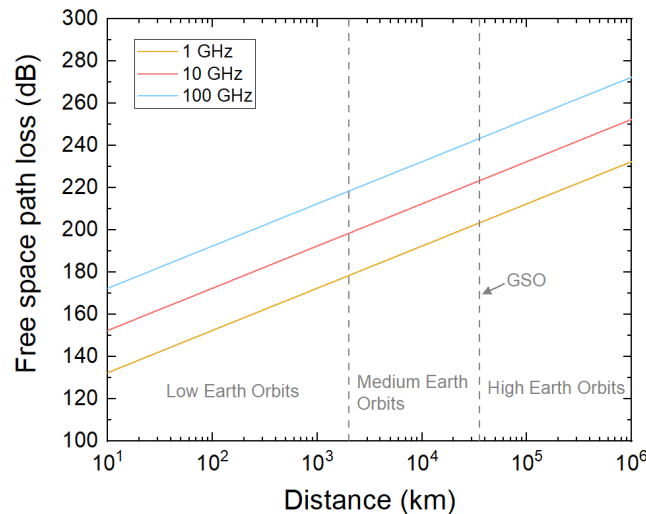


Figure 1.2.1: Free space path loss for different frequencies and distance of the link.

In October 1957, the Soviet Union reached the outer space with the first artificial satellite orbiting around Earth, *Sputnik 1*. This ignited the space race in the United States and also launched their first satellite, *Explorer 1*, in February 1958. By the end of the decade, more than a hundred objects had been launched into space. J. R. Pierce and R. Kompfner collaborated with NASA for the first communication satellite, the *Echo 1* launched in 1960. It was a passive device with no electronic systems to amplify the signal but proved that it was possible to send a message through space

via artificial relays. The *Telstar* project [9], including the *Telstar 1* launched in 1962, which was the world's first active satellite for communications, consisted of a satellite constellation that included 2 W 3.7-4.2 GHz helix TWTs that amplified signals before sending them back to Earth [10].

The next step for those satellites was to increase their area capability, with more powerful amplifiers with a wider bandwidth.

A few days after the launch of the *Telstar 1* in 1962, Europe joined the space race with the creation of two parallel space agencies: the European Space Research Organization (ESRO) which would focus on the scientific aspects of the missions and the European Launcher Development Organization (ELDO) whose goal would be to build a launcher for the missions. These two agencies would later merge to create the current European Space Agency (ESA) in 1975. The first European satellite for communications, *Symphonie A*, was launched on December 1974 containing 13 W C-band TWTs (see Tab. 1.2.1 for the corresponding frequency range).

The rise of the commercial global internet by the late 1980s and early 1990s supposed a huge increase in the demand of the channel capacity and the interest in extending the coverage worldwide. Besides that, microwave signals became fundamental for space missions in order to transmit telemetries, tele-commands or receive scientific data.

The worldwide space agencies and private companies started to work on even wider-band and more powerful TWTs in order to cope with the requirements of the new generation of satellite communications. Currently, state-of-the-art space-borne TWTs are able to operate at frequencies as high as Ka-band and provide output power close to 300 W.

Table 1.2.1: Microwave bands of frequencies [11].

Band	L	S	C	X	Ku	K	Ka	V	W
Frequency (GHz)	1-2	2-4	4-8	8-12	12-18	18-26.5	26.5-40	40-75	75-110

1.3 Satellite communications at W-band

Nowadays, the use of internet is growing exponentially all over the world and has become an indispensable technology for most of the people. The necessity to be connected at every time and every location and the increasing demand of services such as high-definition streaming, videoconferencing or online video games is pushing to advance in the establishment of communication systems beyond Ka-band to enable high data rate transmission over broad bandwidths.

The use of higher frequencies is, thus, becoming necessary. However, in addition to the free space path losses, which increase with higher frequencies, the mm-wave frequency range for telecommunications is severely affected by the atmospheric attenuation (see Fig. 1.3.1), where, for instance, raindrops typically have a diameter

of a few millimetres and are comparable in size to the signal wavelength. Nevertheless, the exploitation of the temporal and spatial properties of the atmosphere by, for instance, the convenient selection of the ground station sites looking for favourable climate conditions, has led to different feasibility studies of the V-band to be used for telecommunications [12].

Despite of that, the oxygen peak near 60 GHz make these frequencies more suited for inter-satellite links in order to avoid atmospheric attenuation. Considering the benefits of using higher frequency bands, the W-band is the current candidate with an encouraging future for the next generation of satellite communication systems and applications are seen in different fields.

The large channel capacity and high data rate transmission could be useful for extraterrestrial communications where the high atmospheric attenuation does not hinder the transmission. Satellite-satellite links or interplanetary missions will be benefited from the capability of sharing greater amounts of data.

Satellite-ground stations links will take advantage from the allocated frequency band from 71 to 76 GHz for downlink services. However, the power required for the link needs to provide enough margin to overcome the atmospheric attenuation and events with greater attenuation than usual. It is estimated that tens of watts of output power are necessary for a feasible link [13], and only traveling wave tubes can provide such power while operating over the whole band.

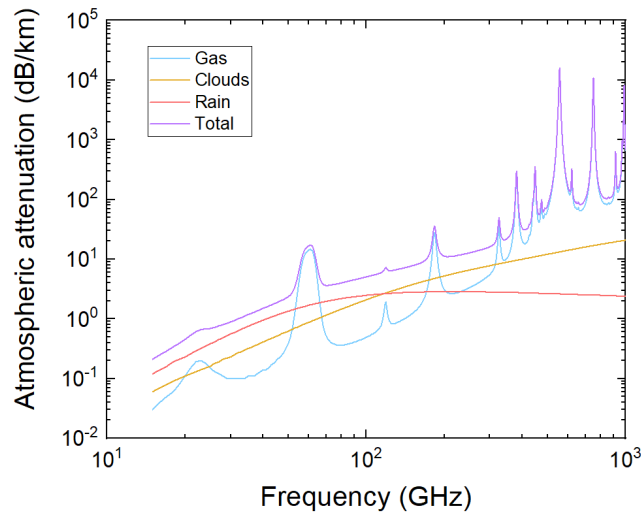


Figure 1.3.1: Total atmospheric attenuation per kilometre composed of the gas, clouds and rain attenuations. A temperature of 293 K, pressure of 1 atm and water vapor density of 7.5 g/m^3 is considered for computing the gas attenuation. The attenuation of the signal propagating through clouds is assumed with the typical cloud liquid water density of 0.5 g/m^3 . The rain attenuation is calculated for a light-moderate rainfall of 2.5 mm/h .

1.4 Traveling wave tubes

Just after the experimental demonstration that electromagnetic waves could propagate through air, Hertz also worked on the first waveguide. He discovered that electromagnetic waves could be guided and, by being reflected on the metal walls, the waves would take more time to cross the guide and therefore were slowed down. He also built the first helical waveguide [14].

The TWT still needed another fundamental idea to work. The addition of an electron beam to a helical slow wave structure was first suggested in 1933 by A. V. Haeff [15] who pointed out the possibility of using an electron beam in between two helical structures in order to obtain amplification.

In 1935, K. Posthumus was the first to describe the working principle of the helix traveling wave amplifiers [16]. As a result of the interaction between the axial component of a traveling electromagnetic wave with velocity equal to the average velocity of the electrons, electron energy was converted to amplification of the RF wave.

The precursor of the current TWT was proposed by N. E. Lindenblad in 1940 and subsequently by R. Kompfner in 1943. Lindenblad modified the original work from Haeff and placed the electron beam inside the helical structure [17]. He also was successfully able to explain the basics of the TWT amplification as well as the possibility to modify the helix pitch in order to maintain synchronism with the electron beam. In the mean time, Kompfner used a helix as slow wave structure to build his first TWT [18]. Kompfner continued to work on the TWT theory aiming to find a model that would enable design optimization.

J. R. Pierce met R. Kompfner at that time and decided to collaborate in order to develop a better theory and improve the future TWTs. Pierce made a huge leap on the TWT design introducing features to the design that nowadays are indispensable in every helix TWT. The helix SWS was accurately positioned and supported by longitudinal insulating rods and a system of solenoids was included to produce a uniform magnetic field for focusing the electron beam. Pierce also described techniques for suppressing backward waves and oscillations [19].

Nowadays, the TWT is essentially composed of four different parts described in the schematic in Fig. 1.4.1:

- The electron gun produces the electrons by thermionic emission that are accelerated towards the end of the tube by a voltage applied across the cathode and anode. An electromagnetic field is also applied to focus the electrons into a beam before entering the interaction region through an aperture in the anode.

To produce a cylindrical beam, the electrons are formed from a cylindrical cathode and focused to enter a smaller circular aperture in the anode. Sheet beams, instead, are more complicated to be formed. There are two options to construct a sheet beam: either by using a cylindrical cathode with elliptical or

rectangular sectional profile or by converting a cylindrical beam into a sheet one using strong magnetic forces.

- A magnetic focusing system is used to provide a magnetic field along the axial direction in order to keep the beam traveling tight; typically in the form of periodic permanent magnets consisting of magnets of alternating polarity which produce a sinusoidally varying axial magnetic field.
- The most important part of the traveling wave tube is the slow wave structure. The RF signal is fed into the SWS, usually via a waveguide, and it is slowed down to a velocity close to that of the electrons in order to produce amplification. The amplified signal is obtained at the end of the tube.
- The electron beam is finally recovered at the collector after it has interacted with the SWS.

Even though the design of the TWT has seen different improvements and variations since it was widely recognized such as, for instance, the addition of multi-stage collectors to improve efficiency, development of new kinds of electron beams or SWSs, the theoretical work developed also by J. R. Pierce and reported in [20], was used and it is still used as the standard reference for the traveling wave tube theory.

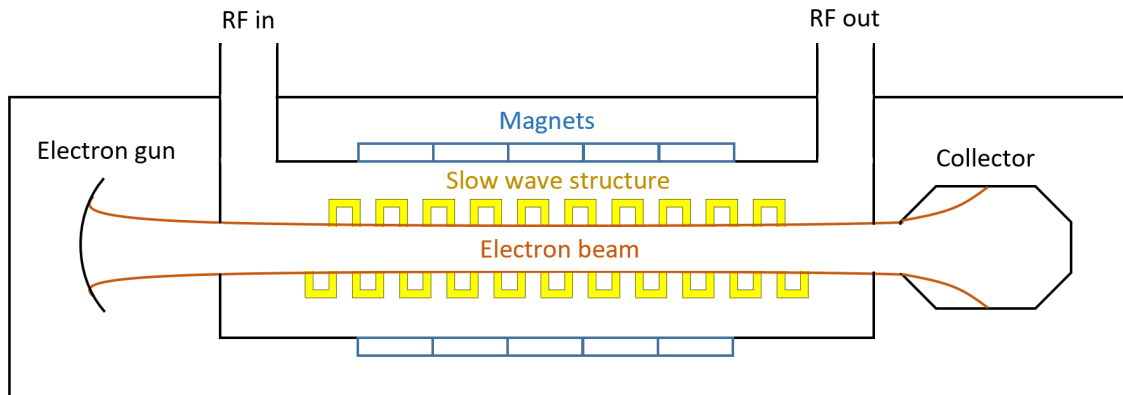


Figure 1.4.1: Schematic of a traveling wave tube.

1.4.1 Beam-wave interaction

The theoretical analysis of a TWT is based on the study of the interaction between an electron beam and a traveling wave on the slow wave circuit. As the electron beam enters the region where the RF circuit is located in a TWT, the longitudinal component of the electric field from the circuit accelerates some electrons and decelerates others inducing the formation of bunches. The energy extracted from decelerating regions is transferred to the circuit field, amplifying the wave. The classical small-signal

theory developed by J. R. Pierce [20] is the starting point for a correct comprehension of the TWT fundamentals.

The current in the beam, i_z , can be derived from an analysis of the space charge effects on electron bunching and is expressed as a function of the longitudinal electric field of the circuit, E_z , as

$$i_z = j \frac{\beta_e}{2Z_e(\beta_e - \beta)^2} E_z \quad (1.4.1)$$

where $Z_e = V_e/I_e$ and β_e are the beam impedance and propagation constant, respectively. β is the propagation constant for the waves on the circuit that interact with the beam. The subscript z refers to the propagation direction of the electron beam and the RF signal.

The equation for the electric field of the circuit, E_z , can be obtained from the analysis of the RF circuit modelled as a transmission line without taking into account the effects of space charge as

$$E_z = j \frac{\beta^2 \beta_c Z_c}{(\beta^2 - \beta_c^2)} i_z \quad (1.4.2)$$

where Z_c and β_c are the impedance and the propagation constant of the circuit.

After combining Eq. 1.4.1 and Eq. 1.4.2, it is possible to determine the propagation constants of the wave on the circuit and the beam by solving the following expression

$$\frac{\beta^2 \beta_e \beta_c}{(\beta - \beta_e)^2 (\beta^2 - \beta_c^2)} = -2 \frac{Z_e}{Z_c}. \quad (1.4.3)$$

Eq. 1.4.3 can be solved in a straightforward way if there is synchronous operation, this is, when the velocity of the electron beam and that of the circuit wave are approximately equal $\beta_e \approx \beta_c$. Assuming that the circuit impedance to beam impedance ratio, Z_c/Z_e , is a very small quantity, the four solutions of Eq. 1.4.3 are obtained as

$$\beta_1 \approx \beta_e \left(1 + (1 + j\sqrt{3}) \frac{1}{2} \sqrt[3]{\frac{Z_c}{4Z_e}} \right), \quad (1.4.4)$$

$$\beta_2 \approx \beta_e \left(1 + (1 - j\sqrt{3}) \frac{1}{2} \sqrt[3]{\frac{Z_c}{4Z_e}} \right), \quad (1.4.5)$$

$$\beta_3 \approx \beta_e \left(1 - \sqrt[3]{\frac{Z_c}{4Z_e}} \right), \quad (1.4.6)$$

$$\beta_4 \approx -\beta_e \left(1 - \frac{Z_c}{2Z_e} \right). \quad (1.4.7)$$

The first two solutions β_1 and β_2 are proportional to the propagation constant of the electron beam β_e plus a real quantity proportional to the ratio of impedances.

This indicates that β_1 and β_2 are forward waves that travel at a slower velocity than β_e . The sign of the imaginary part of the expressions indicates that β_1 is a growing wave while β_2 is a decaying wave. β_3 is also a forward wave but, given the minus sign in front of the additional coefficient, travels at a faster velocity than β_e with constant amplitude. The $-\beta_e$ in β_4 shows that this is a backward wave with constant amplitude. The four solutions are represented in Fig. 1.4.2. The slow growing wave corresponding to β_1 is the one of interest in order to achieve amplification in a TWT.

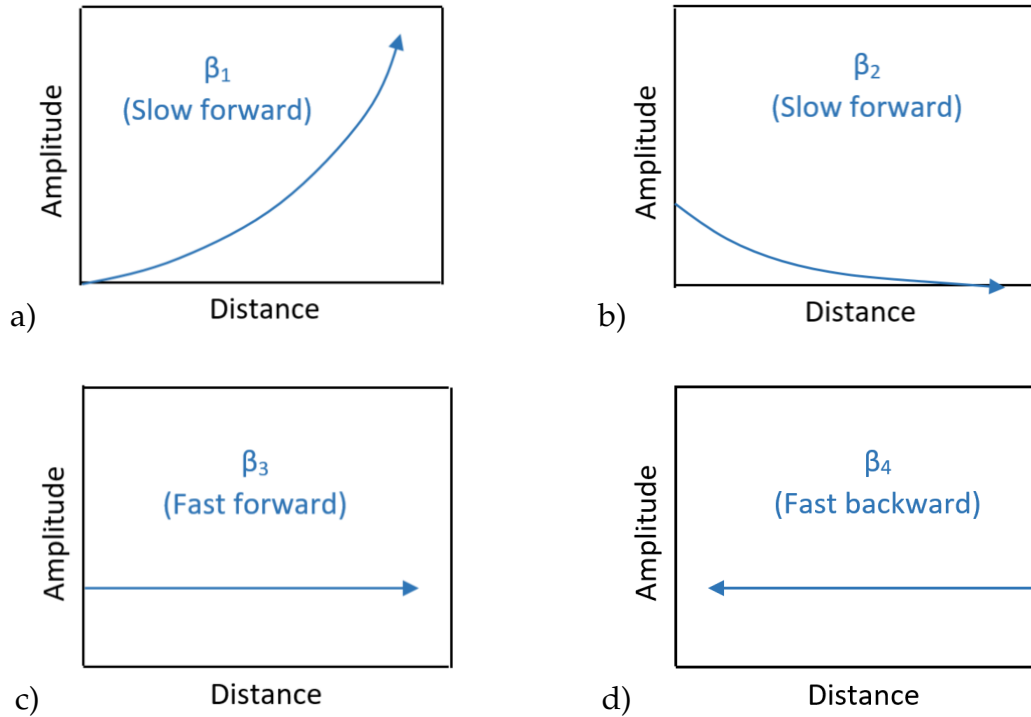


Figure 1.4.2: Solutions of Eq. 1.4.3. a) Slow forward wave with growing amplitude, b) slow forward wave with decaying amplitude, c) fast forward wave with constant amplitude and d) fast backward wave with constant amplitude [21].

In a realistic scenario, the circuit losses limit the exchange of energy between the beam and the electromagnetic wave and the beam needs to travel at a slightly higher velocity than the circuit wave. This attenuation also limits the maximum gain that the forward growing wave can achieve.

As part of the bunching process, some of the electrons within the beam become closer increasing the repulsing forces between them that tend to debunch the electron beam. The space charge forces also reduce the maximum gain of the increasing wave and depend on the beam electron density.

Another reason for saturation of the output in a TWT is the reduction of the average beam velocity when the electron energy is transferred to the circuit. One way to keep synchronism is to modify the circuit so that the velocity of the circuit wave decreases along with the beam velocity, commonly known as velocity tapering.

1.4.2 Electron beam dynamics

The cathode is the source of electrons for the electron beam in every microwave tube. In conventional TWTs, electron emission results from the heating of the cathode surface, also referred to as thermionic emission, that occurs when the energy of an electron is greater than the work function of the cathode material.

By a proper configuration of the internal components of the electron gun, the electrons are able to be focused forming a beam with a given geometry, such a cylindrical or a sheet beam, to be suitable for interaction with the SWS.

The electrons in the electron beam are affected by the electromagnetic fields that the electrons themselves, as charged particles, produce. These fields, commonly referred to as space charge forces, are responsible of several undesirable phenomena related to the beam dynamics. As a consequence, external magnetic fields are used for focusing the beam in nearly every microwave tube.

In addition to the space charge forces, the electron beam interacts with the electromagnetic field created by the input RF signal that is flowing through the SWS.

The motion and trajectory of the electrons (considered non-relativistic) can be then defined in terms of the space charge force and the external fields as

$$m \frac{d\mathbf{v}}{dt} = \mathbf{F}_{RF} + \mathbf{F}_{sc} + \mathbf{F}_{foc} \quad (1.4.8)$$

where m is the electron mass, \mathbf{v} is the velocity of the electrons, \mathbf{F}_{RF} the force produced by the electromagnetic signal, \mathbf{F}_{sc} the space charge forces produced by the electron charge distribution within the beam and \mathbf{F}_{foc} is the applied focusing force.

The motion of the electrons interacting with the external electromagnetic fields is governed by the Lorentz force. Assuming non-zero electric and magnetic field coming from the radiofrequency signal, the expression for the Lorentz force results

$$\mathbf{F}_{RF} = q(\mathbf{E}_{RF} + \mathbf{v} \times \mathbf{B}_{RF}) \quad (1.4.9)$$

where \mathbf{E}_{RF} and \mathbf{B}_{RF} are the electromagnetic fields of the RF signal.

Instead, the space charge forces can be understood from a quasi-stationary analysis of the electron repulsion forces that are driven by the Coulomb's law. Considering a system of n electrons within the beam traveling at a velocity $v \ll c$ with positions \mathbf{r}_i , the space charge force on a single electron can be written as

$$\mathbf{F}_{sc} = \frac{q}{4\pi\epsilon_0} \sum_{i=1}^n q_i \frac{\mathbf{r} - \mathbf{r}_i}{|\mathbf{r} - \mathbf{r}_i|^3}. \quad (1.4.10)$$

The effect of the focusing force by an external applied magnetic field is also described in terms of the Lorentz force as

$$\mathbf{F}_{foc} = q(\mathbf{v} \times \mathbf{B}_{foc}) \quad (1.4.11)$$

where \mathbf{B}_{foc} is the applied magnetic field.

The analysis of Eq. 1.4.8 permits to understand the concept of the beam bunching that is induced in the electrons as they interact with the SWS, the deviations that the electrons suffer when they travel immersed in the electromagnetic fields or how the electron beam can be confined by an external applied magnetic field to reduce the beam spread and oscillations.

For a simpler study of the effect of the forces in the behaviour of the electron beam, every term can be analysed separately. If only the contribution of the electromagnetic field induced by the RF signal is considered, this is $\mathbf{E}_{RF} \neq 0$ and $\mathbf{B}_{RF} \neq 0$ but $F_{sc} = 0$ and $F_{foc} = 0$, the equation of motion of the electrons takes the following form

$$m \frac{d\mathbf{v}}{dt} = q(\mathbf{E}_{RF} + \mathbf{v} \times \mathbf{B}_{RF}). \quad (1.4.12)$$

If the electrons are assumed to enter the interaction region with only longitudinal velocity, this is with velocity parallel to the traveling wave $\mathbf{v} = v_{\parallel}$, the acceleration can be easily split into longitudinal and transverse acceleration. The acceleration in the longitudinal direction, $a_{\parallel} = dv_{\parallel}/dt$, is then given by

$$a_{\parallel} = \frac{q}{m} E_{\parallel,RF}. \quad (1.4.13)$$

Eq. 1.4.13 represents a simple expression to understand the electron beam bunching that is formed in the electron beam due to the longitudinal RF electric field changing the sign periodically along the SWS and which is required to obtain amplification of the RF signal in a TWT as schematically shown in Fig. 1.4.3. With this expression, it can also be understood that if the longitudinal electric field is not uniform within the beam volume, the electrons, depending on their position within the beam, will be accelerated differently and then not bunched uniformly.

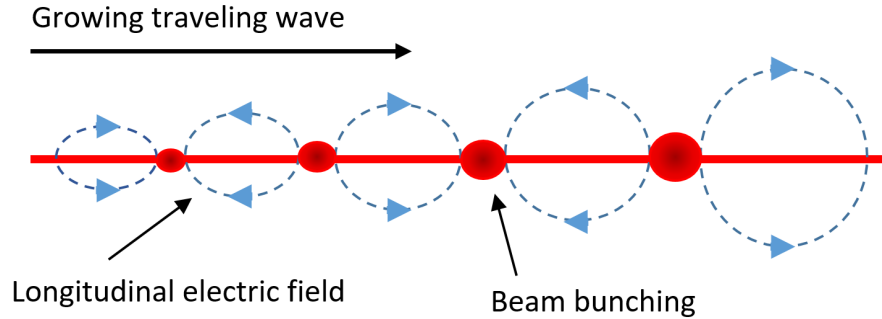


Figure 1.4.3: Illustration of the growing wave and the electron beam bunching.

Instead, the transverse motion of the electrons induced by the RF electromagnetic fields is described by the transverse acceleration or perpendicular to the traveling wave, $a_{\perp} = dv_{\perp}/dt$, as

$$a_{\perp} = \frac{q}{m} (E_{\perp,RF} + v_{\parallel} \times B_{\perp,RF}), \quad (1.4.14)$$

which can be also written as a centripetal acceleration $a_{\perp} = v_{\perp}^2/r$ with radius r , meaning that the electrons will follow a circular movement as a consequence of the induced RF electromagnetic fields.

Depending on the characteristics of the electromagnetic field of the SWS, the transverse forces applied to the electron beam will affect in a different degree to the transmission of the electron beam along the TWT. If the electromagnetic field is not symmetric with respect to the electron beam, this will make the electrons, depending on their position within the beam, to interact with different field intensities and thus being accelerated at different radial velocities.

The electron beam geometry also plays an important role in the correct transmission of the electron beam. For instance, a beam that follows the circular motion of the electrons, such as the cylindrical beam geometry, will travel along the tube requiring focusing forces of less intensity. On the other hand, for a beam geometry such as the sheet beam, where the beam does not follow a radial symmetry, the focusing forces will be less effective due to the centripetal forces that tend to rotate the beam and stronger focusing forces will be required to transmit the electrons along the interaction region in the TWT and avoid undesirable deviations.

Considering now only the effect of the space charge forces as described in Eq. 1.4.10, the acceleration of the electrons within the beam will be proportional to the sum of the distances between them according to

$$\mathbf{a}_{sc} = \frac{q}{4\pi\epsilon_0 m} \sum_{i=1}^n q_i \frac{\mathbf{r} - \mathbf{r}_i}{|\mathbf{r} - \mathbf{r}_i|^3}. \quad (1.4.15)$$

Therefore, the electrons traveling close to the surface of the electron beam will experiment a higher force than those that are surrounded by greater number of electrons whose force components can cancel out. This may force the electrons to follow, for instance, a more elliptical motion instead of a circular one, adding more difficulties to a proper transmission of the beam along the traveling wave tube. The electron density is particularly important in this case, as the space charge force will be higher as more electrons are contained in the beam. The beam geometry is also needed to be taken into account, as the further the electron from the centre of the beam, as is the case of the sheet beam in comparison with a cylindrical one, the higher will be the sum of the repulsion forces at the extremes of the beam as schematically shown in Fig. 1.4.4.

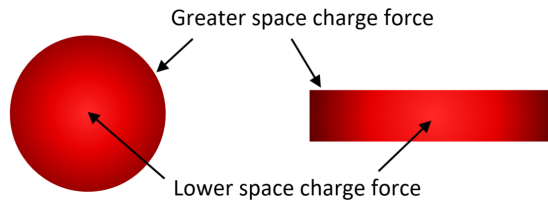


Figure 1.4.4: Space charge force on a cylindrical and a sheet electron beam.

The effect of the space charge force makes the electron beam to quickly diverge making essential to apply focusing forces in order to confine the beam and permit a proper transmission along the traveling wave tube. The focusing forces are commonly applied by means of an external sinusoidally varying magnetic field along the longitudinal direction $\mathbf{B}_{foc} = B_{\parallel}$. This magnetic field helps compensate the effect of the transverse acceleration of the electrons created by the RF electromagnetic fields and the space charge force by an additional transverse acceleration which takes the following expression

$$a_{\perp} = \frac{q}{m}(v_{\perp} \times B_{\parallel}). \quad (1.4.16)$$

The magnetic flux level that produces a magnetic force that exactly balances the space charge force is called the Brillouin flux and depends on the cross-sectional area A , current I and voltage V of the electron beam according to

$$B_B = \sqrt{\frac{\sqrt{2}}{\epsilon_0} \left(\frac{m}{q}\right)^{3/2} \frac{I}{A \sqrt{V}}}. \quad (1.4.17)$$

Increasing the beam current and reducing the beam voltage or the beam cross section will need of stronger magnetic focusing forces to keep the beam traveling tight.

A further analysis of the electron beam dynamics, including simulations with a cylindrical and a sheet beam, will be performed in Sec. 3.3.

1.4.3 Main slow wave structure parameters

The slow wave structure is the most important component in a TWT and drives the final performance of the tube. The role of the SWS is to slow down the RF signal to a phase velocity similar to that of the electron beam. As explained in Sec. 1.4.1, once both the phase velocity of the signal and the velocity of the electrons is comparable, amplification begins to occur in a TWT. The configuration of the SWS will determine the velocity (voltage) at which the electrons need to be accelerated, the efficiency and degree of the amplification and the correct transmission of the RF signal along the TWT. Therefore, a proper knowledge of the main properties of a SWS is fundamental for the design of the TWT.

Dispersion

In order for amplification to occur in a TWT, the electromagnetic wave on the RF circuit must travel at a velocity close to that of the electron beam. In a dispersive circuit, the velocity of the wave changes with frequency, reducing the gain at frequencies different than the optimum ones and limiting the bandwidth of the TWT.

The dispersion of a given SWS can be understood based on the relation between the phase velocity of the electromagnetic wave, v_p , and its variation with frequency, f , as

$$v_p = \frac{\omega}{\beta} \quad (1.4.18)$$

where $\omega = 2\pi f$ is the angular frequency and β is the propagation constant.

To determine if the dispersion of the SWS is low enough to provide amplification over a wide band, dispersion curves are typically presented together with the electron beam line. The velocity of the electrons in the beam, v_e , is a function of the accelerating voltage, V , independent on the frequency of operation, and given by the following expression for non-relativistic electrons

$$v_e = \sqrt{\frac{2qV}{m}}. \quad (1.4.19)$$

As discussed in Sec. 1.4.1, in order to obtain amplification in a TWT, $v_e \gtrsim v_p$. The band of frequencies for which both velocities fulfil that condition is called region of synchronism. Out of this region, the exchange of energy between the RF signal and the electron beam is not optimum and gain starts to decrease.

These concepts are schematically shown in Fig. 1.4.5.

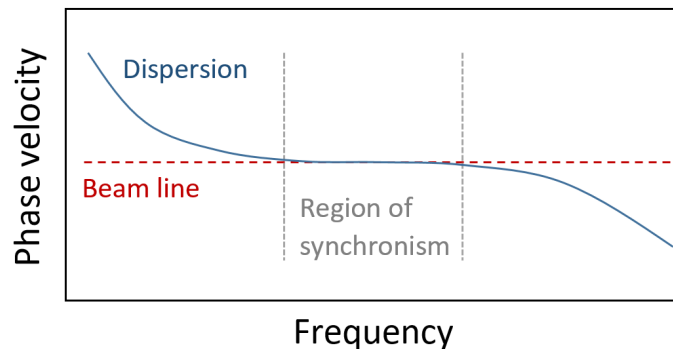


Figure 1.4.5: Variation of the wave phase velocity with frequency for a given SWS and beam line.

A SWS with low dispersion would be ideal for targeting wide-band TWTs. In addition to this, a low phase velocity implies that the TWT needs to operate with a reduced beam voltage. A low beam voltage permits to use lightweight and compact high voltage power suppliers.

Interaction impedance

The interaction impedance of a SWS determines how efficient is the exchange of energy between the electromagnetic wave and the electron beam. A high interaction impedance is desirable in order to increase the efficiency and the gain per period of

the SWS in order to produce more compact and lightweight TWTs. Mathematically, the interaction impedance of a SWS is defined as

$$K = \frac{|E|^2}{2\beta^2 P} \quad (1.4.20)$$

where E is the component of the electric field along the electron beam direction, β is the propagation constant of the electromagnetic wave and P is the power flow through the structure.

S-parameters

The S-parameters permit to properly design the structure and coupling transitions by understanding how the electromagnetic wave propagates through the full structure. Considering a two-port system, the electromagnetic signal, through their way from port 1 to port 2, will be attenuated and suffer losses as a consequence of the intrinsic properties of the medium where the signal travels through. The part of the signal that is transmitted to port 2 and the part that is reflected to port 1 can be quantified by the S-parameters. The S-matrix for a two-port system is defined as [22]

$$\mathbf{S} = \begin{pmatrix} S_{11} & S_{12} \\ S_{21} & S_{22} \end{pmatrix}, \quad (1.4.21)$$

where the S_{ij} components of the matrix permit to quantify the transmission and reflection of the electromagnetic wave.

Schematically, the transmission/reflection through a two-port system can be represented as in Fig. 1.4.6. If an input signal applied to port 1 has an amplitude a_1 and no signal is applied to port 2, thus $a_2 = 0$, the ratio of the signal that is transmitted is given by the coefficient $S_{21} = b_2/a_1$ where b_2 is the amplitude of the signal leaving port 2. The ratio of the signal that is reflected in port 1 is given by the coefficient $S_{11} = b_1/a_1$ where b_1 is the amplitude of the reflected wave.

A proper design of the SWS and the coupling transitions should maximize the transmission ($S_{21} \rightarrow 1$) and minimize the reflected signal ($S_{11} \rightarrow 0$).

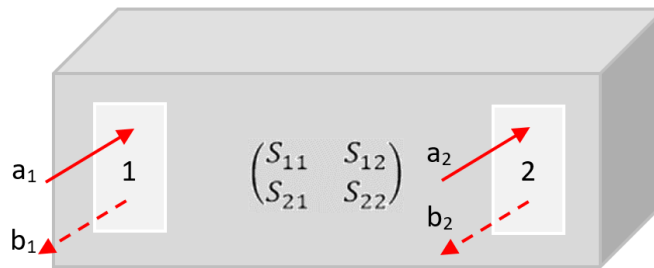


Figure 1.4.6: Incident and reflected signals in a 2-port system.

1.5 Space traveling wave tubes

Traveling wave tubes need to meet several criteria in order to be operational in space. Besides the requirement to deliver a certain power level to ensure a feasible link and the large bandwidth corresponding to the amount of information transmitted, space TWTs must be robust and sturdy to resist shocks and vibrations during its rocket launch and the aggressive space environment. TWTs also need to be reliable to be able to operate over its designed lifetime.

The reliability and overall performance of the TWTs have a major impact on the design and cost of the satellite. Space TWTs are typically expected to operate for 15-20 years on orbit but the finite sources of electrons in the cathode or defects during production may limit the aimed lifetime. A failure of the TWT can lead to a complete loss of the connection with the satellite and, therefore, the end of the service. To avoid this, additional TWTs that can take over during a sudden failure are included on payload, increasing the mass of the spacecraft. An extra kilogram on board may imply an increase of more than 10000 € in the launch and system costs per satellite. Similarly, a power saving of 1 W means saving more than 5000 € [23]. The efficiency, size and weight of a TWT are, therefore, critical features to consider for the design of low-cost satellite communication systems.

The TWT is still widely used in satellites and scientific spacecrafts, even though solid-state power amplifiers (SSPAs) have gained importance especially at low frequencies up to C-band (see Fig. 1.5.1). The more compact size, lighter weight and lower power supply requirements favour the use of SSPAs at low frequencies where very high power is not necessary. However, the use of TWTs at high frequencies to provide high power over a wide bandwidth is still the only option for deep space communications or telecommunications where high data rate is needed.

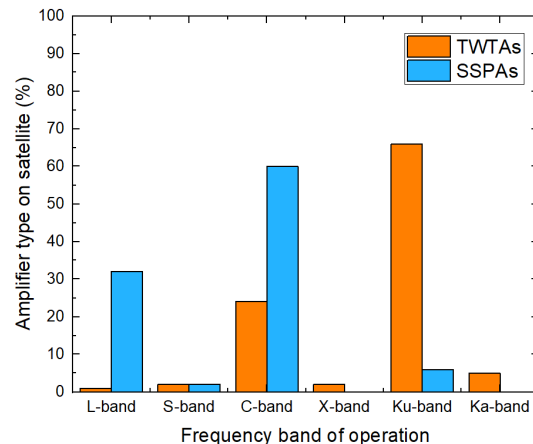


Figure 1.5.1: Percentage of TWT and SSP amplifiers on satellites for different frequency bands [24].

The American Global Positioning System (GPS), consists of a constellation of

thirty-one satellites orbiting on Medium Earth Orbits (MEO). To enable communication with ground stations, the satellites are equipped with SSPAs. However, more recent navigation systems, such as the European Galileo satellites [25], the Indian IRNSS [26] or the Japanese QZSS [27] use TWTs.

The European Copernicus Programme aims to establish a global, continuous and high quality Earth observation capacity. The space component of the programme comprises the Sentinel missions, a group of satellites equipped with X-band TWTAs for providing optical and radar imaging of Earth's surface and monitor the Earth's atmosphere composition [28].

The Voyager 1, launched in 1977 to study the outer Solar System and currently at a distance of more than 22×10^9 km from Earth (150 times the Sun-Earth distance), still communicates with us to receive commands and send data thanks to the three TWT amplifiers on board: one in S-band and two in X-band [29].

The Hubble Space Telescope, which has largely contributed to increase our knowledge about the universe, orbits on a Low Earth Orbit (LEO) and uses SSPAs. But its successor, the James-Webb Space Telescope, scheduled for launch in October 2021, will use K-band TWTs [30]. The incredible discoveries and contributions that this telescope will bring will spark a new era in astronomy and astrophysics, and the collected data will be transmitted to Earth thanks to TWTs.

In addition, the majority of deep space research missions used and will use TWT amplifiers. Some examples are mentioned in Tab. 1.5.1.

Table 1.5.1: TWTs on space missions.

Mission	Purpose	Years	TWT frequency band
Giotto [31]	Flyby the Halley comet	1985-1992	X
Cassini/Huygens [32]	Study Saturn	1997-2017	Ka
Rosetta/Philae [33]	Landing on comet	2004-2016	S and X
Venus Express [34]	Explore Venus	2005-2015	X
BepiColombo [35]	Observe Mercury	2018-	X and Ka
Solar Orbiter [36]	Investigate the Sun	2020-	X

1.6 Traveling wave tubes and slow wave structures at W-band

In recent years, different TWTs have been already demonstrated at W-band for research purposes, but no commercial W-band TWT can be found in the market. The first demonstration of W-band TWT was reported in 2008 [37]. The tested TWT provided a 1% bandwidth around 91 GHz, with 30 dB signal gain and over 250 W peak power and 100 W average power using a beam voltage of 20.8 kV with 316 mA current. The TWT used a folded waveguide slow wave structure whose schematic can be seen in Fig. 1.6.1.

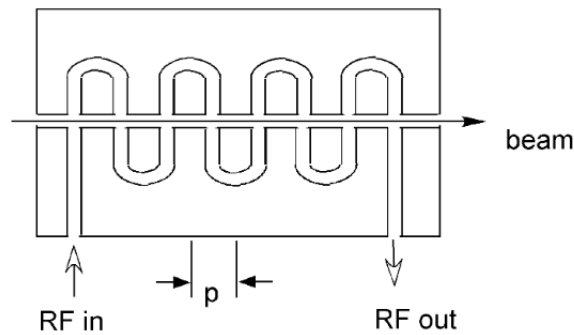


Figure 1.6.1: Schematic of a folded waveguide slow wave structure [38].

The folded waveguide SWS is created by folding a metal rectangular waveguide. The beam tunnel is obtained in the centre of the structure. Since the folded waveguide is obtained from a rectangular waveguide, the structure can be connected to rectangular waveguide flanges with only needing to adjust its width and height. Given the simple coupling, the folded waveguide provides very good transmission.

The interaction impedance of the folded waveguide in the order of 2Ω , implies that the structure needs to be relatively long if high gain is required, limiting its suitability for compact and lightweight devices. Yet, modifications on the basic design can increase the interaction impedance and the performance [39], [40].

Later in 2010, a new prototype TWT was assembled and tested at W-band offering 10 W output power with gain around 25-35 dB from 97 to 102 GHz [41]. A beam voltage of 16 kV and current of 50 mA was used.

In 2014, new tubes were manufactured by two different groups [42], [43]. The experimental test of the W-band TWT reported in [42] provided more than 25 W output power for an electron beam of 16 kV and 50 mA beam current. Two W-band TWTs prototypes were tested [43] providing an output power over 30 W with 10 GHz bandwidth from 90 to 100 GHz using an electron beam of 16 kV with 80 mA current.

Another W-band folded-waveguide TWT was demonstrated in 2017 [44]. The novelty of this work was the inclusion of a phase velocity tapering to improve the interaction circuit and the electronic efficiency. The test was performed using an electron beam voltage of 22.5 kV with beam current 189 mA. With this configuration, the TWT provided a minimum of 250 W output power in the band from 90 GHz to 98 GHz.

The most recent W-band folded-waveguide TWTs were published in 2019 [45], [46]. A picture of the [45] prototype tube can be seen in Fig. 1.6.2. This TWT provided gain over 30 dB and output power over 60 W from 94 to 110 GHz using a beam voltage of 21.88 kV and beam current 160 mA. Instead, the TWT from [46] was designed to operate from 83 to 86 GHz with output power above 30 W for an electron beam voltage of 17 kV.

A folded waveguide SWS was also designed and fabricated purposely for 71-76 GHz satellite communications with predicted gain and output power around 40 dB

and 100 W, respectively [47]. The test samples were fabricated using high precision CNC milling showing good agreement with simulations. The beam voltage was around 15 kV.

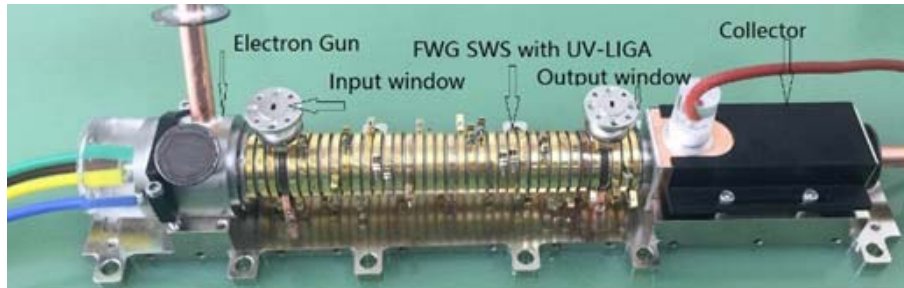


Figure 1.6.2: Picture of the FWSWS TWT built in [45].

The folded waveguide is the predominant SWS for high-frequency TWTs due to its great performance providing high levels of gain and output power with a relatively easy fabrication and assembly. Even though the interaction impedance is low, the dispersion of the structure is relatively low and permits to obtain an approximately constant gain and output power over a wide bandwidth. The folded waveguide SWS also has the disadvantages of requiring a high beam voltage >10 kV and high precision techniques with tolerances in the order of a few microns for manufacturing the structure.

Other works have proposed novel alternative SWSs that look promising at W-band but have not been tested in a TWT yet.

A staggered double vane SWS is presented in [48]. This structure consists of two vane arrays that are added to the top and bottom planes of the waveguide (see Fig. 1.6.3). A sheet electron beam travels through the space between the gratings. The dispersion of this SWS is low but the beam voltage required is also very high over 20 kV. The interaction impedance is also low at W-band. A tapering is required at the ends of the structure in order to couple the electromagnetic mode coming from the waveguide port. The large signal results show promising performance with output power over 1 kW and gain close to 40 dB over 5 GHz at W-band.

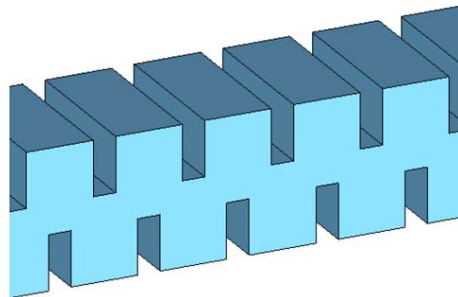


Figure 1.6.3: 3D model of the staggered double van SWS [48].

Another SWS that can be used at W-band is the double corrugated waveguide [49], which is currently being studied at Lancaster University. The structure consists of two rows of metal pillars enclosed inside a rectangular waveguide, as shown in Fig. 1.6.4, where the electron beam travels along the space between the pillars. The hybrid mode of the structure is coupled into the waveguide mode by tapering of the pillars. The double corrugated waveguide benefits from a broad bandwidth and a simple fabrication using high-precision processes. The SWS with reduced number of periods was fabricated at W-band showing good agreement between experimental results and simulations. Large signal simulations give great output power around 70W and gain close to 30 dB for a two-section of the double corrugated waveguide. This kind of SWS requires slightly lower beam voltage than the folded waveguide for a similar low interaction impedance around 1Ω .

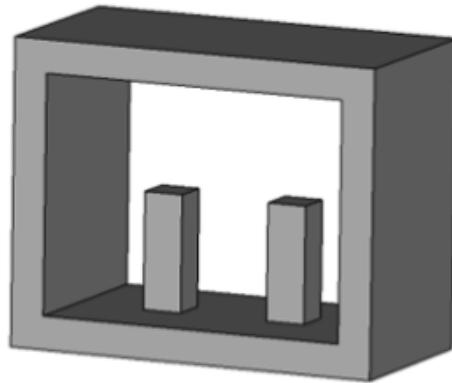


Figure 1.6.4: Unit cell of the double corrugated waveguide [49].

A different novel SWS design is described in [50]. This SWS is based on a rectangular waveguide with H-plane and E-plane loaded metal corrugations as seen in Fig. 1.6.5. The structure is suitable to be manufactured using high-precision techniques and offers high power and wideband operation. The structure was fabricated at W-band showing good correlation in the S-parameters measurements. Large signal simulations show 24 dB gain along the 89-101 GHz bandwidth. The structure makes use of a high 20 kV electron beam voltage with low interaction impedance around 1Ω .

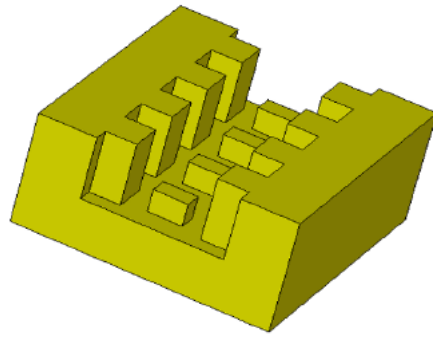


Figure 1.6.5: Schematic of the H-plane and E-plane loaded SWS [50].

All the slow wave structures presented in this section have a few things in common: they are completely made of metal, require a high-voltage electron beam over 10 kV, high-precision fabrication techniques with tolerances in the order of a few microns and offer low interaction impedance with values around 1Ω .

A high beam voltage directly implies the consumption of high power for the operation of the TWT and the use of bulky power supplies. The low interaction impedance means a low gain per period and, therefore, the SWS needs to be made with a great number of periods in order to provide high gain which may increase the size and mass of the TWT. These two features, as previously discussed in Sec. 1.5, correspond to an increased cost in the launch and operation of the satellite. The need of high-precision fabrication for the structure also typically requires the use high-cost procedures and machinery that may increase the cost in case simpler fabrication methods were valid.

1.7 Summary

The first chapter has provided the basis for understanding the importance of satellite communications and the role of the TWT for amplifying the signals before transmission. Since its conception in the middle of the XX century, the interest and research on TWTs quickly escalated to become the most important vacuum tube for telecommunication purposes. Nowadays the TWT is still widely used for long-range links where a lot of information needs to be sent and in deep-space missions.

In order to cope with the increasing demand of services that require to send and receive huge amounts of information, increasing the operation bandwidth and, then, the channel capacity, has become of fundamental importance. The microwave spectrum has started to be insufficient and the mm-wave range is gaining in interest for the next generation of telecommunication satellites. The Ka-band has been already exploited and the next logical step is to move up to V-band. However, given the presence of the oxygen peak around 60 GHz, the huge atmospheric attenuation makes this band to be more suitable for inter-satellite links. Therefore, the next and promising candidate is the W-band. The assigned downlink and uplink frequency

bands (71-76 GHz and 81-86 GHz, respectively) promise to offer a 5 GHz bandwidth with high data rate transfer and a favourable attenuation window.

Targeting higher frequencies has meant a great hindrance for the use of helix geometries as SWSs for TWTs given the impossibility to manufacture such structures due to the small dimensions. The focus has been, then, set on the investigation and development of novel SWSs that are able to provide similar performance as the helix. In that regard, a few TWTs have been already demonstrated at W-band, all of them making use of folded waveguide SWSs. Other full metal alternatives have been also proposed. These SWSs are characterized by the high beam voltage required to achieve amplification over 10 kV, the low interaction impedance close to 1Ω and the necessity of high precision fabrication methods with tolerances in the order of a few microns.

2. The meander line as slow wave structure for traveling wave tubes

The meander line slow wave structure, also suitable for W-band traveling wave tubes, has been deeply studied during the last decade given its numerous benefits. Some of them are, for example, the possibility to use low-voltage electron beams, the high interaction impedance or the straightforward manufacture.

This chapter provides a thorough study of the meander line. It will be performed by the analysis of the main characteristics of these delay lines and a profound literature review containing predominantly cold and hot simulations, this is analyzing the performance of the meander line SWS without and with the electron beam, respectively. Various meander line topologies and alternative configurations that can potentially improve their performance will be described. Different approaches will be presented for the design of a suitable transition between meander lines and waveguides to permit an easy insertion and extraction of the electromagnetic signals to the traveling wave tube. Finally, the main microfabrication techniques that are commonly used to fabricate structures such as the meander line will be briefly described.

2.1 Meander line slow wave structures

The meander line SWS, in its standard configuration, consists of a dielectric substrate where a serpentine-shaped metallized layer has been patterned as shown in Fig. 2.1.1. The meander line provides some advantages in comparison with the full-metal SWS alternatives. They can theoretically match their performance while needing a much lower beam voltage and offering much higher interaction impedance. This has direct implications for reducing costs on space missions considering the lower power consumption and the possibility to produce more compact and lightweight TWTs. The fabrication of such structure is also straightforward by means of standard microfabrication techniques and its suitability for low-cost and high-volume production make the meander line very interesting for its potential use for W-band satellite communications.

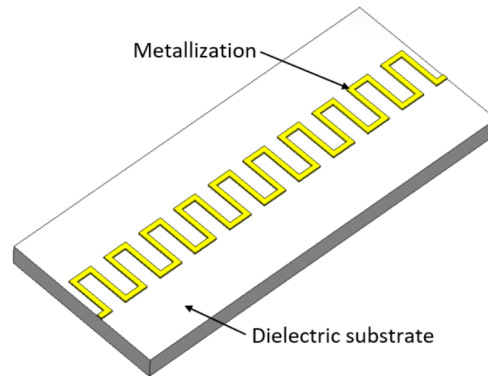


Figure 2.1.1: Model of a conventional meander line slow wave structure.

2.1.1 Dispersion

The electromagnetic wave travels in a meander line through the medium above the metallization and the substrate. This two-media nature of the meander line causes the electric and magnetic field, E and H , to have longitudinal components, making the dominant mode of the meander line to be a hybrid mode. This mode is referred to as quasi-TEM. The electromagnetic lines of the hybrid mode are schematically represented in Fig. 2.1.2.

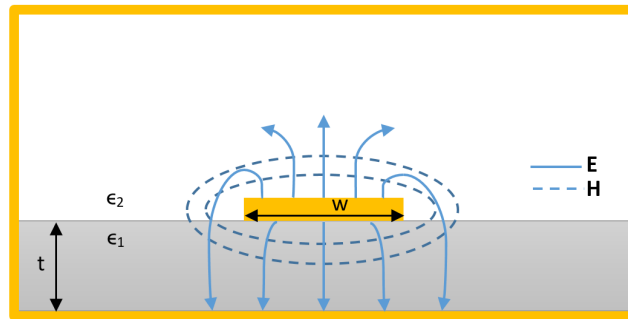


Figure 2.1.2: Electromagnetic field lines of the quasi-TEM mode of the meander line.

Meander lines have higher dispersion than other SWSs, this means that the phase velocity variation is greater when increasing frequency. A plot following the relationship in Eq. 1.4.18 takes the form of Fig. 2.1.3 for meander lines SWSs. In comparison with low-dispersive structures, the phase velocity of the meander line dramatically decreases with frequency, making meander lines to have a narrow frequency band for amplification in a TWT. This can be explained by defining a frequency-dependant meander line permittivity $\epsilon_{eff}(f)$ and its relation with the phase velocity as

$$\epsilon_{eff}(f) = \frac{c^2}{v_p^2(f)}. \quad (2.1.1)$$

This quantity takes into account that most of the electric fields are constrained within the substrate and, as frequency is increased, the fields become even more concentrated in the region underneath the metal strip. Therefore, the effective permittivity increases with frequency and, as a consequence, the electromagnetic wave is progressively slowed down.

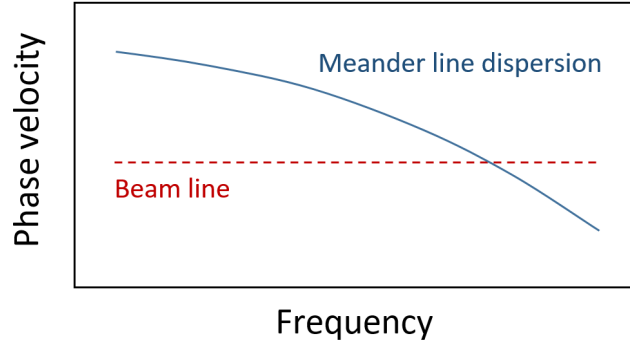


Figure 2.1.3: Variation of the wave phase velocity with frequency for meander lines and a beam line.

The material and dimensions of the substrate as well as the dimensions of the metallized serpentine play an important role on the dispersion curves of meander line slow wave structures. This can be also studied by analyzing the effective permittivity at the low-frequency limit, which can be approximated by [22]

$$\epsilon_{eff} = \frac{\epsilon_1 + \epsilon_2}{2} + \frac{\epsilon_1 - \epsilon_2}{2} \frac{1}{\sqrt{1 + 12t/w}}. \quad (2.1.2)$$

where ϵ_1 and ϵ_2 are the permittivity of the substrate and the permittivity of the medium above the substrate, respectively, t is the thickness of the substrate and w is the width of the meander line as seen in Fig. 2.1.2.

The effective permittivity and thus the phase velocity will vary depending on the substrate permittivity and thickness and also on the strip width. As the permittivity of the substrate ϵ_1 is higher, the effective permittivity increases, reducing the phase velocity. Similarly, as the thickness of the substrate t is reduced or the width of the metallization w is increased, the phase velocity of the meander line is also reduced. A further analysis containing simulations results regarding the optimum meander line configuration will be shown in Sec. 3.1 and 3.2.

Another way to represent the dispersion of a circuit is by means of a Brillouin diagram. This kind of plots displays frequency f versus the propagation constant β or the phase shift βp and permits to obtain more information than the phase velocity plot in Fig. 2.1.3. Fig. 2.1.4 shows an example of the typical Brillouin diagram for meander lines with the three first modes along a beam line. The first cross-point corresponds to the first mode of the electromagnetic signal and will produce the amplification of

the forward-wave over a limited frequency range. The beam line also crosses higher-order modes that corresponds to backward-wave signals of different amplitudes at higher frequencies that may induce oscillations in the amplified forward-wave. The amplitude of the first-mode reflection signal is typically small enough to be ignored as long as the signal and the beam parameters are properly selected. The meander line can be conveniently designed so that the beam line intersects the higher-order modes at frequencies much higher than that of the intersection with the fundamental mode, thus limiting the extent of the backward wave oscillations.

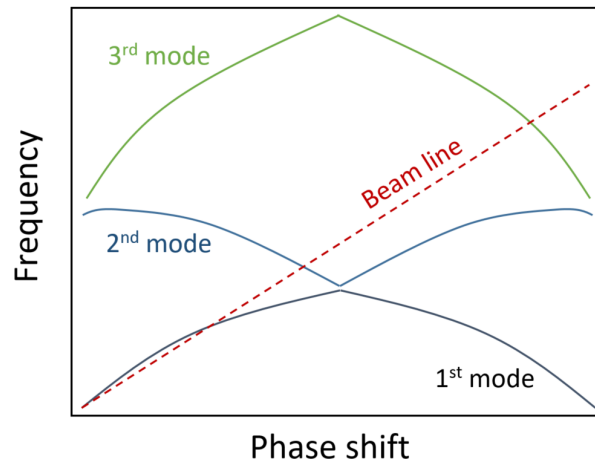


Figure 2.1.4: Brillouin diagram of meander lines representing the first three modes and a beam line.

2.1.2 Interaction impedance

Following the dispersive characteristics of the meander line, the interaction impedance also varies with frequency. The higher concentration of electric fields within the substrate as the frequency is increased will decrease the intensity of the interaction in the area where the electron beam travels. This implies a different interaction between the electric field and the electron beam depending on the frequency, limiting the performance within the bandwidth available for amplification.

The dimensions and materials of the substrate and the metallization of the meander line also play an important role on the interaction impedance of the structure. Similar to the analysis of the phase velocity, a study using simulations regarding the dependence of the interaction impedance on the meander line configuration will be carried out in Sec. 3.1 and 3.2.

2.1.3 S-parameters

The S-parameters for a two-port symmetric structure, measured in decibels, typically behave as in Fig. 2.1.5 for meander line SWSs. The reflection and transmission

coefficients, S_{11} and S_{21} , present noticeable oscillations as a consequence of reflections in the transmission line caused by impedance discontinuities or mismatches.

The amplitude of the ripples in the reflection coefficient, S_{11} , depends on the difference between the port impedance and the impedance of the meander transmission line itself. The greater the mismatch, the more appreciable the oscillations will be. The ripples in the transmission coefficient, S_{21} , are synchronous to those in S_{11} but lower in amplitude bearing in mind that both coefficients are related as $S_{11}^2 + S_{21}^2 = 1$ assuming a lossless transmission line.

The frequency interval between two consecutive oscillations is inversely proportional to the delay time of the reflection. Physically, the longer the meander line, and hence the greater the round trip delay time, the closer the ripples will be. This effect repeats at frequencies where the phase delay is a multiple of one cycle.

A convenient design of the coupling transitions helps reduce the modulation of the ripples and produce smoother curves.

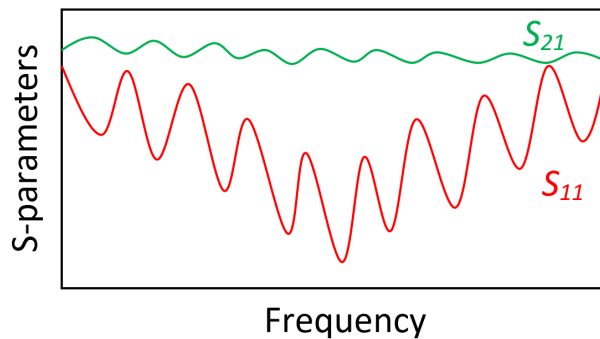


Figure 2.1.5: Typical transmission and reflection coefficients in meander line SWSs.

2.1.4 Meander line topologies

The first use of planar meander lines as SWSs for W-band TWTs was reported in 2005 [51]. The meander line was proposed as an alternative to a folded waveguide and compared with simulations offering 10 times higher interaction impedance and 50% increased RF efficiency. An E-field probe approach was proposed to couple the electromagnetic field coming from the waveguide. The TWT was being developed at that time and expected to be tested in 2006, but no further result was published afterwards.

The study of the meander line gained in importance from 2012 on, when modifications on the meander line topology, on the substrate and on the surrounding metal cavity started to be considered.

A novel V-shaped meander line (see Fig. 2.1.6) was proposed in [52] and compared with the standard meander line shape. This topology shows better dispersion relation, it is designed for an optimum beam voltage of only 3.7 kV and gives high interaction impedance around 20Ω within W-band. The proposed fabrication method

consist of sputtering a $5\ \mu\text{m}$ thick copper layer on a $50\ \mu\text{m}$ boron nitride substrate which is etched to obtain the final meander line. No coupling structure is described for the meander line. A sheet electron beam is used as particle source with a magnetic field of 1.4 T, a value close to the strongest magnets compatible with vacuum applications. Large signal results show peak output power around 90 W at W-band.

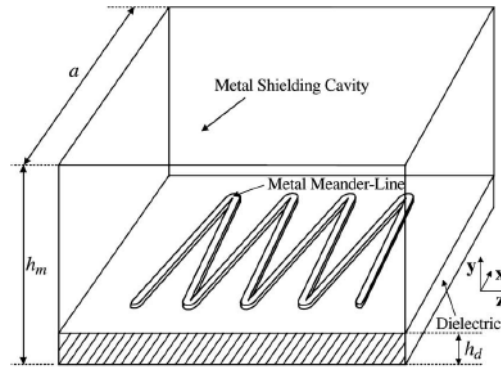


Figure 2.1.6: Drawing of the V-shaped meander line SWS [52].

The same group also presented a rhombus-shaped meander line [53] where the dielectric rod is metallized to form the meander line as seen in Fig. 2.1.7. The reduced dimensions of this structure allows to obtain increased cold bandwidth in order to operate around 140 GHz. A suggested fabrication method is not proposed in the work, only the use of a boron nitride substrate to produce the dielectric rods is mentioned. Also, no coupler for the meander line is given. A sheet beam with current of 90 mA is used as particle source, which allows to obtain high output power close to 100 W in the range 136-148 GHz.

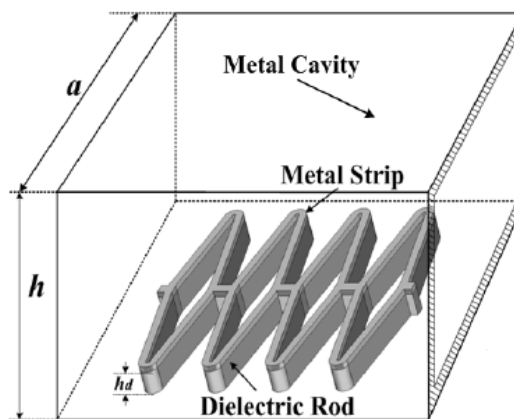


Figure 2.1.7: Model of the rhombus meander line SWS [53].

A meander line similar to the traditional standard line was reported in [54]. The corners of the traditional meander line are rounded for this design, producing the

named U-shaped meander line as shown in Fig. 2.1.8. The copper metal strip is produced on top of the dielectric substrate. The interaction impedance of this structure is around 15Ω at Ka-band being this the designed frequency range. No coupler design is reported. Outstanding output power close to 200 W is obtained with gain 33 dB using a sheet beam of around 5.75 kV and 140 mA current.

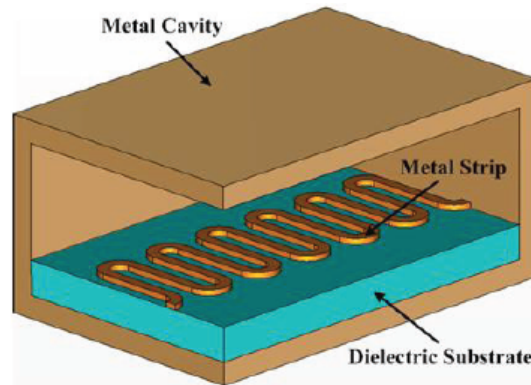


Figure 2.1.8: Model of the U-shaped meander line SWS [54].

A meander line with S-shaped topology (see Fig. 2.1.9) with operation at W-band is presented and compared with the traditional meander line shape [55]. The substrate is designed to be made of boron nitride and the metal strip in copper. The dispersion curve shows a less pronounced slope whereas the interaction impedance is enhanced from 40 GHz on giving around 30Ω at W-band. Scattering results are provided without a coupler design and large signal results are not presented.

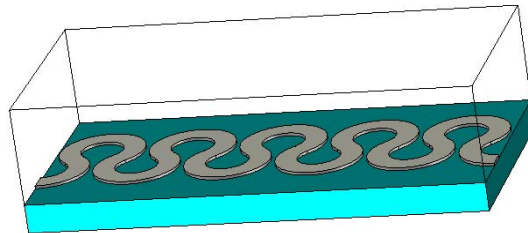


Figure 2.1.9: Model of the S-shaped meander line SWS [55].

Another new meander line topology with the shape of the greek letter Ω (see Fig. 2.1.10) was presented in [56]. This shape is compared with a conventional line of the same dimensions showing worse dispersion but higher interaction impedance within the V-band frequency range. The distance between two consecutive strips of the omega shape line is only $10 \mu\text{m}$ which could compromise the correct fabrication of the structure. The material of the substrate is not given nor a suitable coupler is proposed. The large signal simulations make use of a sheet electron beam with 1 T

magnetic field. The peak output power presents a peak value around 90 W with gain around 30 dB but high variation within the operational bandwidth.

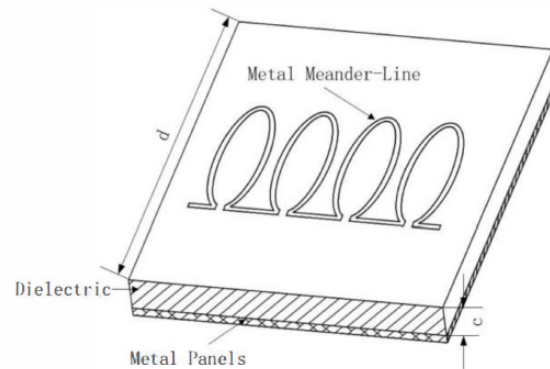


Figure 2.1.10: Schematic of the Ω -shaped meander line SWS [56].

Similar to the U-shaped meander line, a ring-shaped meander line designed at Ka-band is presented in [57]. The ring-shaped meander can be seen in Fig. 2.1.11. A high beam voltage of 11.4 kV is used for the sheet electron beam with 200 mA current and 1 T focusing magnetic field. The large signal analysis shows results with more than 230 W and 39 dB peak output power and gain respectively. The dimensions and materials of the structure are not given.

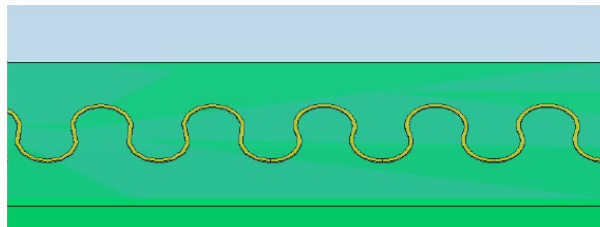


Figure 2.1.11: Schematic of the ring-shaped meander line SWS [57].

The same authors also presented a ring-bar planar microstrip (shown in Fig. 2.1.12) that provides wider cold bandwidth in comparison with the traditional meander line [58]. The structure doubles the cold bandwidth from 25 to 50 GHz. This increase in bandwidth implies also a rise on the operating voltage of the structure, from around 2 kV to more than 5.5 kV. The interaction impedance curve shows lower values for the whole bandwidth in comparison with the standard structure.

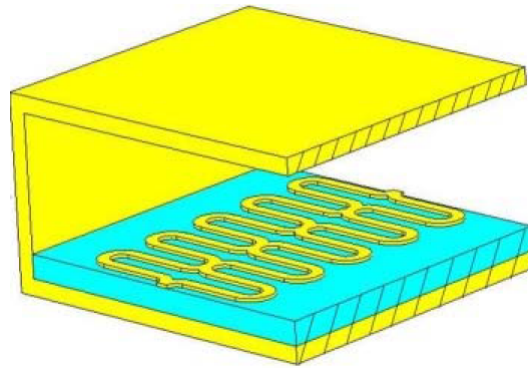


Figure 2.1.12: Schematic of the ring bar shaped meander line SWS [58].

Two new meander line topologies were proposed in [59] suitable for W-band. The dispersion and interaction impedance characteristics are compared with the traditional meander line of the same dimensions. Both shapes show broader cold bandwidth and flatter dispersion but lower interaction impedance. The dimensions and materials of the structure are not reported.

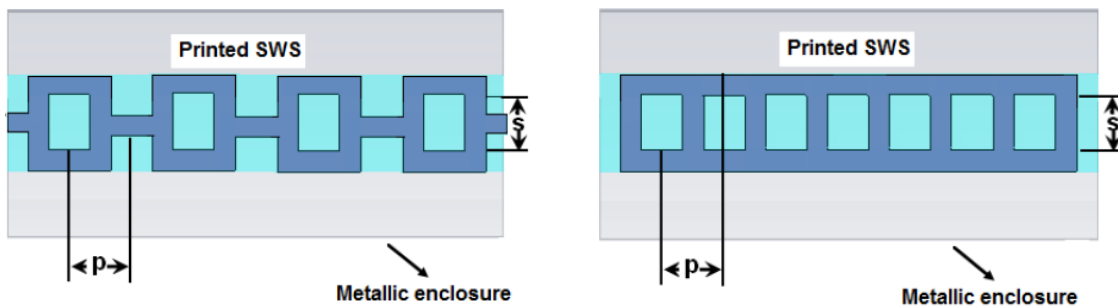


Figure 2.1.13: Model of the ladder meander lines [59].

The few examples already analysed have shown, by simulations, that meander lines can operate using a low beam voltage and provide high interaction impedance. The new topologies are focused on improving the interaction impedance which, in general, worsens the dispersion of the meander line and reduces the available bandwidth. To obtain high gain and output power, most of the works make use of high-current sheet electron beams which require a more complicated electron gun design and to focus the beam with strong magnetic fields.

Only a few works regarding planar slow wave structures have presented experimental results. Fabricated and tested meander lines have been recently shown in [60] and [61].

A new configuration for a Ka-band V-shaped meander line is reported in [60], including experimental results. The fabrication process follows a different approach in order to avoid dicing the individual slow wave structures and using a metal enclosure

for testing. On-wafer measurements are performed using coplanar waveguide sections at the end of the meander line. The meander line and the coplanar waveguide transitions are realized by sputtering a $2\ \mu\text{m}$ copper layer on quartz wafer followed by photolithography and etching. The final fabricated structures can be seen in Fig. 2.1.14. Cold simulations at Ka-band show a operation voltage of less than 4 kV with a pronounced dispersion slope. The interaction impedance values are around $17\ \Omega$. The experimental scattering parameters are in good agreement with the simulation results. Large signal simulations show gain around 20 dB with less than 15 W output power at Ka-band.



Figure 2.1.14: Fabricated V-shaped meander line SWS at Ka-band [60].

A different and novel planar shape was presented in [62]. This topology is designed as a symmetric structure with respect to the axial direction in order to enhance the interaction impedance. However, the dispersion curve for this meander line shows very poor results as the curve dramatically drops as the frequency increases. The metal strip is designed on top of a diamond substrate for W-band frequencies. The suitable beam voltage is very high at 16 kV. Large signal simulations show low gain and output power with 22 dB and 0.64 W, respectively. No coupler is shown in the analysis.

The same structure with some additions was fabricated and tested in [61]. The structure works in V-band and consists of a circular meander with a patch in the middle part in order to increase the interaction impedance. A $5\ \mu\text{m}$ copper layer is deposited on top of a quartz substrate using magnetron sputtering and, after that, CNC laser ablation is used to form the slow wave structure. A picture of the fabricated meander line is shown in Fig. 2.1.15. The measurements are carried out placing the extremes of the structure inside two waveguides. The experimental scattering measurements reveal good transmission at V-band. Large signal simulations show output power and gain close to 20 W and 40 dB, respectively, but the output varies considerably depending on the frequency given the poor dispersion of the structure. A beam voltage of 16 kV is used with 50 mA current and magnetic field of 0.35 T.

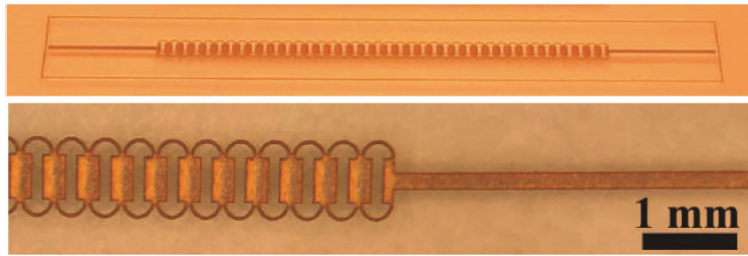


Figure 2.1.15: Novel fabricated meander line SWS at V-band [61].

The realization of a couple of planar meander lines has permitted to validate the simulations of transmission and reflection of the structures by the determination of the S-parameters experimentally. However, measurements of the phase velocity or the interaction impedance are not presented. In any case, the simulations using more realistic meander line SWS have shown a decrease in the gain and output power results compared to the previous simulated meander lines. The use of a cylindrical beam instead of a sheet beam for the simulations may be the reason for this lower performance.

2.1.5 Phase velocity tapering

Applying a phase velocity tapering has traditionally demonstrated to be an effective way to improve the performance of different SWS. This approach has been also applied to meander line giving good results.

In [63], the traditional meander line shape is optimized for higher frequencies at G-band (110-300 GHz). The meander line length is gradually increased with the objective of increasing the efficiency and performance of the structure. A sheet electron beam with 5 kV and 32 mA is used as particle source with a magnetic field of 1.3 T. The gain and output power are close to 40 dB and 50 W around 220 GHz, respectively.

This approach is also analysed in [64] and [65] for a log-periodic meander line. In [64], the structure consists of a fan-shaped dielectric slab and an angular log-periodic meander line metal strip corresponding to a standard planar meander line increased in length from one extreme to another (see Fig. 2.1.16). The dispersion results show a phase velocity with low variation within the frequency band. The operation voltage of this structure is very low, less than 2 kV. A radial sheet beam is used in the simulations to interact with the various meander lines. Gain around 20 dB is obtained from this structure. However, more than 100 W is obtained at Ka-band given the 1 W input power used. A radial sheet beam is used as particle source starting at the wider side of the meander line and finishing at the collector placed in the center of the structure. In the paper, 30 meander lines are designed on the surface of the dielectric substrate and it is assumed that all the signals are in phase at the input and output ports. This assumption would not be feasible in a realistic scenario as the repeatability of the fabrication method is compromised for

each meander and the outputs would be affected by the fabrication tolerances and the synchronism between the different lines. The radial sheet beam is also a theoretical design and no experimental results are provided.

The log-periodic meander line is deeply analysed in [65] without using any complicated configuration for the final design. To improve the efficiency of the log-periodic meander line, the straight 90° corners of the traditional meander line are trimmed away so that the meander strip is presented with two 45° corners or chamfers at every change of direction. The results show that the 45° chamfer microstrip slow wave structure offers lower reflection parameter and transmission loss than the single angle bended microstrip. 15 dB gain and 33 W output power are obtained at Ka-band using a radial sheet electron beam with 1.55 kV voltage.

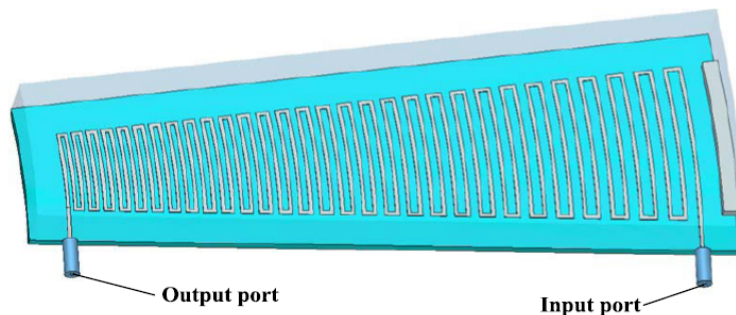


Figure 2.1.16: Model of the phase velocity tapered meander line [64].

The phase tapering approach is shown, in simulations, to improve the performance by increasing the efficiency using a relatively simple modification in the design. However, in order to obtain the most of this approach, a radial sheet beam needs to be used as particle source. This concept is theoretical and has not been demonstrated experimentally.

2.1.6 Double-substrate and 3D meander lines

Different research groups have explored the possibility of finding new configurations of the meander line that could enhance the efficiency and the performance for two different cases: accommodating a cylindrical beam or improving the results when using a sheet electron beam.

The first and simpler idea was to add a second substrate on top of the bottom one, leaving a channel for the electron beam in between. Following this approach, different works have been reported.

The standard V-shaped meander presented in [52] was adapted to a double substrate design in [66]. The bottom meander line is replicated at the top wall of the metal enclosure making both meander lines face each other and leaving a free channel in between for the electron beam as shown in Fig. 2.1.17. The symmetric structure offers enhanced electric field intensity at the position of the electron beam in comparison

with the single V-shaped meander. The dispersion curve for the double and single V-shaped strips coincide for the whole bandwidth. However, the double V-shaped meander line shows an enhanced interaction impedance by around 30% at W-band. The hot results for gain and output power are much better for the double V-shaped meander line providing more than 100 W output power using a sheet beam with voltage 4.57 kV and current 100 mA. Some difficulties are foreseen with this design for practical applications such as the alignment of the two halves and the synchronism of phase and amplitude of the signal coupled into the top and bottom halves of the circuit. No couplers are designed for this structure in the paper and a complicated approach is necessary to ensure synchronisation between the two halves.

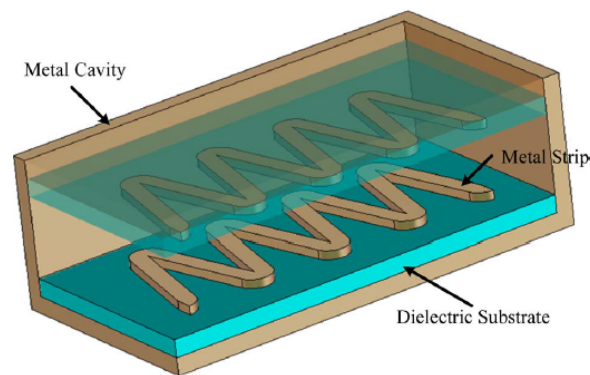


Figure 2.1.17: Model of double V-shaped meander line [66].

As an extension of the double V-shaped meander structure, the next step was to join top and bottom meander lines by some sort of pillars. One example was presented in [67] and is shown in Fig. 2.1.18. For this approach, cold simulations show a steeper dispersion curve at W-band but an increased interaction impedance by around 20%. A 6 kV, 200 mA sheet beam with high 1.5 T focusing magnetic field is used for the simulations. The hot results show improved gain, output power and efficiency with respect of the double V-shape meander line.

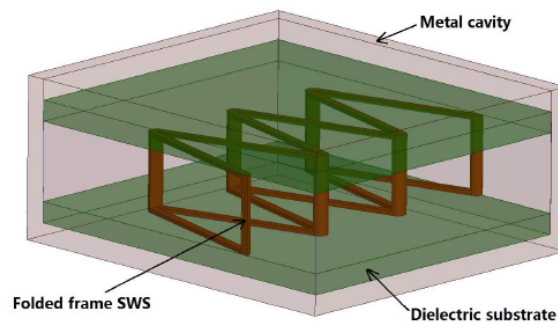


Figure 2.1.18: 3D view of the folded frame meander slow wave structure [67].

A similar configuration was also used in [68] as a continuation of the work in [64] adding a second log periodic meander line opposite to the bottom one showing enhanced interaction impedance at Ka-band.

A double-substrate meander line designed at W-band was also presented in [69]. The novelty of this work is the use of CVD diamond as substrate in order to achieve good heat relief and low dielectric loading and the use of a channel underneath the substrate (see Fig. 2.1.19) in order to increase the interaction impedance. Cold simulations show a great increment on the phase velocity and, therefore, the operation voltage up to 15.6 kV. The interaction impedance shows values around 20Ω . No coupler is presented in the work. Hot simulations show low gain around 15 dB for the whole bandwidth. A sheet beam is used as particle source.

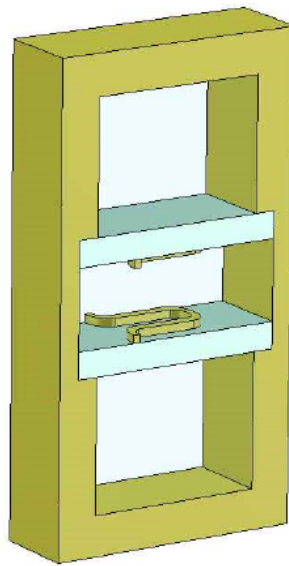


Figure 2.1.19: 3D view of a single period of the double meander with channels [69].

Others authors have suggested shifting one of the meander structures in respect to the other one [70], [71].

In [70], the slow wave structure on the top of the waveguide is shifted by half period along the axial direction with respect to the bottom meander line. A rectangular air channel is also established in the metallic shield underneath the substrates. This channel almost doubles the cold bandwidth of the structure. However, the phase velocity and the corresponding beam voltage is increased up to a value of 16 kV at 92 GHz. The interaction impedance at this frequency is close to 17Ω . Moreover, rectangular patches are added to every period of the meander line which results in an increase of a factor of two on the interaction impedance value. Gain and output power are around 35 dB and 15 W, respectively, but with great variation within the band as a result of the poor dispersion curve for this structure.

Instead, in [71], a traditional meander line topology is inverted at the top part of the structure enhancing the coupling impedance by around 20% in comparison

with the single standard meander line. The structure is designed and simulated for frequencies up to 45 GHz and only cold results are presented. According to the results, the dispersion curve is improved in respect of the single meander.

None of these 3D meander line slow waves structures have been fabricated and tested except for the works presented in [72] and [73] by the same group.

A three-dimensional slow wave structure was designed and fabricated consisting of planar helix with straight-edge connections and operating at W-band. The structure consists of three parts, the bottom and top horizontal layers and the vertical pillars that connect the two horizontal layers. To create the planar helix, a liftoff process is used to produce the metal layers on top of a silicon substrate. The pillars are formed by lithography and subsequent electroplating. A second layer is deposited on the thick photoresist for electroplating of the third metallization layer and forming the suspended helix bridges. The structure is finally released after several etching processes. A view under the microscope of the structure is shown in Fig. 2.1.20. A coplanar feed is used as coupling structure between the three-dimensional helix and the waveguide ports. Good agreement is shown between the simulated scattering parameters and experimental results. The fabrication process present different challenges like the production of the high aspect ratio vertical pillars or the formation of the suspended helix bridges on top of the photoresist which requires a good connection between the pillars and bridges.

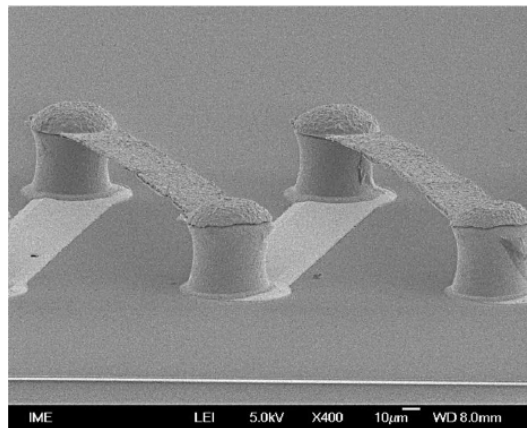


Figure 2.1.20: Perspective view of the 3D meander structure [72].

A similar design is developed in [73] at much lower frequency around 3 GHz in order to facilitate the fabrication process. The structure is compared with the double V-shaped meander line showing advantages in circuit attenuation, bandwidth, gain and efficiency. The structure is fabricated using a Roger 4003 printed circuit board and the measured scattering and dispersion are provided. The results for this structure are given for the frequency range from 2 to 4 GHz. The simulated dispersion curve is flatter and the interaction impedance is higher in comparison with the double V-shaped meander line. For the hot simulations, a cylindrical beam with 3.7 kV and

250 mA is used. The gain and output power are also improved for this structure. The experimental results of S-parameters and phase velocity are close to the simulated ones with the differences attributed to fabrication tolerances.

The investigation and development of the 3D structures has been shown to provide increased performance by the enhancement of the electric field intensity in the electron beam area. This approach is particularly useful for a cylindrical beam geometry which is seen to provide much better performance. The use of a sheet beam electron is also favoured by the addition of the extra dimension. However, the use of two or more independent meander lines is limited by the necessity of designing a coupling transition for such structures.

2.1.7 Modifications on the substrate

Another possibility for improving the performance of meander lines is to model the substrate in such a way that increases the interaction impedance and favours the overall interaction with the electron beam. Such designs are typically very complicated to fabricate using standard microfabrication techniques, however, different authors have proposed some structures.

A folded meander line is presented in [74]. A trench is produced in the substrate where the central part of the meander line is placed. The extremes of the strip are extended to the side walls of the substrate, making in this way a sort of three-dimensional meander line or folded meander line (see Fig. 2.1.21). Cold simulations are given for this structure which show slightly lower interaction impedance but flatter dispersion relation for Ka-band and W-band. This design presents different fabrication limitations, as the microfabrication methods available to grow the strip typically only are able to work in two dimensions. This process will involve either the connection between three separate substrates, every part with its corresponding fabricated strips, or a high aspect ratio LIGA process in order to grow the side strips from the bottom plane.

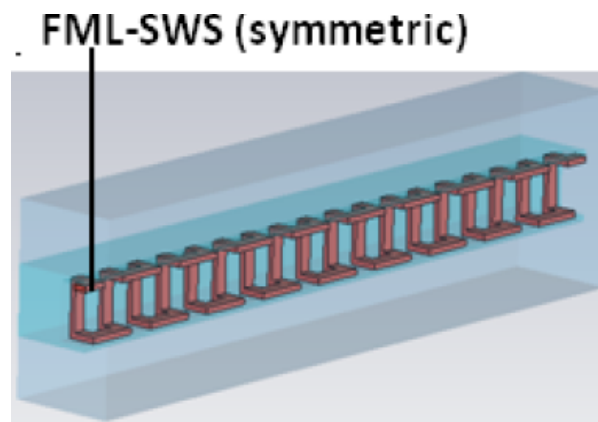


Figure 2.1.21: Schematic of the symmetric folded meander line [74].

The winding microstrip proposed in [75] also shows a different approach to the design of the structure as shown in Fig. 2.1.22. Considering the curvature of the substrate, standard fabrication techniques are not feasible taking into account the necessity of a flat surface to deposit and grow the metal strips. However, the results for the output power are good as this kind of design is optimized for a cylindrical electron beam that is surrounded by the metal strip and substrate.

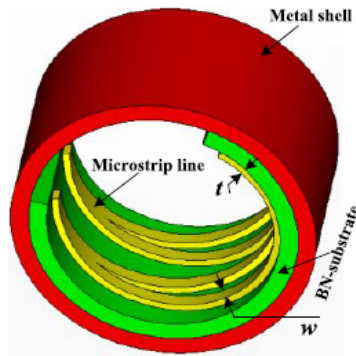


Figure 2.1.22: Model of the winding meander line [75].

The interaction impedance can be also increased by leaving the substrate only underneath the metallization and trimming away the remaining dielectric as was proposed in [76]. The fabrication of the meander line is based on the metallization of only the top of a high aspect ratio dielectric ridge. To do that, the majority of the dielectric is removed from beneath the metal so that the electric field intensity is increased above the metallization, where the beam propagates, for increased interaction impedance. The average interaction impedance for a cylindrical beam is increased to 13.3Ω from 4.5Ω of the simple configuration. The length of the meander is also reduced by more than 60% due to the increased efficiency.

The same configuration was simulated in [77] following the previously designed log-periodic meander line in [64]. A step further in this approach was proposed in [78] where the dielectric is embedded in the metallization (see Fig. 2.1.23), thus increasing the interaction impedance in around 50% in comparison with the standard meander line. For the hot analysis, a sheet electron beam is used as particle source with 6 kV voltage. The hot results show gain and output power at Ka-band close to 29 dB and 80 W, respectively.

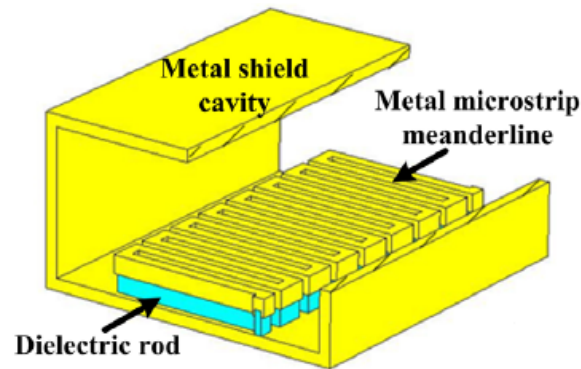


Figure 2.1.23: Model of the embedded meander line [78].

Modifications of the structure trying to surround the electron beam have been shown to be useful to improve the performance. The electric field intensity is increased in the area of the beam enhancing the interaction impedance and efficiency of the meander line. However, this kind of constructions require the use of more complicated fabrication processes, if feasible. Another option is to reduce the amount of dielectric substrate underneath the metallization. With this approach, the electric field is more concentrated on top of the metallization enhancing the interaction impedance where the beam travels. Again, this also increases the difficulty of the fabrication of the structure.

2.1.8 Attenuators on meander lines

In order to improve the efficiency and suppress backward wave oscillations, some articles have proposed the use of metal structures on the bottom plane of the substrate, opposite to the meander line plane as shown in Fig. 2.1.24, to work as attenuators [79], [80]. The aim with this design is to reduce oscillation and generate steady output power.

The absorber is typically designed to have the same pitch length as the meander line. This kind of structures are also easily manufactured by microfabrication techniques.

Cold simulations show a worse dispersion relation with more pronounced slope but 50% enhanced interaction impedance in comparison with the meander line without attenuator. The circuit attenuation is also improved in around 20%. The large signal simulations show a relatively flat gain with increased output power in comparison with the structure without the attenuator. In [80], the structure was fabricated and tested at low frequency showing good S-parameters agreement with simulations.

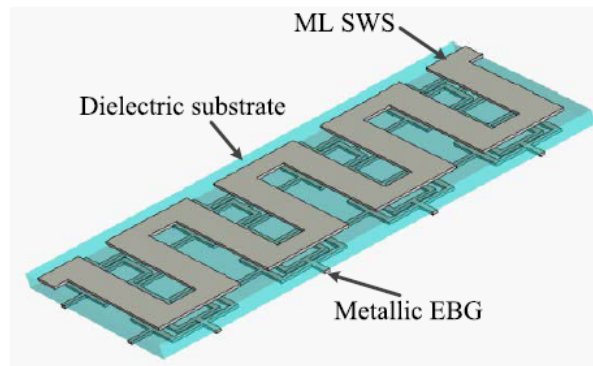


Figure 2.1.24: Design of the meander line with the absorption structure on the bottom side [80].

The addition of attenuating structures has been demonstrated to be effective for suppressing oscillations and improve performance. The fabrication of such designs is also easy to reproduce using microfabrication techniques. However, for this kind of structures to be effective, a second substrate is necessary under the attenuator, which may be complicated to implement at high frequencies due to misalignments and bonding techniques.

2.2 Meander line - Waveguide transitions

In traveling wave tubes, the RF signal is transferred in and out by rectangular waveguide flanges. A suitable transition between the waveguide flanges and the meander lines needs then to be designed in order to provide mode conversion between the TE_{10} mode of the waveguide and the quasi-TEM mode of the meander line. A proper design of the coupler is of fundamental importance since this would greatly affect the transmission properties of the structure and the final performance of the device.

Different coupling transitions have been proposed in literature:

- Transitions along the propagation direction of the waveguide [81], [82]. The meander line can be coupled to a waveguide by using a ridged waveguide as transition. As can be seen in Fig. 2.2.1, the ridge is extended to the substrate top of the meander line to join the metal strip. By progressively reducing the thickness of the ridge, the transition converts the mode in the meander line to that in the rectangular waveguide.

This coupler requires to manufacture the ridge on the waveguide which adds an extra step on the fabrication process that could be delicate considering the overall small dimensions at high frequencies. Moreover, the ridge needs to be joined to the metallization of the meander line which raises concerns in terms of proper alignment and assembly.

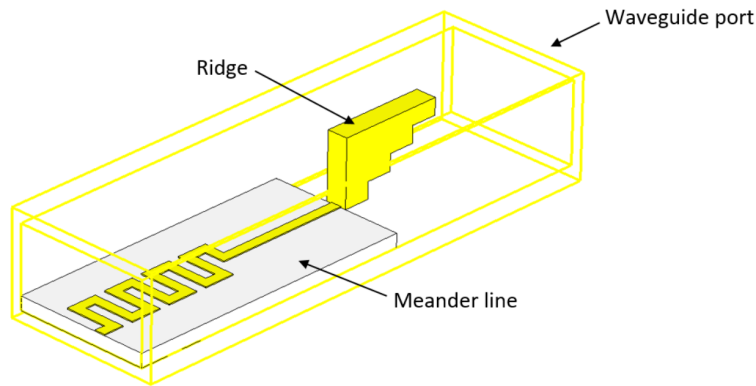


Figure 2.2.1: Configuration of a meander line-waveguide transition by using a ridged waveguide.

- Transitions by means of apertures in the ground plane of the meander line [83], [84]. To use this kind of couplers, the meander line needs to have a metallized ground plane. The ground plane will present a slotline so that the signal can be recovered at the bottom plane of the substrate and coupled to the waveguide as schematically presented in Fig. 2.2.2. The coupling between the meander line and the waveguide can be controlled by the size and position of the slotline.

With this design, a slot needs to be performed on the bottom metallized ground plane of the meander line. Performing the slot requires a high-accuracy additional processing that can be complicated to produce at mm-waves. If the slot is made mechanically, this could produce scratches or cracks on the substrate as a consequence of the process. Instead, if a chemical approach is followed, it would require an etching process to produce the slot.

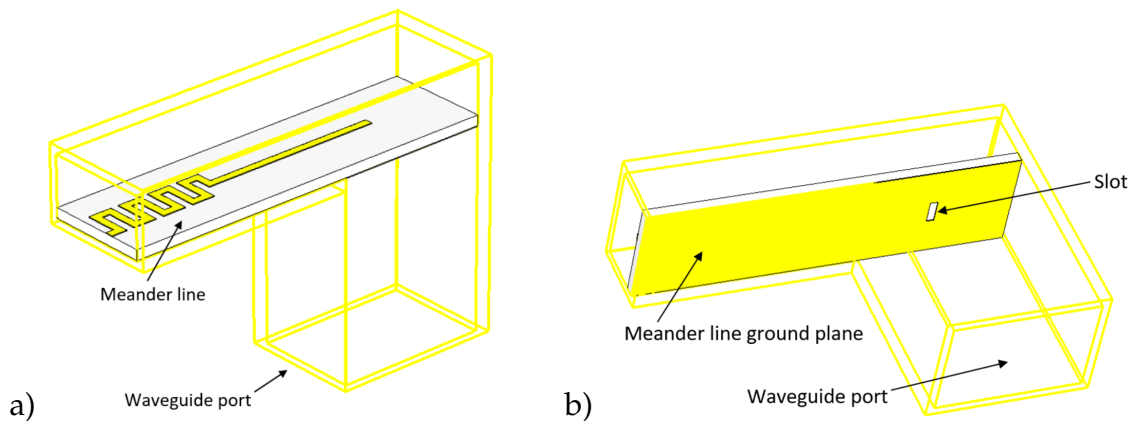


Figure 2.2.2: Configuration of a meander line-waveguide transition by means of a slot on the ground plane of the meander line. a) Lateral and b) bottom view of the coupler.

- Transitions using probes transverse to the propagation direction of the waveguide [85], [86]. This coupler has two possible configurations represented in Fig. 2.2.3. In both ways, the meander line is extended by straight probes that will enter the waveguide through a window on one of the walls. In the first case, the substrate extends into the waveguide with its surface facing the direction of propagation of the waveguide. In the second case, the surface of the substrate aligns the direction of propagation of the waveguide. The probe width, length and distance to the back wall determine the correct coupling between the meander line and the waveguide.

This kind of coupler does not require additional fabrication steps, as producing the probes can be done within the same fabrication process as for the meander line. Moreover, the ease of machining and the absence of tight-tolerance joints or features is very convenient at mm-waves where the dimensions are very small. This design was also experimentally demonstrated in [51]. Therefore, this is the coupling approach that has been followed for the design and manufacture of the meander line SWSs.

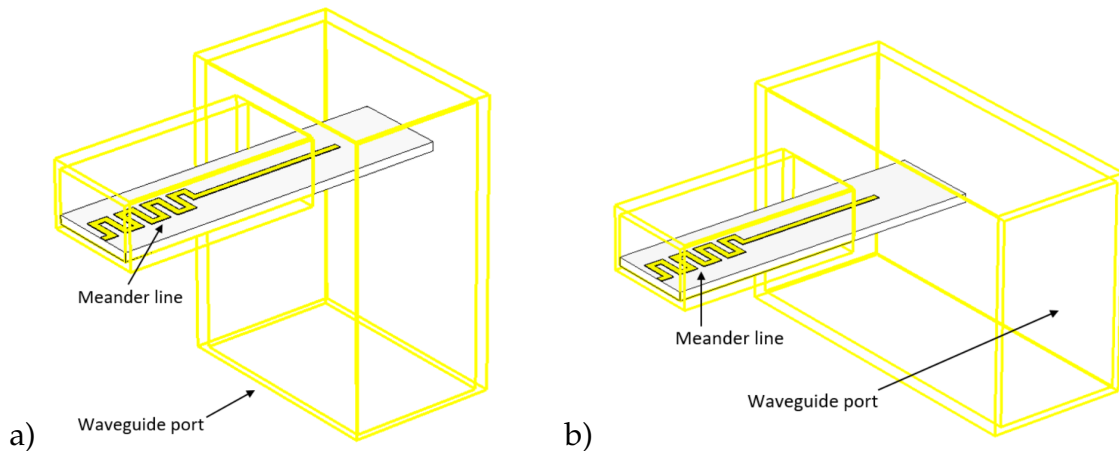


Figure 2.2.3: Two configurations of the meander line extended into the waveguide by means of coupling probes. a) The substrate faces the propagation direction of the waveguide and b) the substrate is parallel to the propagation direction.

2.3 Microfabrication techniques

Different methods are typically used to fabricate meander line SWSs. Techniques that permit to deposit a thin metal film over dielectric substrates, such as sputtering or thermal evaporation, are used for the fabrication of very thin meander line metal strips in the order of a few microns or as preliminary layer to increase adherence and grow thicker meander lines. To pattern the serpentine topology of the meander lines, photomasks are used in lithography processes. If thick meander lines are targeted in the order of tens of microns, a process such electroplating is more appropriate. If

even thicker, high-aspect-ratio meander lines or 3D microstructures are pretended, in the order of hundreds of microns, a LIGA process is the most suitable method. The remaining metallization that is not desirable is commonly removed by using dry or wet etching techniques.

2.3.1 Sputtering

Sputtering consists of high-energy ion or atom (typically Argon) bombardment of a target material, whose atoms are removed, ejected and deposited onto a substrate as schematically represented in Fig. 2.3.1. The physical nature of this process allows its use with virtually any existing material. The inert ions bombarding the target are produced in direct-current or RF plasma. In a simple parallel-plate system, the bottom electrode is the target and the substrates are placed horizontally on top of the bottom electrode. Sputtering systems are often able to deposit more than one material simultaneously or sequentially. This capability is very useful to obtain alloys and multilayer films. For certain low-reactivity metals such as Au (gold) and Cu (copper), the previous deposition of a thin layer of another metal is needed to improve adhesion. Ti (titanium) and Cr (chromium) are two frequently used adhesion promoters. The deposition rates are much higher than for most chemical vapour deposition techniques. However, due to stress accumulation and cracking, thickness beyond $2\ \mu\text{m}$ is rarely deposited with these processes.

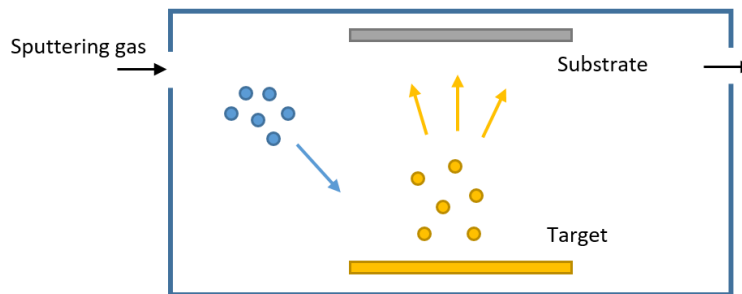


Figure 2.3.1: Schematic of a sputter deposition process.

2.3.2 Lithography

Lithography is the technique used to transfer a pattern onto a substrate. Although photolithography, i.e. lithography using an ultraviolet light source, is by far the most widely used lithography technique in microelectronic fabrication, electron-beam and x-ray lithography are two other alternatives with considerable interest for higher aspect ratios and resolution designs.

The photolithography process commonly starts with spin-coating the substrate with a photoresist. This is a polymeric photosensitive material which can be spun onto the substrate in liquid form. The spinning speed and photoresist viscosity

will determine the final resist thickness. Two different kinds of photoresist are available: positive and negative. With positive resist, exposed areas are dissolved in the subsequent development stage using organic removal solvents, whereas with negative photoresist, the exposed areas remain intact after the development.

The lithography process is visually explained in Fig. 2.3.2.

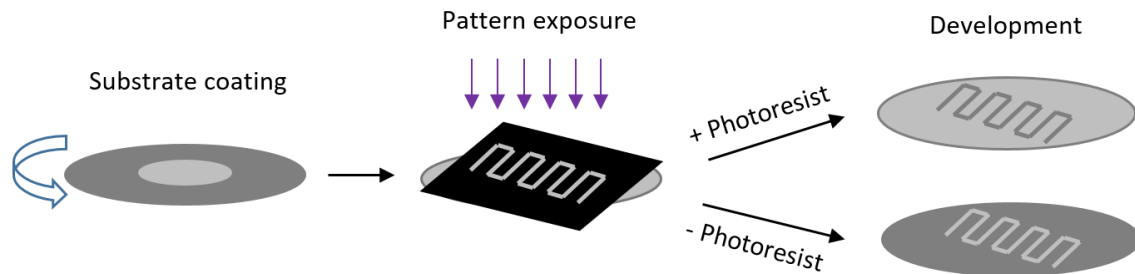


Figure 2.3.2: Typical photolithography steps. The substrate is coated with the photoresist, then the mask is exposed to create the desired design after developing the photoresist.

2.3.3 Electroplating

Electroplating is a process typically used to obtain thick (tens or hundreds of μm) metal structures. The sample to be electroplated is introduced into a solution containing a reducible form of the ion of the desired metal and is maintained at a negative potential (cathode) relative to a counterelectrode (anode) as seen in Fig. 2.3.3. The ions are reduced at the sample surface and the insoluble metal atoms are incorporated into the surface. As can be deduced from the process mechanism, the surface to be electroplated has to be electrically conductive, and preferably of the same material as the deposited one if good adhesion is desired. In order to electrodeposit metals on top of an insulator (the most frequent case) a thin film of the same metal, called the seed layer, is previously deposited on the surface. Masking of the seed layer with a resist permits selective electroplating of the patterned areas.

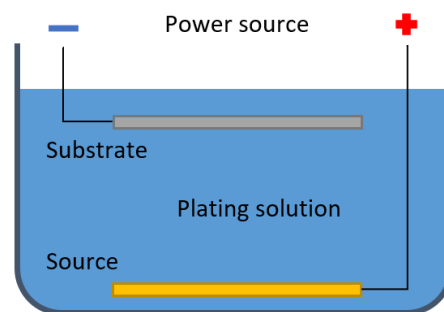


Figure 2.3.3: Setup of an electroplating process.

2.3.4 Etching

Thin-film etching is another fabrication step that is of fundamental importance to microfabrication. The various etching techniques can be divided into wet and dry categories:

- Wet etching techniques consist of attacking the target material chemically. A reaction on the surface of the material etches the material away. Wet etchants show superior selectivity to the masking layer as compared with various dry techniques. However, due to the lateral undercut, the minimum feature size achievable with wet etchants is limited to a few μm . Metals can be etched using various combinations of acid and base solutions. For instance, Cu (copper) is etched by (also diluted) HNO_3 (nitric acid) as well as saturated 30% FeCl_3 (ferric chloride) solution.
- Most of the dry etching techniques are plasma based wherein a flow of atoms attacks the target surface and the material is detached. They have several advantages when compared with wet etching. These include smaller undercut (allowing smaller features to be patterned) and higher anisotropy (allowing high-aspect-ratio vertical structures). However, the selectivity of dry etching techniques is lower than that of using wet etchants. There are three basic dry etching techniques, namely high-pressure plasma etching, reactive-ion etching, and ion milling.

2.3.5 LIGA (Lithography, Electroplating and Molding)

LIGA is a high-aspect-ratio micromachining process which relies on a combination of the aforementioned processes, mainly lithography and electroplating. After the design is patterned on a substrate by lithography, electroplating is used to grow high-aspect-ratio metal structures. With standard UV photolithography and photoresists, the maximum thickness achievable is in the order of a few tens of microns with maximum aspect ratios around 20:1, and the resulting metal structures show tapered walls. Instead, by using X-ray lithography and special photoresists, metal structures can be achieved with thickness ranging from a few microns to a few millimeters with almost vertical side-walls. Due to their short wavelength, x-rays are able to penetrate through a thick photoresist layer with no scattering and define features with lateral dimensions down to $0.2 \mu\text{m}$ (aspect ratio greater than 100:1). Depending on the application, UV-LIGA can be used to reduce the cost if very high quality samples are not needed.

2.4 Summary

The use of a slow wave structure that potentially offers low operation voltage, high interaction impedance and simple fabrication, is of great interest for the design and

production of low-cost traveling wave tubes. Bearing all these benefits in mind, meander lines have been extensively investigated and studied to potentially become the suitable SWS for a new generation of mm-wave space TWTa.

Meander lines have been thoroughly studied through the analysis of different topologies and approaches to improve their performance. The dispersion of meander lines is, however, a concern for the production of broad bandwidth TWTs. The more suitable interaction with a sheet electron beam of meander lines also needs the use of more complex electron guns and high focusing magnetic fields to avoid deviations in the electron beam. The investigation of novel topologies with lower dispersion and new structures more suitable to interact with a cylindrical beam will be a key part of this thesis. The design of a suitable transition between the meander line and the waveguide is also important to obtain good transmission of the RF signal along the traveling wave tube.

Finally, the comprehension of the fundamentals of microfabrication techniques is necessary to create feasible new designs of meander line SWSs that can improve the performance of TWTs.

3. Analysis and design of novel planar meander line slow wave structures

This chapter reports the analysis, by means of simulations, of the interaction between meander line slow wave structures and different electron beam geometries. It will be shown that meander lines are more suitable to interact with sheet beams, and the use of the well-established cylindrical beams is limited by the poor interaction efficiency. Starting from this study, this chapter will deal with the study of planar meander lines and sheet electron beams. A rigorous analysis of the optimum substrate material and dimensions as well as the most adequate configuration of the metallization will be carried out. Two novel meander lines, which provide improved performance, are proposed and compared with two conventional meander lines. In total, four different planar meander line topologies have been designed at W-band and will be described as well as the housing where the meander lines will be placed in to be tested. The structures have been also designed at Ka-band for facilitating the preliminary fabrication process and tests.

All the simulations have been performed using the 3D electromagnetic software CST Microwave Studio [87].

3.1 Effect of the dimensions and material of the substrate

The standard meander line (SML) is used as a reference to understand the effect of the dimensions and material of the substrate. The substrate plays an important role in the transmission of the electromagnetic wave through the delay line. The properties of the substrate, such as the permittivity or the thickness, will determine the energy that will be stored in the substrate. Understanding how this affects the dispersion and interaction impedance of the meander line is fundamental to properly design the slow wave structure. In order to investigate this matter, a parametric sweep has been performed over the substrate thickness and length, and different dielectric materials have been analysed.

A schematic of the structure with the parameters that have been modified is

presented in Fig. 3.1.1. The meander line is simulated with four different materials: Rogers Duroid RT6002, Quartz, Silicon and Alumina. The dielectric constant, tensile modulus and thermal conductivity for such materials are given in Tab. 3.1.1.

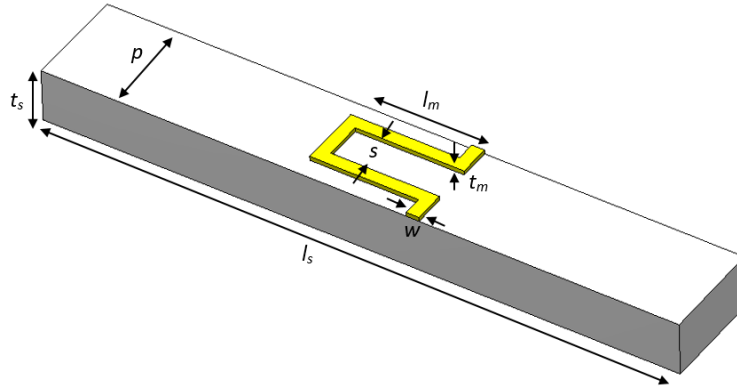


Figure 3.1.1: Schematic and dimensions of the standard meander line (SML) used as a reference.

Table 3.1.1: Properties of the substrate materials.

	RT6002	Quartz	Alumina	Silicon
Dielectric constant	2.94	3.75	9.9	11.9
Loss tangent	0.0012	0.0001	0.0003	0.015
Tensile modulus (GPa)	0.83	73	350	113
Thermal conductivity (W/(m·K))	0.6	1.46	30	120

Every material has different properties that change the performance of the meander line. In particular, the Rogers RT6002 laminate is a composite material that provides low loss and good performance at high frequency. As seen in Fig. 3.1.2, the low relative permittivity of the substrate allows to have high interaction impedance but also increases the phase velocity needing a high-voltage electron beam to get amplification. The dimensions of the structure would need to be bigger in order to take advantage of one of the main benefits of meander lines which is being able to interact with a low-voltage electron beam. This would also increase the size of the final tube, making it less compact. The low tensile modulus of the material means that it would be easily bent and could be affected by an undesired curvature of the substrate.

A substrate made of quartz gives similar results in terms of phase velocity and interaction impedance as the RT6002 laminate. The low relative permittivity would require a high-voltage electron beam or a bigger design of the structure. The meander line would benefit from a very low loss substrate with good thermal conductivity.

Alumina and silicon materials provide a reduced phase velocity curve that would allow the meander line to interact with a low-voltage electron while keeping reduced

dimensions of the structure. The interaction impedance is lower for these two substrates in comparison with the RT6002 laminate and the quartz substrate, but still much higher than the full-metal alternatives at W-band. The dispersion of alumina and silicon is lower in comparison with the RT6002 laminate and the quartz substrate, which will increase the bandwidth of operation and permit a flatter gain and output power within the band.

Specifically, alumina provides a low signal loss and good thermal stability and conductivity which helps dissipate the metallization heating when including the electron beam. The mechanical aspects of the material are also interesting offering high mechanical strength and hardness which helps manipulate the sample during fabrication and testing. Alumina is also a well-known and well-tested material for vacuum, electronics and space applications.

Alumina is, therefore, chosen as the substrate material for the following simulations and fabrication of the meander lines. To understand the effect of the thickness and length of the substrate, a parametric sweep is performed starting from the values in Tab. 3.1.2.

The phase velocity and the interaction impedance curves after the length of the substrate l_s has been swept from 1 mm to 2 mm are presented in Fig. 3.1.3. The results show that the effect of this length on the properties of the slow wave structure is negligible since the curves mostly coincide regardless of the value. The thickness of the substrate t_s is also varied between the typical dimensions that are available commercially, starting from 127 μm (0.005 inch) as seen in Fig. 3.1.4. The phase velocity and interaction impedance curves vary considerably with the substrate thickness. When the thickness is reduced, the phase velocity becomes flatter which is necessary in order to improve the flatness of the gain over the bandwidth of interest. Instead, the interaction impedance becomes lower when the thickness is reduced.

As a conclusion, the length of the substrate is irrelevant for the performance of the meander line, but a relatively long substrate would be interesting for a better manipulation of the samples considering the small overall dimensions. On the other hand, the substrate should be as thin as possible in order to reduce the dispersion and increase the bandwidth of the traveling wave tube.

Table 3.1.2: Starting dimensions of the standard meander line for the parametric sweeps.

Parameter	Initial value (μm)
l_m	350
t_m	10
w	50
s	70
p	240
l_s	1500
t_s	254

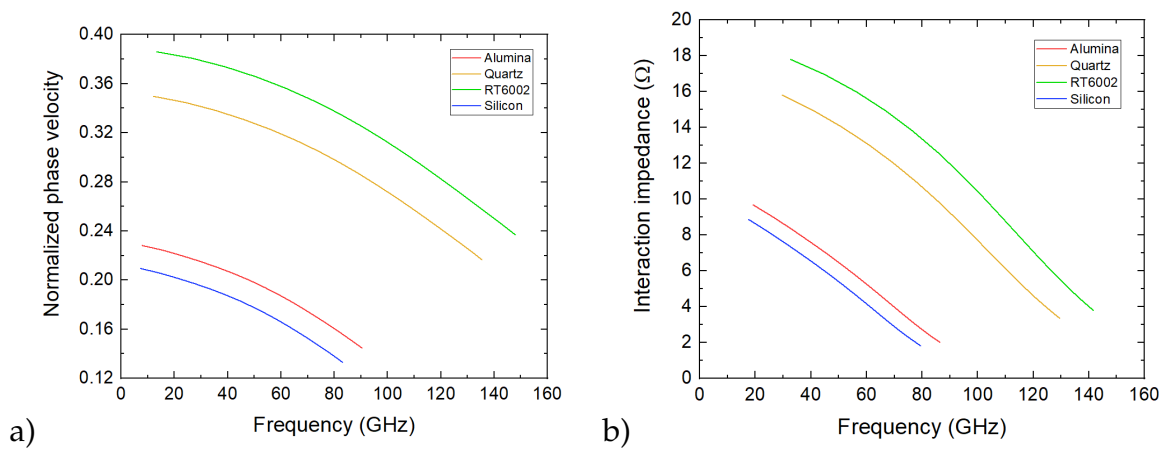


Figure 3.1.2: a) Results for the phase velocity and b) the interaction impedance for different substrate materials.

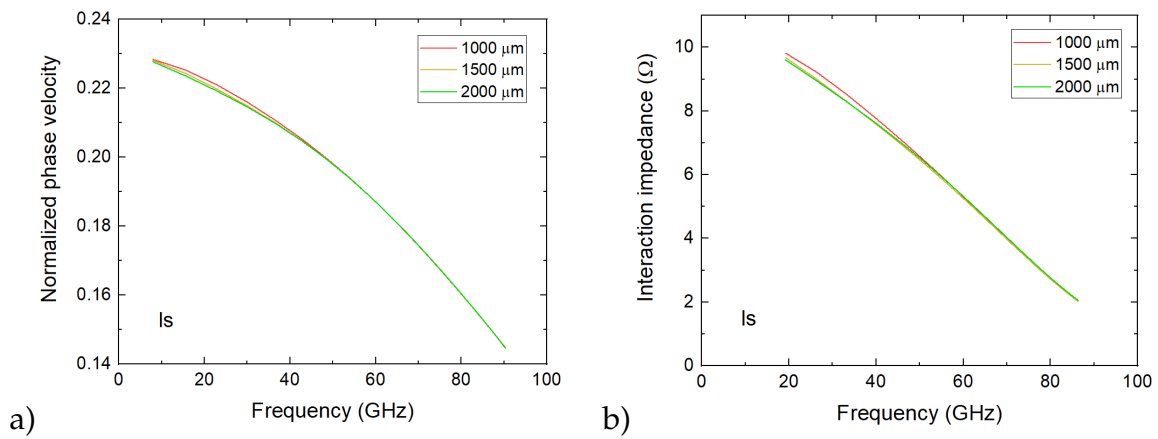


Figure 3.1.3: a) Results for the phase velocity and b) the interaction impedance after sweeping the parameter l_s .

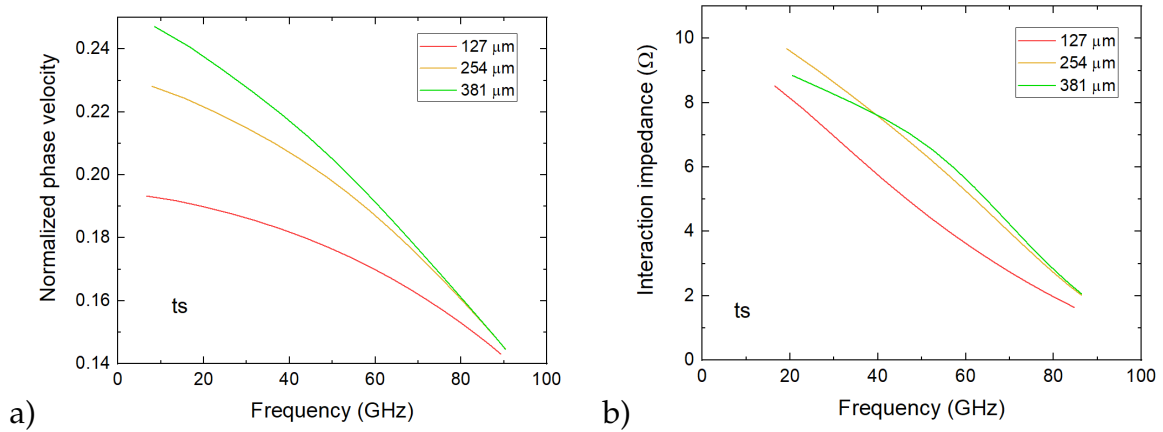


Figure 3.1.4: a) Results for the phase velocity and b) the interaction impedance after sweeping the parameter t_s .

3.2 Effect of the dimensions of the metallization

The dimensions of the metallization also change the performance of the meander line. Starting from the initial dimensions in Tab. 3.1.2 and using alumina for the dielectric substrate, the parameters related to the metallization have been swept.

If the length of the metallization, l_m , is increased, the bandwidth is reduced drastically as can be seen in Fig. 3.2.1. In addition, the phase velocity is also reduced while the dispersion increases for longer meander lines. The interaction impedance becomes higher at low frequencies but decreases rapidly as the length of the meander line is increased.

The effect of the thickness of the metallization, t_m , is analysed in Fig. 3.2.2. The phase velocity curve is moved up when the thickness is increased. The interaction impedance presents a different behaviour; as the meander thickness is reduced, the interaction impedance is increased at low frequencies but decreased at high frequencies.

The pitch of the meander line is related with the width of the metal strip and the space in between two consecutive strips as $p = 2w + 2s$ for the standard meander line (see again Fig. 3.1.1). To understand the effect of these parameters, first w and s are swept while fixing the pitch length p . These results are presented in Fig. 3.2.3, and show that increasing the width of the meander line strips while also reducing the space between them, increases the cold bandwidth, the beam voltage and the dispersion. At high frequencies, the interaction impedance is increased with the width of the meander line.

If the space s between two consecutive strips of the meander line is fixed, a variation of the width w of the strip will also modify the pitch length p of the structure. The results for this case are shown in Fig. 3.2.4. The cold bandwidth and dispersion of the curves remain approximately stable while the phase velocity

is greatly increased when the width and pitch are also increased. The interaction impedance is also increased at high frequencies when the width is increased.

If the width w is kept constant while varying the space s and the pitch p , the curves are modified according to Fig. 3.2.5. As the space between two consecutive strips is reduced, the bandwidth is increased but the beam voltage is reduced. In addition, the interaction impedance is also increased when the space is reduced.

The conclusion to this analysis is that a reduced length, l_m , and the combination of small width, w , and large space, s , are fundamental to keep low the dispersion of the meander line. The effect of the other parameters is not as noticeable on the dispersion and are more focused on changing the beam voltage and the interaction impedance. A convenient combination of them is important for optimizing the configuration of the meander line.

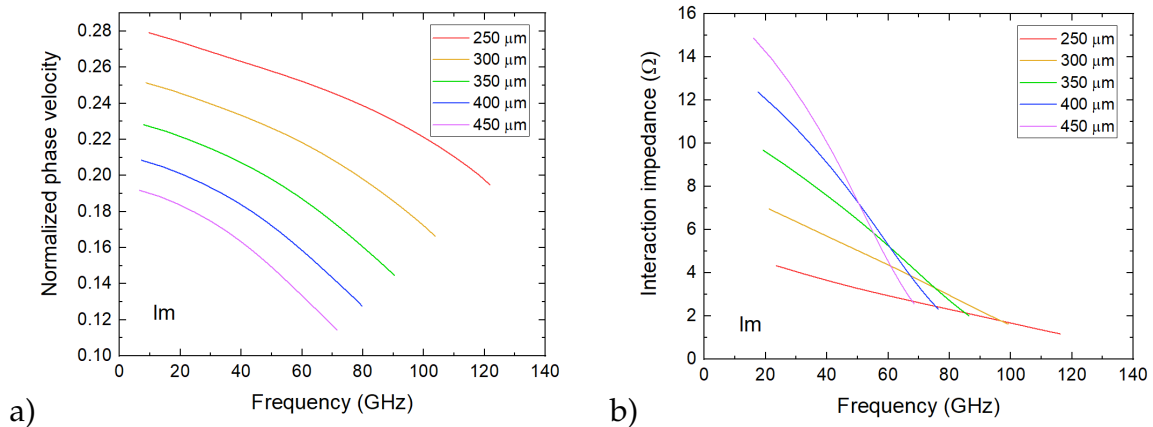


Figure 3.2.1: a) Results for the phase velocity and b) the interaction impedance after sweeping the parameter l_m .

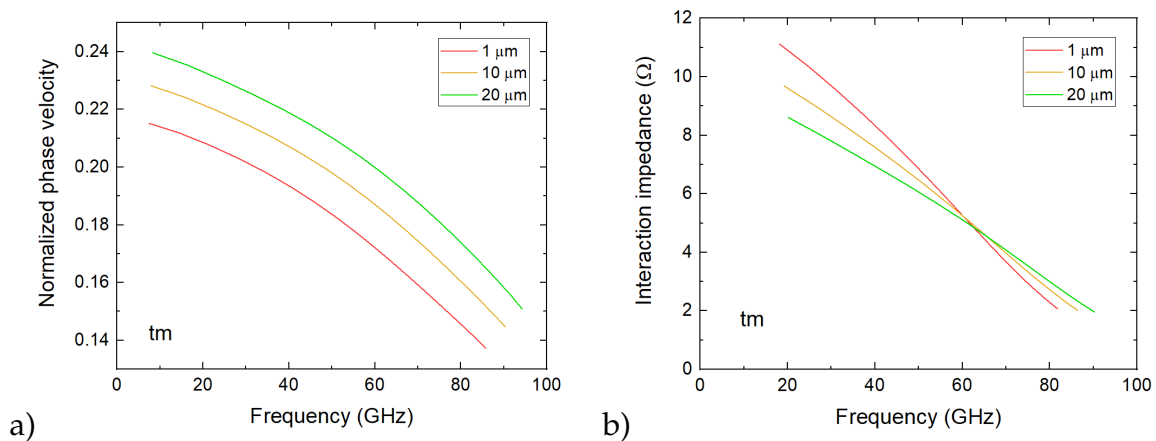


Figure 3.2.2: a) Results for the phase velocity and b) the interaction impedance after sweeping the parameter t_m .

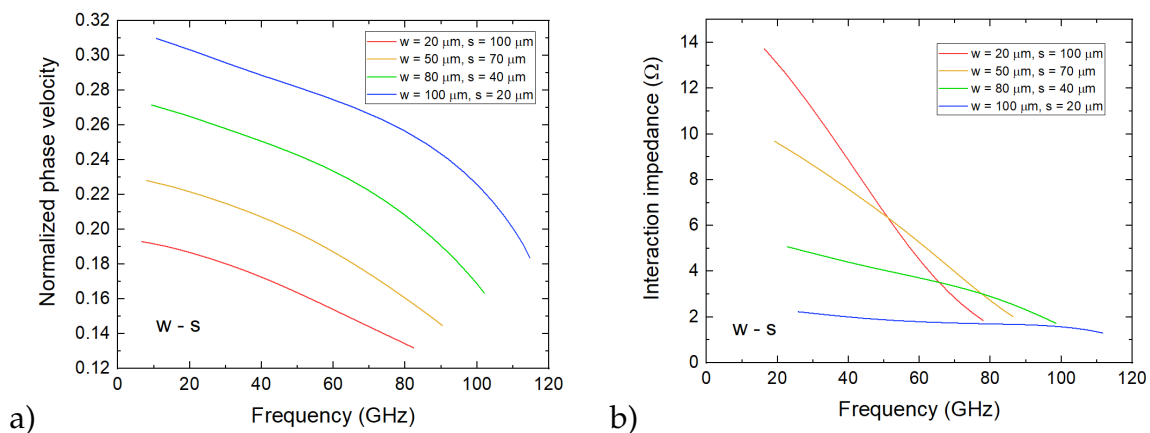


Figure 3.2.3: a) Results for the phase velocity and b) the interaction impedance after sweeping the parameters w and s while keeping a fixed p .

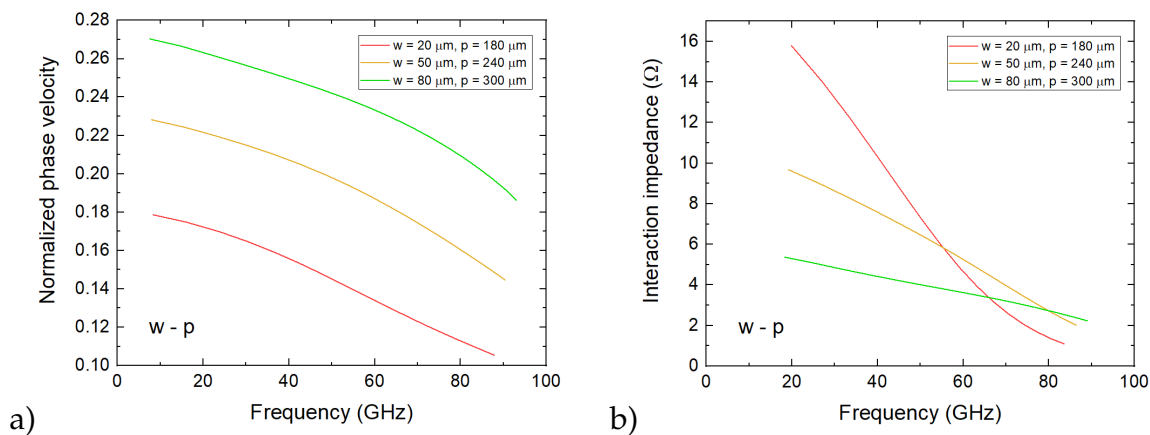


Figure 3.2.4: a) Results for the phase velocity and b) the interaction impedance after sweeping the parameters w and p while keeping a fixed s .

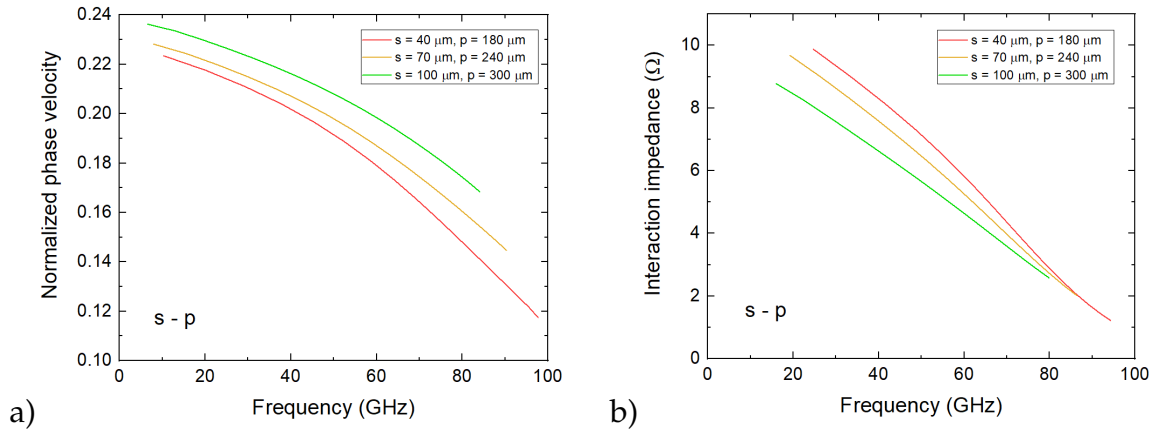


Figure 3.2.5: a) Results for the phase velocity and b) the interaction impedance after sweeping the parameters p and s while keeping a fixed w .

3.3 Beam geometry analysis

The interaction of the meander line electromagnetic field with the electron beam drives the final performance of the TWT. A proper understanding of this interaction is necessary to better design the meander line slow wave structures and improve the efficiency and output results.

The longitudinal component of the electric field for a number of periods of the standard meander line is represented in Fig. 3.3.1 and 3.3.2 from two different axial planes. The electric field profile shows that it is modulated from positive to negative after some periods as required in order to induce bunching in the electron beam. As seen in Fig. 3.3.2, due to the intrinsic design of the planar meander line, the electromagnetic fields are concentrated close to the interface metallization-substrate.

Fig. 3.3.3 shows a longitudinal plane view of the longitudinal electric field at half pitch of the planar meander line and a cylindrical and sheet beams contour superimposed situated at $50 \mu\text{m}$ from the metallization. The electric field of the meander line is extended along the line, thus favouring a geometry that spans the full cross section. Moreover, a rectangular geometry permits a thinner design in order to benefit from the higher field intensity closer to the interface. This has made sheet beams to be the preferred beam geometry to interact with planar lines due to the expected greater performance given the more suitable electromagnetic field distribution. However, experimental knowledge using sheet beams on TWTs is very limited and it is required a higher magnetic field for focusing the electron beam. Cylindrical beams have been widely used on every commercial TWT and the experimental knowledge is very valuable. A deeper look into the electron beam-meander line field is analysed in this section for both cylindrical and sheet beams in order to understand which beam geometry would be the most appropriate for this study.

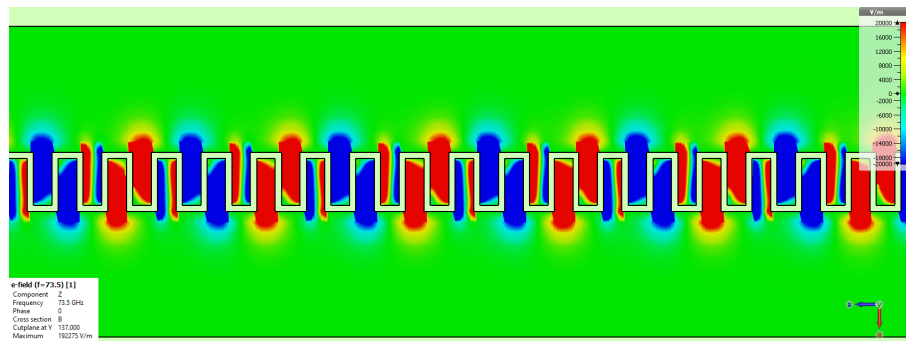


Figure 3.3.1: y -plane axial view of the longitudinal electric field component of the standard meander line.

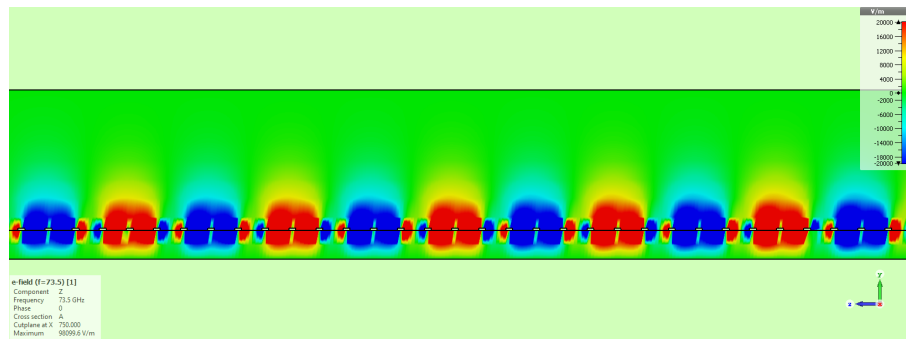


Figure 3.3.2: x -plane axial view of the longitudinal electric field component of the standard meander line.

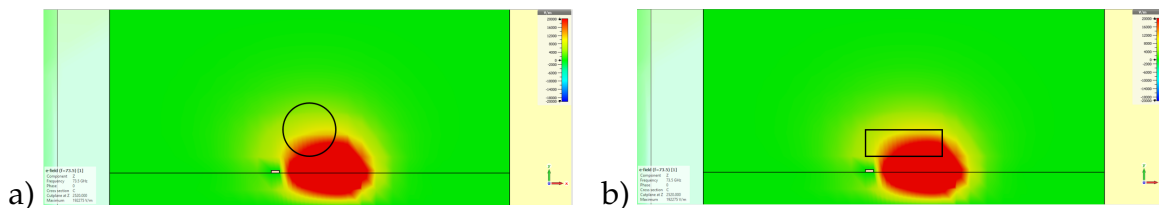


Figure 3.3.3: z -plane longitudinal view at half pitch of the longitudinal electric field component of the standard meander line with a) superimposed cylindrical beam and b) sheet beam contours.

3.3.1 Cylindrical beam

The cylindrical beam is analysed when it interacts with the planar meander line electromagnetic field. For the simulations, a cylindrical beam with radius $r_b = 100 \mu\text{m}$ placed at a distance $d_b = 50 \mu\text{m}$ from the metallization, following the schematic in Fig. 3.3.4, is considered at W-band.

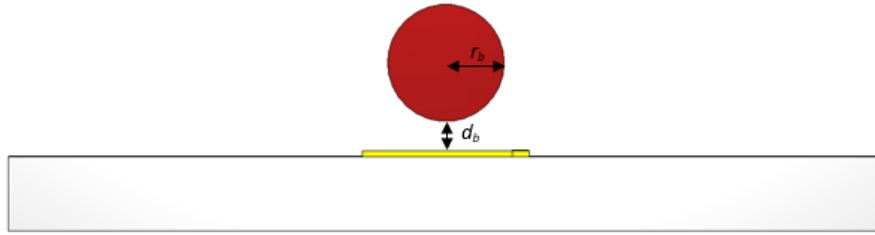


Figure 3.3.4: Schematic of a cylindrical electron beam on top of the meander line.

The electron beam energy modulation can be seen in Fig. 3.3.5 and shows a non-uniform bunching with the bottom part of the electron beam presenting greater modulation than the top part given the more intense longitudinal electric field close to the metallization.

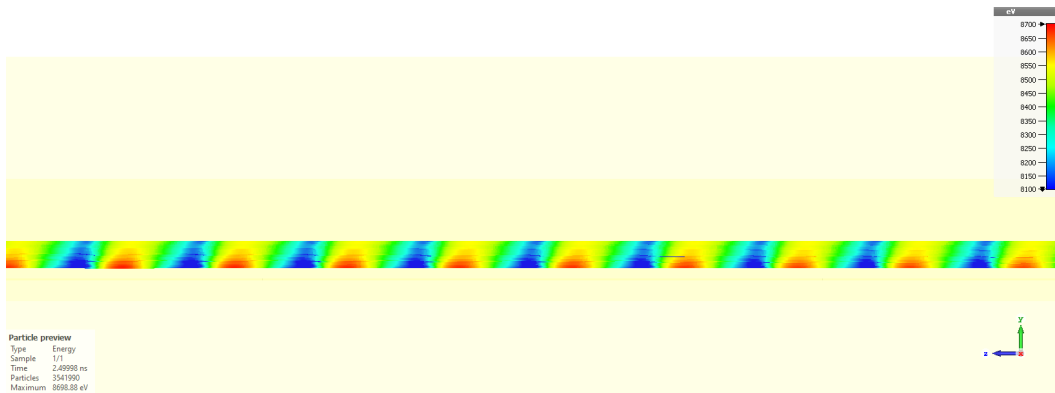


Figure 3.3.5: Lateral view of the cylindrical electron beam bunching.

A longitudinal cross section of the electron beam is presented in Fig. 3.3.6 for different distances within the meander line full structure. The cylindrical beam is focused using 1 T magnetic field. It can be seen that the circular profile of the beam tends to shift to a more elliptical shape as it interacts with the electric field and travels along the meander line. This behaviour coincides with what was discussed in Sec. 1.4.2.

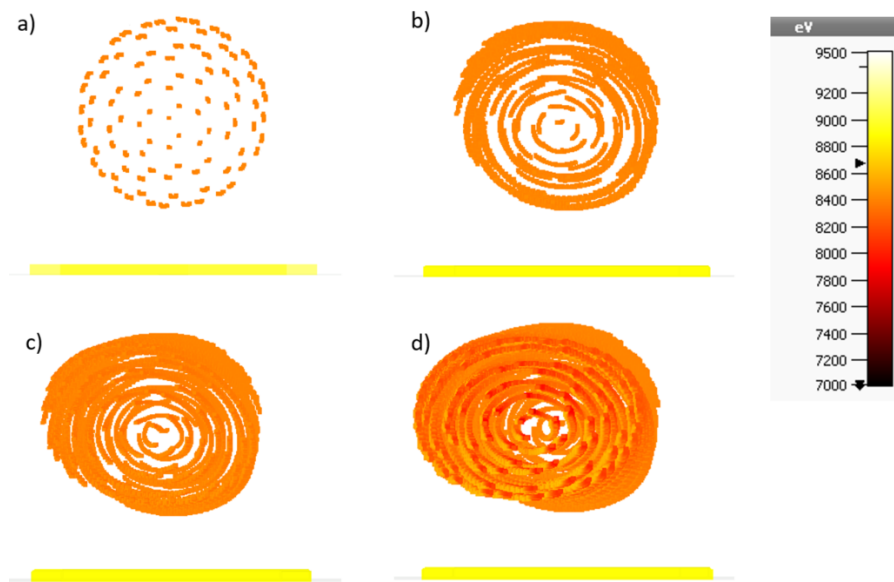


Figure 3.3.6: Longitudinal cross section of the cylindrical electron beam for different distances along the meander line. a) at the beginning of the interaction b) at 1/3 of the full line length c) at 2/3 of the full line length and d) at the end of the interaction.

With the same configuration, the interaction impedance within the cylindrical electron beam area is studied in Fig. 3.3.7. The interaction impedance at the bottom part of the beam can reach values a hundred times greater than at the top part, this reduces the efficiency of the final amplification and increases the number of periods necessary to reach saturation as the gain per period is diminished.

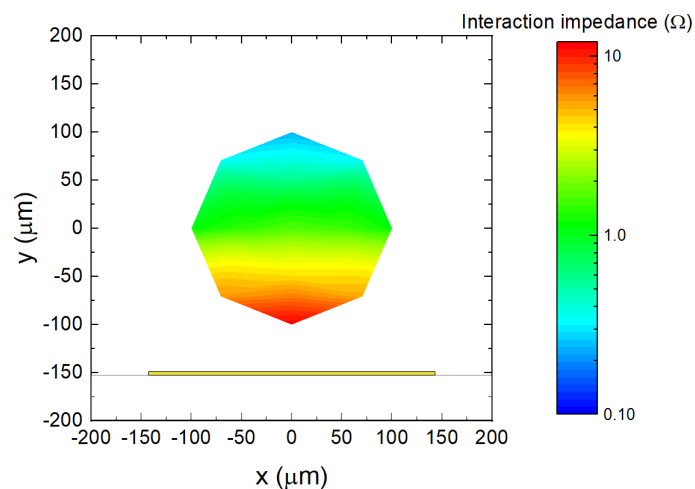


Figure 3.3.7: Interaction impedance over the cylindrical beam area with radius 100 μm .

Large signal simulations are also performed comparing a cylindrical beam with

two different radius, $100 \mu\text{m}$ and $143 \mu\text{m}$ (for the same diameter as the meander line length), and using the same other beam parameters. The results can be seen in Tab. 3.3.1. The cylindrical beam with lower radius has a higher average interaction impedance and, therefore, reaches saturation at a shorter length and number of periods. Instead, a greater radius allows to obtain slightly higher gain as a bigger area of the electron beam is closer to the metallization and presents higher interaction impedance.

Gain and output power at W-band for the case of the cylindrical electron beam with radius $100 \mu\text{m}$ is shown in Fig. 3.3.8. The output results are poor for this configuration, with output power lower than 10 W for the whole band. These values are not enough for satellite communications at W-band, and different approaches are necessary.

Table 3.3.1: Performance of a cylindrical electron beam with two different radius when interacting with the standard meander line topology at W-band.

Beam radius (μm)	100	143
Average interaction impedance (Ω)	2.3	1.4
Saturated number of periods	400	450
Saturated gain (dB)	31.2	32.1

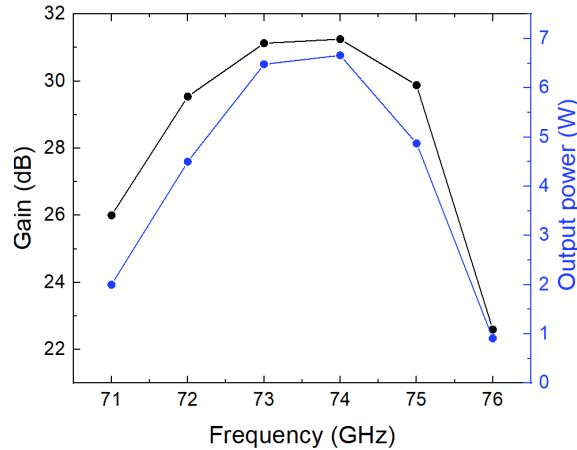


Figure 3.3.8: Gain and output power of the standard meander line at W-band using a cylindrical electron beam.

3.3.2 Sheet beam

A sheet beam with aspect ratio 4:1 is used to analyse this beam geometry and the energy modulation at different distances along the interaction with the meander line. The length of the beam is the same as the meander line, $l_b = 286 \mu\text{m}$, and the height is reduced to $h_b = 71.5 \mu\text{m}$ for a distance $d_b = 50 \mu\text{m}$ from the metallization according

to the schematic in Fig. 3.3.9. A magnetic focusing field of 1 T, the same as for the cylindrical beam, is used in the simulations.

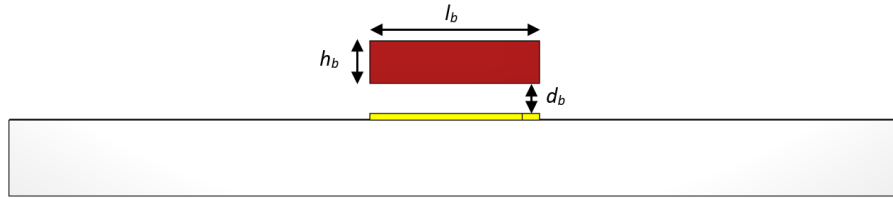


Figure 3.3.9: Schematic of a sheet electron beam on top of the meander line and parameters to be analysed.

According to Fig. 3.3.10, the rectangular profile of the sheet beam is turned into an elliptical shape as the beam interacts with the electromagnetic field. At the end of the interaction, the strong space charge forces even make some of the electrons to leave the beam and hit the substrate.

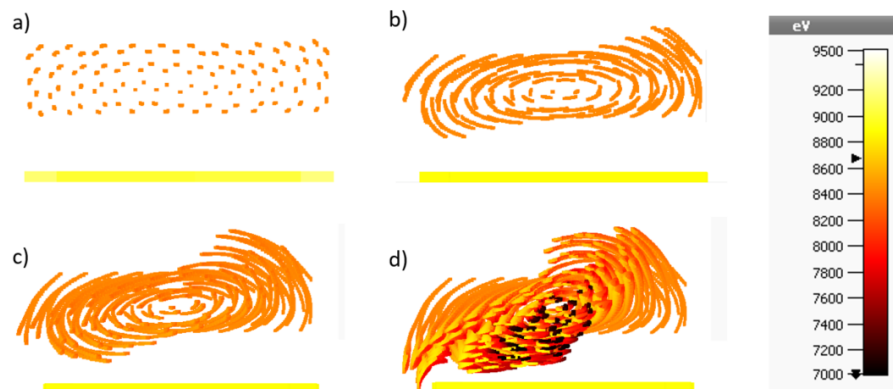


Figure 3.3.10: Longitudinal cross section of the sheet electron beam with aspect ratio 4:1 for different distances along the meander line. a) at the beginning of the interaction b) at 1/3 of the full line length c) at 2/3 of the full line length and d) at the end of the interaction.

This effect can be reduced by lowering the aspect ratio of the electron beam, for example to an aspect ratio of 2:1, thus increasing the cross-sectional area of the beam and reducing the magnetic field needed to compensate the space charge force as discussed in Sec. 1.4.2. Therefore, for the same applied magnetic field of 1 T, the effect of the space charge force should be diminished. The length of the beam is again $286 \mu\text{m}$, but the height is increased to $143 \mu\text{m}$. As shown in Fig. 3.3.11, the sheet beam still shifts to an elliptical form but no electrons are seen to hit the substrate.

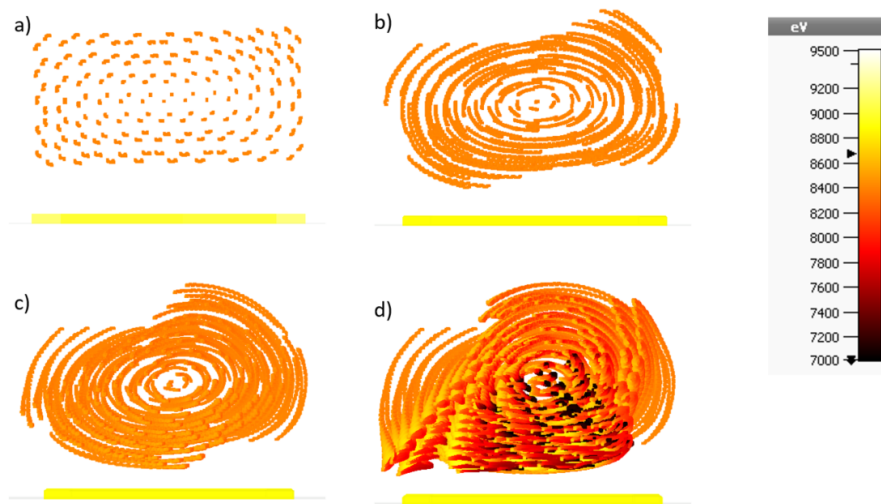


Figure 3.3.11: Longitudinal cross section of the cylindrical electron beam with aspect ratio 2:1 for different distances along the meander line. a) at the beginning of the interaction b) at $1/3$ of the full line length c) at $2/3$ of the full line length and d) at the end of the interaction.

A further study is performed using the sheet beam with aspect ratio 2:1. The beam energy modulation is presented in Fig. 3.3.12 and shows a better bunching when compared with the cylindrical beam in Fig. 3.3.5. This is due to the fact that the sheet beam presents shorter height and longer length than the cylindrical beam and is more immersed into the high intensity area of the longitudinal electric field.

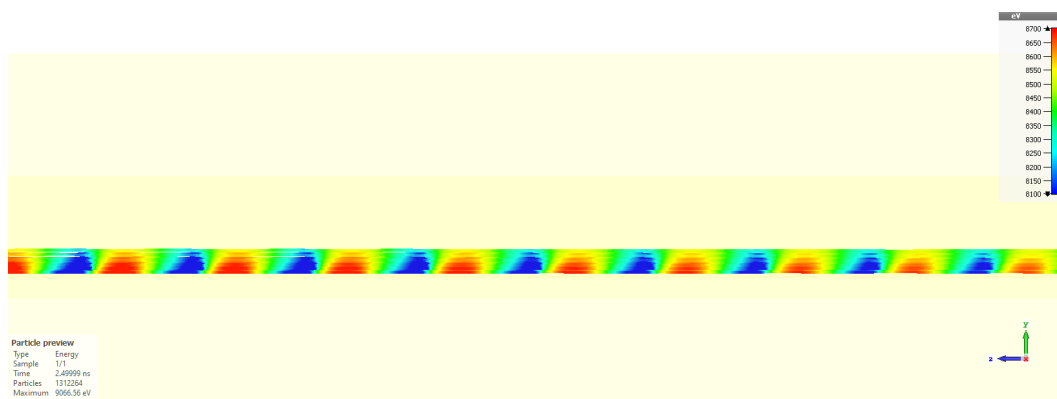


Figure 3.3.12: Lateral view of the sheet electron beam bunching.

The interaction impedance within the sheet beam area is also analysed in Fig. 3.3.13, where it can be seen that approximately the bottom half of the beam presents high interaction impedance. This area is much smaller for the cylindrical beam. The minimum values of the interaction impedance are also higher for the sheet beam

configuration. This should provide better performance increasing the efficiency and the gain per period of the traveling wave tube.

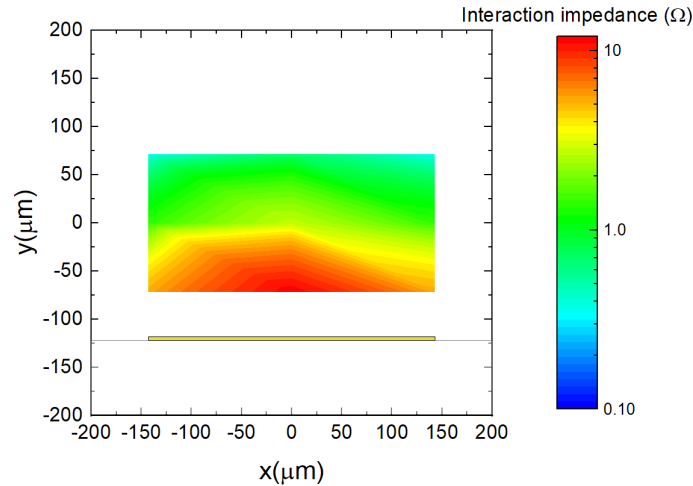


Figure 3.3.13: Interaction impedance over the sheet beam area.

In order to further analyse the sheet beam-meander field interaction, large signal simulations are performed for different configurations of the electron beam. Specifically, the distance from the electron beam to the meander line d_b , the length l_b and the height h_b of the sheet beam are swept, and the gain and number of periods at saturation are analysed in Tab. 3.3.2, 3.3.3 and 3.3.4 while keeping the hot parameters unchanged. A sheet beam with the same length as the meander line $l_b = 286 \mu\text{m}$ is taken as reference for comparison as in Fig. 3.3.9.

According to Tab. 3.3.2, a longer sheet beam than the meander line shows to provide higher efficiency and also slightly increases the gain. However, if the beam length is shorter than the meander line, the efficiency is similar but the gain is greatly reduced.

Tab. 3.3.3 shows the performance of the structure for different aspect ratios. Considering the same magnetic focusing field for the three cases analysed, a higher height offers similar gain but increases the number of periods required to reach saturation. Instead, a lower height should increase both gain and efficiency, but the magnetic field required to confine such beam would be stronger than when the aspect ratio is 2:1.

Finally, Tab. 3.3.4 shows that the closer the sheet beam to the meander line, the higher the efficiency and the gain. As seen in Fig. 3.3.13, the area of the sheet beam closer to the meander line presents higher interaction impedance. Therefore, if the distance to the meander line can be reduced, a bigger area of the sheet beam would have high interaction impedance, thus increasing the gain per period of the system. However, a closer distance increases the thermal energy on the meander line and the probability of electrons hitting the substrate surface.

The sheet electron beam, even with a low aspect ratio, has been shown to provide much better results than a cylindrical electron beam. This low aspect ratio also permits to focus the beam using a relatively low magnetic field. This configuration of the electron beam with its length equalling the length of the meander line and aspect ratio 2:1, is the chosen one for the subsequent simulations and final design of the planar meander line slow wave structures.

Table 3.3.2: Performance of a sheet electron beam with different lengths and fixed $h_b = 143 \mu\text{m}$ and $d_b = 50 \mu\text{m}$.

Length of the beam (μm)	143	286	429
Saturated number of periods	300	300	243
Saturated gain (dB)	29.54	36.77	36.9

Table 3.3.3: Performance of a sheet electron beam with different heights and fixed $l_b = 286 \mu\text{m}$ and $d_b = 50 \mu\text{m}$.

Height of the beam (μm)	71.5	143	214.5
Saturated number of periods	330	300	350
Saturated gain (dB)	33.98	36.77	36.9

Table 3.3.4: Performance of a sheet electron beam at different distances to the meander line and fixed $l_b = 286 \mu\text{m}$ and $h_b = 143 \mu\text{m}$.

Distance to the meander (μm)	25	50	100
Saturated number of periods	217	300	500
Saturated gain (dB)	37.03	36.77	34.15

3.4 Designs at W-band: Standard meander line (SML)

Following the analysis from Sec. 3.1 and 3.2, the standard meander line is designed at W-band using an alumina substrate with gold metallization. The dimensions used for the meander line and the substrate are described in Fig. 3.4.1 and Tab. 3.4.1. The standard meander line is designed to interact with an electron beam of 8.5 kV.

Similar to the E-field probe approach explained in Sec. 2.2, the meander line is extended at both ends of the serpentine line in order to couple the electromagnetic field coming from the waveguide. The schematic and dimensions of the probes are shown in Fig. 3.4.2 and Tab. 3.4.2.

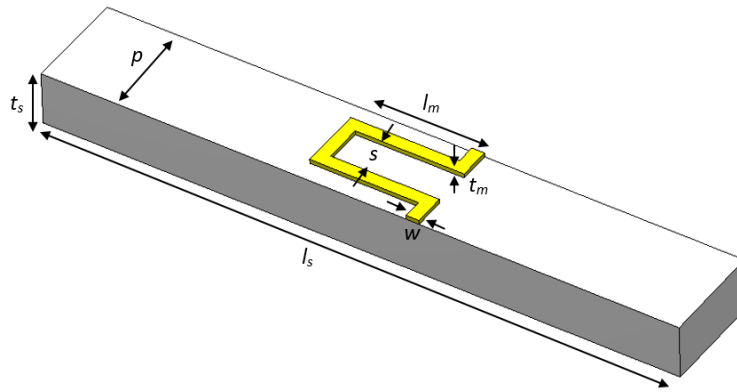


Figure 3.4.1: Schematic and dimensions of the standard meander line (SML).

Table 3.4.1: Final dimensions of the standard meander line.

Parameter	Value (μm)
l_m	286
t_m	10
w	30
s	90
p	240
l_s	1500
t_s	127

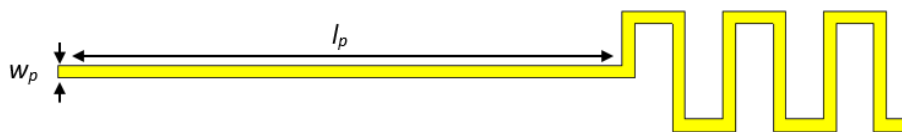


Figure 3.4.2: Schematic and parameters of the coupling probe of the standard meander line.

Table 3.4.2: Dimensions of the coupling probe of the standard meander line.

Parameter	Value (μm)
l_p	1300
w_p	30

3.5 Designs at W-band: Standard meander line with round corners (SMLR)

The standard meander line with round corners is designed as seen in Fig. 3.5.1 with the dimensions described in Tab. 3.5.1. As the right corners of the meander line are trimmed, the electromagnetic wave can travel with less reflections and more smoothly through the metallization. The objective with this design is to slightly reduce dispersion and improve transmission along the structure. The SMLR is also designed to interact with a 8.5 kV voltage electron beam.

The probe designed for SMLR is very similar to the one for the standard meander but with slight changes in the dimensions as seen in Fig. 3.5.2 and Tab. 3.5.2.

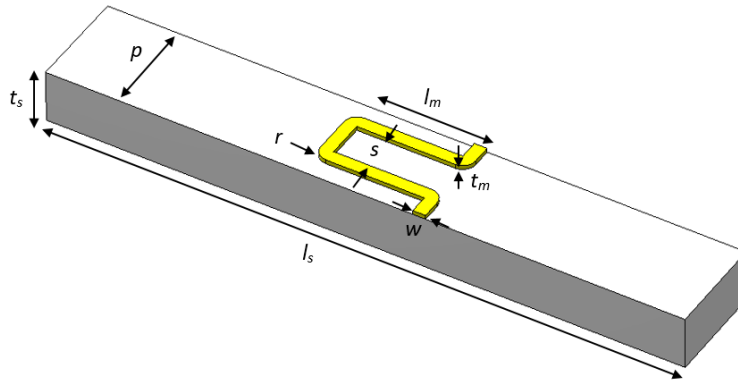


Figure 3.5.1: Schematic and dimensions of SMLR.

Table 3.5.1: Final dimensions of SMLR.

Parameter	Value (μm)
l_m	291
t_m	10
w	30
s	90
r	30
p	240
l_s	1500
t_s	127



Figure 3.5.2: Schematic and parameters of the coupling probe of SMLR.

Table 3.5.2: Dimensions of the coupling probe of SMLR.

Parameter	Value (μm)
l_p	1350
w_p	30

3.6 Designs at W-band: New meander line 1 (NML1)

The dispersion of meander line slow wave structure supposes a disadvantage in order to obtain amplification over a wide bandwidth as demonstrated in Sec. 2.1.1. As discussed in Sec. 3.1 and Sec. 3.2, the dimensions and materials of both the substrate and the metallization can be conveniently selected to reduce the dispersion of the structure. However, a more important change on the dispersion can be produced by choosing a different configuration of the meander line. A novel meander line was designed with the purpose of reducing even more the dispersion and obtain higher and flatter gain over the 71-76 GHz bandwidth. The schematic of the novel design can be seen in Fig. 3.6.1 and the dimensions of the structure are presented in Fig. 3.6.1. The novel meander line (NML1) is also designed to interact with a 8.5 kV beam voltage.

The design of the transition probe to couple the electromagnetic field from the rectangular waveguide is shown in Fig. 3.6.2 and the dimensions are described in Tab. 3.6.2.

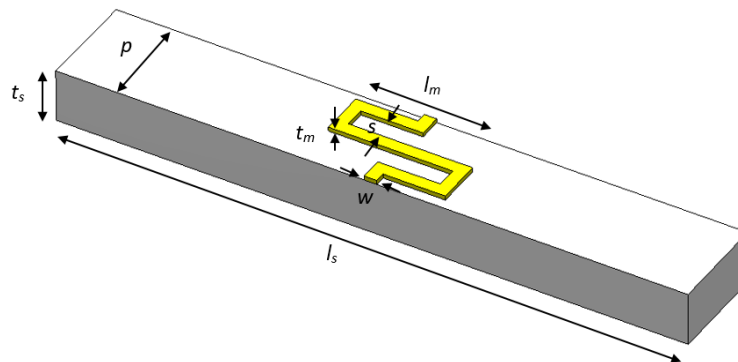


Figure 3.6.1: Schematic and dimensions of NML1.

Table 3.6.1: Final dimensions of NML1.

Parameter	Value (μm)
l_m	325
t_m	10
w	30
s	50
p	240
l_s	1500
t_s	127

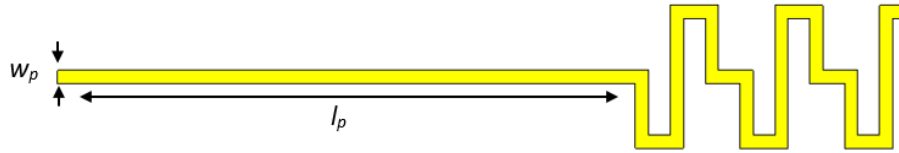


Figure 3.6.2: Schematic and parameters of the coupling probe of NML1.

Table 3.6.2: Dimensions of the coupling probe of NML1.

Parameter	Value (μm)
l_p	1300
w_p	30

3.7 Designs at W-band: New meander line 2 (NML2)

Given the intrinsic field distribution of planar meander line slow wave structures, the electron beam interacts with regions of different electric field intensity that make the electrons to require different distances to start bunching. As demonstrated in Sec. 3.3, a cylindrical or a sheet beam suffers from a much higher interaction impedance at the area closer to the metallization in comparison with the top part of the electron beam. In order to obtain better interaction and increase efficiency, the overall interaction impedance can be increased by conveniently selecting the dimensions and materials of the substrate and the meander line as shown in Sec. 3.1 and 3.2. Besides that, the planar meander line configuration can be designed to enhance the interaction impedance and obtain better efficiency within a narrower bandwidth. A novel design (NML2) was created with that objective. The novel meander line can be seen in Fig. 3.7.1 and the dimensions of the structure are described in Tab. 3.7.1.

The coupling probe for NML2 and its dimensions can be seen in Fig. 3.7.2 and Tab. 3.7.2, respectively.

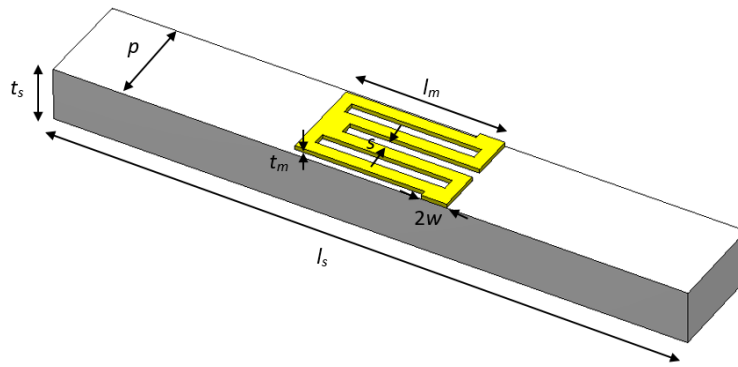


Figure 3.7.1: Schematic and dimensions of NML2.

Table 3.7.1: Final dimensions of NML2.

Parameter	Value (μm)
l_m	367
t_m	10
w	30
s	30
p	240
l_s	1500
t_s	127

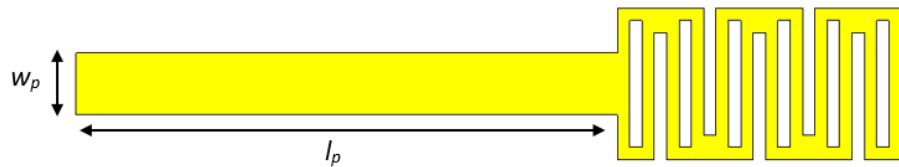


Figure 3.7.2: Schematic and parameters of the coupling probe of NML2.

Table 3.7.2: Dimensions of the coupling probe of NML2.

Parameter	Value (μm)
l_p	1300
w_p	150

3.8 W-band housing

The input signal inserted into the meander line and the amplified signal extracted from it is transferred and obtained to/from the slow wave structure by means of

rectangular waveguide ports. The housings where the meander lines are placed in are, therefore, designed with rectangular waveguide terminations. As described in Sec. 2.2, the meander lines are designed with transition probes in order to couple the electromagnetic fields coming and leaving from the waveguide. Housings with two different lengths, 20 and 40 periods of the meander lines, are designed and manufactured in order to simulate the S-parameters and measure the phase velocity as will be later explained in Sec. 5.1. The same housing is used for the four different designed meander lines in order to optimize the fabrication process.

The full housing design at W-band for the 20 periods meander lines is shown in Fig. 3.8.1. The dimensions of the housing are presented in Tab. 3.8.1 for the 20 and 40 periods structures. The housings are divided into two parts, as seen in Fig. 3.8.2, in order to be able to place in the meander lines and take them out after every measurement. Both parts are then joined with screws through the holes that are drilled at different positions of the housing in order to ensure a proper joint. As seen in Fig. 3.8.1, the waveguide ports design takes into account the screws and pins of the waveguide flanges. At W-band, the ports are designed with WR10 dimensions, this is 2.54 mm x 1.27 mm. A hole is drilled at both ends of the meander line enclosure with the objective of easily introduce and extract a dielectric perturbation as required for the measurements of the interaction impedance as will be explained in Sec. 5.2.

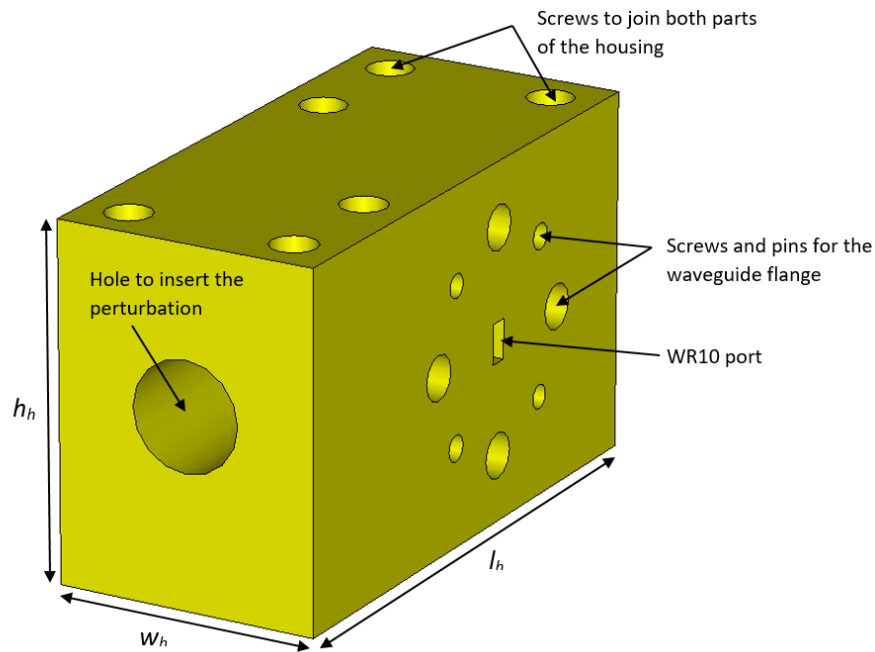


Figure 3.8.1: Final design of the 20-period housing at W-band.

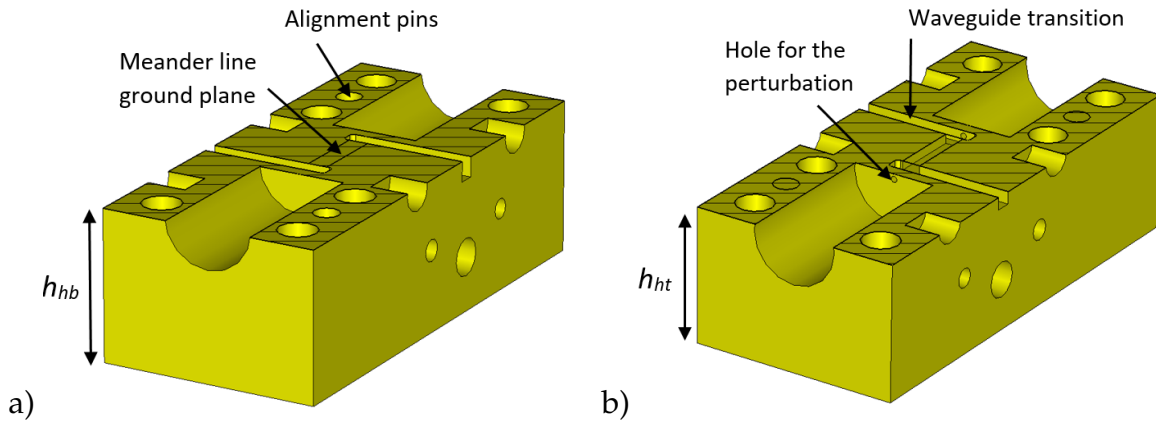


Figure 3.8.2: Final design of both parts of the 20-period housing at W-band. a) Bottom part and b) top part.

Table 3.8.1: Dimensions of the 20- and 40-period housing at W-band.

Parameter (mm)	20 periods	40 periods
h_h	22.54	22.54
h_{hb}	11.54	11.54
h_{ht}	11	11
w_h	17	17
l_h	36.34	41.14

3.9 Results and comparison of SML, SMLR, NML1 and NML2

The four meander lines, following the dimensions described in previous sections, are simulated to understand their performance and benefits for potential subsequent fabrication. The dispersion and interaction impedance curves of the four meander lines are compared in Fig. 3.9.1. The dispersion curves for SML, SMLR and NML1 are similar, with the ones for SMLR and NML1 being slightly flatter in comparison with SML. The dispersion curve of NML2 has, instead, a more pronounced slope. Then, it is expected a narrower bandwidth from NML2. The interaction impedance is similar for SML and SMLR, but it is increased for the two novel meander lines NML1 and NML2.

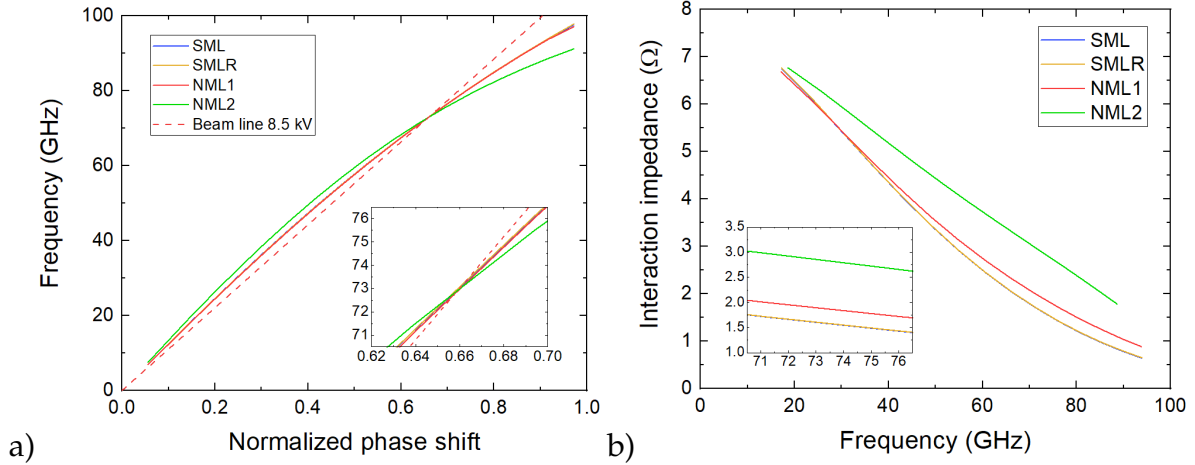


Figure 3.9.1: a) Dispersion and b) interaction impedance curves of the four meander lines at W-band.

The scattering parameters using the dimensions and designs for the probes of every meander line are computed in Fig. 3.9.2 for 20 and 40 periods length. The four meander lines provide a reflection coefficient, S_{11} , below -15 dB within the 71-76 GHz bandwidth.

The behaviour of the S-parameters coincides with what was explained in Sec. 1.4.3. The oscillations for the 40-period meander lines are closer in frequency than the 20-period ones given the longer size of the structures. The amplitude of the ripples for NML2 is lower compared to the other meander lines; the wider coupling probe of this design seems to improve the impedance matching between the meander line and the waveguide ports.

The structures are made to interact with a sheet electron beam of length the same as the length of the metallization and with aspect ratio 2:1. The same hot parameters have been used for all the simulations as can be checked in Tab. 3.9.1.

Table 3.9.1: Dimensions of the sheet beam and the hot parameters used for the four meander lines at W-band.

	SML	SMLR	NML1	NML2
l_b (μm)	286	291	325	367
h_b (μm)	143	145.5	162.5	183.5
d_b (μm)	50	50	50	50
Voltage (kV)	8.5	8.5	8.5	8.5
Current density (A/cm^2)	180	180	180	180
Magnetic field (T)	1	1	1	1
Input RF signal (mW)	5	5	5	5
Number of periods	300	300	300	270

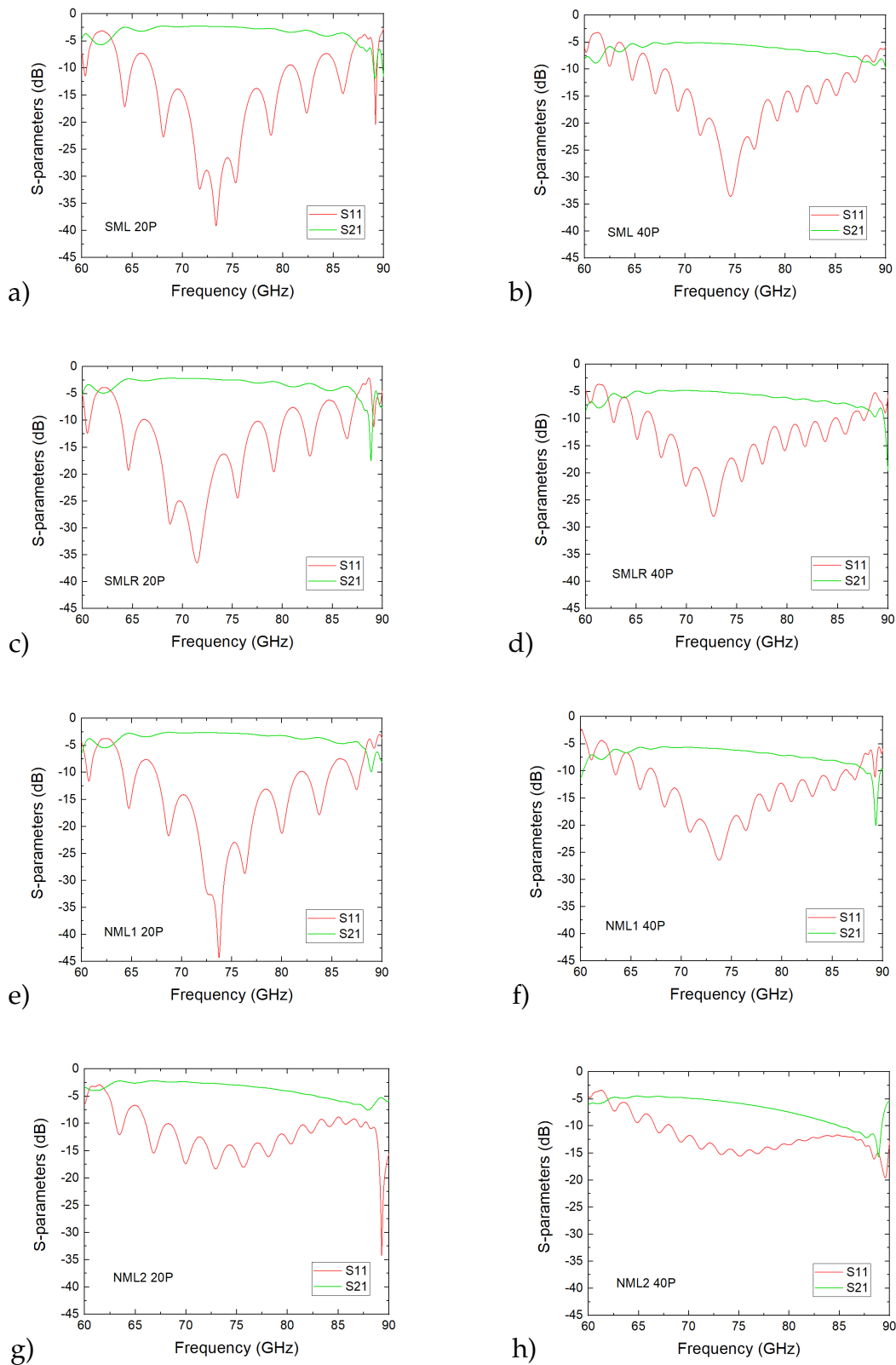


Figure 3.9.2: S-parameters of SML, SMLR, NML1 and NML2 for 20 and 40 periods length at W-band. a) SML 20 periods, b) SML 40 periods, c) SMLR 20 periods, d) SMLR 40 periods, e) NML1 20 periods, f) NML1 40 periods, g) NML2 20 periods and h) NML2 40 periods.

The gain and output power of the four designed meander line are compared in Fig. 3.9.3. The standard meander line with round corners (SMLR) shows slightly higher gain and output power than the standard line with straight corners (SML). The better dispersion also allows to obtain flatter gain at W-band.

SML provides peak gain of 36.75 dB at 75 GHz with 1.2 dB difference within the band. The peak output power is 23.7 W. The results for SMLR show a peak gain and output power of 36.88 dB and 24.36 W, respectively, with a 1.1 dB gain difference within the band.

NML1 is the meander line that provides the highest gain and output power at W-band. This meander also gives flatter dispersion than SML. Instead, NML2 is shown to provide higher gain and output power than the standard meander line (SML), but only over a narrower bandwidth at W-band. The higher interaction impedance of NML2 reduces the number of periods required to reach saturation by 10% in comparison with the other meander lines.

NML1 and NML2 provide peak gain and output power values higher than those for the standard meander line topologies. Specifically, NML1 shows a peak gain and output power of 37.55 dB and 28.43 W, respectively, while NML2 gives 37.41 dB peak gain and 27.53 W peak output power. The gain difference within the 71-76 GHz is 1.32 dB for NML1 while this quantity is increased up to 5.03 dB for NML2.

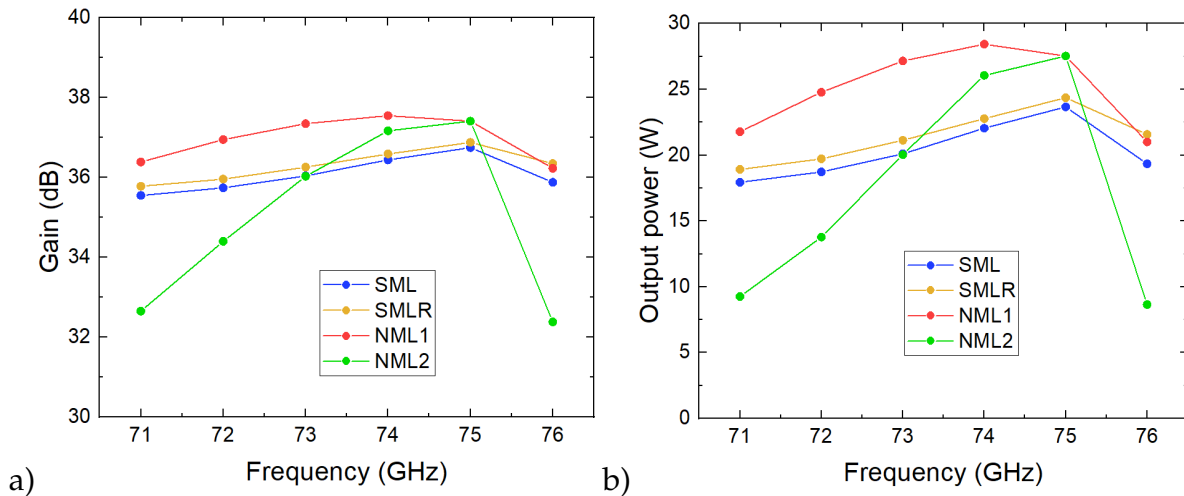


Figure 3.9.3: Comparison of the gain and output power of the four designed meander lines.

3.10 Designs at Ka-band: Soft substrate

To prove the concept, for the first tests, the standard meander line (SML) and the new meander line (NML1) were designed and fabricated at Ka-band using RT/duroid 6002 laminates available at the Engineering Department in Lancaster University.

SML and NML1 are designed with the dimensions shown in Tab. 3.10.1. The phase velocity and the interaction impedance for both meander lines are shown in Fig. 3.10.1. The simulations show that the phase velocity at Ka-band is higher for the new meander line but the slope of the dispersion curve is less steep. The interaction impedance for NML1 is higher at Ka-band than for SML.

Both meander lines are designed for 20 periods and 40 periods length in order to measure the phase velocity. The structures are also terminated in coupling probes as they are placed inside two aluminium housings in order to perform the measurements. The design and dimensions of the probes are shown in Fig. 3.10.2 and 3.10.3 and Tab. 3.10.2, respectively. The coupling structure is designed with a transition extension that remains inside the metal enclosure and the coupling probe that enters the waveguide aperture. The simulated S-parameters using the described design are shown in Fig. 3.10.4 for both meander lines and both 20 periods and 40 periods lengths. Both meander lines present reflection coefficient S11 under -15dB for more than 10% bandwidth.

Table 3.10.1: Dimensions of SML and NML1 using RT/duroid 6002 laminates at Ka-band.

Parameter (μm)	SML	NML1
l_m	1250	1400
t_m	35	35
w	100	100
s	200	100
p	600	600
l_s	2000	2000
t_s	510	510

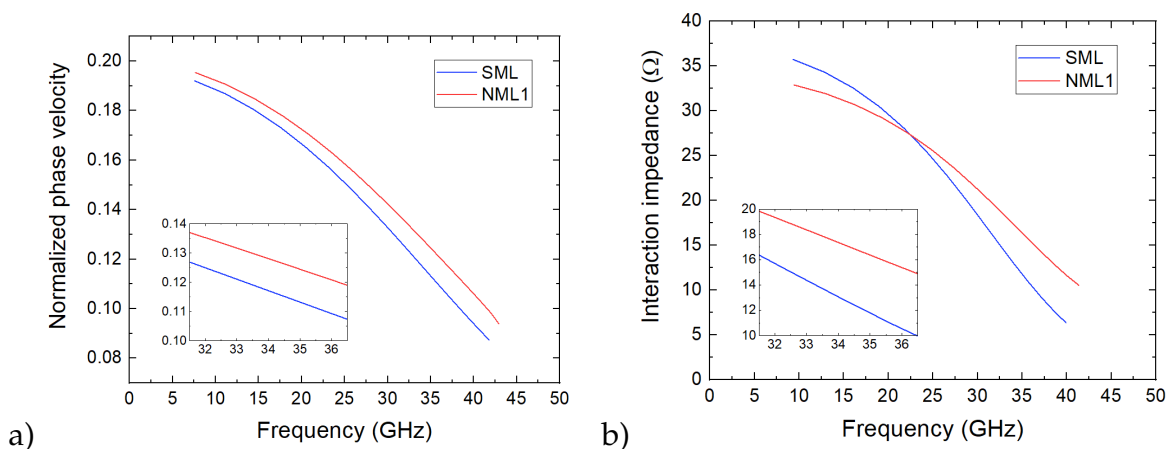


Figure 3.10.1: a) Normalized phase velocity and b) interaction impedance of SML and NML1 on RT6002 substrate at Ka-band.

Table 3.10.2: Dimensions of the coupling probe for SML and NML1 using RT/duroid 6002 substrate at Ka-band.

Parameter (μm)	SML	NML1
l_p	1850	1850
w_p	650	650
l_t	1000	1000
w_t	250	250

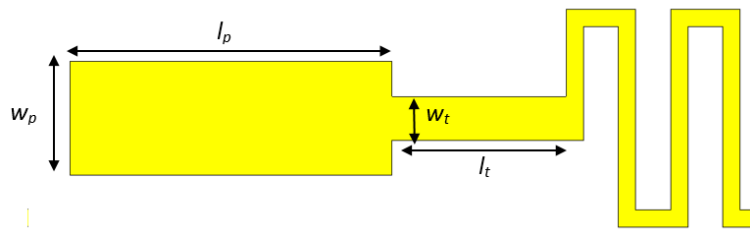


Figure 3.10.2: Schematic and parameters of the coupling probe of SML using RT6002 substrate at Ka-band.

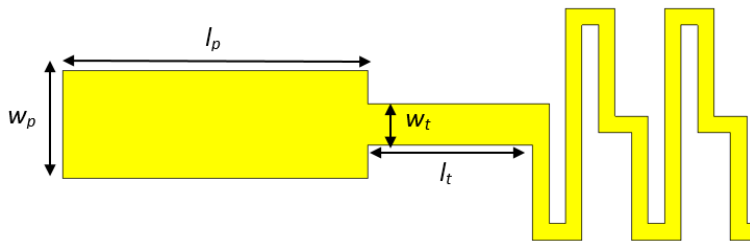


Figure 3.10.3: Schematic and parameters of the coupling probe of NML1 using RT6002 substrate at Ka-band.

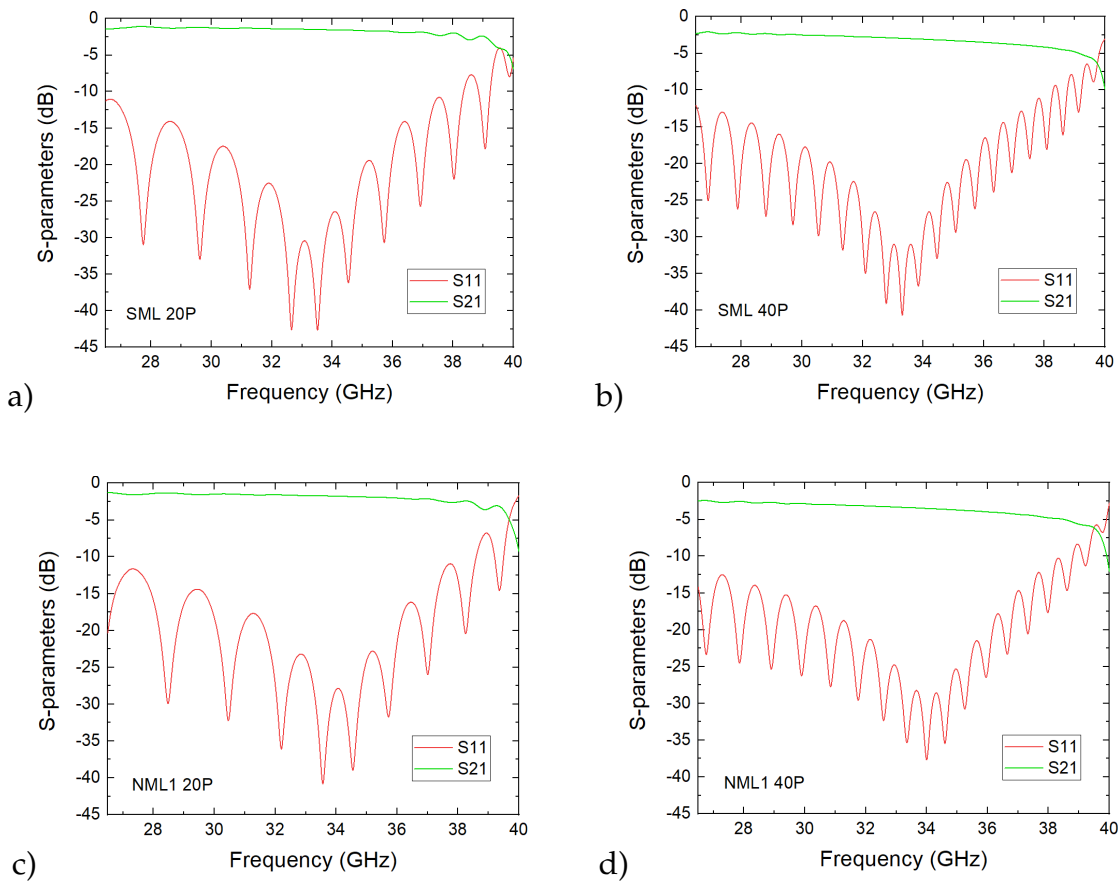


Figure 3.10.4: S-parameters of SML and NML1 using RT/duroid 6002 substrate for 20 and 40 periods length. a) SML 20 periods, b) SML 40 periods, c) NML1 20 periods and d) NML1 40 periods.

3.11 Designs at Ka-band: Alumina substrate

The four meander line designs (SML, SMLR, NML1 and NML2) were prepared and fabricated on alumina substrate at Ka-band for an easier manufacture and test. The same housings as for the soft substrate samples were used, so the meander lines were redesigned for alumina substrate. The dimensions of the meander lines are shown in Tab. 3.11.1. The phase velocity and interaction impedance of the four meander lines are compared in Fig. 3.11.1. The interaction impedance is averaged over a circular beam area with radius $100 \mu\text{m}$ at $50 \mu\text{m}$ from the metallization. NML1 and SMLR show flatter phase velocity at Ka-band than the other two meander lines. Instead, the interaction impedance is higher for NML2.

The design of the coupling probes for the meander lines on alumina is similar to the one of the meander lines on RT/duroid 6002 substrate. The dimensions of the coupling probes for every meander are shown in Tab. 3.11.1. The S-parameters for every meander line and the two lengths are shown in Fig. 3.11.2. The reflection

parameter, S_{11} , shows a 10% transmission window for the four meander lines within the range 33-37 GHz.

Table 3.11.1: Dimensions of SML, SMLR, NML1 and NML2 on alumina substrate at Ka-band.

Parameter (μm)	SML	SMLR	NML1	NML2
l_m	650	650	700	1200
t_m	10	10	10	10
w	100	100	100	75
s	200	200	100	75
p	600	600	600	600
l_s	3000	3000	3000	3000
t_s	127	127	127	127

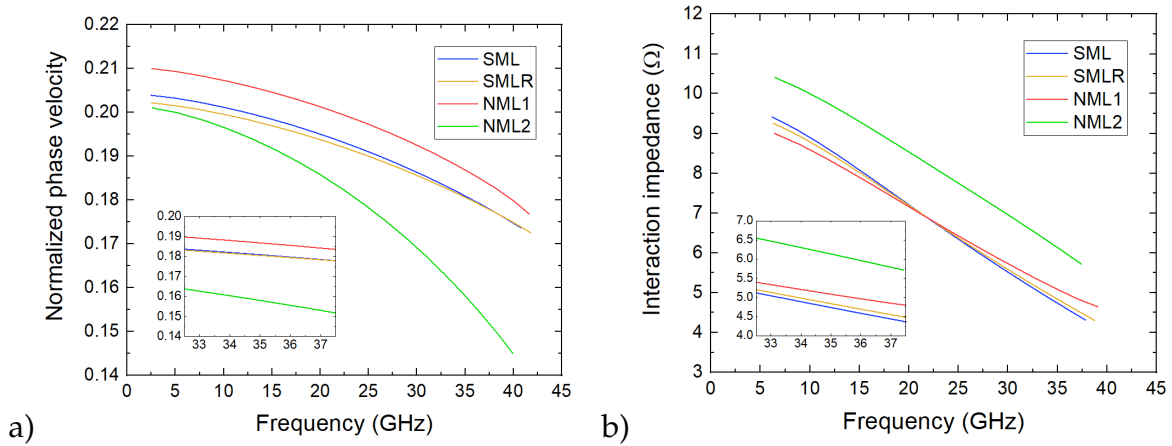


Figure 3.11.1: a) Phase velocity and b) interaction impedance of the four meander lines at Ka-band.

Table 3.11.2: Dimensions of the coupling probe for SML, SMLR, NML1 and NML2 using alumina substrate at Ka-band.

Parameter (μm)	SML	SMLR	NML1	NML2
l_p	1200	1200	1200	1600
w_p	650	650	300	200
l_t	1000	1000	1000	1000
w_t	200	200	200	100

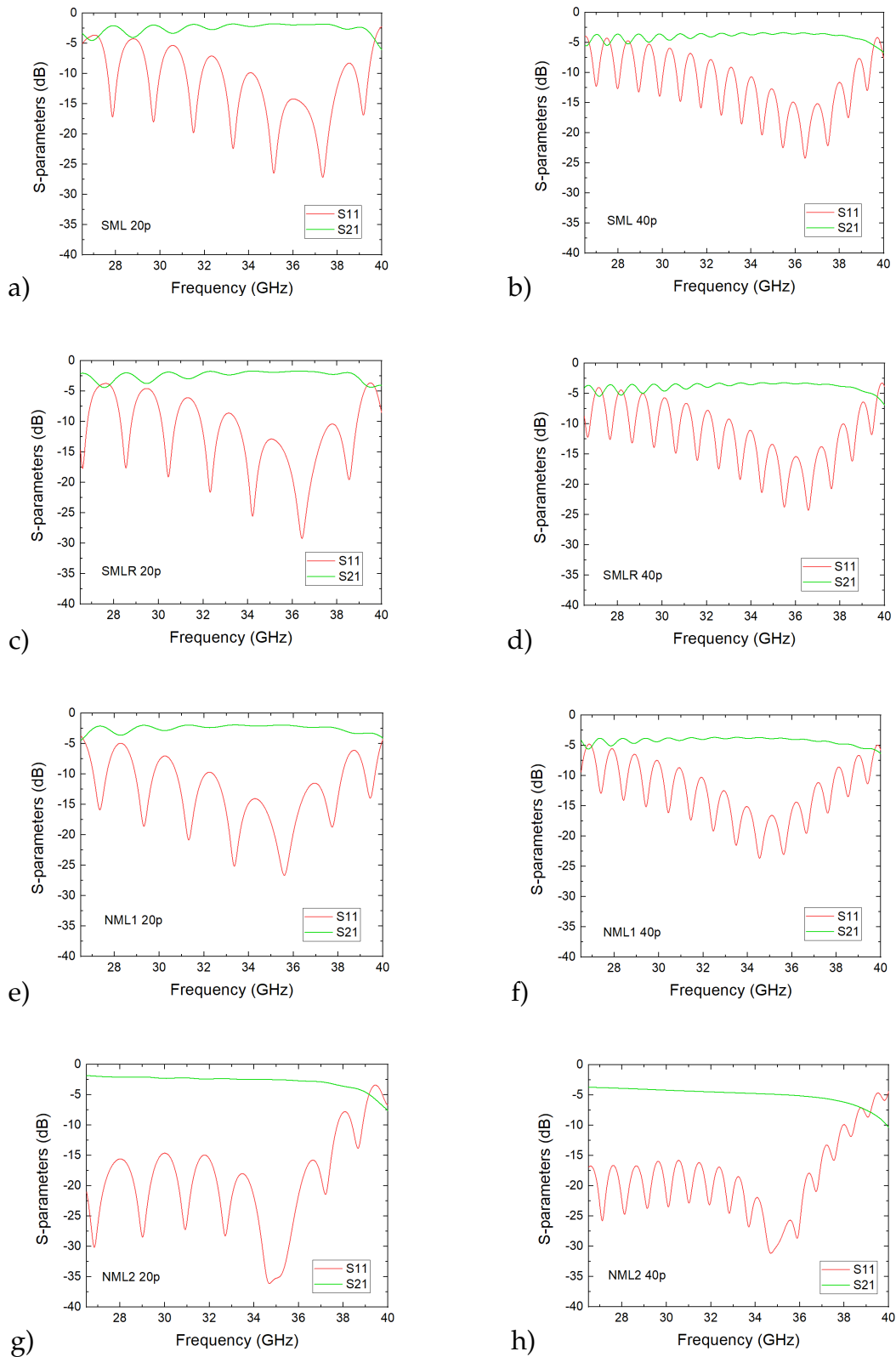


Figure 3.11.2: S-parameters of SML, SMLR, NML1 and NML2 using alumina substrate for 20 and 40 periods length. a) SML 20 periods, b) SML 40 periods, c) SMLR 20 periods, d) SMLR 40 periods, e) NML1 20 periods, f) NML1 40 periods, g) NML2 20 periods and h) NML2 40 periods.

3.12 Ka-band housing

The housings at Ka-band are designed in a similar way as those at W-band. The same housing with two different lengths, 20 and 40 periods of the meander lines, are designed at Ka-band. The 40-period housing is shown in Fig. 3.12.1 and the two parts of the housing are presented in Fig. 3.12.2. The final dimensions of the housings are described in Tab. 3.12.1. The housings are terminated in two WR28 ports with dimensions 7.112 mm \times 3.556 mm. An additional space is added at both ends of the meander line enclosure in order to make an additional support of the structure given the use of soft substrates that may bend if they are suspended.

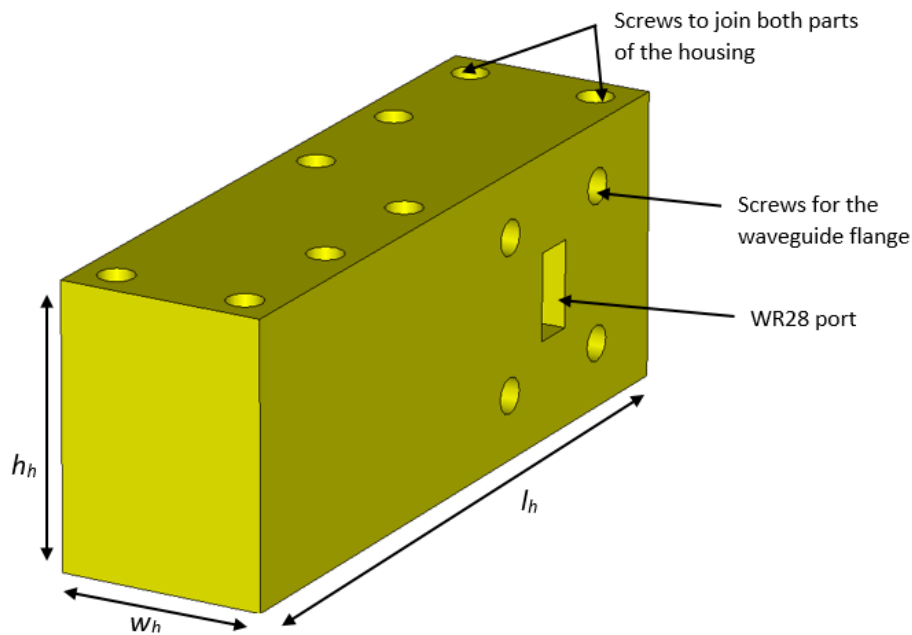


Figure 3.12.1: Final design of the 40-period housing at Ka-band.

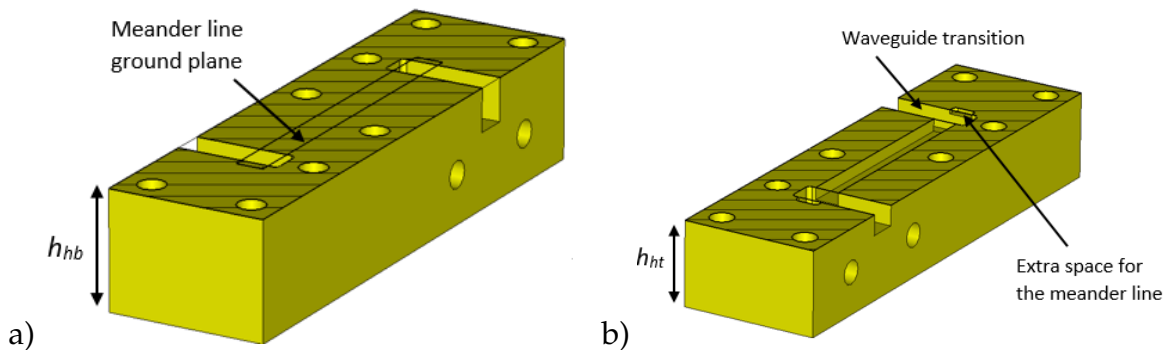


Figure 3.12.2: Final design of both parts of the 40-period housing at Ka-band. a) Bottom part and b) top part.

Table 3.12.1: Dimensions of the 20- and 40-period housing at Ka-band.

Parameter (mm)	20 periods	40 periods
h_h	23.112	23.112
h_{hb}	12.612	12.612
h_{ht}	10.5	10.5
w_h	17	17
l_h	46.912	58.912

3.13 Other meander line structures

Other novel meander line structures, different from the ones that were chosen to be fabricated, were also studied as part of the optimization process. This section presents the cold results of alternative meander line SWSs with interesting properties, but which were finally discarded to move on to the manufacture stage.

Different novel topologies were analysed and compared with the cold performance of SML. The design of some of these structures is shown in Fig. 3.13.1. The phase velocity and interaction impedance for these designs and SML are presented in Fig. 3.13.2. The design in Fig. 3.13.1b shows slightly flatter dispersion curve and similar interaction impedance than SML which is positive in order to obtain flatter gain within the band. However, NML1 outperforms this design providing even flatter dispersion curve while also increasing the interaction impedance. The topology in 3.13.1c is similar in design to NML1 but with curved connections to the middle strip. As seen when compared to SML in Fig. 3.13.2, these curved connections make the phase velocity to greatly increase for the whole bandwidth and, at the same time, the interaction impedance is also substantially reduced. The meander line in Fig. 3.13.1d presents a closed path to the electromagnetic wave. Such kind of designs are characterized by a very high phase velocity and very low interaction impedance as seen in Fig. 3.13.2.

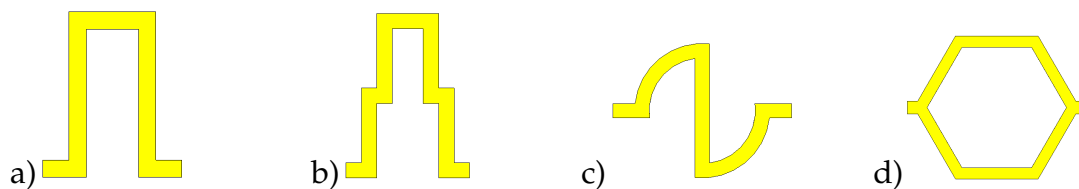


Figure 3.13.1: Design of some novel alternative meander lines. a) SML and b), c), d) novel designs.

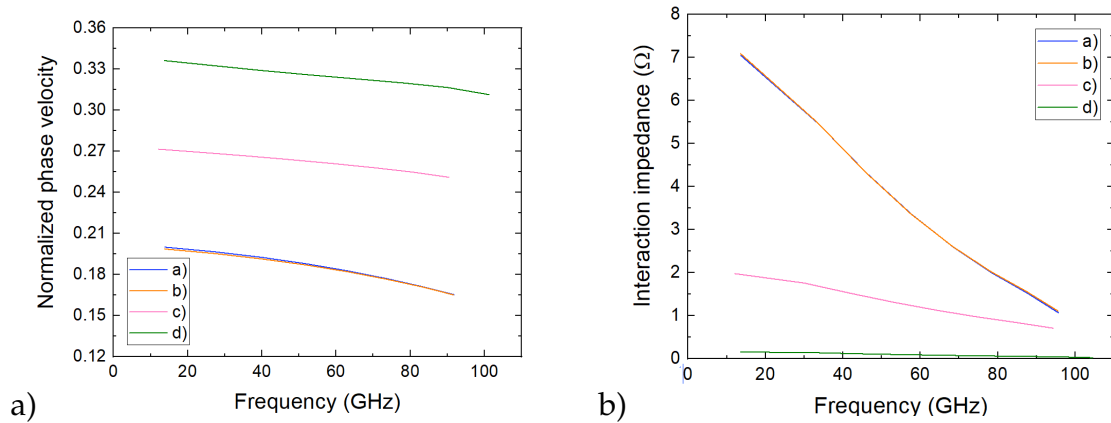


Figure 3.13.2: Phase velocity and interaction impedance of the designs in Fig. 3.13.1.

The addition of a second meander line on top of the electron beam may help increase the gain and output power of the structure. Two-meander line systems are compared in Fig. 3.13.4 with the single SML for cold simulations. Two variations of the structure are analysed, one with the top meander line facing the bottom one with the same orientation, and the other with the top meander line rotated by 180° with respect to the bottom meander as seen in Fig. 3.13.3. Both structures show the same phase velocity curve as SML but a very low interaction impedance. However, the behaviour of the interaction impedance is different depending on the orientation of the top meander line. If the top meander line has the same orientation as the bottom line, the interaction impedance is high at low frequencies and decreases with increasing the frequency. The performance of the double meander line with the top metallization rotated by 180° presents the opposite behaviour. The interaction impedance is low at low frequencies while it increases as the frequency is also increased. The double meander line system also complicates the design of a coupling transition.

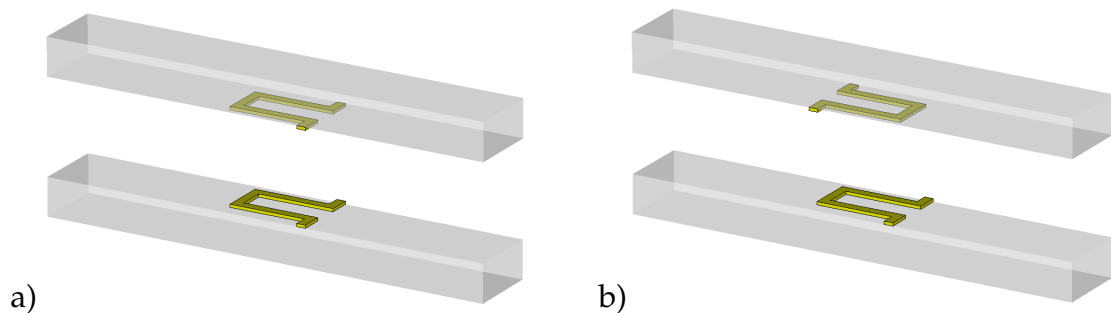


Figure 3.13.3: Design of the double meander line with a) the top meander facing the bottom meander with the same orientation and b) with the top meander rotated by 180° .

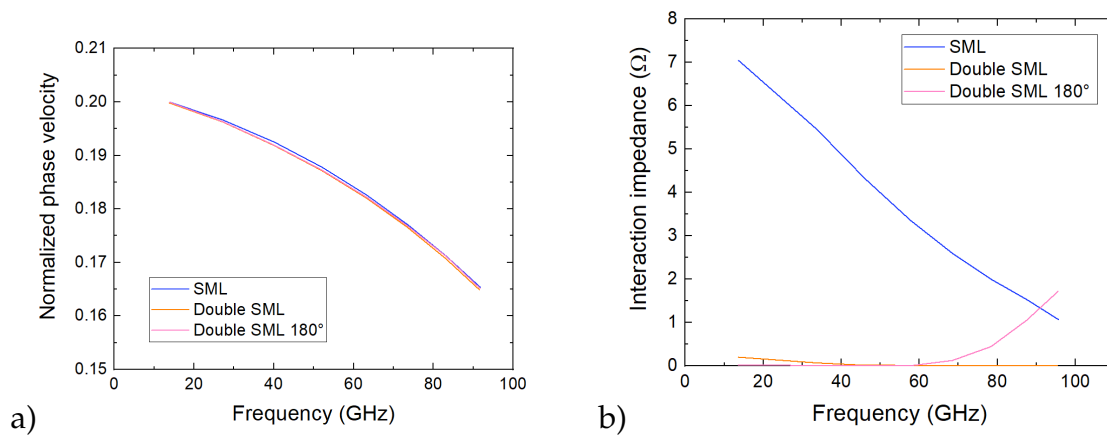


Figure 3.13.4: Phase velocity and interaction impedance of double meander lines.

Another possibility to improve the performance of meander lines is to make modification on the surrounding metal enclosure. Following this approach, the structure is modified by leaving a channel in the part of the enclosure underneath the substrate. Three different cases are studied as seen in Fig. 3.13.5, a channel with the width of the metallization, the substrate sustained by a metal pedestal with the width of the metallization and no metallization at all under the substrate. The cold results are compared with SML in Fig. 3.13.6. The inclusion of a channel under the substrate allows to greatly increase the interaction impedance, but the dispersion of the structure is also increased reducing the bandwidth of operation. The wider the channel, the more is the effect on both interaction impedance and phase velocity. Instead, if a pedestal is left under the metallization as seen in Fig. 3.13.5b, both curves are changed in a similar way but in a much less extent as the interaction impedance and the dispersion are slightly increased in comparison with the SML results.

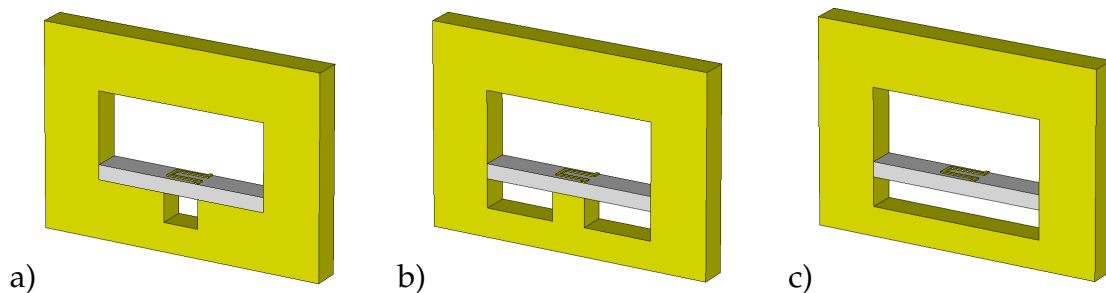


Figure 3.13.5: Design of the meander line with a) channel b) pedestal and c) no metallization below the substrate.

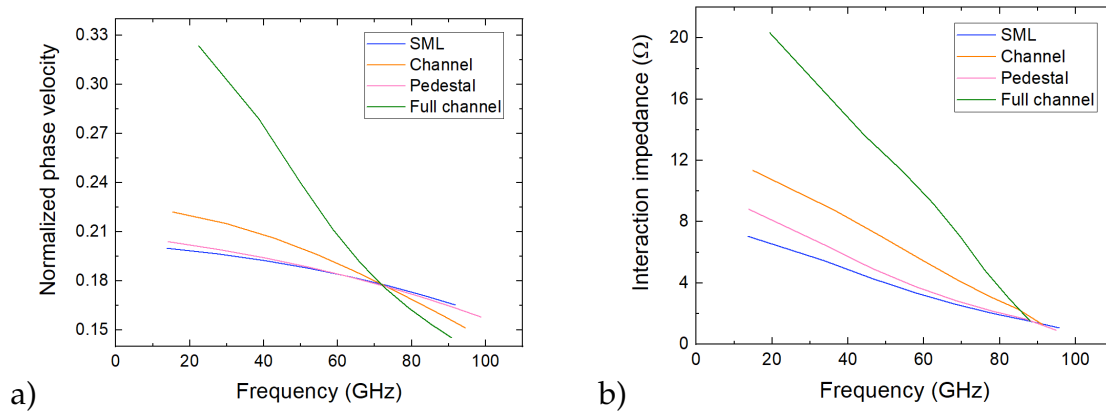


Figure 3.13.6: Phase velocity and interaction impedance of the meander lines with different channels underneath the substrate.

3.14 Summary

This chapter has described the analysis, by means of simulations results, of the characteristics of different meander line SWSs in order to find the optimum designs for W-band TWTs.

Simulations regarding the configuration of the substrate of the meander line revealed that both the material and the thickness of the substrate play an important role to reduce the dispersion of the meander line, which is fundamental in order to accomplish structures that can operate over a broad bandwidth. Specifically, materials with high permittivity are more suitable to reduce the dispersion and the beam voltage, while producing thinner substrates is also important to get low-dispersive structures.

The analysis of the configuration of the metallization of the meander line showed that a proper combination of the different parameters and dimensions could also lead to a more advantageous meander line design. In particular, a reduced length of the metallization is useful to reduce the dispersion.

The study of the beam geometry and its interaction with meander line SWSs concluded that, preferably, meander lines are more suitable to interact with a planar beam geometry such as the sheet electron beam. The interaction of a planar meander line with cylindrical beam geometries is not efficient enough to allow to obtain the output levels required for W-band telecommunications. The adoption of a relatively low aspect ratio sheet electron beam has been a key point in order to provide the meander line with a suitable electron beam geometry that does not require excessively high focusing magnetic field and can provide good enough output results.

Four different planar meander lines have been designed for later manufacture at W-band. These meander line SWSs are named as SML, SMLR, NML1 and NML2, every one of them having its own purpose. SML was designed as the reference meander line for comparison with the novel designs. SMLR was thought with a

similar purpose, but in order to understand the benefits of rounding the straight corners of the metallization, an approach that provides better transmission of the electromagnetic wave along the meander line. The two novel meander lines, NML1 and NML2, are characterized by different reasons: NML1 offers lower dispersion and helps increase the bandwidth and flatten the gain of the TWT. Instead, NML2 offers higher interaction with the objective of increasing the efficiency and performance of the TWT over a narrower band.

The four meander lines were designed with coupling probes at the end of the serpentine line, which, with the design of the housing terminated in waveguide ports, permits a straightforward test and characterization of the SWSs.

As a previous step to the fabrication of the structures at W-band, SML and NML1 were designed at Ka-band using soft substrates for an easier fabrication and test. Similarly, the four meander lines were designed again at Ka-band using alumina substrate before moving up to the target frequency at W-band. These structures at lower frequencies also required the redesign of the corresponding housings to make them suitable for accommodating the Ka-band structures.

4. Analysis and design of novel three-dimensional meander line slow wave structures

As previously described in Sec. 3.3, the interaction of planar meander lines with cylindrical beams is not efficient and the sheet beam is more suitable to obtain higher output power. Nevertheless, while the experimental knowledge on sheet beams is limited, cylindrical beams have been extensively used and tested in TWTs. The reduced magnetic field required to confine the beam, as analysed in Sec. 1.4.2, is also a plus in order to manufacture more reliable and cost-effective TWTs.

In this chapter, three-dimensional designs are derived from the conventional planar meander line to create novel structures that are more suitable to interact with cylindrical beams. Two novel structures are presented: the pillared meander line (PML) where the longitudinal metal strips are extended in height and surround the electron laterally, and the 3D meander line (3DML) where the full planar line is extended in height with an additional substrate on top of the meander line leaving a tunnel in the middle of the metallization. An illustration of the two novel structures is shown in Fig. 4.0.1.

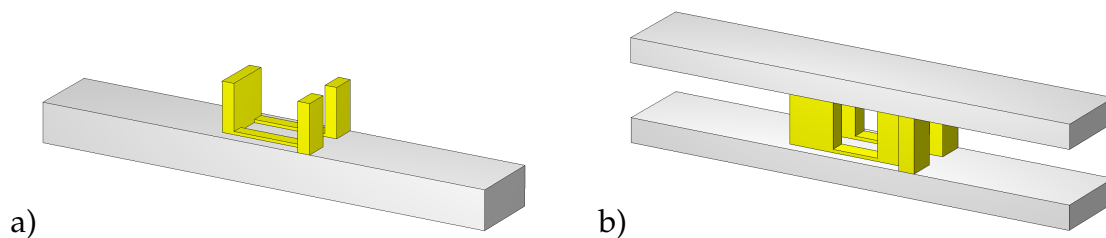


Figure 4.0.1: a) Design of the pillared meander line and b) design of the 3D meander line.

4.1 Pillared meander line (PML)

The pillared meander line is designed at W-band according to the schematic and parameters shown in Fig. 4.1.1 and Tab. 4.1.1. The cold results for this structure are shown in Fig. 4.1.2. The pillared meander line interacts with an electron beam of 6.5 kV within the 71-76 GHz band. The interaction impedance within than range is over 10Ω , a value much higher in comparison with planar meander lines.

The coupling transition for the pillared meander line is similar to the one designed for planar meander lines. In this case, the bottom metallization of the structure is extended at both ends to serve as a probe to couple the electromagnetic wave coming from the waveguide. A schematic of the coupler and the dimensions at W-band are presented in Fig. 4.1.3 and Tab. 4.1.2. The S-parameters using 15 periods of this design are shown in Fig. 4.1.4. A reflection coefficient under -20 dB is obtained from 71 to 76 GHz.

Gain and output power of the structure are simulated using a cylindrical beam with radius $80 \mu\text{m}$, 6.5 kV voltage, current density of 200 A/cm^2 (current of 40 mA) and focused with 0.6 T magnetic field. A RF signal with 50 mW input power is applied. The results are shown in Fig. 4.1.5. Gain over 25 dB and output power over 18 W is obtained at W-band. The peak gain and output power are 28.3 dB and 33.6 W, respectively. These results clearly outperform those of planar meander lines interacting with cylindrical beam geometries and are similar to what it can be achieved using planar meander lines with sheet beams.

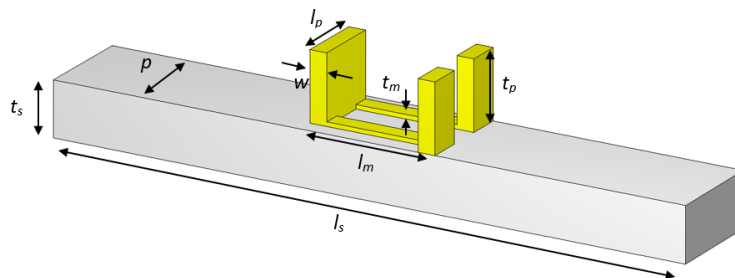


Figure 4.1.1: Dimensions of the pillared meander line at W-band.

Table 4.1.1: Dimensions of the pillared meander line at W-band.

Parameter	Value (μm)
l_m	320
t_m	10
w	40
l_p	160
t_p	150
p	240
l_s	1500
t_s	127

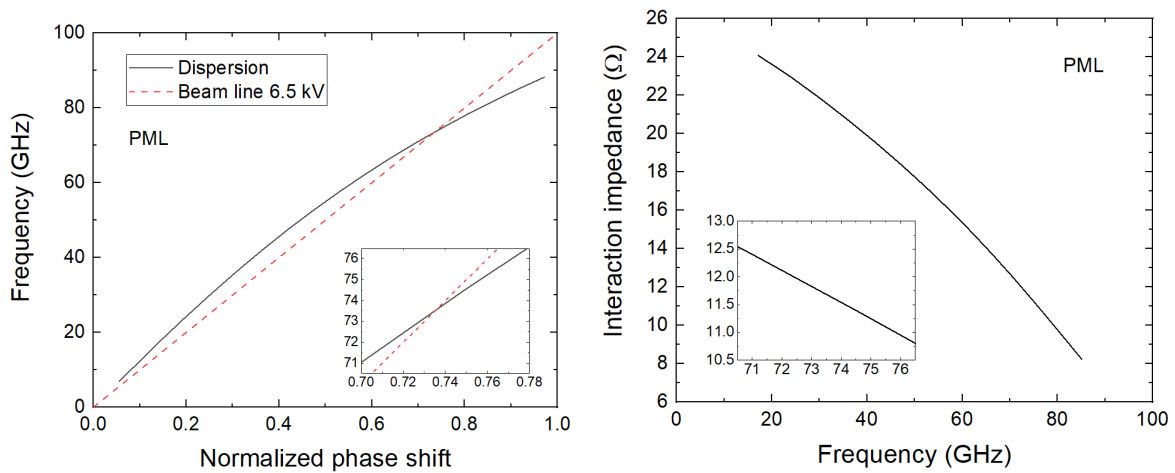


Figure 4.1.2: Dispersion and interaction impedance for the pillared meander line at W-band.

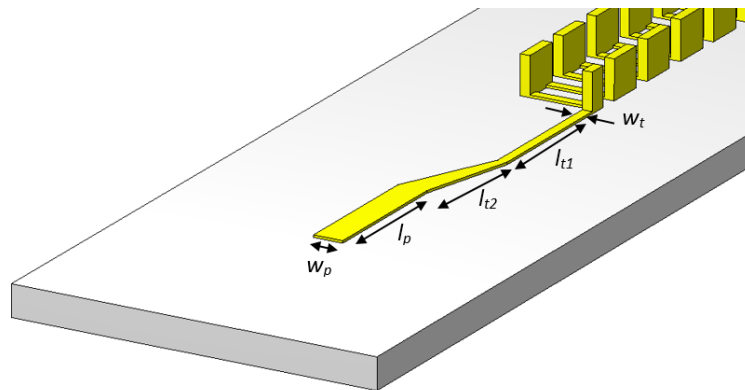


Figure 4.1.3: Schematic and parameters of the coupling probe of the pillared meander line.

Table 4.1.2: Dimensions of the coupling probe of the pillared meander line at W-band.

Parameter	Value (μm)
l_p	600
w_p	120
l_{t1}	650
l_{t2}	400
w_t	40

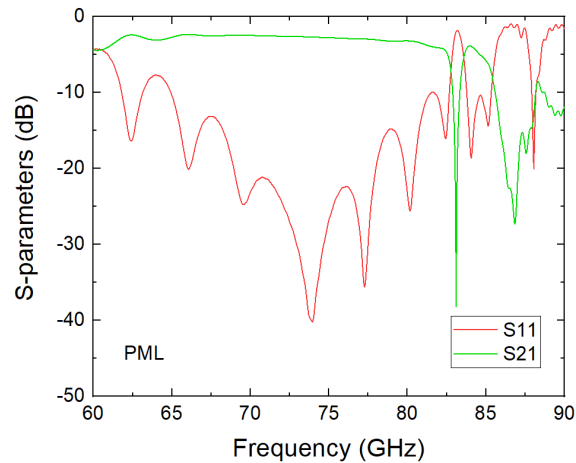


Figure 4.1.4: S-parameters of the pillared meander line at W-band.

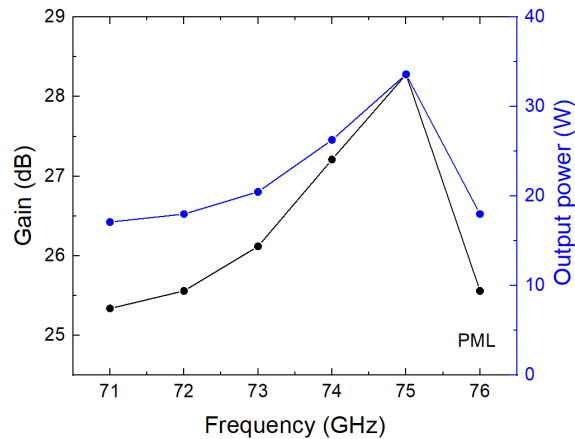


Figure 4.1.5: Gain and output power of the pillared meander line at W-band.

4.2 3D meander line (3DML)

The design of the novel 3D meander line is shown in Fig. 4.2.1. The top substrate has been hidden for a better visualization of the parameters and dimensions which are

described, at W-band, in Tab. 4.2.1. The cold results for this structure are presented in Fig. 4.2.2 and show an operation voltage of 6.5 kV and an average interaction impedance of 13.5Ω in the frequency range from 71 to 76 GHz. The interaction impedance is even higher in comparison with the pillared meander line, which will further increase the gain per period of the SWS.

The design of the coupler is based on extending the planar meander lines into the waveguides as seen in Fig. 4.2.3. The S-parameters results at W-band are shown in Fig. 4.2.4. The structure shows good transmission and low reflection along the 71-76 GHz band.

The same beam parameters have been used as for the pillared meander line to compute the gain and output power of the structure. This is a cylindrical beam with radius $80 \mu\text{m}$, beam voltage of 6.5 kV, current density of 200 A/cm^2 (current of 40 mA) and magnetic focusing field of 0.6 T. The input power of the RF signal is 50 mW. The results are shown in Fig. 4.2.5 showing maximum gain and output power close to 30 dB and 50 W, respectively, with less than 1.5 dB variation within the band. These results show an improvement of the performance in respect of the pillared meander line using the same cylindrical electron beam and also in comparison with the results of the planar meander lines analysed using sheet beams.

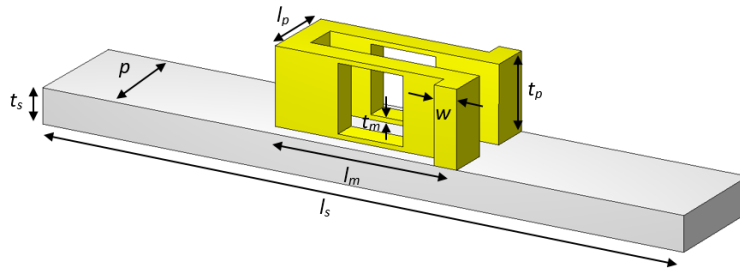


Figure 4.2.1: Schematic of the 3D meander line with the top substrate hidden and parameters.

Table 4.2.1: Dimensions of the 3D meander line at W-band.

Parameter	Value (μm)
l_m	400
t_m	10
w	40
l_p	160
t_p	260
p	240
l_s	1500
t_s	127

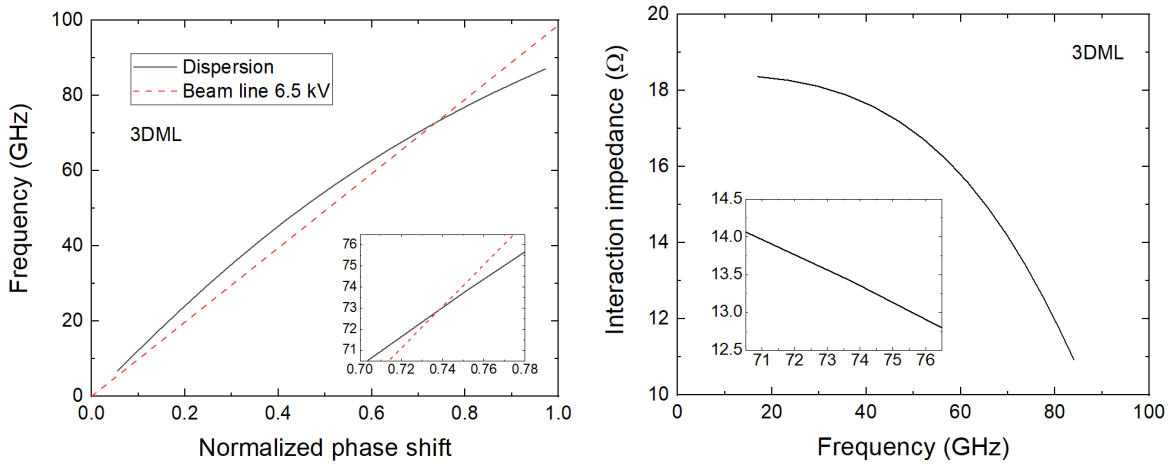


Figure 4.2.2: Dispersion and interaction impedance for the 3D meander line designed at W-band.

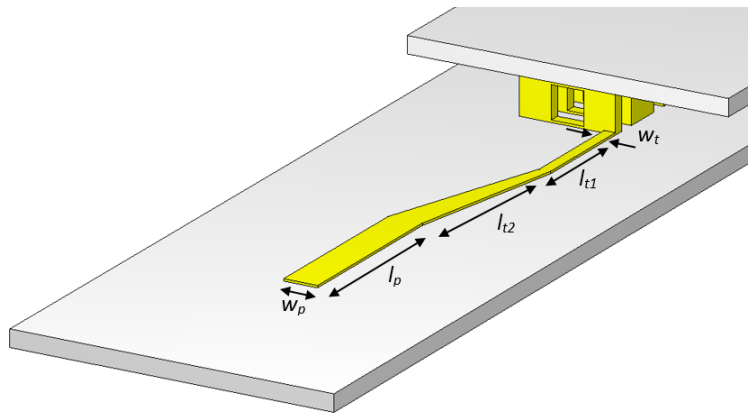


Figure 4.2.3: Schematic and parameters of the coupling probe of the 3D meander line.

Table 4.2.2: Dimensions of the coupling probe of the 3D meander line at W-band.

Parameter	Value (μm)
l_p	450
w_p	120
l_{t1}	550
l_{t2}	500
w_t	40

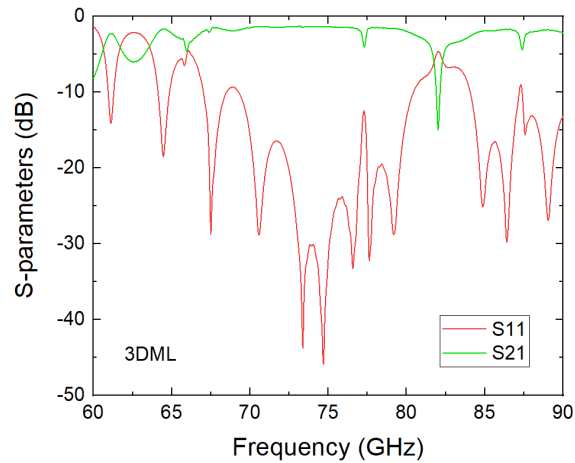


Figure 4.2.4: Scattering parameters for the 3D meander line. The transmission coefficient is plotted in green while the reflection coefficient is the red curve.

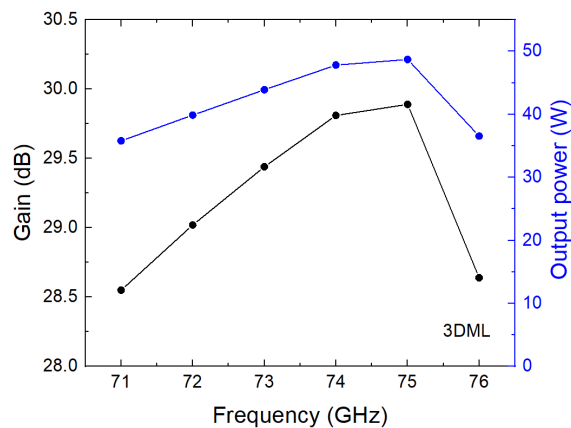


Figure 4.2.5: Gain and output power for the 3D meander line at W-band.

4.3 Cylindrical beam interaction analysis

The improved performance of these novel three-dimensional structures in comparison with the planar meander lines can be explained by analysing the interaction of the electromagnetic field with the cylindrical electron beam.

The electric field of a planar meander line is concentrated close to the metal line as was shown in Fig. 3.3.2, this implies that a cylindrical beam traveling on top of the metal line will not interact uniformly with the electric field. This effect was appreciated in Fig. 3.3.5 and discussed in Sec. 3.3.

The electric field distribution in the transmission direction of the pillared meander line and the 3D meander line are plotted in Fig. 4.3.1. Both electric field distributions

are more suitable, in comparison with planar meander lines, in order to accommodate a cylindrical beam as the whole electron beam is immersed in the electric field.

The electron beam energy modulation, shown in Fig. 4.3.2 for the pillared meander line and the 3D meander respectively, also presents a more uniform bunching. However, the pillared meander line still presents a slight difference between the top and bottom parts of the beam, being the modulation in the bottom half more intense than in the top half. Instead, no difference can be appreciated in the beam energy modulation of the 3D meander line between the top and bottom sides of the electron beam.

Both novel structures should then provide much better performance than a planar meander line interacting with a cylindrical electron beam, with the 3D meander line producing even better results than the meander line with pillars.

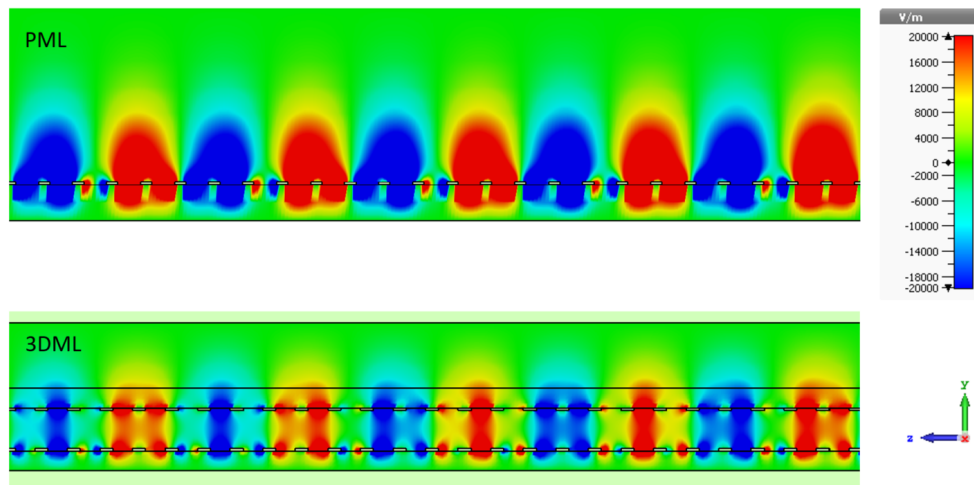


Figure 4.3.1: Lateral view of the longitudinal electric field profile of the pillared meander line and the 3D meander line.

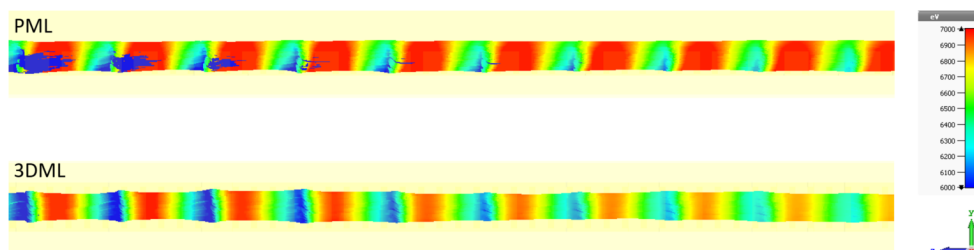


Figure 4.3.2: Lateral view of the beam energy modulation of the pillared meander line and the 3D meander line.

4.4 Fabrication

The fabrication of a three-dimensional structure at W-band is a more demanding task in comparison with planar configurations. Nevertheless, possible fabrication processes for the pillared meander line and the 3D meander line are given in this section.

The pillared meander line can be fabricated following the procedure proposed in Fig. 4.4.1. After preparation of the substrate, it needs to be metallized in order to improve adhesion with low-reactivity metals (4.4.1a). This first layer can be grown by a standard sputtering process. Once the substrate is metallized, a photoresist is applied and exposed to UV-light to pattern the meander line design following a photolithography process. After the photoresist is developed, the meander line can be grown by electroplating (4.4.1b). A subsequent photoresist application and electroplating process can be performed in order to grow the second layer of pillars (4.4.1c). After the full structure is created, the photoresist can be removed and the remaining metallization etched (4.4.1d).

The 3D meander line can be produced by splitting the fabrication into two parts. The bottom part of the 3D meander line can be made by following the same process as for the meander line with pillars. The second part of the structure, containing a planar meander line, can be grown in parallel to the part with the pillars. Finally, both parts can be joined by following a brazing process. This procedure is schematically illustrated in Fig. 4.4.2.

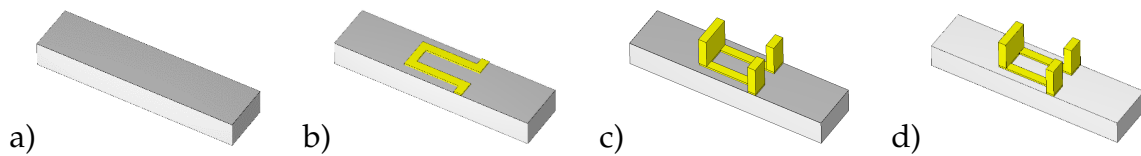


Figure 4.4.1: Process flow of the fabrication of the meander line with pillars.

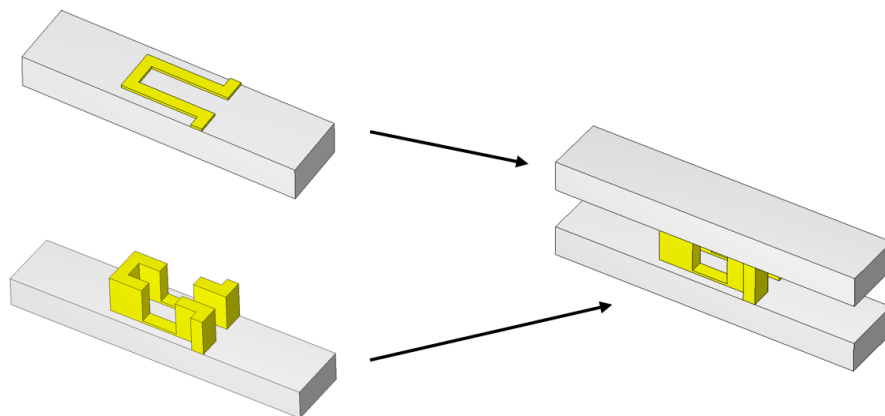


Figure 4.4.2: Fabrication of the 3D meander line.

4.5 Summary

The beam geometry analysis performed in Sec. 3.3 revealed that novel configurations of the meander line different from the planar disposition are needed in order to obtain better performance using a cylindrical beam. Two novel three-dimensional structures (PML and 3DML) have been proposed in that regard, showing much better performance than planar meander lines interacting with cylindrical beam geometries. Both structures can provide the output levels required for W-band satellite communications while also benefiting from the advantages of planar meander lines and the use of a cylindrical electron beam. Even though fabricating such structures at W-band is a more complicated task compared to planar lines, a feasible fabrication approach has been given for the three-dimensional structures.

5. Development of theoretical models for the experimental determination of phase velocity and interaction impedance of meander line slow wave structures

Phase velocity and interaction impedance are two of the most important parameters for the design and characterization of traveling wave tubes. Both parameters cannot be measured directly in a laboratory testbed, but they can be indirectly determined from the measurement of other parameters as long as a relationship between them can be found. Finding these relationships is usually a tough task and needs of a strong mathematical background to derive the required expressions.

Different methods have been proposed to experimentally calculate both the phase velocity and interaction impedance in different kinds of SWSs. The main effort has been focused on helix SWSs where the phase velocity and the interaction impedance can be determined, for instance, by means of solving the field equations [88] or using resonant or non-resonant perturbation methods [89], [90].

Despite the interest on meander lines, experimental results are rare to find in literature, and they are usually limited to validation of the S-parameters. The phase velocity and interaction impedance are commonly obtained from simulations using 3D electromagnetic software. The experimental determination of phase velocity and interaction impedance in meander line SWSs would be crucial for the validation and development of novel topologies and configurations.

This chapter will present and develop the theoretical models that will permit to indirectly measure the phase velocity and the interaction impedance of meander line SWSs in Ch. 6. It will be shown that the phase velocity can be easily derived from the measurement of the phase delay of the same meander line with two different lengths while the interaction impedance can be experimentally determined, also in a straightforward manner, from measurements of the phase difference between the same perturbed and unperturbed meander line SWS.

5.1 Calculation of the phase velocity

The phase velocity of a SWS can be experimentally calculated from measurements of the phase difference of two identical SWSs with different lengths (l_1 and l_2) or number of periods (n_1 and n_2). The difference in lengths is conveniently chosen to be a multiple integer $n = n_2 - n_1$ of the pitch length p of the periodic structure. Therefore, the difference in lengths can be written as $\Delta l = l_2 - l_1 = np$. The phase delay, τ , can be defined as the ratio between the variation of phase and frequency $\tau = \Delta\phi/\Delta\omega$, and then, the difference between the phase delay of the SWSs with different lengths is $\Delta\tau = \Delta\phi_2/\Delta\omega - \Delta\phi_1/\Delta\omega$.

The phase velocity $v_p = \Delta l/\Delta\tau$ is, therefore, computed as

$$v_p = \frac{np}{\Delta\phi_2/\Delta\omega - \Delta\phi_1/\Delta\omega}. \quad (5.1.1)$$

As it will be detailed in Ch. 6, the experimental procedure to quantify the phase velocity will consist of measuring the phase delay of the same meander line with $n_1 = 20$ periods and $n_2 = 40$ periods (τ_1 and τ_2 , respectively) using a Vector Network Analyzer (VNA). Then, the phase velocity can be indirectly determined using Eq. 5.1.1.

5.2 Determination of the interaction impedance

A perturbation method approach, similar to the one presented in [89] for helix slow wave structures based on the work from [91], has been applied to derive an expression that relates the interaction impedance K with a measurable quantity such as the propagation constant shift $\Delta\beta$.

The general equation for the calculation of the interaction impedance for the m th transverse and n th axial harmonics at any given point of a particular slow wave structure is given by [21]

$$K_{mn}(x, y, z) = \frac{E_{z,mn}(x, y, z)E_{z,mn}^*(x, y, z)}{2\beta_n^2 P} \quad (5.2.1)$$

where $\beta_n = \beta + \frac{2\pi n}{p}$, with β_n being the axial phase constant of the n th space harmonic, β the fundamental axial phase constant, p the pitch length and m and n integers. $E_{z,mn}$ is the longitudinal electric field magnitude of the n th axial and m th transverse space harmonics, $E_{z,mn}^*$ its complex conjugate and P is the time averaged RF power flow.

When a physical perturbation is introduced in the system under analysis, the propagation constant shift between the perturbed and unperturbed signals can be defined as [91]

$$\Delta\beta_n = \frac{\omega(\epsilon' - \epsilon_2) \int_{\Delta V} E'_{mn}(x, y, z) \cdot E_{mn}^*(x, y, z) dV}{4Pp} \quad (5.2.2)$$

where E'_{mn} is the perturbed electric field and E_{mn}^* is the complex conjugate of the electric field without perturbation. ϵ' and V are the permittivity and the volume of the perturbation, respectively. ϵ_2 is the permittivity of the original medium where the perturbation is applied.

Eq. 5.2.1 and 5.2.2 are valid for any slow wave structure. However, expressions for the electric fields in these equations need to be derived specifically for meander lines SWSs. In particular, expressions for the electromagnetic fields are derived for the four different meander line topologies studied and presented in Sec. 3.4-3.7. Nevertheless, the procedure permits to obtain a general expression for the interaction impedance regardless of the meander line topology.

The model uses a selection of trigonometric functions to compute the meander line electromagnetic fields. Even though there is some consensus in the selection of this kind of basis functions, slight differences can be found in literature to describe the fields depending on the approach adopted [92], [93].

The meander line SWS can be assumed to be made of perfect conductor metal with infinitesimal thickness and placed on a lossless and uniform dielectric substrate. The substrate is surrounded by perfect conductor walls and ground plane. Following these assumptions, the expressions for the longitudinal components of the electromagnetic field in meander lines can be written as (adapted from [94] for a more general case)

$$E_z(x, y, z) = \sum_{m,n=-\infty}^{\infty} A_{jk,mm} \frac{\sinh(\alpha_{ijk,mm} Y_i)}{\sinh(\alpha_{ijk,mm} B_i)} \sin(k_{jk,m} X_{jk}) e^{-j\beta_n z}, \quad (5.2.3)$$

$$H_z(x, y, z) = \sum_{m,n=-\infty}^{\infty} B_{jk,mm} \frac{\cosh(\alpha_{ijk,mm} Y_i)}{\cosh(\alpha_{ijk,mm} B_i)} \cos(k_{jk,m} X_{jk}) e^{-j\beta_n z} \quad (5.2.4)$$

where $\alpha_{ijk,mm}^2 = k_{jk,m}^2 + \beta_n^2 - \omega^2 \mu \epsilon_i$.

These expressions contain three indexes i, j and k that vary according to the spatial disposition of the structure and are fundamental to correctly characterize the electromagnetic fields of every particular meander line topology. Specifically, each index is linked to one spacial dimension; i and k to the transverse vertical and horizontal coordinates, respectively, and j to the longitudinal coordinate.

A standard meander line (SML) enclosed in a rectangular housing, similar to the experimental configuration of the meander line, is considered as an example to describe the index association. As schematically seen in Fig. 5.2.1, the index i (coordinate y) can be either 1 or 2 depending on the region of analysis if the metallization is considered to be infinitesimally thin: the substrate with permittivity ϵ_1 or the surrounding medium with permittivity ϵ_2 . Similarly, the indexes j and k (coordinates z and x , respectively) can be defined taking as a reference the schematic shown in Fig. 5.2.2. For the standard meander topology, the index j varies from 1 to 5 in order to consider the regions where the electromagnetic fields are different. The

index k moves from 1 to 3 to be able to distinguish between the substrate and metal regions.

As seen in Fig. 5.2.1, the expressions for Y_i and B_i in Eq. 5.2.3 and 5.2.4 do not depend on the meander line topology if this is considered infinitesimally thin. However, the other parameters, the field amplitudes A_{jk} and B_{jk} , and X_{jk} and k_{jk} do depend on the meander line disposition and vary accordingly.

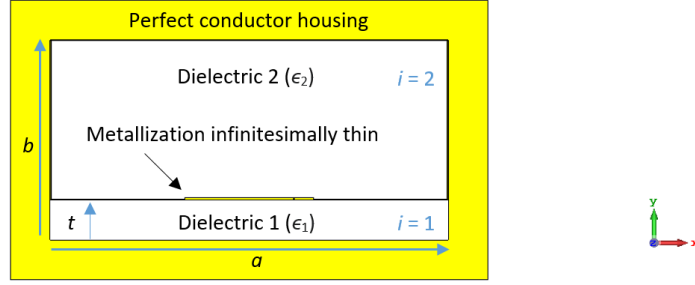


Figure 5.2.1: xy -plane view of the two regions of the meander line to be analyzed. t is the thickness of the substrate, a is the length of the substrate and b is the height of the perfect conductor cavity.

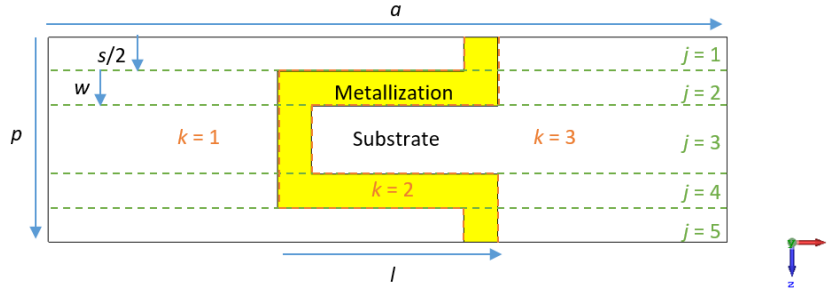


Figure 5.2.2: xz -plane view of the standard meander line. There are five and three regions along the z and x axis, respectively. s is the distance between two consecutive strips, w is the strip width, p is the pitch length, a is the length of the substrate and l is the length of the metallization.

Applying Maxwell's equations to Eq. 5.2.3 and 5.2.4 allows to obtain general expressions for the transverse electric field components as

$$E_x(x, y, z) = \sum_{m,n=-\infty}^{\infty} j \frac{\sinh(\alpha_{ijk,mn} Y_i) \cos(k_{jk,m} X_{jk})}{\beta_n^2 - \omega^2 \mu \epsilon_i} e^{-j\beta_n z} \left(A_{jk,mn} \frac{\partial X_{jk}}{\partial x} \frac{k_{jk,m} \beta_n}{\sinh(\alpha_{ijk,mn} B_i)} + B_{jk,mn} \frac{\partial Y_i}{\partial y} \frac{\alpha_{ijk,mn} \omega \mu}{\cosh(\alpha_{ijk,mn} B_i)} \right), \quad (5.2.5)$$

$$E_y(x, y, z) = \sum_{m,n=-\infty}^{\infty} j \frac{\cosh(\alpha_{ijk,mn} Y_i) \sin(k_{jk,m} X_{jk})}{\beta_n^2 - \omega^2 \mu \epsilon_i} e^{-j\beta_n z} \left(A_{jk,mn} \frac{\partial Y_i}{\partial y} \frac{\alpha_{ijk,mn} \beta_n}{\sinh(\alpha_{ijk,mn} B_i)} + B_{jk,mn} \frac{\partial X_{jk}}{\partial x} \frac{k_{jk,m} \omega \mu}{\cosh(\alpha_{ijk,mn} B_i)} \right). \quad (5.2.6)$$

Next, a dielectric perturbation with permittivity ϵ' is placed in the region $i = 2$. Three regions now exist: the region within the substrate ($i = 1$), the region above the substrate external to the perturbation ($i = 2$) and the region within the perturbation. Fig. 5.2.3 shows an example of a dielectric cylindrical rod introduced as a perturbation in the system similar to the experimental setup followed for the measurements.

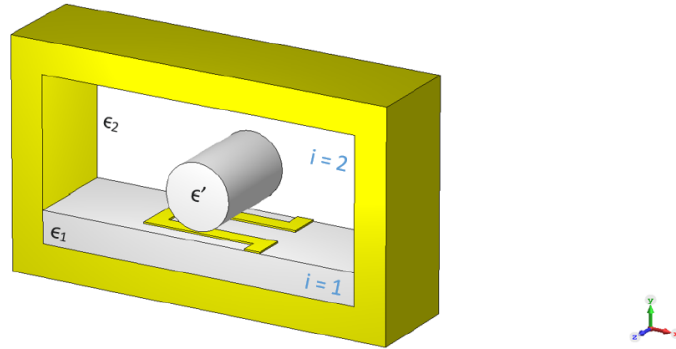


Figure 5.2.3: 3D view of the three regions to be analysed including the perturbation.

The fields within the perturbed region are changed in such a way that the field amplitudes A_{jk} and B_{jk} , and the propagation constant β_n are shifted to the equivalent parameters A'_{jk} , B'_{jk} and β'_n , respectively. Making $i = 2$ in Y_i and B_i as the perturbation is placed in this region, the perturbed field components are then expressed as

$$E'_z(x, y, z) = \sum_{m,n=-\infty}^{\infty} A'_{jk,mn} \frac{\sinh(\alpha'_{jk,mn} Y_2)}{\sinh(\alpha'_{jk,mn} B_2)} \sin(k_{jk,m} X_{jk}) e^{-j\beta'_n z}, \quad (5.2.7)$$

$$E'_x(x, y, z) = \sum_{m,n=-\infty}^{\infty} j \frac{\sinh(\alpha'_{jk,mn} Y_2) \cos(k_{jk,m} X_{jk})}{\beta_n'^2 - \omega^2 \mu \epsilon'} e^{-j\beta'_n z} \left(A'_{jk,mn} \frac{\partial X_{jk}}{\partial x} \frac{k_{jk,m} \beta'_n}{\sinh(\alpha'_{jk,mn} B_2)} + B'_{jk,mn} \frac{\partial Y_2}{\partial y} \frac{\alpha'_{jk,mn} \omega \mu}{\cosh(\alpha'_{jk,mn} B_2)} \right), \quad (5.2.8)$$

$$E'_y(x, y, z) = \sum_{m,n=-\infty}^{\infty} j \frac{\cosh(\alpha'_{jk,mn} Y_2) \sin(k_{jk,m} X_{jk})}{\beta_n'^2 - \omega^2 \mu \epsilon'} e^{-j\beta'_n z} \left(A'_{jk,mn} \frac{\partial Y_2}{\partial y} \frac{\alpha'_{jk,mn} \beta'_n}{\sinh(\alpha'_{jk,mn} B_2)} + B'_{jk,mn} \frac{\partial X_{jk}}{\partial x} \frac{k_{jk,m} \omega \mu}{\cosh(\alpha'_{jk,mn} B_2)} \right). \quad (5.2.9)$$

The interaction impedance can be defined at one arbitrary point (x_0, y_0) according to Eq. 5.2.1 as

$$K_{mn}(x_0, y_0) = \frac{E_{z,mn}(x_0, y_0)E_{z,mn}^*(x_0, y_0)}{2\beta_n^2 P}. \quad (5.2.10)$$

To relate the interaction impedance at this particular point $K_{mn}(x_0, y_0)$ with the measurable quantity $\Delta\beta_n$, it is necessary to find the relation between the product of fields from Eq. 5.2.10 with that from Eq. 5.2.2.

The approach to find this relation is based on the application of interface conditions, first, between the dielectric perturbation and its surrounding medium, and second, between the meander line substrate and the medium over it. For the first case, the perturbation is assumed to be uniform along the axial direction. Therefore, the continuity of the tangential E_t and normal D_n field components used to relate the perturbed and unperturbed axial field components are valid at any point of the perturbation surface and independent of the z coordinate. Similarly for the second case, at the interface between the substrate and the medium on top of it, the tangential E_t field and the normal D_n components are continuous.

Applying all these conditions, the following relationships between the electric fields can be found

$$E'_{z,mn}(x, y, z)E_{z,mn}^*(x, y, z) = E_{z,mn}(x_0, y_0)E_{z,mn}^*(x_0, y_0) \cdot G_{jk,z} \sinh(\alpha'_{jk,mn} Y_2) \sinh(\alpha_{2jk,mn} Y_2) \sin^2(k_{jk,m} X_{jk}), \quad (5.2.11)$$

$$E'_{x,mn}(x, y, z)E_{x,mn}^*(x, y, z) = E_{z,mn}(x_0, y_0)E_{z,mn}^*(x_0, y_0) \cdot G_{jk,x} \sinh(\alpha'_{jk,mn} Y_2) \sinh(\alpha_{2jk,mn} Y_2) \cos^2(k_{jk,m} X_{jk}), \quad (5.2.12)$$

$$E'_{y,mn}(x, y, z)E_{y,mn}^*(x, y, z) = E_{z,mn}(x_0, y_0)E_{z,mn}^*(x_0, y_0) \cdot G_{jk,y} \cosh(\alpha'_{jk,mn} Y_2) \cosh(\alpha_{2jk,mn} Y_2) \sin^2(k_{jk,m} X_{jk}) \quad (5.2.13)$$

with $G_{jk,z}$, $G_{jk,x}$ and $G_{jk,y}$ being coefficients that contain the particularities of every interface condition applied.

Every expression obtained for the product between the perturbed and unperturbed field components (Eq. 5.2.11-5.2.13) can be then replaced into Eq. 5.2.2 as

$$\Delta\beta_n = \frac{\omega(\epsilon' - \epsilon_2)}{4Pp} E_{z,mn}(x_0, y_0)E_{z,mn}^*(x_0, y_0) \int_{\Delta V} \sum_{jk} [G_{jk,z} \sinh(\alpha'_{jk,mn} Y_2) \sinh(\alpha_{2jk,mn} Y_2) \sin^2(k_{jk,m} X_{jk}) + G_{jk,x} \sinh(\alpha'_{jk,mn} Y_2) \sinh(\alpha_{2jk,mn} Y_2) \cos^2(k_{jk,m} X_{jk}) + G_{jk,y} \cosh(\alpha'_{jk,mn} Y_2) \cosh(\alpha_{2jk,mn} Y_2) \sin^2(k_{jk,m} X_{jk})] dV. \quad (5.2.14)$$

Finally, solving for the product $E_{z,mn}(x_0, y_0)E_{z,mn}^*(x_0, y_0)$ in Eq. 5.2.14 and replacing into Eq. 5.2.10, the interaction impedance at one selected point $K_{mn}(x_0, y_0)$ can be calculated in terms of the measurable quantities β_n and $\Delta\beta_n$ according to

$$K_{mn}(x_0, y_0) = \frac{2p}{\omega(\epsilon' - \epsilon_2)} \frac{\Delta\beta_n}{\beta_n^2} \frac{1}{I_{mn}} \quad (5.2.15)$$

where I_{mn} is the numerical result of the integral from Eq. 5.2.14.

As derived in Eq. 5.2.15, β and $\Delta\beta$ are the quantities that need to be measured in order to experimentally determine the interaction impedance. Values for β are obtained from the phase velocity measurements as $\beta = \omega/v_p$. To measure $\Delta\beta$, as it will be described with more detail in Ch. 6, a perturbation in the form of a dielectric rod will be placed close to the meander line to measure the perturbed phase ϕ' using a VNA. By a subsequent measurement of the phase of the same meander line without the perturbation, ϕ , the propagation constant shift will be calculated as $\Delta\beta = \Delta\phi/l$, where l is the length of the circuit. Introducing the measured propagation constant β and propagation constant shift $\Delta\beta$ values into Eq. 5.2.15 will permit to easily determine the experimental interaction impedance of the different meander line SWSs.

Considering the coupling transition chosen for the meander line as described in Sec. 2.2, the perturbation has an effect not only in the transmission of the radiofrequency signal along the SWS but also in the coupling from the waveguide to the meander line. In order to correctly quantify the interaction impedance, the contribution of the perturbation to the coupling should be subtracted.

The propagation constant shift due to the perturbation can be described as $\Delta\beta = \beta' - \beta$, where β' and β are the perturbed and unperturbed propagation constants, respectively. When the perturbation is placed on top of the whole circuit, β' contains both the contribution of the perturbation to the SWS and to the coupling transition, this is $\Delta\beta_{sws+c} = \beta'_{sws+c} - \beta$. Instead, if the perturbation is placed only on top of the coupling probes, the perturbation only affects the coupling transition, $\Delta\beta_c = \beta'_c - \beta$. Therefore, it is possible to calculate the interaction impedance of the meander line considering only the contribution of the perturbation to the slow wave circuit if the propagation constant shift is defined as $\Delta\beta_{sws} = \Delta\beta_{sws+c} - \Delta\beta_c$.

5.2.1 Derivation of the coefficients $G_{jk,z}$, $G_{jk,x}$ and $G_{jk,y}$

The product between the axial components of the perturbed and the complex unperturbed fields, Eq. 5.2.7 and the conjugate equivalent of Eq. 5.2.3, can be written as

$$E'_{z,mn}(x, y, z)E_{z,mn}^*(x, y, z) = \frac{A'_{jk,mn}}{A_{jk,mn}} A_{jk,mn}^* A_{jk,mn} \frac{\sinh(\alpha'_{jk,mn} Y_2) \sinh(\alpha_{ijk,mn} Y_i)}{\sinh(\alpha'_{jk,mn} B_2) \sinh(\alpha_{ijk,mn} B_i)} \sin^2(k_{jk,m} X_{jk}) e^{-j(\beta'_n - \beta_n)z}. \quad (5.2.16)$$

The unperturbed axial field component at one given point (x_0, y_0) within the region of perturbation is defined, according to Eq. 5.2.3, as

$$E_{z,mn}(x_0, y_0, z) = A_{jk,mn} \frac{\sinh(\alpha_{2jk,mn} Y_2^0)}{\sinh(\alpha_{2jk,mn} B_2)} \sin(k_{jk,m} X_{jk}^0) e^{-j\beta_n z}, \quad (5.2.17)$$

and multiplying with its complex conjugate gives

$$E_{z,mn}(x_0, y_0) E_{z,mn}^*(x_0, y_0) = A_{jk,mn} A_{jk,mn}^* \frac{\sinh^2(\alpha_{2jk,mn} Y_2^0)}{\sinh^2(\alpha_{2jk,mn} B_2)} \sin^2(k_{jk,m} X_{jk}^0). \quad (5.2.18)$$

Solving for the product between the field amplitudes gives

$$A_{jk,mn} A_{jk,mn}^* = E_{z,mn}(x_0, y_0) E_{z,mn}^*(x_0, y_0) \frac{\sinh^2(\alpha_{2jk,mn} B_2)}{\sinh^2(\alpha_{2jk,mn} Y_2^0) \sin^2(k_{jk,m} X_{jk}^0)}. \quad (5.2.19)$$

The continuity of the tangential axial field component at the perturbation surface implies that at one given point (x_1, y_1) of the surface, $E'_z(x_1, y_1, z) = E_z(x_1, y_1, z)$. From there, a relation between the unperturbed and perturbed field coefficients is found

$$\frac{A'_{jk,mn}}{A_{jk,mn}} e^{-j(\beta'_n - \beta_n)z} = \frac{\sinh(\alpha_{2jk,mn} Y_2^1) \sinh(\alpha'_{jk,mn} B_2)}{\sinh(\alpha'_{jk,mn} Y_2^1) \sinh(\alpha_{2jk,mn} B_2)}. \quad (5.2.20)$$

Finally, replacing the expressions from Eq. 5.2.19 and 5.2.20 into Eq. 5.2.16, the product of the perturbed and unperturbed fields is rewritten in terms of the product between the original and complex unperturbed axial field components as (Eq. 5.2.11)

$$E'_{z,mn}(x, y, z) E_{z,mn}^*(x, y, z) = E_{z,mn}(x_0, y_0) E_{z,mn}^*(x_0, y_0) \cdot G_{jk,z} \sinh(\alpha'_{jk,mn} Y_2) \sinh(\alpha_{2jk,mn} Y_2) \sin^2(k_{jk,m} X_{jk}), \quad (5.2.21)$$

with

$$G_{jk,z} = \frac{\sinh(\alpha_{2jk,mn} Y_2^1)}{\sinh(\alpha'_{jk,mn} Y_2^1) \sinh^2(\alpha_{2jk,mn} Y_2^0) \sin^2(k_{jk,m} X_{jk}^0)}.$$

Eq. 5.2.12 and 5.2.13 can be derived in a similar fashion applying the interface conditions that correspond to each field component. For the transverse components $E_x(x, y, z)$ and $E_y(x, y, z)$, the field expressions are written in terms of two different coefficients, $A_{jk,mn}$ and $B_{jk,mn}$. In order to eliminate one coefficient and relate the perturbed and unperturbed fields, two interface conditions are needed.

For the perturbed fields, it is used that at the same position of the perturbation surface where the axial component is continuous (x_1, y_1) , the normal field component is also continuous $\epsilon' E'_y(x_1, y_1, z) = \epsilon_2 E_y(x_1, y_1, z)$. For the unperturbed fields, the tangential field components at the interface dielectric-dielectric ($y_2 = t$) are continuous, and then $E_{x(i=1)}(x, y_2, z) = E_{x(i=2)}(x, y_2, z)$.

With these considerations, the coefficients $G_{jk,x}$ and $G_{jk,y}$ result

$$G_{jk,x} = \left(\frac{k_{jk,m}^2 \beta_n \beta'_n \left(1 - \frac{\alpha_{jk,mn}^2}{k_{jk,m}^2}\right) \sinh(\alpha_{2jk,mn} Y_2^1)}{(\beta_n'^2 - \omega^2 \mu \epsilon') (\beta_n^2 - \omega^2 \mu \epsilon_2) \sinh^2(\alpha_{2jk,mn} Y_2^2) \sinh(\alpha'_{jk,mn} Y_2^1)} \right. \\ \left. - \frac{\epsilon_2 \beta_n^2 \alpha_{2jk,mn} \alpha'_{jk,mn} \cosh(\alpha_{2jk,mn} Y_2^1) F_{jk}}{\epsilon' (\beta_n^2 - \omega^2 \mu \epsilon_2)^2 \sinh^2(\alpha_{2jk,mn} Y_2^2) \cosh(\alpha'_{jk,mn} Y_2^1)} \right) F_{jk} \frac{\sinh^2(\alpha_{2jk,mn} Y_2^2)}{\sinh^2(\alpha_{2jk,mn} Y_2^0) \sin^2(k_{jk,m} X_{jk}^0)},$$

$$G_{jk,y} = \frac{\epsilon_2 \alpha_{2jk,mn}^2 \beta_n^2 \cosh(\alpha_{2jk,mn} Y_2^1) F_{jk}^2}{\epsilon' (\beta_n^2 - \omega^2 \mu \epsilon_2)^2 \cosh(\alpha'_{jk,mn} Y_2^1) \sinh^2(\alpha_{2jk,mn} Y_2^0) \sin^2(k_{jk,m} X_{jk}^0)},$$

with

$$F_{jk} = -1 + \frac{k_{jk,m}^2 \omega^2 \mu (\epsilon_2 - \epsilon_1)}{\alpha_{2jk,mn}^2 (\beta_n^2 - \omega^2 \mu \epsilon_1) \left(1 + \frac{\alpha_{1jk,mn} (\beta_n^2 - \omega^2 \mu \epsilon_2) \tanh(\alpha_{1jk,mn} Y_1^2)}{\alpha_{2jk,mn} (\beta_n^2 - \omega^2 \mu \epsilon_1) \tanh(\alpha_{2jk,mn} Y_2^2)}\right)}.$$

5.2.2 Derivation of the parameters Y_i , B_i , X_{jk} and k_{jk}

Assuming an infinitesimal thickness for the metallization, the characterization over the transverse vertical component is straightforward regardless of the meander topology. As seen in Fig. 5.2.1, the structure is divided in two regions along the y coordinate ($i = 1, 2$). To obtain the values for Y_i and B_i , these two regions need to satisfy the boundary conditions of the structure, this is $E_z = 0$ at $y = 0$ and $y = b$. Therefore, expressions for the longitudinal component of the electric field can be obtained depending on the region of analysis as

$0 < y < t$ or $i = 1$

$$E_z(x, y, z) = \sum_{m,n=-\infty}^{\infty} A_{jk,mn} \frac{\sinh(\alpha_{1jk,mn} Y_1)}{\sinh(\alpha_{1jk,mn} B_1)} \sin(k_{jk,m} X_{jk}) e^{-j\beta_n z}$$

with $Y_1 = y$ and $B_1 = t$.

$t < y < b$ or $i = 2$

$$E_z(x, y, z) = \sum_{m,n=-\infty}^{\infty} A_{jk,mn} \frac{\sinh(\alpha_{2jk,mn} Y_2)}{\sinh(\alpha_{2jk,mn} B_2)} \sin(k_{jk,m} X_{jk}) e^{-j\beta_n z}$$

with $Y_2 = b - y$ and $B_2 = b - t$.

As seen in Fig. 5.2.1, the analysis along the y coordinate does not depend on the meander line topology if this is considered to be infinitesimally thin. However, the study over the x and z coordinates depends on the particular configuration of the meander line since this would dictate the electromagnetic field behaviour. Therefore, expressions for the four different meander line topologies described in Sec. 3.4-3.7 need to be derived. The analysis of the two novel meander lines, NML1 and NML2, will be performed in App. A.

The longitudinal electric field expressions for the standard meander line (SML) and the standard meander line with round corners (SMLR) are derived according to Fig. 5.2.4. The only difference between both meander line topologies is the curvature of the external corners, which will change the limits of application of every electric field expression. However, since the perturbation is assumed to be shorter than the length of the meander lines, the analysis of the standard meander line is also valid for the calculation of the interaction impedance on the standard meander line with round corners.

Five regions can be defined along the z coordinate, $j = 1, 2, 3, 4, 5$, and three regions over the x coordinate, $k = 1, 2, 3$, where the electromagnetic field will change. The regions $k = 1$ and $k = 3$ make reference to the left and right hand side of the substrate free from any metallization, respectively, whereas $k = 2$ is the region containing the metal strip. Therefore the limits for the regions along the x coordinate are not fixed and depend on the z position of analysis; both coordinates should be linked together for a correct analysis and description of the fields. For the case of the standard meander line topology, the fields from regions $j = 1$ and $j = 5$ are the same and also those from regions $j = 2$ and $j = 4$.

In order to derive expressions for the parameters $k_{jk,m}$ and X_{jk} , boundary conditions of the structure are applied. Since the meander lines are considered to be surrounded by perfect conductor walls, $E_z = 0$ at $x = 0$ and $x = a$. In addition, $E_z = 0$ also on the areas where the metal strip is located.

With all these considerations, the longitudinal electric field adopts the following expressions depending on the area of analysis:

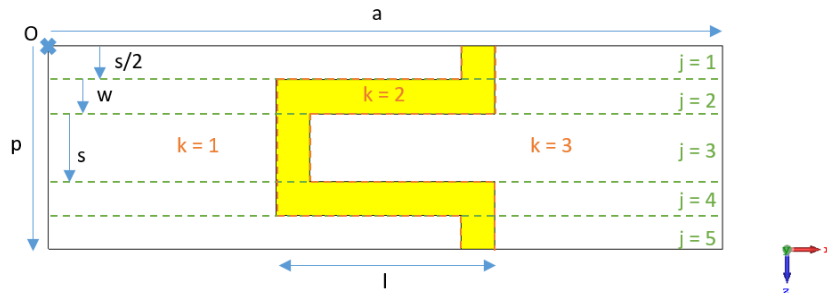


Figure 5.2.4: xz -plane view of the SML. There are five and three regions along the z and x axis. s is the distance between two consecutive strips, w is the strip width, p is the pitch length, a is the length of the substrate and l is the length of the metallization.

$0 < z < s/2, s/2 + w + s + w < z < p$ and $0 < x < a/2 + l/2 - w$ or $j = 1, 5$ and $k = 1$

$$E_z(x, y, z) = \sum_{m,n=-\infty}^{\infty} A_{11,mn} \frac{\sinh(\alpha_{i11,mn} Y_i)}{\sinh(\alpha_{i11,mn} B_i)} \sin(k_{11,m} X_{11}) e^{-j\beta_n z}$$

with $k_{11,m} = \frac{(2m-1)\pi}{a/2+l/2-w}$ and $X_{11} = x$.

$0 < z < s/2, s/2 + w + s + w < z < p$ and $a/2 + l/2 - w < x < a/2 + l/2$ or $j = 1, 5$ and $k = 2$

$$E_z(x, y, z) = 0$$

$0 < z < s/2, s/2 + w + s + w < z < p$ and $a/2 + l/2 < x < a$ or $j = 1, 5$ and $k = 3$

$$E_z(x, y, z) = \sum_{m,n=-\infty}^{\infty} A_{13,mn} \frac{\sinh(\alpha_{i13,mn} Y_i)}{\sinh(\alpha_{i13,mn} B_i)} \sin(k_{13,m} X_{13}) e^{-j\beta_n z}$$

with $k_{13,m} = \frac{(2m-1)\pi}{a/2-l/2}$ and $X_{13} = a - x$.

$s/2 < z < s/2 + w, s/2 + w + s < z < s/2 + w + s + w$ and $0 < x < a/2 - l/2$ or $j = 2, 4$ and $k = 1$

$$E_z(x, y, z) = \sum_{m,n=-\infty}^{\infty} A_{21,mn} \frac{\sinh(\alpha_{i21,mn} Y_i)}{\sinh(\alpha_{i21,mn} B_i)} \sin(k_{21,m} X_{21}) e^{-j\beta_n z}$$

with $k_{21,m} = \frac{(2m-1)\pi}{a/2-l/2}$ and $X_{21} = x$.

$s/2 < z < s/2 + w, s/2 + w + s < z < s/2 + w + s + w$ and $a/2 - l/2 < x < a/2 + l/2$ or $j = 2, 4$ and $k = 2$

$$E_z(x, y, z) = 0$$

$s/2 < z < s/2 + w, s/2 + w + s < z < s/2 + w + s + w$ and $a/2 + l/2 < x < a$ or $j = 2, 4$ and $k = 3$

$$E_z(x, y, z) = \sum_{m,n=-\infty}^{\infty} A_{23,mn} \frac{\sinh(\alpha_{i23,mn} Y_i)}{\sinh(\alpha_{i23,mn} B_i)} \sin(k_{23,m} X_{23}) e^{-j\beta_n z}$$

with $k_{23,m} = \frac{(2m-1)\pi}{a/2-l/2}$ and $X_{23} = a - x$.

$s/2 + w < z < s/2 + w + s$ and $0 < x < a/2 - l/2$ or $j = 3$ and $k = 1$

$$E_z(x, y, z) = \sum_{m,n=-\infty}^{\infty} A_{31,mn} \frac{\sinh(\alpha_{i31,mn} Y_i)}{\sinh(\alpha_{i31,mn} B_i)} \sin(k_{31,m} X_{31}) e^{-j\beta_n z}$$

with $k_{31,m} = \frac{(2m-1)\pi}{a/2-l/2}$ and $X_{31} = x$.

$s/2 + w < z < s/2 + w + s$ and $a/2 - l/2 < x < a/2 - l/2 + w$ or $j = 3$ and $k = 2$

$$E_z(x, y, z) = 0$$

$s/2 + w < z < s/2 + w + s$ and $a/2 - l/2 + w < x < a$ or $j = 3$ and $k = 3$

$$E_z(x, y, z) = \sum_{m,n=-\infty}^{\infty} A_{33,mn} \frac{\sinh(\alpha_{i33,mn} Y_i)}{\sinh(\alpha_{i33,mn} B_i)} \sin(k_{33,m} X_{33}) e^{-j\beta_n z}$$

with $k_{33,m} = \frac{(2m-1)\pi}{a/2+l/2-w}$ and $X_{33} = a - x$.

5.3 Summary

Although the interest in meander lines has recently increased, most of the results in literature are on cold parameters obtained by simulations using 3D electromagnetic software. Finding experimental results in literature is a hard task, and limited to validation of S-parameters.

This chapter presented experimental procedures to determine both the phase velocity and the interaction impedance on meander line SWSs. The experimental validation of the phase velocity was based on the measurement of the phase difference between the same meander line with two different lengths while a perturbation method approach was followed to develop a theory to experimentally determine the interaction impedance from measurements of the phase difference between a perturbed and an unperturbed meander line SWS.

The techniques developed in this chapter will provide new and useful experimental tools for the design and test of novel meander line topologies and configurations for mm-wave TWTs.

6. Characterization of planar meander line slow wave structures at Ka-band

One of the most important milestones of a research is the experimental validation of the theoretical and computational findings. With that objective in mind, this chapter will present experimental results of meander line SWSs.

The experimental activity of the research has involved the test of different meander lines at Ka-band. A lower-frequency range than W-band was chosen for an easier fabrication and characterization. Specifically, two different runs were performed. The test considering soft substrates will be explained by recreating the whole fabrication process at Lancaster University. For the subsequent test using alumina substrate, the meander lines were manufactured externally and tested at the European Space Research and Technology Centre of the European Space Agency (ESTEC-ESA). The measurement results obtained with both tests will be described and analysed in the following sections.

The measurements involved the determination of the S-parameters of the different meander line SWSs as well as the experimental validation of the two approaches developed in Ch. 5 for measuring both phase velocity and interaction impedance. Equations 5.1.1 and 5.2.15 have been used to indirectly determine the experimental phase velocity and interaction impedance from measurements of the phase delay and perturbed phase, respectively, of the different meander line SWSs.

The experimental results have been compared with simulations performed by CST Microwave Studio.

6.1 Meander lines on soft substrate

6.1.1 Fabrication

SML and NML1 were fabricated, for 20 and 40 periods, using RT6002 laminates available at the Engineering Department in Lancaster University. This substrate, already cladded with copper, was chosen for the first trial of fabrication given the easier fabrication approach. The structures were fabricated inside a clean room class 100 using the facilities of the Physics Department at Lancaster University. Three

different machines were used throughout the process: hot plate, spinner and mask aligner, which are shown in Fig. 6.1.1.



Figure 6.1.1: Hot plate (1), spinner (2) and mask aligner (3) used during the fabrication of SML and NML1 on RT6002 substrates.

Four 2-inch diameter wafers are prepared for the fabrication: two of them will contain five samples of 20 periods of SML and NML1, and the other two will contain three samples of 40-period meander lines. As the substrates are already covered with a copper layer, a photoresist pattern will be deposited onto the copper surface using a photomask, so that only the copper below the photoresist remains after etching the copper from the substrate. For this process, negative photoresist is deposited using spin coating. Once the photoresist is spun onto the surface, a soft-baking process is used to improve adhesion of the photoresist to the copper layer. The substrates are then exposed using a mercury discharge lamp inside a mask aligner where the four photomasks designed for the fabrication (see Fig. 6.1.2) are placed. A subsequent baking process is applied to cross-link the meander line pattern prior to the development of the photoresist where the parts that have not been exposed remain soluble and are washed away.

An example of the result after developing the photoresist can be seen in Fig. 6.1.3. As seen in Fig. 6.1.3, the negative photoresist pattern should be present only at the areas where the samples have been exposed. The view under the microscope shows that the photoresist presents a well-defined pattern for every structure, however small cracks and imperfections appear to be visible at some points of the photoresist.

The samples are then immersed in a FeCl_3 (ferric chloride) solution to etch the copper from the surface and, after that, the remaining photoresist is detached from the surface using acetone. Fig. 6.1.4 shows the 20-period SML from different zooms under the microscope. It can be appreciated that the width of the metal line has

been reduced as a consequence of the copper etchant which has clearly affected the copper below the edges of the photoresist. The corners of the copper line present now a round shape instead of the designed sharp edges. It can be also seen that there are still remnants of the etched copper at the inner sides of the strip. This issue is more severe for NML1 as the space between two consecutive strips is narrower. A more prolonged time of the sample immersed in the copper etchant could have likely removed the remaining copper at the inner parts of the strips but it would have reduced even more the width of the strip. The current results were chosen trying to compensate both factors.

Finally, the samples are trimmed to the designed size of the substrate and will be placed inside the aluminium holder ready to be analysed. The holder and the 20-period samples can be seen in Fig. 6.1.5.

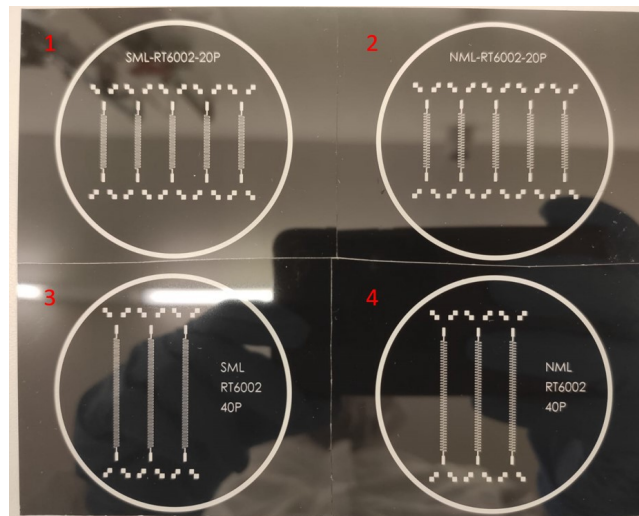


Figure 6.1.2: The four different mask designed for the fabrication. 1- 20 periods of SML, 2- 20 periods of NML1, 3- 40 periods of SML and 4- 40 periods of NML1.

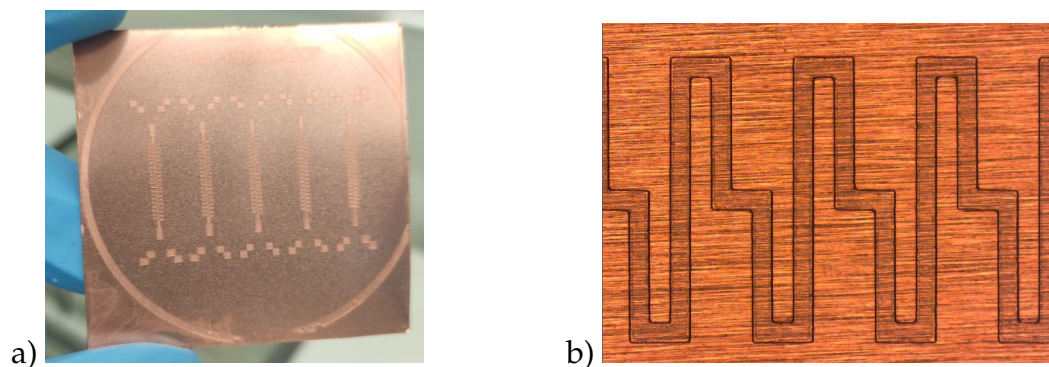


Figure 6.1.3: a) Example of the 20 period NML1 after developing the photoresist and b) view under the microscope

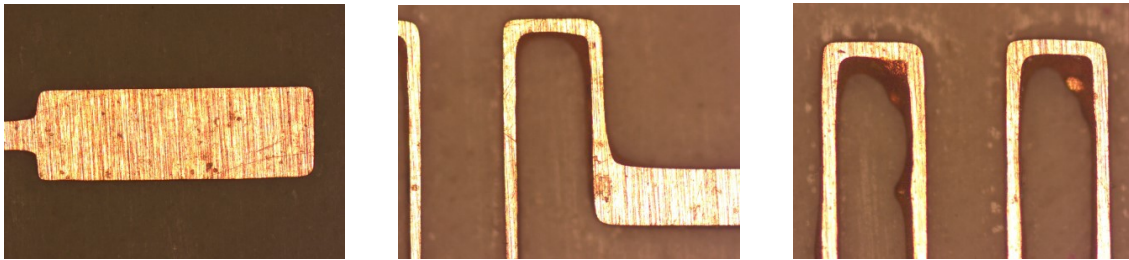


Figure 6.1.4: Fabricated 20 period SML after the etching process.

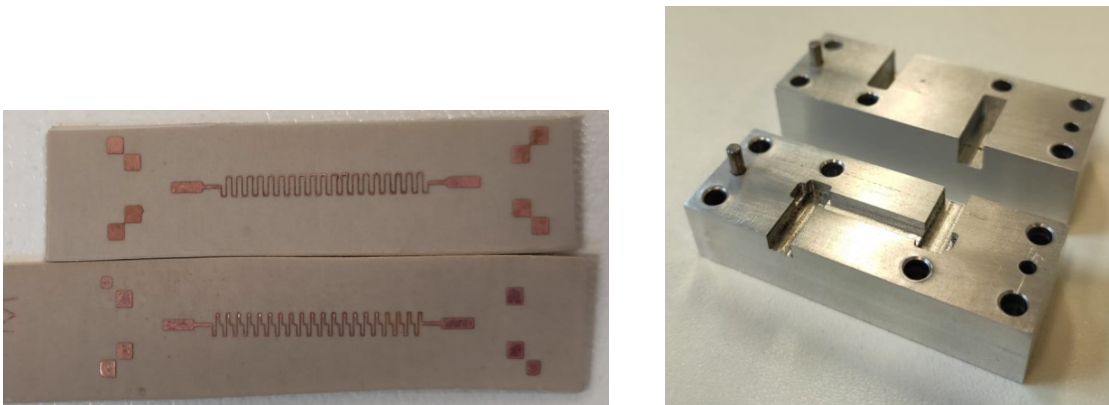


Figure 6.1.5: Fabricated meander lines and aluminium holder for 20 periods.

Once the fabrication process is finished, the samples are measured mechanically to determine the discrepancy in the dimensions in comparison with the designed values. Tab. 6.1.1 and 6.1.2 show the comparison between the values of the simulated design and the average range that can be measured for every parameter considering that there are differences in the values measured for different strips and also within the same strip depending on the position where the measurement is taken. The results are calculated after measuring several periods randomly selected along the meander line. The parameters are described in the schematic from Fig. 6.1.6 for SML and Fig. 6.1.7 for NML1.

According to Tab. 6.1.1 and 6.1.2, a clear reduction in the dimensions of every parameter is noticeable. This effect is worse for NML1. Besides the reduction in the dimensions of the metal strip compared to the expected design, it is also seen during the measurements that every rectangular corner has been trimmed to round corners. The photoresist has not been able to protect the copper properly and the etchant has also impregnated the area under the photoresist, trimming it.

It is worth mentioning that various fabrication runs were performed in order to get familiarized with the different equipment, gain ability and optimize the fabrication. The results presented in Tab. 6.1.1 and 6.1.2 correspond to the best-quality samples produced during the last and best fabrication run. The quality of the samples was found to be in a different extent depending on the samples analysed. In some of them,

the etchant had trimmed the whole width of the copper strip, cutting the continuous path for the transmission of the RF signal, making these samples to be completely useless.

Even though the quality of the samples was not the best, it was decided to continue with the measurements and understand if any useful information and results could be extracted from these samples.

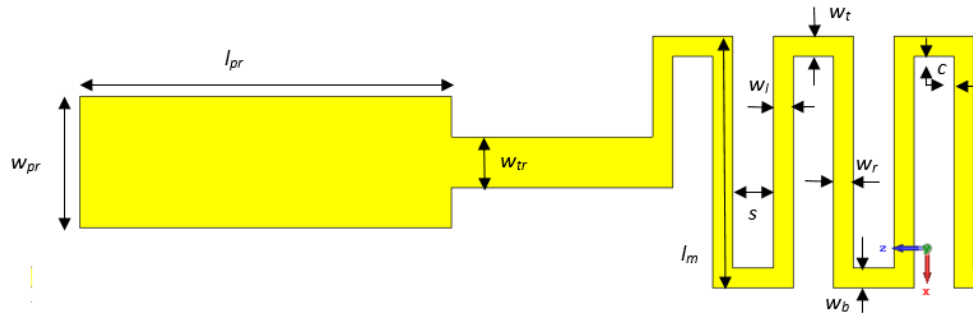


Figure 6.1.6: Schematic of the designed SML with the probe termination. The parameters w_r , w_l , w_t and w_b make reference to the average right, left, top and bottom width of the strip for a single period, respectively. The parameter c characterizes the average width of the partially etched copper that remains next to every strip. The parameter s is then the average distance between this partially etched copper and not directly between two consecutive strips.

Table 6.1.1: Results of the mechanical measurement of SML and comparison with the designed dimensions.

	Simulation (μm)	Measurement 20p (μm)	Measurement 40p (μm)
w_r	100	36-42	24-39
w_l	100	35-41	25-34
w_t	100	42-50	22-29
w_b	100	40-49	41-48
s	200	230-245	225-250
c	0	10-20	15-30
l_m	1250	1165-1175	1160-1170
w_{tr}	250	180-190	160-180
w_{pr}	650	575-590	540-580
l_{pr}	1850	1770-1805	1760-1800

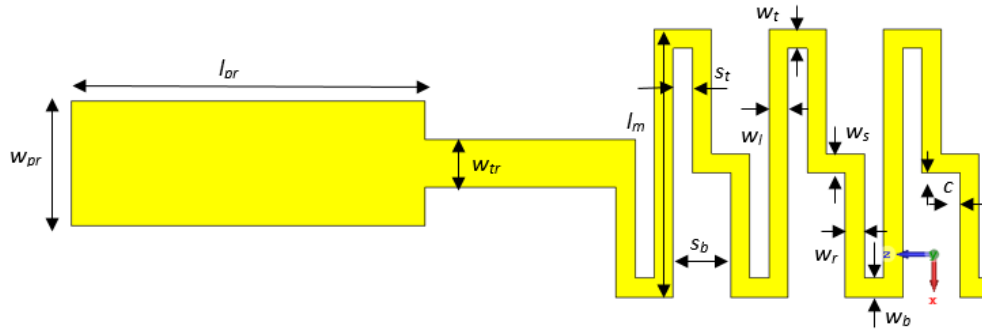


Figure 6.1.7: Schematic of the designed NML with the probe termination.

Table 6.1.2: Results of the mechanical measurement of NML1 and comparison with the designed dimensions.

	Simulation (μm)	Measurement 20p (μm)	Measurement 40p (μm)
w_r	100	24-31	27-36
w_l	100	24-31	28-42
w_s	100	31-37	34-51
w_t	100	34-38	48-59
w_b	100	40-47	31-41
s_t	100	125-135	60-80
s_b	300	340-355	280-335
c	0	20-40	40-60
l_m	1400	1300-1315	1300-1320
w_{tr}	250	155-170	150-165
w_{pr}	650	555-570	545-560
l_{pr}	1850	1710-1780	1720-1790

6.1.2 S-parameters

The scattering parameters of four meander lines, the best-quality samples of both topologies (SML and NML1) and the two different lengths (20 and 40 periods), were measured using a Vector Network Analyser (VNA) available at the Engineering Department in Lancaster University following the experimental setup as shown in Fig. 6.1.8 where the aluminium housings are connected to the WR28 waveguide flanges. The results are presented in Fig. 6.1.9 and compared with simulations. The reflection coefficient, S_{11} , for the 20-period SML can be found below -12 dB from approximately 32 to 35 GHz. Instead, for NML1, the reflection coefficient is below that value from 34 to 36.3 GHz. The transmission coefficient is around -3 dB for both structures. For the 40-period SML, the reflection value is below -10 dB from 32 to 35 GHz. The output for the 40 period NML1 shows a narrow transmission window below -10 dB from 28.5 to 30 GHz.

The experimental results presented in Fig. 6.1.9 greatly differ from those of the simulations. It is evident that it is necessary to improve the fabrication method in order to achieve compatible results between experiment and simulation. Nevertheless, the measurements serve to demonstrate that the transition designs followed for the coupler between the meander line and the waveguide are feasible, provide coupling and can be used for future structures.

Unlike the results for NML1, the S-parameters for 20 and 40 periods of SML seem to be compatible, although the comparison with simulation shows great discrepancy. SML is considered for the subsequent analysis and calculation of the phase velocity and interaction impedance.

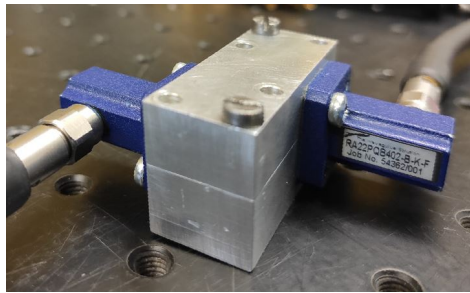


Figure 6.1.8: Experimental setup for the measurement of the S-parameters.

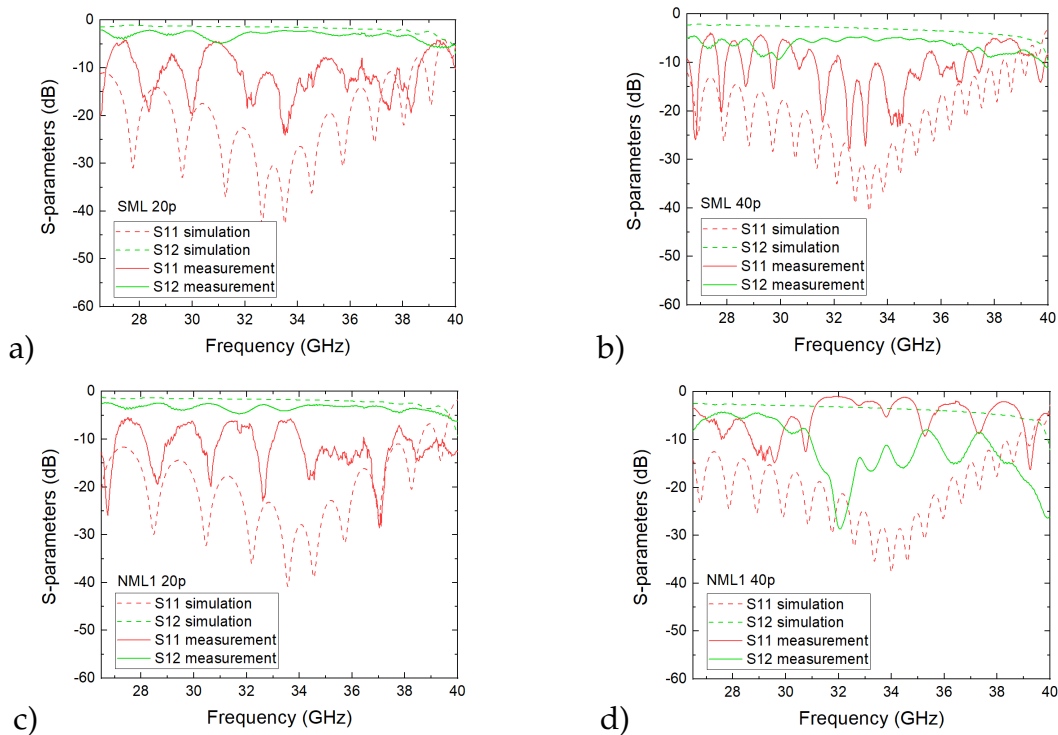


Figure 6.1.9: Experimental and simulated S-parameters for the RT6002 laminate. a) SML 20 periods, b) SML 40 periods, c) NML1 20 periods and d) NML1 40 periods

6.1.3 Phase velocity

Fig. 6.1.10 shows the comparison between the simulated (using CST Microwave Studio) and experimental curves obtained after measuring the phase delay for the two different lengths of SML and applying Eq. 5.1.1 to compute the phase velocity. For the simulated results computed in CST Microwave Studio, it has been used both the designed and actual dimensions of the structure according to the values presented in Tab. 6.1.1.

As expected, the simulation using the actual values fits better the measurements. The discrepancy can be explained considering that, for the simulations, an average value for every parameter has been taken. Instead, the fabricated structure presents different dimensions depending on every particular strip and period. It is also noticeable that the simulated curve using the actual dimensions is much more irregular in comparison with the curve using the designed dimensions; this is likely a consequence of the variable strip dimension within the same period.

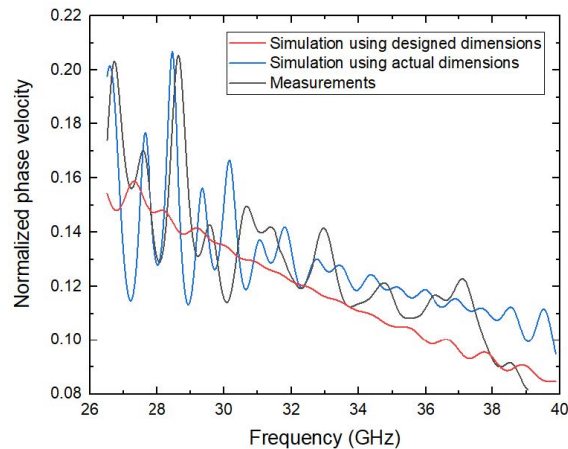


Figure 6.1.10: Simulated and experimental results for the normalized phase velocity using Eq. 5.1.1 for the calculation.

6.1.4 Interaction impedance

The interaction impedance of the fabricated SML has been experimentally derived after measuring the perturbed and unperturbed phase, and applying Eq. 5.2.15 for a perturbing nylon rod ($\epsilon' = 3.4$) with radius $230 \mu\text{m}$ and placed at $50 \mu\text{m}$ from the meander line metallization. The interaction impedance has been averaged over the perturbing rod area and compared with the simulation given by CST Microwave Studio. The results are presented in Fig. 6.1.11 and show good agreement. The ripples of the experimental curve are due to the poor quality of the fabricated samples.

Further results are obtained using Eq. 5.2.15 in order to quantify how precise the measurement method needs to be. Fig. 6.1.12 shows the variation in the interaction impedance computed at the centre of the perturbation when the permittivity of the

dielectric rod is shifted 5% from the original 3.4 value. This shift is translated in a similar way to the interaction impedance where the values are also shifted by approximately this 5%.

In Fig. 6.1.13, the variation of the interaction impedance is analysed when there exists a deviation in the correct positioning of the perturbing rod both vertically and horizontally. According to Fig. 6.1.13, the deviation in the vertical coordinate is much more important than in the horizontal position which is almost negligible for a maximum deviation of $50 \mu\text{m}$ from the original position. However, a vertical shift of $10 \mu\text{m}$ already produces a change close to 5% in the values of the interaction impedance.

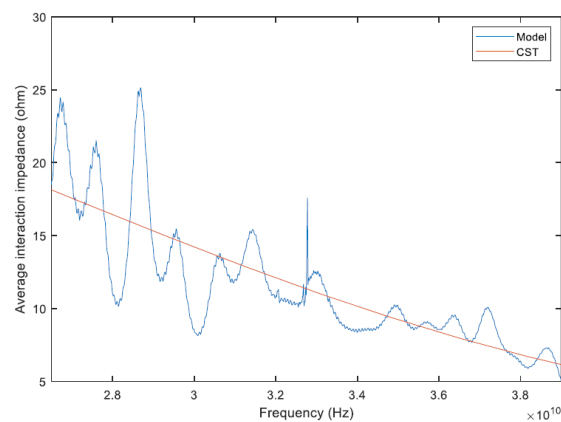


Figure 6.1.11: Comparison of the results obtained by the proposed theoretical model using Eq. 5.2.15 and the CST simulation.

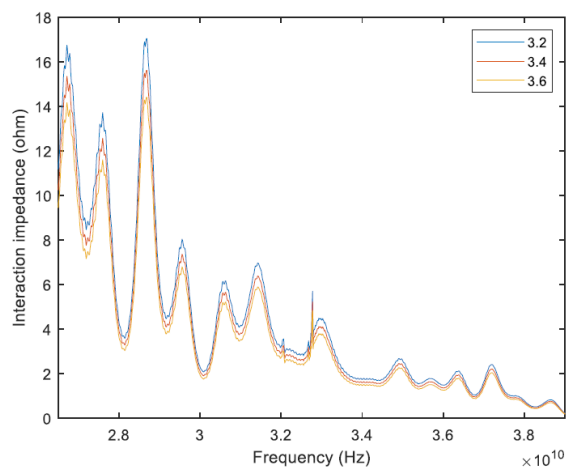


Figure 6.1.12: Comparison of the experimental interaction impedance for different values of the permittivity of the perturbing dielectric rod.

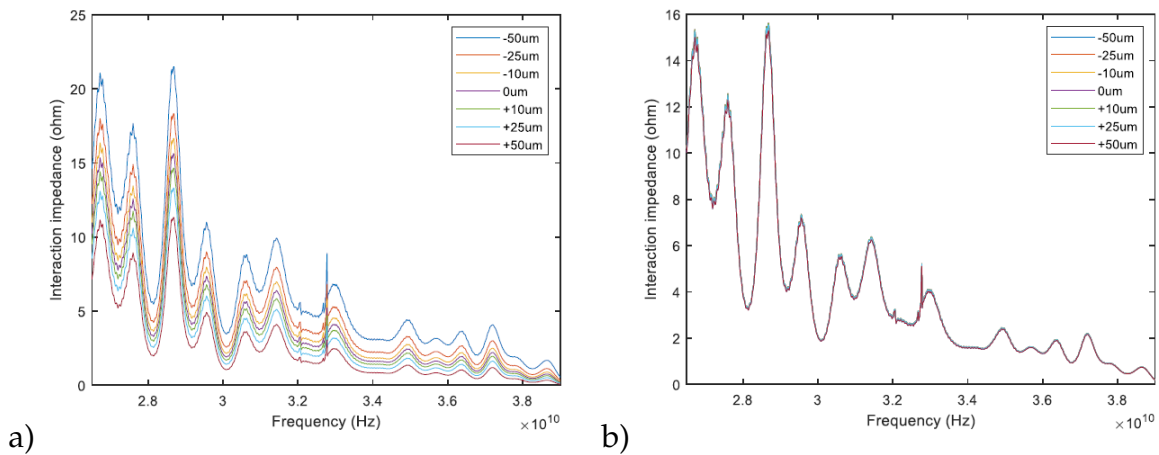


Figure 6.1.13: Comparison of the experimental interaction impedance accounting for a deviation in the original position of the perturbing rod a) vertically or b) horizontally.

6.2 Meander lines on alumina substrate

The four different meander line topologies, SML, SMLR, NML1 and NML2, were later manufactured by an external company at Ka-band in order to test high-quality samples before moving up to W-band. SML and SMLR to be used as reference for comparison, NML1 offering flatter dispersion curve and therefore, increasing the bandwidth of the TWT and NML2 providing higher interaction impedance increasing the efficiency and gain of the TWT over a narrow band. The structures were fabricated for two different lengths of $n_1 = 20$ and $n_2 = 40$ periods in order to be able to measure the phase velocity. The dimensions of the substrate are 21.812 mm \times 2.9 mm for the 20 period length and 33.812 mm \times 2.9 mm for the 40 period length. The substrates are made of alumina with relative permittivity $\epsilon_1 = 9.9$ and 127 μm thickness. The metallization is made of gold with 10 μm thickness. A picture of the four 20-period meander lines is shown in Fig. 6.2.1.

To assemble the meander lines in the waveguide, the same two aluminium housings corresponding to the two different lengths of the meander line that were manufactured for the meander lines on soft substrate are used. The 20-period housing is shown in Fig. 6.2.2 together with the final configuration of one of the meander lines inserted into the housing.

This run of measurements was performed at the facilities of the European Space Agency at the European Space Research and Technology Centre in Noordwijk, The Netherlands.

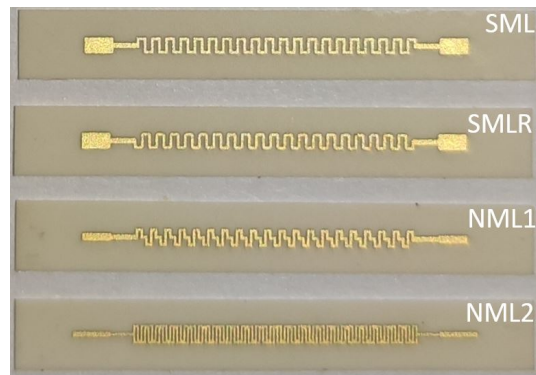


Figure 6.2.1: 20 periods and the coupling terminations of the four different meander line topologies manufactured for the experiment.

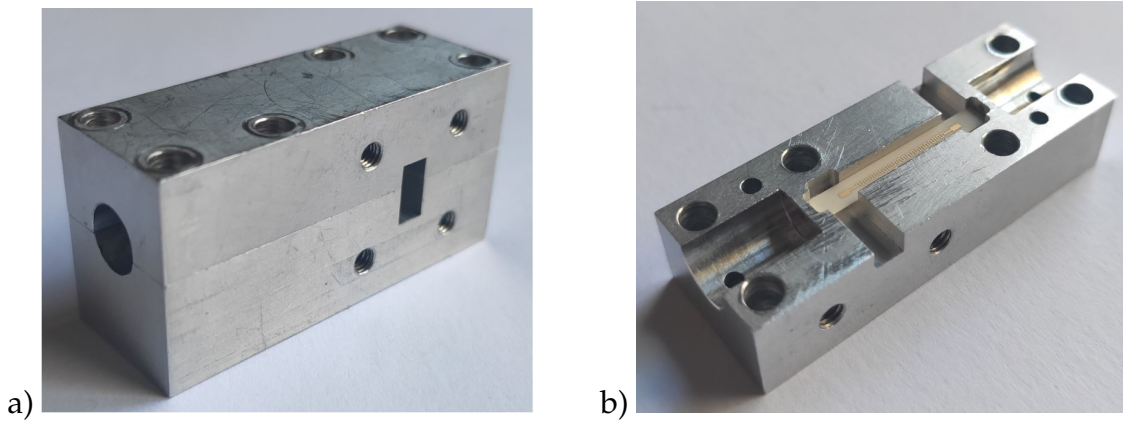


Figure 6.2.2: a) 20 period housing used for the measurements and b) bottom half of the housing with one of the meander lines placed inside.

6.2.1 S-parameters

Measurements of the S-parameters are presented in Fig. 6.2.3 for the SML, SMLR and NML1. The results show, in general, good agreement with the simulations. A 10% transmission window centred around 35-36 GHz is obtained for SML, SMLR and NML1 as can be checked in Fig. 6.2.3.

As seen in Fig. 6.2.4a and 6.2.4b, the results for NML2 show a great discrepancy with measurements. However, if the meander line is simulated moving the substrate horizontally by $100\ \mu\text{m}$ from its original position, the results show much better agreement according to Fig. 6.2.4c and 6.2.4d. A non-accurate position of the substrate inside the meander line seems to be the reason for this discrepancy.

The experimental transmission coefficient, S_{12} , is compared for every topology in Fig. 6.2.5. NML1 shows the best transmission among all the meander lines followed by a slightly improvement of SMLR in comparison with SML. NML2, instead, shows the worse transmission coefficient.

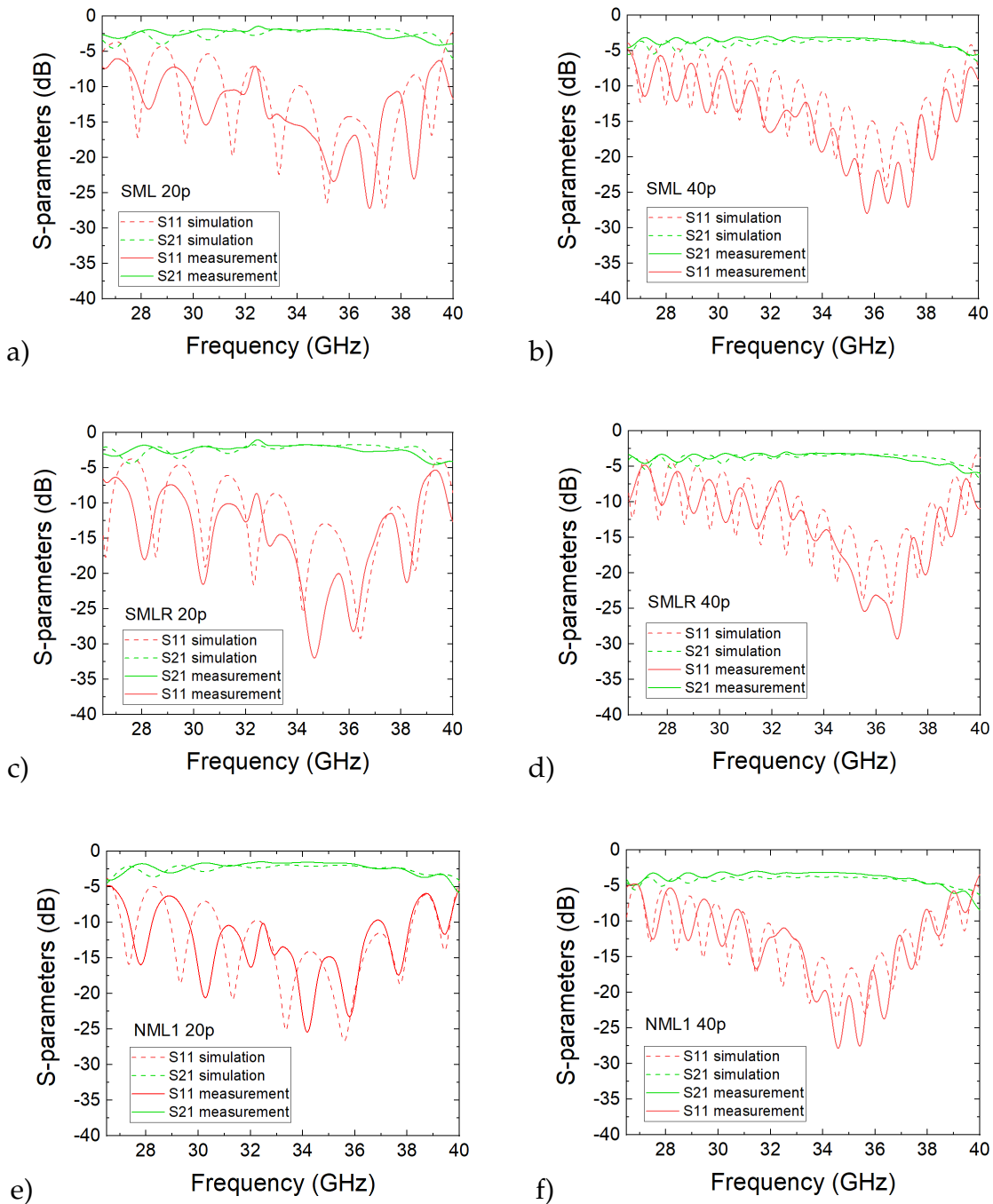


Figure 6.2.3: S-parameters of the SML, SMLR and NML1 for 20 and 40 periods length. The solid lines represent the measurement results while the dashed lines represent the simulations. a) SML 20 periods, b) SML 40 periods, c) SMLR 20 periods, d) SMLR 40 periods, e) NML1 20 periods and f) NML1 40 periods.

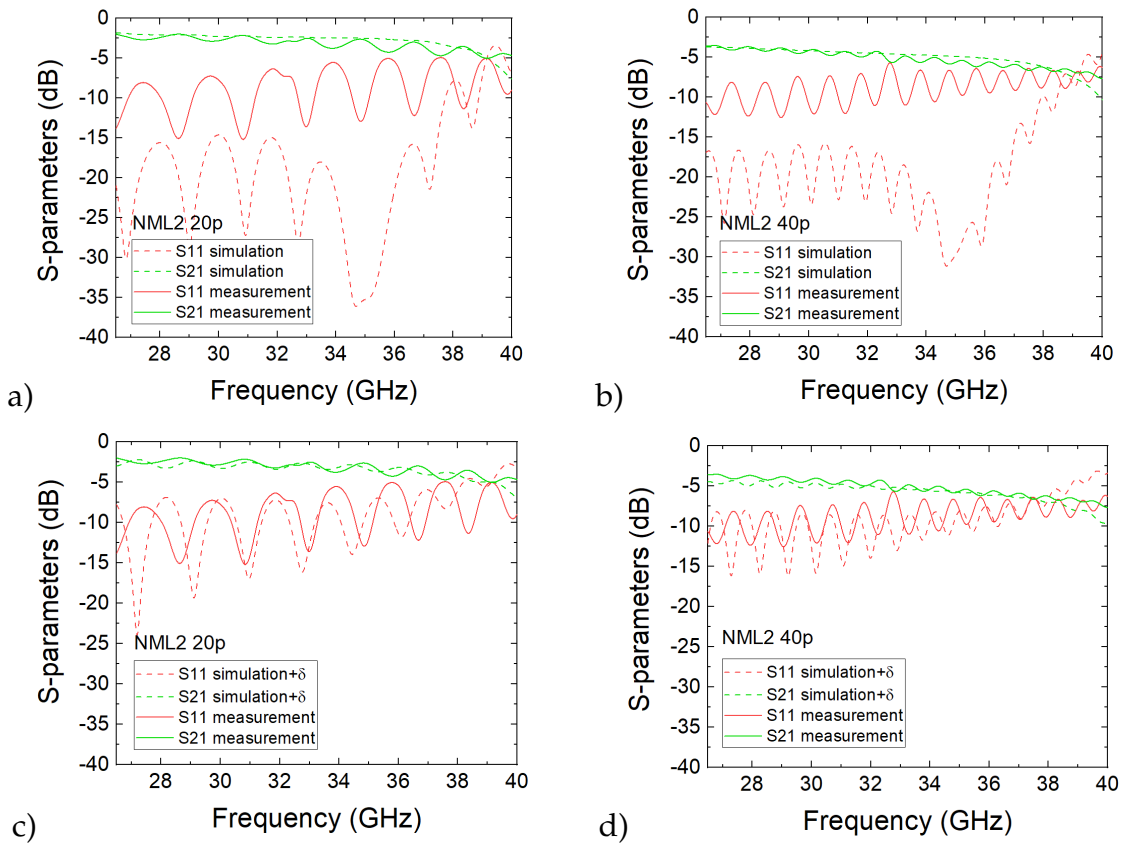


Figure 6.2.4: S-parameters of NML2 for 20 and 40 periods length. The solid lines represent the measurement results while the dashed lines represent the simulations. a) NML2 20 periods, b) NML2 40 periods, c) NML2 20 periods with the substrate in the simulation moved horizontally and d) NML2 40 periods with the substrate in the simulation moved horizontally.

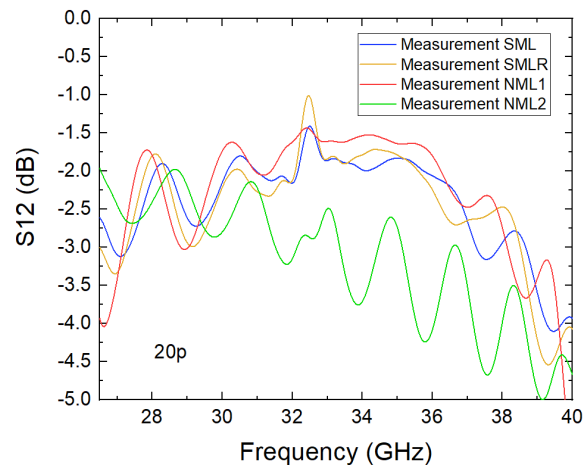


Figure 6.2.5: Measurement of S_{12} for the four different meander line topologies.

6.2.2 Phase velocity

The experimental curves of the phase velocity for all the four meander lines are obtained after measuring the phase delay for every pair of meander lines with 20 and 40 periods and applying Eq. 5.1.1 to derive the phase velocity. The results are presented in Fig. 6.2.6. An error has been added to the results considering that, for the same meander line, different samples were available. In particular, two 20-period and 40-period samples of SML and SMLR and three 20-period and 40-period samples of NML1 and NML2. Therefore, to calculate the phase velocity, four curves were obtained for SML and SMLR while nine curves were computed for NML1 and NML2. The measurement error, represented with shadowed area in Fig. 6.2.6, is the area between the highest and lowest phase velocity given by the various samples available. The measurement curves, which are drawn with solid lines in Fig. 6.2.6, are the mean value of the results obtained from the various samples.

The measurement results for NML1 and NML2 (Fig. 6.2.6c and 6.2.6d) show good correlation with the simulated curves from CST Microwave Studio. However, the experimental curves for SML and SMLR (Fig. 6.2.6a and 6.2.6b) show values slightly higher than the obtained from the simulations at the low-half frequency band. This difference could be due to manufacture tolerances or slight deviations in the position of the meander line inside the housing.

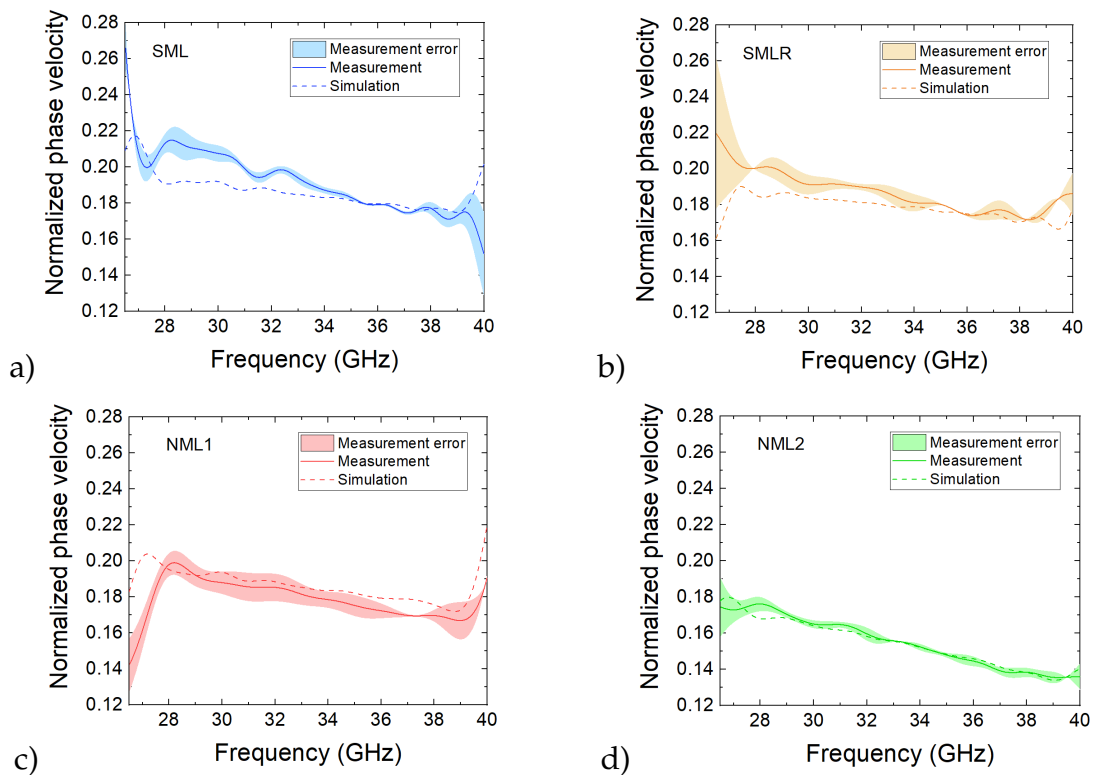


Figure 6.2.6: Comparison of the phase velocity measurements with the simulation curves. a) SML, b) SMLR, c) NML1 and d) NML2.

Fig. 6.2.7 compares the experimental curves of the four meander lines that have been tested. SMLR and NML1 show the flattest phase velocity curves while SML and NML2 show a more steeper slope. Therefore, SMLR and NML1 will provide a flatter gain than SML and NML2 over the same bandwidth.

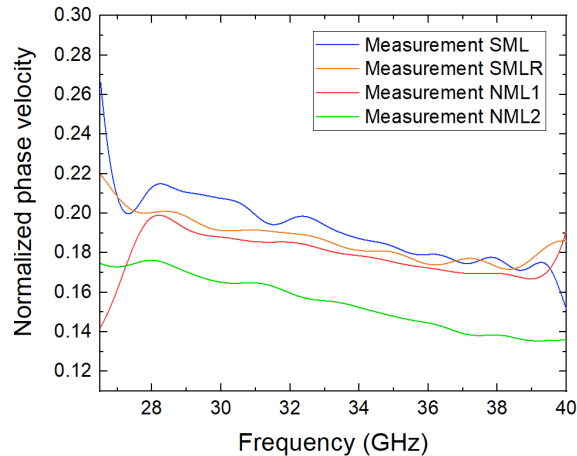


Figure 6.2.7: Measured phase velocity curves for the four meander line topologies.

6.2.3 Interaction impedance

To compute the interaction impedance, the perturbed phase is measured after introducing a nylon ($\epsilon' = 3.4$) rod with radius $120 \mu\text{m}$ and placed at $450 \mu\text{m}$ from the metal strip as shown in Fig. 6.2.8. The dielectric rod is introduced in the housing by means of two holes that were drilled at both ends of the aluminium holder. The interaction impedance is then obtained after measuring also the unperturbed phase and applying Eq. 5.2.15.

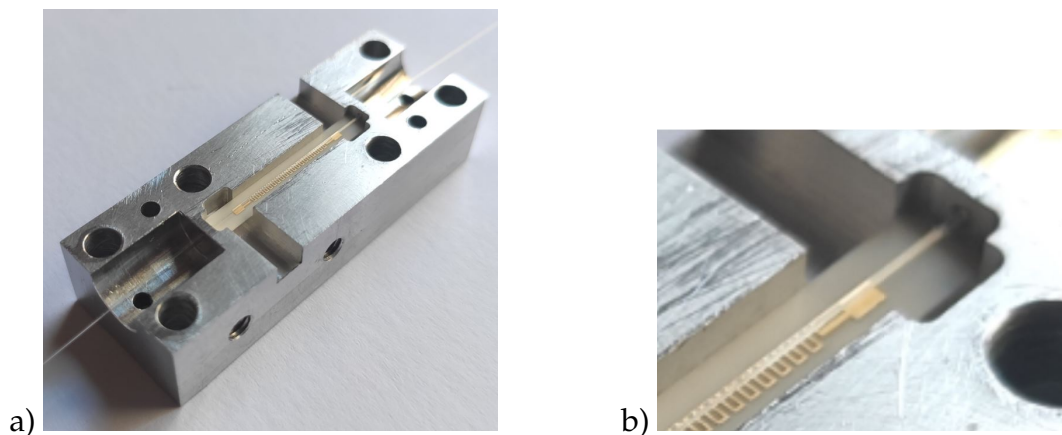


Figure 6.2.8: a) Bottom half of the housing with the perturbation introduced on top of the meander line and b) detail of the perturbation.

The experimental interaction impedance curves for every meander line are compared with the simulation results (CST Microwave Studio) in Fig. 6.2.9a and 6.2.9b for SML and SMLR, and 6.2.9c and 6.2.9d for NML1 and NML2. Similar to the measurements of the phase velocity, two samples of SML and SMLR and three samples of NML1 and NML2 have been used for the tests. Therefore, the shadowed areas in Fig. 6.2.9, account for the deviation from the mean value considering the different samples of the same meander line. The interaction impedance is computed at the centre of the perturbation, this is at a distance of $570 \mu\text{m}$ from the metallization ($450 \mu\text{m} + 120 \mu\text{m}$ of the rod radius). The model shows good agreement with the simulations.

The four experimental curves are compared in Fig. 6.2.10. NML2 shows the highest interaction impedance among the four meander lines, NML1 also shows higher interaction impedance than SML and SMLR. NML2 will then provide higher gain over a narrower bandwidth in comparison with the other meander lines. The low values of the interaction impedance are due to the far position where the perturbation rod is placed, and therefore, where the interaction impedance is computed.

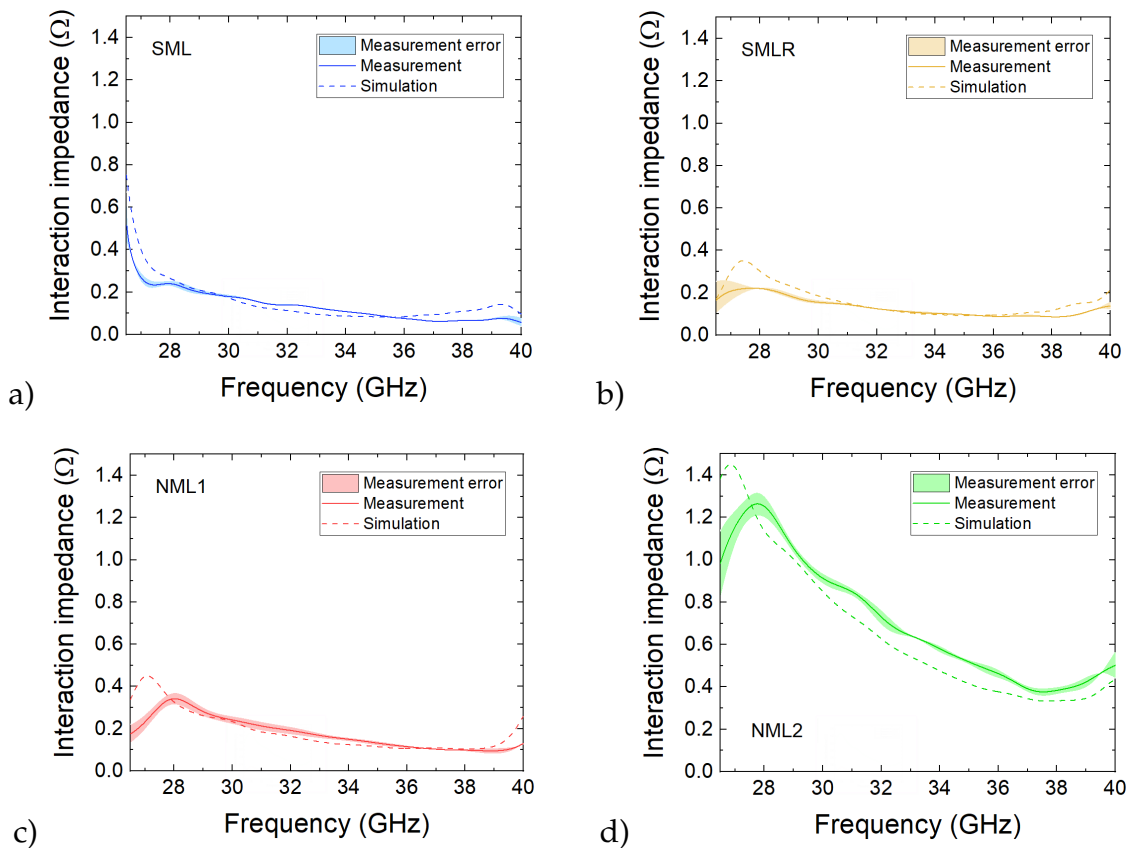


Figure 6.2.9: Comparison of the interaction impedance measurements with the simulation curves. a) SML, b) SMLR, c) NML1 and d) NML2

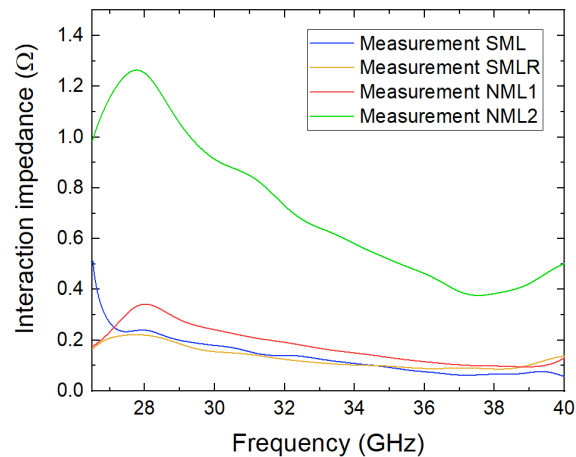


Figure 6.2.10: Measured interaction impedance curves for the four meander line topologies.

6.3 Summary

This chapter has presented the experimental results after measuring the S-parameters, phase velocity and interaction impedance of the manufactured meander line SWSs at Ka-band.

A first run of measurements was performed after fabricating two meander lines at Ka-band, SML and NML1, using the facilities available at Lancaster University. A RT6002 soft substrate with copper cladding was used to create this first set of meander lines. This fabrication process, based on photolithography, was not suitable for the production of high-quality structures. However, the measurements were useful to demonstrate the feasibility of using the designed coupling transition for meander lines. The developed phase velocity and interaction impedance models were applied to SML and showed to provide reasonable results considering the poor quality of the fabricated meander lines.

Later, the four meander lines, SML, SMLR, NML1 and NML2, were manufactured externally, again at Ka-band, in order to obtain high-quality samples that could be useful to correctly demonstrate the developed theories. The measurements of the S-parameters, phase velocity and interaction impedance were validated providing good agreement with simulation results. NML1 and NML2 were also shown experimentally to be better alternatives than SML and SMLR. NML1 provides flatter phase velocity and higher interaction impedance, while NML2 gives notably higher interaction impedance.

7. Conclusions and future work

This research was proposed with the aim of investigating and gaining more knowledge and experience about meander line SWSs and assessing their feasibility and suitability for millimetre-wave TWTs for high-capacity satellite communications. In particular, the W-band was the targeted frequency range (71-76 GHz for satellite downlink) given the opportunity to obtain great channel capacity and high data rate transmission for facing the increasing demand of telecommunication services that are currently exhausting lower frequency bands. The necessity of amplifying the signal to overcome the huge atmospheric attenuation at W-band, has made the use of TWTs indispensable in order to provide the required high power over the bandwidth.

The impossibility of manufacturing helix SWSs at W-band has raised the interest of investigating alternative and novel SWSs that could provide similar performance. Meander lines appeared as a very promising SWS due to their potential benefits such as low beam voltage, high interaction impedance and low-cost manufacture, with special interest for space applications where saving power and reducing mass of payload are fundamental features to reduce the mission cost.

Before the realization of this thesis, very little experimental results could be found in literature regarding meander line SWSs. One of the objectives of this research was to provide novel experimental tools that could permit to easily and accurately characterize meander line SWSs. With that consideration in mind, experimental procedures for measuring the phase velocity and the interaction impedance were developed during the research. The phase velocity can be determined from the phase difference between the same meander line with two different lengths whereas an experimental model with a strong theoretical background based on the measurement of the phase difference between the same unperturbed and perturbed meander line was proposed for computing the interaction impedance. Both methods were validated after manufacturing and testing different meander line SWSs.

The experimental study of four different meander line SWSs, including two novel topologies, has allowed to confirm the benefits of this kind of SWSs with what concerns to cold parameters. The demonstration that meander line SWSs can operate with low beam voltage and provide high interaction impedance will be a useful information to be considered for the design of novel low-cost space TWTs.

The four meander line SWSs are currently being manufactured at W-band. Near-

future work will involve the test of the SWSs at W-band to evaluate their performance at the 71-76 GHz frequency range. The next step should be focused on validating the large signal results of meander line SWSs. The inclusion and test of the manufactured meander line SWSs as part of the full TWT should provide valuable knowledge about the potential use of meander line SWSs for mm-wave TWTs.

Even though some of the properties of meander line SWSs are theoretically advantageous for space TWTs, meander line SWSs are also characterized by a great dispersion and better interaction with planar beam geometries. Part of this research was focused on studying different ways to minimize these disadvantages.

The great dispersion of meander lines limits the bandwidth of operation, supposing a constraint for the production of wide-band TWTs as the ones required for satellite communications. Nevertheless, the relatively narrow 71-76 GHz band of interest (less than 10% bandwidth) is a feasible bandwidth for meander line SWSs. A novel meander line SWS (NML1) was developed to improve the dispersion and provide gain and output power with low variation at the 71-76 GHz targeted frequency range. NML1 showed optimum results at W-band with output power in the range 20-30 W within the 71-76 GHz band. Future work in this field could involve the investigation of novel topologies or approaches to reduce even more the dispersion and obtain improved performance.

The analysis of the electromagnetic field of planar meander line SWSs showed that this is concentrated at the interface dielectric-metallization. Therefore, the interaction of planar meander line SWSs with sheet beams is more suitable in order to optimize the results. However, such geometries require of more complex electron guns and stronger magnetic focusing fields to minimize the effect of the centripetal and space charge forces that may deviate the electron beam from its designed path. This work proposed the use of a relatively low-aspect-ratio sheet electron beam that can be focused with a relatively low magnetic field and permits to improve the performance and the results of gain and output power.

Nevertheless, the well-established cylindrical beam technology for TWTs has encouraged the investigation of meander line SWSs that could interact with cylindrical electron beams and provide enough power to be suitable for W-band space communications. A novel planar meander line SWS, NML2, was designed with the objective of enhancing the interaction impedance. However, the results interacting with a cylindrical beam were not yet good enough.

The consideration of three-dimensional structures to interact with cylindrical electron beams has been fundamental to greatly increase the output power in comparison with what planar meander line SWSs can provide. Two novel three-dimensional structures have been proposed in this research, PML and 3DML, that give the same benefits as planar meander line SWSs in terms of low beam voltage and high interaction impedance while greatly increasing the overall performance. In particular, PML was shown to provide output power close to 35 W, while 3DML reached output power close to 50 W, both at W-band. These output levels should be high enough to overcome atmospheric attenuation at W-band and establish a feasible link for the

transmission of huge data amounts at high transfer rates for future mm-wave satellite communication systems.

The design of both three-dimensional structures as in this thesis is based on the standard meander line topology. For future work, it would be interesting to change the basis topology and analyse if, for instance, the improved performance that NML1 and NML2 provide in planar configurations, can be translated into a three-dimensional configuration. An experimental demonstration of the structures will be also very useful to understand if the proposed fabrication methods can be successfully completed and the promising performance that the simulations show can be matched experimentally.

In conclusion, this research has demonstrated that meander line SWSs are a very promising candidate for a new family of low-cost, lightweight and compact space TWTs. However, substantial work is still needed, mostly in the experimental field, in order to determine if meander line SWSs can be a viable option for future cost-effective mm-wave satellite communication networks.

Bibliography

- [1] H. R. Hertz, "Über die Ausbreitungsgeschwindigkeit der electrodynamischen Wirkungen", *Ann. der Physik*, vol. 270, no. 7, pp. 551-569, 1888.
- [2] J. C. Maxwell, "A Dynamical Theory of the Electromagnetic Field", *Philos. Trans. Royal Soc. London*, vol. 155, pp. 459-512, 1865.
- [3] L. de Forest, "Space Technology", *U. S. Patent*, No. 879532, Feb. 1908.
- [4] R. J. Clayton, D. C. Espley, G. W. S. Grith and J. M. C. Pinkham, "The London-Birmingham television radio-relay link", *J. Inst. Electr. Eng.*, no. 7, pp. 222-226, 1951.
- [5] G. Dawson, L. L. Hall, K. G. Hodgson, R. A. Meers and J. H. H Merriman, "The Manchester-Kirk o'Shotts television radio-relay system", *Proc. IEE - Part I: General*, vol. 101, no. 169, pp. 93-109, 1954.
- [6] D. D. Grieg, S. Metzger and R. Waer, "Considerations of Moon-Relay Communication", *Proc. IRE*, vol. 36, no. 5, pp. 652-663, 1948.
- [7] T. Gootee, "Radar reaches the Moon", *Radio News*, vol. 35, no. 4, pp. 25-27, 1946.
- [8] J. R. Pierce, "Orbital Radio Relays", *Jet Propulsion*, vol. 25, no. 4, pp. 153-157, 1955.
- [9] A. B. Crawford, C. C. Cutler, R. Kompfner and T. C. Tillotson, "The research background of the Telstar experiment", *Bell Labs Tech. J.*, vol. 42, no. 4, pp. 747-751, 1963.
- [10] M. G. Bodmer, J. P. Laico, E. G. Olsen and A. T. Ross, "The satellite traveling wave tube", *Bell Labs Tech. J.*, vol. 42, no. 4, pp. 1703-1748, 1963.
- [11] 521-2019, "IEEE Standard Letter Designations for Radar-Frequency Bands", Feb. 2020.
- [12] F. Cuervo, A. Martellucci, J. Rivera-Castro, M. Schmidt and M. Schonhuber, "The Alphasat Aldo Paraboni scientific and communication experiments at Ka and Q/V bands in Austria", *Int. J. Sat. Comm. Net.*, vol. 37, no. 5, pp. 437-448, May 2019.

- [13] C. Paoloni, F. Magne, F. Andre, X. Begaud, V. Krozer, M. Marilier, A. Ramirez, J. R. Ruiz-Carrasco, R. Vilar and R. Zimmerman, "TWEETHER Future Generation of W-band Backhaul and Access Network Technology", in *Proc. European Conf. Net. Comm.*, Oulu, Finland, Jun. 2017.
- [14] H. R. Hertz, "Die Krafte electrischer Schwingungen, behandelt nach der Maxwellschen Theorie", *Ann. der Physik*, Vol. 272, no. 1, pp. 1-22, 1889.
- [15] A. V. Haeff, "Device for and method of controlling high frequency currents", *U. S. Patent*, no. 2064469, Dec. 1936.
- [16] K. Posthumus, "Oscillations in split anode magnetron", *Wireless Engineer*, vol. 12, no. 138, pp. 126-132, 1935.
- [17] N. E. Lindenblad, "Electron discharge device system", *U. S. Patent*, no. 2300052, Oct. 1942.
- [18] R. Kompfner, "The traveling wave tube as an amplifier at microwaves", *Proc. IRE*, vol. 35, no. 2, pp. 124-127, 1947.
- [19] J. R. Pierce and L. M. Field, "Traveling-wave tubes", *Proc. IRE*, vol. 35, no. 2, pp. 108-111, 1947.
- [20] J. R. Pierce, "Traveling wave tube", *New York: Van Nostrand*, 1950.
- [21] A. S. Gilmour, "Principles of Traveling Wave Tubes", Artech House Radar Library, Michigan Univ., Boston, MA, USA, Dec. 1994.
- [22] D. M. Pozar, "Microwave engineering", *Wiley*, 2011.
- [23] G. Kornfeld and E. Bosch, "From History to Future of Satellite TWT Amplifiers", *Frequenz*, vol. 55, no. 9-10, pp. 258-262, Sep. 2001.
- [24] W. Q. Lohmeyer, R. J. Aniceto and K. L. Cahoy, "Communication satellite power amplifiers: current and future SSPA and TWTA technologies", *Int. J. Satell. Commun. Network*, vol. 34, pp. 95-113, Mar. 2015.
- [25] P. Ehret, H. Vogt, A. Peters and E. Bosch, "L-band TWTAAs for Navigation Satellites", *IEEE Trans. Electron Devices*, Vol. 52, no. 5, May 2005.
- [26] "S-band and L-band Linearized TWTA", *IRNSS Program*, Jun. 2018.
- [27] "The Japanese Quasi-Zenith Satellite System", *5th Int. Comm. on GNSS*, Torino, Italy, Oct. 2010.
- [28] Sentinel missions. [Online]. Available: <https://sentinel.esa.int/web/sentinel/missions>
- [29] Voyager1 space probe. [Online]. Available: <https://voyager.jpl.nasa.gov/>

- [30] James Webb Space Telescope. [Online] Available: <https://www.jwst.nasa.gov/>
- [31] H. R. Nye and A. Morani, "The Giotto Extended Mission", *ESA bulletin, Bulletin ASE, European Space Agency*, Mar. 1993.
- [32] A. N. Curren, J. A. Dayton, R. W. Palmer, D. A. Force, R. N. Tamashiro, J. F. Wilson, L. Dombro and W. L. Harvey, "A Low Power, High Efficiency Ka-Band TWTA", in *Proc. Int. Electron Devices Meeting*, Washington, USA, Dec. 1991.
- [33] M. Patzold et al, "Rosetta Radio Science Investigations", *Space Science Reviews*, Vol. 128, May 2007.
- [34] R. Ghail, T. Widemann and C. Wilson, "Venus Mission Plans in Europe" *VEXAG meeting 13*, Oct. 2015.
- [35] BepiColombo mission. [Online]. Available: <https://www.thalesgroup.com/en/market-specific/microwave-imaging-sub-systems/news/7-years-89-billion-kilometers-thales-embarks>
- [36] C. Damasio, A. Jacobs, S. Morgan, M. Sprague and D. Wild, "Thermal Test Campaign of the Solar Orbiter STM", *46th Int. Conf. Env. Syst.*, Vienna, Austria, Jul. 2016.
- [37] A. J. Theiss, C. L. Meadows, R. Freeman, R. B. True, J. M. Martin and K. L. Montgomery, "High-average-power W-band TWT development", *IEEE Trans. Plasma Science*, vol. 38, no. 6, pp. 1239-1243, Jun. 2010.
- [38] J. H. Booske, M. C. Converse, C. L. Kory, C. T. Chevalier, D. A. Gallagher, K. E. Kreischer, V. O. Heinen and S. Bhattacharjee, "Accurate parametric modeling of folded waveguide circuits for millimeter-wave traveling wave tubes", *IEEE Trans. Electron Devices*, vol. 52, no. 5, pp. 685-694, May 2005.
- [39] J. Cai, X. Wu and J. Feng, "A cosine-shaped vane-folded and ridge waveguide coupler", *IEEE Trans. Electron Devices*, vol. 63, no. 6, pp. 2544-2549, Jun. 2016.
- [40] W. Zhang, Y. Wang and B. Qu, "Design of folded double-ridged waveguide slow-wave structure", in *Proc. 19th Int. Vac. Electron. Conf.*, Monterey, USA, Apr. 2018.
- [41] J. Feng, Y. Hu, J. Cai, S. Ma and X. Wu, "Progress of W-band 10W CW TWT", in *Proc. 11th Int. Vac. Electron. Conf.*, Monterey, USA, May 2010.
- [42] Y. Wei, G. Guo, Y. Gong, L. Yue, G. Zhao, L. Zhang, C. Ding, T. Tang, M. Huang, W. Wang, Z. Gao and X. Li, "Novel W-band ridge-loaded folded waveguide traveling wave tube", *IEEE Electron Device Lett.*, vol. 35, no. 10, pp. 1058-1060, Oct. 2014.

- [43] Y. Hu, J. Feng, J. Cai, X. Wu, Y. Du, J. Liu, J. Chen and X. Zhang, "Design and experimental study of a wide bandwidth W-band folded waveguide continuous wave TWT", *IEEE Trans. Plasma Science*, vol. 42, no. 10, pp. 3380-3386, Oct. 2014.
- [44] X. Zhang, J. Feng, J. Cai, X. Wu, Y. Du, J. Chen, S. Li and W. Meng, "Design and experimental study of 250 W W-band pulsed TWT with 8 GHz bandwidth", *IEEE Trans. Electron Devices*, vol. 64, no. 12, pp.5151-5156, Dec. 2017.
- [45] Y. Du, J. Cai, P. Pan, R. Dong, X. Zhang, S. Liu, X. Wu and J. Feng, "Experimental investigation of a ultrawide bandwidth W-band pulsed traveling wave tube with microfabricated folded waveguide circuits", *IEEE Trans. Plasma Science*, vol. 47, no. 1, pp. 219-225, Jan. 2019.
- [46] R. Ji, Z. Yang, Z. Guo, Q. Wang, P. Hang and H. Gong, "Design and experiment of an E-band folded waveguide traveling wave tube", in *Proc. 20th Int. Vac. Electron. Conf.*, Busan, South Korea, Apr. 2019.
- [47] C. W. Robertson, A. W. Cross, C. Gilmour, D. Dyson, P. G. Huggard, F. Cahill, M. Beardsley, R. Dionisio and K. Donald, "71-76 GHz folded waveguide TWT for satellite communications", in *Proc. 20th Int. Vac. Electron. Conf.*, Busan, South Korea, Apr. 2019.
- [48] J. Lai, Y. Gong, X. Xu, Y. Wei, Z. Duan, W. Wang and J. Feng, "W-band 1 kW staggered double vane traveling wave tube", *IEEE Trans. Electron Devices*, vol. 59, no. 2, pp. 496-503, Feb. 2012.
- [49] X. Li, X. Huang, S. Mathisen, R. Letizia and C. Paoloni, "Design of 71-76 GHz double-corrugated waveguide traveling-wave tube for satellite downlink", *IEEE Trans. Electron Devices*, vol. 65, no. 6, pp. 2195-2200, Jun. 2018.
- [50] L. R. Billa, M. N. Akram, C. Paoloni and X. Chen, "H- and E-Plane loaded slow wave structure for W-band TWT", *IEEE Trans. Electron Devices*, vol. 67, no. 1, pp. 309-313, Jan. 2020.
- [51] C. Kory, L. Ives, M. Read, J. Booske, H. Jiang, D. van der Weide and P. Phillips, "Microfabricated W-band traveling wave tubes", in *Proc. 30th Int. Conf. Infrared mm. Wav. and 13th Conf. THz Electron.*, Williamsburg, USA, Sep. 2005.
- [52] F. Shen, Y. Wei, H. Yin, Y. Gong, X. Xu, S. Wang, W. Wang and J. Feng, "A novel V-shaped microstrip meander line slow wave structure for W-band MMPM", *IEEE Trans. Plasma Science*, vol. 40, no. 2, pp. 463-469, Feb. 2012.
- [53] F. Shen, Y. Wei, X. Xu, J. Lai, M. Huang, G. Zhao and Y. Gong, "Rhombus-shaped microstrip meander-line slow-wave structure for 140 GHz traveling-wave tube", in *Proc. 13th Int. Vac. Electron. Conf.*, Monterey, USA, Apr. 2012.

- [54] F. Shen, Y. Wei, X. Xu, Y. Liu, M. Huang, T. Tang and Y. Gong, "U-shaped microstrip meander-line slow-wave structure for Ka-band traveling-wave tube", in *Proc. Int. Conf. Microw. mm. Wav. Tech.*, Shenzhen, China, May 2012.
- [55] N. Bai, L. Gu, C. Shen, J. Feng, F. Liao and X. Sun, "S-shaped microstrip meander-line slow-wave structure for W-band traveling-wave tube", in *Proc. 14th Int. Vac. Electron. Conf.*, Paris, France, May 2013.
- [56] L. Liao, Y. Wei, L. Lu, L. Yue, T. Tang, W. Wang and Y. Gong, "A novel omega-shaped microstrip slow-wave structure for 60 GHz traveling wave tube", *Int. Workshop Microw. mm. Wav. Circ. and Syst. Tech.*, Chengdu, China, Oct. 2013.
- [57] C. Ding, Y. Wei, L. Zhang, G. Guo, Y. Wang, M. Zhang, Z. Lu, Y. Gong, W. Wang, D. Li and J. Feng, "Beam-wave interaction study on a novel Ka-band ring-shaped microstrip meander-line slow wave structure", in *Proc. 39th Int. Conf. Infrared, mm., THz-Wav*, Tucson, USA, Sep. 2014.
- [58] C. Ding, Y. Wei, Y. Wang, J. Xu, T. Tang, M. Huang, L. Zhang, Q. Li, X. Lei, Y. Gong, W. Wang and D. Li, "2-Dimensional microstrip meander line for broadband planar TWTs", in *Proc. 17th International Vacuum Electronics Conference (IVEC)*, Monterey, USA, Apr. 2016.
- [59] M. Sumathy and S. K. Datta, "Analysis of ladder structures for broadband W-band TWTs", *Asia-Pacific Microw. Conf.*, New Delhi, India, Dec. 2016.
- [60] S. Wang, S. Aditya, X. Xia, Z. Ali and J. Miao, "On-wafer microstrip meander-line slow-wave structure at Ka-band", *IEEE Trans. Electron Devices*, vol. 65, no. 6, pp. 2142-2148, Jun. 2018.
- [61] G. Ulisse, V. Krozer, N. Ryskin, A. Staroudubov, A. Serdobintsev, A. Pavlov, V. Galushka and M. Samarskiy, "Fabrication and measurements of a planar slow wave structure operating in V-band", in *Proc. 20th International Vacuum Electronics Conference (IVEC)*, Busan, South Korea, Apr. 2019.
- [62] G. Ulisse and V. Krozer, "Investigation of a planar metamaterial slow wave structure for traveling wave tube applications", in *Proc. 18th Int. Vac. Electron. Conf.*, London, UK, Apr. 2017.
- [63] E. Tahanian and G. R. Dadashzadeh, "An improved U-shaped microstrip meander line slow wave structure for high efficiency G-band traveling wave tubes", *Rec. Adv. in Electric. & Electron. Eng.*, vol. 9, no. 1, pp. 68-72, Dec. 2015.
- [64] S. Wang, Y. Gong, Y. Hou, Z. Wang, Y. Wei, Z. Duan and J. Cai, "Study of a log-periodic slow wave structure for Ka-band radial sheet beam traveling wave tube", *IEEE Trans. Plasma Science*, vol. 41, no. 8, pp. 2277-2282, Aug. 2013.

- [65] X. Li, Y. Xu, S. Wang, Z. Wang, X. Shi, Z. Duan, Y. Wei, J. Feng and Y. Gong, "Study on phase velocity tapered microstrip angular log-periodic meander line travelling wave tube", *IET Microw. Antennas Propag.*, vol. 10, no. 8, pp. 902-907, May 2016.
- [66] F. Shen, Y. Wei, X. Xu, Y. Liu, M. Huang, T. Tang, Z. Duan and Y. Gong, "Symmetric double V-shaped microstrip meander-line slow-wave structure for W-band traveling-wave tube", *IEEE Trans. Electron Devices*, vol. 59, no. 5, pp. 1551-1557, May 2012.
- [67] G. Guo, Y. Wei, M. Zhang, G. Travish, L. Yue, J. Xu, H. Yin, M. Huang, Y. Gong and W. Wang, "Novel folded frame slow-wave structure for millimeter-wave traveling-wave tube", *IEEE Trans. Electron Devices*, vol. 60, no. 11, pp. 3895-3900, Nov. 2013.
- [68] S. Wang, Y. Gong, Z. Wang, Y. Wei, Z. Duan and J. Feng, "Study of the symmetrical microstrip angular log-periodic meander-line traveling-wave tube", *IEEE Trans. Plasma Science*, vol. 44, no. 9, pp. 1787-1793, Sep. 2016.
- [69] A. Galdetskiy and E. Rakova, "New slow wave structure for W-band TWT", in *Proc. 18th Int. Vac. Electron. Conf.*, London, UK, Apr. 2017.
- [70] G. Ulisse and V. Krozer, "W-band traveling wave tube amplifier based on planar slow wave structure", *IEEE Electron Device Let.*, vol. 38, no. 1, pp. 126-129, Jan. 2017.
- [71] C. Feng, N. Bai, C. Shen, H. Fan, X. Zhao, X. Sun, Y. Hu, F. Liao and J. Feng, "Double reversed U-shaped meander line slow wave structure", in *Proc. 18th Int. Vac. Electron. Conf.*, London, UK, Apr. 2017.
- [72] C. Chua, J. M. Tsai, S. Aditya, M. Tang, S. Wee Ho, Z. Shen and L. Wang, "Microfabrication and Characterization of W-band planar helix slow-wave structure with straight-edge connections", *IEEE Trans. Electron Devices*, vol. 58, no. 11, pp. 4098-4105, Nov. 2011.
- [73] C. Chua and S. Aditya, "A 3D U-shaped meander-line slow-wave structure for traveling-wave-tube applications", *IEEE Trans. Electron Devices*, vol. 60, no. 3, pp. 1251-1256, Mar. 2013.
- [74] M. Sumathy, S. K. Datta and Lalit Kumar, "Folded meander-line slow-wave structure for millimeter-wave TWTs", in *Proc. 14th Int. Vac. Electron. Conf.*, Paris, France, May 2013.
- [75] L. Liu, Y. Wei, F. Shen, G. Zhao, L. Yue, Z. Duan, W. Wang, Y. Gong, L. Li and J. Feng, "A novel winding microstrip meander line slow wave structure for V-band TWT", *IEEE Electron Device Let.*, vol. 34, no. 10, pp. 1325-1327, Oct. 2013.

- [76] S. Sengele, H. Jiang, J. H. Booske, C. L. Kory, D. W. van der Weide and R. L. Ives, "Microfabrication and characterization of a selectively metallized W-band meander-line TWT circuit", *IEEE Trans. Electron Devices*, vol. 56, no. 5, pp. 730-737, May 2009.
- [77] T. He, X. Li, D. Xu, H. Wang, N. Shi, Z. Wang, L. Yue, T. Tang, Z. Duan, Y. Wei, Y. Gong and J. Feng, "Angular log-periodic meander line traveling wave tube based on quartz substrate", in *Proc. 19th Int. Vac. Electron. Conf.*, Monterey, USA, Apr. 2018.
- [78] D. Chong, W. Yanyu, L. Qian, Z. Luqi, G. Guo and G. Yubin, "A dielectric-embedded microstrip meander line slow-wave structure for minituarized traveling wave tube", *J. Elec. Wav. App.*, vol. 31, no. 17, pp. 1938-1946, Aug. 2017.
- [79] N. Bai, M. Shen and X. Sun, "Investigation of microstrip meander-line traveling-wave tube using EBG ground plane", *IEEE Trans. Electron Devices*, vol. 62, no. 5, pp. 1622-1627, May 2015.
- [80] N. Bai, C. Feng, Y. Liu, H. Fan, C. Shen and X. Sun, "Integrated microstrip meander line traveling wave tube based on metamaterial absorber", *IEEE Trans. Electron Devices*, vol. 64, no. 7, pp. 2949-2954, Jul. 2017.
- [81] H. W. Yao, A. Abdelmonem, J. F. Liang and K. A. Zaki, "Analysis and design of microstrip to waveguide transitions", *IEEE Trans. Microw. Theory Techn.*, vol. 45, no. 12, pp. 2371-2380, Dec. 1994.
- [82] W. Menzel and A. Klaassen, "On the transition from ridged waveguide to microstrip", *19th European Microw. Conf.*, London, UK, Sep. 1989.
- [83] A. A. Omar and N. I. Dib. "Analysis of slot coupled transitions from microstrip to microstrip and microstrip to waveguides", *IEEE Trans. on Microw. Theory Techn.*, vol. 45, no. 7, pp. 1127-1132, Jul. 1997.
- [84] X. Huang and K. L. Wu, "A broadband U-slot Coupled Microstrip to Waveguide transition", *IEEE Trans. on Microw. Theory Techn.*, vol. 60, no. 5, pp. 1210-1217, May 2012.
- [85] Y. C. Shih, T. N. Ton and L. Q. Bui, "Waveguide to microstrip transitions for millimetre wave applications", in *Proc. IEEE Int. Microw. Symp.*, New York, May 1988.
- [86] Y. C. Leong and S. W., "Full band waveguide to microstrip probe transitions", in *Proc. IEEE Int. Microw. Symp.*, Anaheim, USA, Jun. 1999.
- [87] CST Microwave Studio. [Online]. Available: <https://www.cst.com/products/csts2>

- [88] S. D'Agostino, F. Emma and C. Paoloni, "Accurate Analysis of Helix Slow-Wave Structures", *IEEE Trans. Electron Devices*, vol. 45, no. 7, pp. 1605-1613, Jul. 1998.
- [89] C. L. Kory and J. A. Dayton, "Computational Investigation of Experimental Interaction Impedance Obtained by Perturbation for Helical Traveling-Wave Tube Structures", *IEEE Trans. Electron Devices*, vol. 45, no. 9, pp. 2063-2071, Dec. 1998.
- [90] S. J. Rao, S. Ghosh, P. K. Jain and B. N. Basu, "Nonresonant Perturbation Measurements on Dispersion and Interaction Impedance Characteristics of Helical Slow-Wave Structures", *IEEE Trans. Microw. Theory Techn.*, vol. 45, no. 9, pp. 1585-1593, Sep. 1997.
- [91] R. P. Lagerstrom, "Interaction impedance measurements by perturbation of traveling waves", Tech. Rep. no. 7, Stanford Electronics Laboratories, Stanford Univ., Stanford, CA, USA, Feb. 1957.
- [92] T. Itoh and R. Mittra, "Spectral-Domain Approach for Calculating the Dispersion Characteristics of Microstrip Lines", *IEEE Trans. Microw. Theory Techn.*, vol. 21, no. 7, pp. 496-499, Jul. 1973.
- [93] J. A. Weiss, "Dispersion and Field Analysis of a Microstrip Meander-Line Slow-Wave Structure", *IEEE Trans. Microw. Theory Techn.*, vol. 22, No. 12, pp. 1194-1201, Dec. 1974.
- [94] D. G. Zhang, Edward K. N. Yung and H. Y. Ding, "Dispersion characteristics of a novel shielded periodic meander line", *Microw. and Opt. Techn. Lett.*, vol. 12, no. 1, pp. 1-5, May 1996.

A. Derivation of the parameters X_{jk} and k_{jk} for NML1 and NML2

New meander line 1 (NML1)

The longitudinal electric field component expressions for the NML1 are obtained taking into account the regions defined in Fig. A.0.1. Seven and three regions are represented along the z and x axis, $j = 1, 2, 3, 4, 5, 6, 7$ and $k = 1, 2, 3$. The region $k = 2$ is associated to the area where the metallization exists. For this topology, the fields from region $j = 1$ and $j = 7$ are the same.

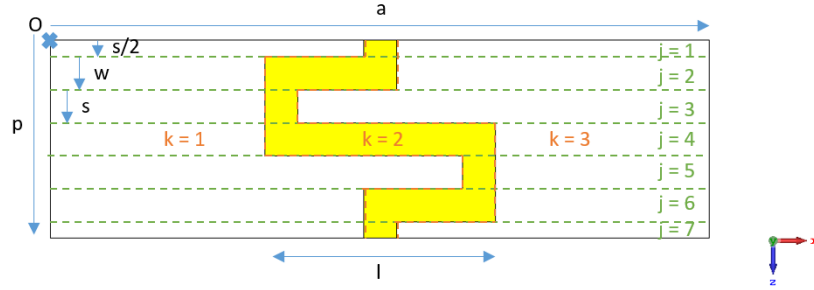


Figure A.0.1: xz -plane view of the first new meander line. There are seven and three regions along the z and x axis, respectively. s is the distance between two consecutive strips, w is the strip width, p is the pitch length, a is the length of the substrate and l is the length of the metallization.

$$0 < z < s/2, s/2 + w + s + w + s + w < z < p \text{ and } 0 < x < a/2 - w/2 \text{ or } j = 1, 7 \text{ and } k = 1$$

$$E_z(x, y, z) = \sum_{m,n=-\infty}^{\infty} A_{11,mn} \frac{\sinh(\alpha_{i11,mn} Y_i)}{\sinh(\alpha_{i11,mn} B_i)} \sin(k_{11,m} X_{11}) e^{-j\beta_n z}$$

$$\text{with } k_{11,m} = \frac{(2m-1)\pi}{a/2-w/2} \text{ and } X_{11} = x.$$

$0 < z < s/2, s/2 + w + s + w + s + w < z < p$ and $a/2 - w/2 < x < a/2 + w/2$ or $j = 1, 7$ and $k = 2$

$$E_z(x, y, z) = 0$$

$0 < z < s/2, s/2 + w + s + w + s + w < z < p$ and $a/2 + w/2 < x < a$ or $j = 1, 7$ and $k = 3$

$$E_z(x, y, z) = \sum_{m,n=-\infty}^{\infty} A_{13,mn} \frac{\sinh(\alpha_{i13,mn} Y_i)}{\sinh(\alpha_{i13,mn} B_i)} \sin(k_{13,m} X_{13}) e^{-j\beta_n z}$$

with $k_{13,m} = \frac{(2m-1)\pi}{a/2-w/2}$ and $X_{13} = a - x$.

$s/2 < z < s/2 + w$ and $0 < x < a/2 - l/2$ or $j = 2$ and $k = 1$

$$E_z(x, y, z) = \sum_{m,n=-\infty}^{\infty} A_{21,mn} \frac{\sinh(\alpha_{i21,mn} Y_i)}{\sinh(\alpha_{i21,mn} B_i)} \sin(k_{21,m} X_{21}) e^{-j\beta_n z}$$

with $k_{21,m} = \frac{(2m-1)\pi}{a/2-l/2}$ and $X_{21} = x$.

$s/2 < z < s/2 + w$ and $a/2 - l/2 < x < a/2 + w/2$ or $j = 2$ and $k = 2$

$$E_z(x, y, z) = 0$$

$s/2 < z < s/2 + w$ and $a/2 + w/2 < x < a$ or $j = 2$ and $k = 3$

$$E_z(x, y, z) = \sum_{m,n=-\infty}^{\infty} A_{23,mn} \frac{\sinh(\alpha_{i23,mn} Y_i)}{\sinh(\alpha_{i23,mn} B_i)} \sin(k_{23,m} X_{23}) e^{-j\beta_n z}$$

with $k_{23,m} = \frac{(2m-1)\pi}{a/2-w/2}$ and $X_{23} = a - x$.

$s/2 + w < z < s/2 + w + s$ and $0 < x < a/2 - l/2$ or $j = 3$ and $k = 1$

$$E_z(x, y, z) = \sum_{m,n=-\infty}^{\infty} A_{31,mn} \frac{\sinh(\alpha_{i31,mn} Y_i)}{\sinh(\alpha_{i31,mn} B_i)} \sin(k_{31,m} X_{31}) e^{-j\beta_n z}$$

with $k_{31,m} = \frac{(2m-1)\pi}{a/2-l/2}$ and $X_{31} = x$.

$s/2 + w < z < s/2 + w + s$ and $a/2 - l/2 < x < a/2 - l/2 + w$ or $j = 3$ and $k = 2$

$$E_z(x, y, z) = 0$$

$s/2 + w < z < s/2 + w + s$ and $a/2 - l/2 + w < x < a$ or $j = 3$ and $k = 3$

$$E_z(x, y, z) = \sum_{m,n=-\infty}^{\infty} A_{33,mn} \frac{\sinh(\alpha_{i33,mn} Y_i)}{\sinh(\alpha_{i33,mn} B_i)} \sin(k_{33,m} X_{33}) e^{-j\beta_n z}$$

with $k_{33,m} = \frac{(2m-1)\pi}{a/2+l/2-w}$ and $X_{33} = a - x$.

$s/2 + w + s < z < s/2 + w + s + w$ and $0 < x < a/2 - l/2$ or $j = 4$ and $k = 1$

$$E_z(x, y, z) = \sum_{m,n=-\infty}^{\infty} A_{41,mn} \frac{\sinh(\alpha_{i41,mn} Y_i)}{\sinh(\alpha_{i41,mn} B_i)} \sin(k_{41,m} X_{41}) e^{-j\beta_n z}$$

with $k_{41,m} = \frac{(2m-1)\pi}{a/2-l/2}$ and $X_{41} = x$.

$s/2 + w + s < z < s/2 + w + s + w$ and $a/2 - l/2 < x < a/2 + l/2 + w$ or $j = 4$ and $k = 2$

$$E_z(x, y, z) = 0$$

$s/2 + w + s < z < s/2 + w + s + w$ and $a/2 + l/2 < x < a$ or $j = 4$ and $k = 3$

$$E_z(x, y, z) = \sum_{m,n=-\infty}^{\infty} A_{43,mn} \frac{\sinh(\alpha_{i43,mn} Y_i)}{\sinh(\alpha_{i43,mn} B_i)} \sin(k_{43,m} X_{43}) e^{-j\beta_n z}$$

with $k_{43,m} = \frac{(2m-1)\pi}{a/2-l/2}$ and $X_{43} = a - x$.

$s/2 + w + s + w < z < s/2 + w + s + w + s$ and $0 < x < a/2 + l/2 - w$ or $j = 5$ and $k = 1$

$$E_z(x, y, z) = \sum_{m,n=-\infty}^{\infty} A_{51,mn} \frac{\sinh(\alpha_{i51,mn} Y_i)}{\sinh(\alpha_{i51,mn} B_i)} \sin(k_{51,m} X_{51}) e^{-j\beta_n z}$$

with $k_{51,m} = \frac{(2m-1)\pi}{a/2+l/2-w}$ and $X_{51} = x$.

$s/2 + w + s + w < z < s/2 + w + s + w + s$ and $a/2 + l/2 - w < x < a/2 + l/2$ or $j = 5$ and $k = 2$

$$E_z(x, y, z) = 0$$

$s/2 + w + s + w < z < s/2 + w + s + w + s$ and $a/2 + l/2 < x < a$ or $j = 5$ and $k = 3$

$$E_z(x, y, z) = \sum_{m,n=-\infty}^{\infty} A_{53,mn} \frac{\sinh(\alpha_{i53,mn} Y_i)}{\sinh(\alpha_{i53,mn} B_i)} \sin(k_{53,m} X_{53}) e^{-j\beta_n z}$$

with $k_{53,m} = \frac{(2m-1)\pi}{a/2-l/2}$ and $X_{53} = a - x$.

$s/2 + w + s + w + s < z < s/2 + w + s + w + s + w$ and $0 < x < a/2 - w/2$ or $j = 6$ and $k = 1$

$$E_z(x, y, z) = \sum_{m,n=-\infty}^{\infty} A_{61,mn} \frac{\sinh(\alpha_{i61,mn} Y_i)}{\sinh(\alpha_{i61,mn} B_i)} \sin(k_{61,m} X_{61}) e^{-j\beta_n z}$$

with $k_{61,m} = \frac{(2m-1)\pi}{a/2-w/2}$ and $X_{61} = x$.

$s/2 + w + s + w + s < z < s/2 + w + s + w + s + w$ and $a/2 - w/2 < x < a/2 + l/2$
or $j = 6$ and $k = 2$

$$E_z(x, y, z) = 0$$

$s/2 + w + s + w + s < z < s/2 + w + s + w + s + w$ and $a/2 + l/2 < x < a$ or $j = 6$ and $k = 3$

$$E_z(x, y, z) = \sum_{m,n=-\infty}^{\infty} A_{63,mn} \frac{\sinh(\alpha_{i63,mn} Y_i)}{\sinh(\alpha_{i63,mn} B_i)} \sin(k_{63,m} X_{63}) e^{-j\beta_n z}$$

with $k_{63,m} = \frac{(2m-1)\pi}{a/2-l/2}$ and $X_{63} = a - x$.

New meander line 2 (NML2)

The longitudinal electric field component expressions for the NML2 are calculated according to the regions defined in Fig. A.0.2. Nine and four regions are represented along the z and x axis, $j = 1, 2, 3, 4, 5, 6, 7, 8, 9$ and $k = 1, 2, 3, 4$. The region $k = 2$ is defined for the metallization whereas the region $k = 4$ defines the area of the inner space between two consecutive strips. For this meander line, the fields from regions $j = 1$ and $j = 9$ are the same, also the fields from regions $j = 2, j = 4, j = 6$ and $j = 8$, and finally the fields from regions $j = 3$ and $j = 7$.

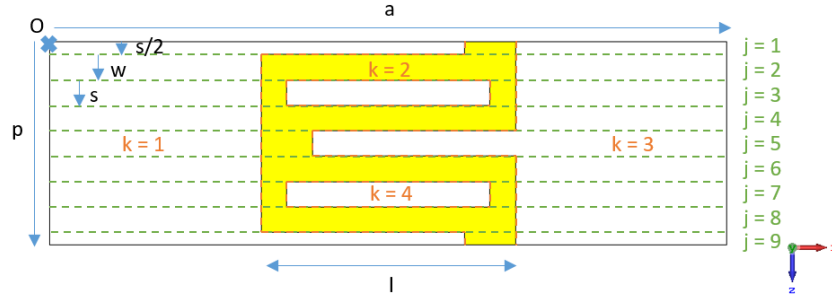


Figure A.0.2: xz -plane view of the second new meander line. There are nine and four regions along the z and x coordinates, respectively. s is the distance between two consecutive strips, w is the strip width, p is the pitch length, a is the length of the substrate and l is the length of the metallization.

$0 < z < s/2, s/2 + w + s + w + s + w + s + w < z < p$ and $0 < x < a/2 + l/2 - 2w$ or $j = 1, 9$
and $k = 1$

$$E_z(x, y, z) = \sum_{m,n=-\infty}^{\infty} A_{11,mn} \frac{\sinh(\alpha_{i11,mn} Y_i)}{\sinh(\alpha_{i11,mn} B_i)} \sin(k_{11,m} X_{11}) e^{-j\beta_n z}$$

with $k_{11,m} = \frac{(2m-1)\pi}{a/2+l/2-2w}$ and $X_{11} = x$.

$0 < z < s/2, s/2 + w + s + w + s + w + s + w < z < p$ and $a/2 + l/2 - 2w < x < a/2 + l/2$
or $j = 1, 9$ and $k = 2$

$$E_z(x, y, z) = 0$$

$0 < z < s/2, s/2 + w + s + w + s + w + s + w < z < p$ and $a/2 + l/2 < x < a$ or $j = 1, 9$ and
 $k = 3$

$$E_z(x, y, z) = \sum_{m,n=-\infty}^{\infty} A_{13,mn} \frac{\sinh(\alpha_{i13,mn} Y_i)}{\sinh(\alpha_{i13,mn} B_i)} \sin(k_{13,m} X_{13}) e^{-j\beta_n z}$$

with $k_{13,m} = \frac{(2m-1)\pi}{a/2-l/2}$ and $X_{13} = a - x$.

$s/2 < z < s/2 + w, s/2 + w + s < z < s/2 + w + s + w, s/2 + w + s + w + s < z <$
 $s/2 + w + s + w + s + w, s/2 + w + s + w + s + w + s < z < s/2 + w + s + w + s + w + s + w$
and $0 < x < a/2 - l/2$ or $j = 2, 4, 6, 8$ and $k = 1$

$$E_z(x, y, z) = \sum_{m,n=-\infty}^{\infty} A_{21,mn} \frac{\sinh(\alpha_{i21,mn} Y_i)}{\sinh(\alpha_{i21,mn} B_i)} \sin(k_{21,m} X_{21}) e^{-j\beta_n z}$$

with $k_{21,m} = \frac{(2m-1)\pi}{a/2-l/2}$ and $X_{21} = x$.

$s/2 < z < s/2 + w, s/2 + w + s < z < s/2 + w + s + w, s/2 + w + s + w + s < z <$
 $s/2 + w + s + w + s + w, s/2 + w + s + w + s + w + s < z < s/2 + w + s + w + s + w + s + w$
and $a/2 - l/2 < x < a/2 + l/2$ or $j = 2, 4, 6, 8$ and $k = 2$

$$E_z(x, y, z) = 0$$

$s/2 < z < s/2 + w, s/2 + w + s < z < s/2 + w + s + w, s/2 + w + s + w + s < z <$
 $s/2 + w + s + w + s + w, s/2 + w + s + w + s + w + s < z < s/2 + w + s + w + s + w + s + w$
and $a/2 + l/2 < x < a$ or $j = 2, 4, 6, 8$ and $k = 3$

$$E_z(x, y, z) = \sum_{m,n=-\infty}^{\infty} A_{23,mn} \frac{\sinh(\alpha_{i23,mn} Y_i)}{\sinh(\alpha_{i23,mn} B_i)} \sin(k_{23,m} X_{23}) e^{-j\beta_n z}$$

with $k_{23,m} = \frac{(2m-1)\pi}{a/2-l/2}$ and $X_{23} = a - x$.

$s/2 + w < z < s/2 + w + s$ and $0 < x < a/2 - l/2$ or $j = 3, 7$ and $k = 1$

$$E_z(x, y, z) = \sum_{m,n=-\infty}^{\infty} A_{31,mn} \frac{\sinh(\alpha_{i31,mn} Y_i)}{\sinh(\alpha_{i31,mn} B_i)} \sin(k_{31,m} X_{31}) e^{-j\beta_n z}$$

with $k_{31,m} = \frac{(2m-1)\pi}{a/2-l/2}$ and $X_{31} = x$.

$s/2 + w < z < s/2 + w + s$ and $a/2 - l/2 < x < a/2 - l/2 + w$ or $j = 3, 7$ and $k = 2$

$$E_z(x, y, z) = 0$$

$s/2 + w < z < s/2 + w + s$ and $a/2 + l/2 < x < a$ or $j = 3, 7$ and $k = 3$

$$E_z(x, y, z) = \sum_{m,n=-\infty}^{\infty} A_{33,mn} \frac{\sinh(\alpha_{i33,mn} Y_i)}{\sinh(\alpha_{i33,mn} B_i)} \sin(k_{33,m} X_{33}) e^{-j\beta_n z}$$

with $k_{33,m} = \frac{(2m-1)\pi}{a/2-l/2}$ and $X_{33} = a - x$.

$s/2 + w < z < s/2 + w + s$ and $a/2 - l/2 + w < x < a/2 + l/2 - w$ or $j = 3, 7$ and $k = 4$

$$E_z(x, y, z) = \sum_{m,n=-\infty}^{\infty} A_{34,mn} \frac{\sinh(\alpha_{i34,mn} Y_i)}{\sinh(\alpha_{i34,mn} B_i)} \sin(k_{34,m} X_{34}) e^{-j\beta_n z}$$

with $k_{34,m} = \frac{(2m-1)\pi}{l-2w}$ and $X_{34} = a/2 + l/2 - w - x$.

$s/2 + w + s + w < z < s/2 + w + s + w + s$ and $0 < x < a/2 - l/2$ or $j = 5$ and $k = 1$

$$E_z(x, y, z) = \sum_{m,n=-\infty}^{\infty} A_{51,mn} \frac{\sinh(\alpha_{i51,mn} Y_i)}{\sinh(\alpha_{i51,mn} B_i)} \sin(k_{51,m} X_{51}) e^{-j\beta_n z}$$

with $k_{51,m} = \frac{(2m-1)\pi}{a/2-l/2}$ and $X_{51} = x$.

$s/2 + w + s + w < z < s/2 + w + s + w + s$ and $a/2 - l/2 < x < a/2 - l/2 + 2w$ or $j = 5$ and $k = 2$

$$E_z(x, y, z) = 0$$

$s/2 + w + s + w < z < s/2 + w + s + w + s$ and $a/2 - l/2 + 2w < x < a$ or $j = 5$ and $k = 3$

$$E_z(x, y, z) = \sum_{m,n=-\infty}^{\infty} A_{53,mn} \frac{\sinh(\alpha_{i53,mn} Y_i)}{\sinh(\alpha_{i53,mn} B_i)} \sin(k_{53,m} X_{53}) e^{-j\beta_n z}$$

with $k_{53,m} = \frac{(2m-1)\pi}{a/2+l/2-2w}$ and $X_{53} = a - x$.

B. Interaction impedance computational codes

The codes developed for computing the interaction impedance according to the model presented in Sec. 5.2 are attached in this appendix. The codes have been created and run using Matlab v9.6.0.1062519 (R2019a).

```

%SML and SMLR

%Variable definition
syms x;
syms y;

s = ; %Space between two consecutive metal strips
w = ; %Width of the metallization
l = ; %Length of the metallization
r = ; %Radius of the perturbation
d = ; %Distance from the metallization to the perturbation
t = ; %Thickness of the substrate
a = ; %Length of the enclosure
b = ; %Height of the enclosure
p = ; %Pitch of the meander line
n = ; %Axial mode
m = ; %Transverse mode

Y1 = y;
B1 = t;
Y2 = b-y;
B2 = b-t;

k11m = (2*m-1)*pi/(a/2+l/2-w);
X11 = x;
k13m = (2*m-1)*pi/(a/2-l/2);
X13 = a-x;
k21m = (2*m-1)*pi/(a/2-l/2);
X21 = x;
k23m = (2*m-1)*pi/(a/2-l/2);
X23 = a-x;
k31m = (2*m-1)*pi/(a/2-l/2);
X31 = x;
k33m = (2*m-1)*pi/(a/2+l/2-w);
X33 = a-x;

f = ; %Frequency
omega = 2*pi*f; %Angular frequency

mu0 = ; %Vacuum permeability
epsilon0 = ; %Vacuum permittivity
epsilon1 = ; %Permittivity substrate
epsilon2 = ; %Permittivity medium
epsilonp = ; %Permittivity perturbation

betan = ; %Propagation constant
Deltabetan = ; %Propagation constant shift
betapn = Deltabetan + betan;

alpha11mn = sqrt(k11m^2 + betan.^2 - omega.^2*mu0*epsilon1*epsilon0);
alpha211mn = sqrt(k11m^2 + betan.^2 - omega.^2*mu0*epsilon2*epsilon0);
alpha113mn = sqrt(k13m^2 + betan.^2 - omega.^2*mu0*epsilon1*epsilon0);
alpha213mn = sqrt(k13m^2 + betan.^2 - omega.^2*mu0*epsilon2*epsilon0);
alpha121mn = sqrt(k21m^2 + betan.^2 - omega.^2*mu0*epsilon1*epsilon0);
alpha221mn = sqrt(k21m^2 + betan.^2 - omega.^2*mu0*epsilon2*epsilon0);

```

```

alpha123mn = sqrt(k23m^2 + betan.^2 - omega.^2*mu0*epsilon1*epsilon0);
alpha223mn = sqrt(k23m^2 + betan.^2 - omega.^2*mu0*epsilon2*epsilon0);
alpha131mn = sqrt(k31m^2 + betan.^2 - omega.^2*mu0*epsilon1*epsilon0);
alpha231mn = sqrt(k31m^2 + betan.^2 - omega.^2*mu0*epsilon2*epsilon0);
alpha133mn = sqrt(k33m^2 + betan.^2 - omega.^2*mu0*epsilon1*epsilon0);
alpha233mn = sqrt(k33m^2 + betan.^2 - omega.^2*mu0*epsilon2*epsilon0);

alphap11mn = sqrt(k11m^2 + betapn.^2 - omega.^2*mu0*epsilonp*epsilon0);
alphap13mn = sqrt(k13m^2 + betapn.^2 - omega.^2*mu0*epsilonp*epsilon0);
alphap21mn = sqrt(k21m^2 + betapn.^2 - omega.^2*mu0*epsilonp*epsilon0);
alphap23mn = sqrt(k23m^2 + betapn.^2 - omega.^2*mu0*epsilonp*epsilon0);
alphap31mn = sqrt(k31m^2 + betapn.^2 - omega.^2*mu0*epsilonp*epsilon0);
alphap33mn = sqrt(k33m^2 + betapn.^2 - omega.^2*mu0*epsilonp*epsilon0);

%Integral 11x
I11xiny = int(sinh(alphap11mn.*Y2).*sinh(alpha211mn.*Y2),y,t+d+r-sqrt(r^2-(x-
a/2)^2),t+d+r+sqrt(r^2-(x-a/2)^2));

I11xinx = vpa(int(I11xiny.*cos(k11m*X11).^2,x,a/2-r,a/2+r),4);

%Integral 11y
I11yiny = int(cosh(alphap11mn.*Y2).*cosh(alpha211mn.*Y2),y,t+d+r-sqrt(r^2-(x-
a/2)^2),t+d+r+sqrt(r^2-(x-a/2)^2));

I11yinx = vpa(int(I11yiny.*sin(k11m*X11).^2,x,a/2-r,a/2+r),4);

%Integral 11z
I11ziny = int(sinh(alphap11mn.*Y2).*sinh(alpha211mn.*Y2),y,t+d+r-sqrt(r^2-(x-
a/2)^2),t+d+r+sqrt(r^2-(x-a/2)^2));

I11zinx = vpa(int(I11ziny.*sin(k11m*X11).^2,x,a/2-r,a/2+r),4);

%Integral 33x
I33xiny = int(sinh(alphap33mn.*Y2).*sinh(alpha233mn.*Y2),y,t+d+r-sqrt(r^2-(x-
a/2)^2),t+d+r+sqrt(r^2-(x-a/2)^2));

I33xinx = vpa(int(I33xiny.*cos(k33m*X33).^2,x,a/2-r,a/2+r),4);

%Integral 33y
I33yiny = int(cosh(alphap33mn.*Y2).*cosh(alpha233mn.*Y2),y,t+d+r-sqrt(r^2-(x-
a/2)^2),t+d+r+sqrt(r^2-(x-a/2)^2));

I33yinx = vpa(int(I33yiny.*sin(k33m*X33).^2,x,a/2-r,a/2+r),4);

%Integral 33z
I33ziny = int(sinh(alphap33mn.*Y2).*sinh(alpha233mn.*Y2),y,t+d+r-sqrt(r^2-(x-
a/2)^2),t+d+r+sqrt(r^2-(x-a/2)^2));

I33zinx = vpa(int(I33ziny.*sin(k33m*X33).^2,x,a/2-r,a/2+r),4);

%Point of calculation of K
x0 = ;
y0 = ;
X110 = x0;

```

```

X130 = a-x0;
X210 = x0;
X230 = a-x0;
X310 = x0;
X330 = a-x0;
Y10 = y0;
Y20 = b-y0;

%Point of first interface condition perturbation-surrounding medium
x1 = ;
y1 = ;
X111 = x1;
X131 = a-x1;
X211 = x1;
X231 = a-x1;
X311 = x1;
X331 = a-x1;
Y11 = y1;
Y21 = b-y1;

%Point of second interface condition substrate-surrounding medium
y2 = ;
Y12 = y2;
Y22 = b-y2;

%Coefficient 1lx
brack11 = -1 + (k11m^2*omega.^2*mu0*(epsilon2-
epsilon1)*epsilon0)/(alpha211mn.^2.*(betan.^2-
omega.^2*mu0*epsilon1*epsilon0).*(1+(alpha11mn.*(betan.^2-
omega.^2*mu0*epsilon2*epsilon0).*tanh(alpha11mn*Y12))/(alpha211mn.*(betan.^
2-omega.^2*mu0*epsilon1*epsilon0).*tanh(alpha211mn*Y22))));

G11x = ((k11m^2*betan.*betapn.*(1-
alphap11mn.^2/(k11m^2)).*sinh(alpha211mn*Y21))/(betapn.^2-
omega.^2*mu0*epsilonp*epsilon0).*(betan.^2-
omega.^2*mu0*epsilon2*epsilon0).*sinh(alpha211mn*Y22).^2.*sinh(alphap11mn*Y21
))-
(epsilon2*epsilon0*betan.^2.*alpha211mn.*alphap11mn.*cosh(alpha211mn*Y21)).*b
rack11./(epsilonp*epsilon0*(betan.^2-
omega.^2*mu0*epsilon2*epsilon0).^2.*sinh(alpha211mn*Y22).^2.*cosh(alphap11mn*
Y21))).*brack11.*sinh(alpha211mn*Y22).^2./(sinh(alpha211mn.*Y20).^2.*sin(k11m.
*X110).^2);

%Coefficient 1ly
G11y =
(epsilon2*epsilon0*alpha211mn.^2.*betan.^2.*cosh(alpha211mn*Y21).*brack11.^2)
./(epsilonp*epsilon0*(betan.^2-
omega.^2*mu0*epsilon2*epsilon0).^2.*cosh(alphap11mn*Y21).*sinh(alpha211mn.*Y2
0).^2.*sin(k11m.*X110).^2);

%Coefficient 1lz
G11z =
sinh(alpha211mn*Y21)/(sinh(alpha211mn.*Y20).^2.*sinh(alphap11mn*Y21).*sin(k1
1m.*X110).^2);

```

```

%Coefficient 33x
brack33 = -1 + (k33m^2*omega.^2*mu0*(epsilon2-
epsilon1)*epsilon0)/(alpha233mn.^2.*(betan.^2-
omega.^2*mu0*epsilon1*epsilon0).*(1+(alpha133mn.*(betan.^2-
omega.^2*mu0*epsilon2*epsilon0).*tanh(alpha133mn*Y12))/(alpha233mn.*(betan.^
2-omega.^2*mu0*epsilon1*epsilon0).*tanh(alpha233mn*Y22))));

G33x = ((k33m^2*betan.*betapn.*(1-
alphap33mn.^2/(k33m^2)).*sinh(alpha233mn*Y21))/(betapn.^2-
omega.^2*mu0*epsilonp*epsilon0).*(betan.^2-
omega.^2*mu0*epsilon2*epsilon0).*sinh(alpha233mn*Y22).^2.*sinh(alphap33mn*Y21
))-
(epsilon2*epsilon0*betan.^2.*alpha233mn.*alphap33mn.*cosh(alpha233mn*Y21)).*b
rack33./(epsilonp*epsilon0*(betan.^2-
omega.^2*mu0*epsilon2*epsilon0).^2.*sinh(alpha233mn*Y22).^2.*cosh(alphap33mn*
Y21)).*brack33.*sinh(alpha233mn*Y22).^2./(sinh(alpha233mn.*Y20).^2*sin(k33m.
*X330).^2);

%Coefficient 33y
G33y =
(epsilon2*epsilon0*alpha233mn.^2.*betan.^2.*cosh(alpha233mn*Y21).*brack33.^2)
./(epsilonp*epsilon0*(betan.^2-
omega.^2*mu0*epsilon2*epsilon0).^2.*cosh(alphap33mn*Y21).*sinh(alpha233mn.*Y2
0).^2.*sin(k33m.*X330).^2);

%Coefficient 33z
G33z =
sinh(alpha233mn*Y21)/(sinh(alpha233mn.*Y20).^2.*sinh(alphap33mn*Y21).*sin(k3
3m.*X330).^2);

%Full term 11x
T11x = s*G11x.*I11xinx;

%Full term 11y
T11y = s*G11y.*I11yinx;

%Full term 11z
T11z = s*G11z.*I11zinx;

%Full term 33x
T33x = s*G33x.*I33xinx;

%Full term 33y
T33y = s*G33y.*I33yinx;

%Full term 33z
T33z = s*G33z.*I33zinx;

%Sum of terms
I = T11x + T11y + T11z + T33x + T33y + T33z;

%Interaction impedance
KSML = 2*p*Deltabetan./((epsilonp-epsilon2)*epsilon0*omega.*betan.^2.*I);

```

```

%NML1

%Variable definition
syms x;
syms y;

s = ; %Space between two consecutive metal strips
w = ; %Width of the metallization
l = ; %Length of the metallization
r = ; %Radius of the perturbation
d = ; %Distance from the metallization to the perturbation
t = ; %Thickness of the substrate
a = ; %Length of the enclosure
b = ; %Height of the enclosure
p = ; %Pitch of the meander line
n = ; %Axial mode
m = ; %Transverse mode

Y1 = y;
B1 = t;
Y2 = b-y;
B2 = b-t;

k11m = (2*m-1)*pi/(a/2-w/2);
X11 = x;
k13m = (2*m-1)*pi/(a/2-w/2);
X13 = a-x;
k21m = (2*m-1)*pi/(a/2-l/2);
X21 = x;
k23m = (2*m-1)*pi/(a/2-w/2);
X23 = a-x;
k31m = (2*m-1)*pi/(a/2-l/2);
X31 = x;
k33m = (2*m-1)*pi/(a/2+l/2-w);
X33 = a-x;
k41m = (2*m-1)*pi/(a/2-l/2);
X41 = x;
k43m = (2*m-1)*pi/(a/2-l/2);
X43 = a-x;
k51m = (2*m-1)*pi/(a/2+l/2-w);
X51 = x;
k53m = (2*m-1)*pi/(a/2-l/2);
X53 = a-x;
k61m = (2*m-1)*pi/(a/2-w/2);
X61 = x;
k63m = (2*m-1)*pi/(a/2-l/2);
X63 = a-x;

f = ; %Frequency
omega = 2*pi*f; %Angular frequency

mu0 = ; %Vacuum permeability
epsilon0 = ; %Vacuum permittivity
epsilon1 = ; %Permittivity substrate
epsilon2 = ; %Permittivity medium
epsilonop = ; %Permittivity perturbation

```

```

betan = ; %Propagation constant
Deltabetan = ; %Propagation constant shift
betapn = Deltabetan + betan;

alpha111mn = sqrt(k11m^2 + betan.^2 - omega.^2*mu0*epsilon1*epsilon0);
alpha211mn = sqrt(k11m^2 + betan.^2 - omega.^2*mu0*epsilon2*epsilon0);
alpha113mn = sqrt(k13m^2 + betan.^2 - omega.^2*mu0*epsilon1*epsilon0);
alpha213mn = sqrt(k13m^2 + betan.^2 - omega.^2*mu0*epsilon2*epsilon0);
alpha121mn = sqrt(k21m^2 + betan.^2 - omega.^2*mu0*epsilon1*epsilon0);
alpha221mn = sqrt(k21m^2 + betan.^2 - omega.^2*mu0*epsilon2*epsilon0);
alpha123mn = sqrt(k23m^2 + betan.^2 - omega.^2*mu0*epsilon1*epsilon0);
alpha223mn = sqrt(k23m^2 + betan.^2 - omega.^2*mu0*epsilon2*epsilon0);
alpha131mn = sqrt(k31m^2 + betan.^2 - omega.^2*mu0*epsilon1*epsilon0);
alpha231mn = sqrt(k31m^2 + betan.^2 - omega.^2*mu0*epsilon2*epsilon0);
alpha133mn = sqrt(k33m^2 + betan.^2 - omega.^2*mu0*epsilon1*epsilon0);
alpha233mn = sqrt(k33m^2 + betan.^2 - omega.^2*mu0*epsilon2*epsilon0);
alpha141mn = sqrt(k41m^2 + betan.^2 - omega.^2*mu0*epsilon1*epsilon0);
alpha241mn = sqrt(k41m^2 + betan.^2 - omega.^2*mu0*epsilon2*epsilon0);
alpha143mn = sqrt(k43m^2 + betan.^2 - omega.^2*mu0*epsilon1*epsilon0);
alpha243mn = sqrt(k43m^2 + betan.^2 - omega.^2*mu0*epsilon2*epsilon0);
alpha151mn = sqrt(k51m^2 + betan.^2 - omega.^2*mu0*epsilon1*epsilon0);
alpha251mn = sqrt(k51m^2 + betan.^2 - omega.^2*mu0*epsilon2*epsilon0);
alpha153mn = sqrt(k53m^2 + betan.^2 - omega.^2*mu0*epsilon1*epsilon0);
alpha253mn = sqrt(k53m^2 + betan.^2 - omega.^2*mu0*epsilon2*epsilon0);
alpha161mn = sqrt(k61m^2 + betan.^2 - omega.^2*mu0*epsilon1*epsilon0);
alpha261mn = sqrt(k61m^2 + betan.^2 - omega.^2*mu0*epsilon2*epsilon0);
alpha163mn = sqrt(k63m^2 + betan.^2 - omega.^2*mu0*epsilon1*epsilon0);
alpha263mn = sqrt(k63m^2 + betan.^2 - omega.^2*mu0*epsilon2*epsilon0);

alphap11mn = sqrt(k11m^2 + betapn.^2 - omega.^2*mu0*epsilonpn*epsilon0);
alphap13mn = sqrt(k13m^2 + betapn.^2 - omega.^2*mu0*epsilonpn*epsilon0);
alphap21mn = sqrt(k21m^2 + betapn.^2 - omega.^2*mu0*epsilonpn*epsilon0);
alphap23mn = sqrt(k23m^2 + betapn.^2 - omega.^2*mu0*epsilonpn*epsilon0);
alphap31mn = sqrt(k31m^2 + betapn.^2 - omega.^2*mu0*epsilonpn*epsilon0);
alphap33mn = sqrt(k33m^2 + betapn.^2 - omega.^2*mu0*epsilonpn*epsilon0);
alphap41mn = sqrt(k41m^2 + betapn.^2 - omega.^2*mu0*epsilonpn*epsilon0);
alphap43mn = sqrt(k43m^2 + betapn.^2 - omega.^2*mu0*epsilonpn*epsilon0);
alphap51mn = sqrt(k51m^2 + betapn.^2 - omega.^2*mu0*epsilonpn*epsilon0);
alphap53mn = sqrt(k53m^2 + betapn.^2 - omega.^2*mu0*epsilonpn*epsilon0);
alphap61mn = sqrt(k61m^2 + betapn.^2 - omega.^2*mu0*epsilonpn*epsilon0);
alphap63mn = sqrt(k63m^2 + betapn.^2 - omega.^2*mu0*epsilonpn*epsilon0);

%Integral 11x
I11xiny = int(sinh(alphap11mn.*Y2).*sinh(alpha211mn.*Y2),y,t+d+r-sqrt(r^2-(x-
a/2)^2),t+d+r+sqrt(r^2-(x-a/2)^2));

I11xinx = vpa(int(I11xiny.*cos(k11m*X11).^2,x,a/2-r,a/2+r),4);

%Integral 11y
I11yiny = int(cosh(alphap11mn.*Y2).*cosh(alpha211mn.*Y2),y,t+d+r-sqrt(r^2-(x-
a/2)^2),t+d+r+sqrt(r^2-(x-a/2)^2));

I11yinx = vpa(int(I11yiny.*sin(k11m*X11).^2,x,a/2-r,a/2+r),4);

```

```

%Integral 11z
I11ziny = int(sinh(alphap11mn.*Y2).*sinh(alpha211mn.*Y2),y,t+d+r-sqrt(r^2-(x-
a/2)^2),t+d+r+sqrt(r^2-(x-a/2)^2));

I11zinx = vpa(int(I11ziny.*sin(k11m*X11).^2,x,a/2-r,a/2+r),4);

%Integral 13x
I13xiny = int(sinh(alphap13mn.*Y2).*sinh(alpha213mn.*Y2),y,t+d+r-sqrt(r^2-(x-
a/2)^2),t+d+r+sqrt(r^2-(x-a/2)^2));

I13xinx = vpa(int(I13xiny.*cos(k13m*X13).^2,x,a/2-r,a/2+r),4);

%Integral 13y
I13yiny = int(cosh(alphap13mn.*Y2).*cosh(alpha213mn.*Y2),y,t+d+r-sqrt(r^2-(x-
a/2)^2),t+d+r+sqrt(r^2-(x-a/2)^2));

I13yinx = vpa(int(I13yiny.*sin(k13m*X13).^2,x,a/2-r,a/2+r),4);

%Integral 13z
I13ziny = int(sinh(alphap13mn.*Y2).*sinh(alpha213mn.*Y2),y,t+d+r-sqrt(r^2-(x-
a/2)^2),t+d+r+sqrt(r^2-(x-a/2)^2));

I13zinx = vpa(int(I13ziny.*sin(k13m*X13).^2,x,a/2-r,a/2+r),4);

%Integral 23x
I23xiny = int(sinh(alphap23mn.*Y2).*sinh(alpha223mn.*Y2),y,t+d+r-sqrt(r^2-(x-
a/2)^2),t+d+r+sqrt(r^2-(x-a/2)^2));

I23xinx = vpa(int(I23xiny.*cos(k23m*X23).^2,x,a/2-r,a/2+r),4);

%Integral 23y
I23yiny = int(cosh(alphap23mn.*Y2).*cosh(alpha223mn.*Y2),y,t+d+r-sqrt(r^2-(x-
a/2)^2),t+d+r+sqrt(r^2-(x-a/2)^2));

I23yinx = vpa(int(I23yiny.*sin(k23m*X23).^2,x,a/2-r,a/2+r),4);

%Integral 23z
I23ziny = int(sinh(alphap23mn.*Y2).*sinh(alpha223mn.*Y2),y,t+d+r-sqrt(r^2-(x-
a/2)^2),t+d+r+sqrt(r^2-(x-a/2)^2));

I23zinx = vpa(int(I23ziny.*sin(k23m*X23).^2,x,a/2-r,a/2+r),4);

%Integral 33x
I33xiny = int(sinh(alphap33mn.*Y2).*sinh(alpha233mn.*Y2),y,t+d+r-sqrt(r^2-(x-
a/2)^2),t+d+r+sqrt(r^2-(x-a/2)^2));

I33xinx = vpa(int(I33xiny.*cos(k33m*X33).^2,x,a/2-r,a/2+r),4);

%Integral 33y
I33yiny = int(cosh(alphap33mn.*Y2).*cosh(alpha233mn.*Y2),y,t+d+r-sqrt(r^2-(x-
a/2)^2),t+d+r+sqrt(r^2-(x-a/2)^2));

I33yinx = vpa(int(I33yiny.*sin(k33m*X33).^2,x,a/2-r,a/2+r),4);

```

```

%Integral 33z
I33ziny = int(sinh(alphap33mn.*Y2).*sinh(alpha233mn.*Y2),y,t+d+r-sqrt(r^2-(x-
a/2)^2),t+d+r+sqrt(r^2-(x-a/2)^2));

I33zinx = vpa(int(I33ziny.*sin(k33m*X33).^2,x,a/2-r,a/2+r),4);

%Integral 51x
I51xiny = int(sinh(alphap51mn.*Y2).*sinh(alpha251mn.*Y2),y,t+d+r-sqrt(r^2-(x-
a/2)^2),t+d+r+sqrt(r^2-(x-a/2)^2));

I51xinx = vpa(int(I51xiny.*cos(k51m*X51).^2,x,a/2-r,a/2+r),4);

%Integral 51y
I51yiny = int(cosh(alphap51mn.*Y2).*cosh(alpha251mn.*Y2),y,t+d+r-sqrt(r^2-(x-
a/2)^2),t+d+r+sqrt(r^2-(x-a/2)^2));

I51yinx = vpa(int(I51yiny.*sin(k51m*X51).^2,x,a/2-r,a/2+r),4);

%Integral 51z
I51ziny = int(sinh(alphap51mn.*Y2).*sinh(alpha251mn.*Y2),y,t+d+r-sqrt(r^2-(x-
a/2)^2),t+d+r+sqrt(r^2-(x-a/2)^2));

I51zinx = vpa(int(I51ziny.*sin(k51m*X51).^2,x,a/2-r,a/2+r),4);

%Integral 61x
I61xiny = int(sinh(alphap61mn.*Y2).*sinh(alpha261mn.*Y2),y,t+d+r-sqrt(r^2-(x-
a/2)^2),t+d+r+sqrt(r^2-(x-a/2)^2));

I61xinx = vpa(int(I61xiny.*cos(k61m*X61).^2,x,a/2-r,a/2+r),4);

%Integral 61y
I61yiny = int(cosh(alphap61mn.*Y2).*cosh(alpha261mn.*Y2),y,t+d+r-sqrt(r^2-(x-
a/2)^2),t+d+r+sqrt(r^2-(x-a/2)^2));

I61yinx = vpa(int(I61yiny.*sin(k61m*X61).^2,x,a/2-r,a/2+r),4);

%Integral 61z
I61ziny = int(sinh(alphap61mn.*Y2).*sinh(alpha261mn.*Y2),y,t+d+r-sqrt(r^2-(x-
a/2)^2),t+d+r+sqrt(r^2-(x-a/2)^2));

I61zinx = vpa(int(I61ziny.*sin(k61m*X61).^2,x,a/2-r,a/2+r),4);

%Point of calculation of K
x0 = ;
y0 = ;
X110 = x0;
X130 = a-x0;
X210 = x0;
X230 = a-x0;
X310 = x0;
X330 = a-x0;
X410 = x0;
X430 = a-x0;

```

```

X510 = x0;
X530 = a-x0;
X610 = x0;
X630 = a-x0;
Y10 = y0;
Y20 = b-y0;

%Point of first interface condition perturbation-surrounding medium
x1 = ;
y1 = ;
X111 = x1;
X131 = a-x1;
X211 = x1;
X231 = a-x1;
X311 = x1;
X331 = a-x1;
X411 = x1;
X431 = a-x1;
X511 = x1;
X531 = a-x1;
X611 = x1;
X631 = a-x1;
Y11 = y1;
Y21 = b-y1;

%Point of second interface condition substrate-surrounding medium
y2 = ;
Y12 = y2;
Y22 = b-y2;

%Coefficient 11x
brack11 = -1 + (k11m^2*omega.^2*mu0*(epsilon2-
epsilon1)*epsilon0)/(alpha211mn.^2.*(betan.^2-
omega.^2*mu0*epsilon1*epsilon0).*(1+(alpha111mn.*(betan.^2-
omega.^2*mu0*epsilon2*epsilon0).*tanh(alpha111mn*Y12))/(alpha211mn.*(betan.^
2-omega.^2*mu0*epsilon1*epsilon0).*tanh(alpha211mn*Y22))));

G11x = ((k11m^2*betan.*betapn.*(1-
alphap11mn.^2/(k11m^2)).*sinh(alpha211mn*Y21))/(betapn.^2-
omega.^2*mu0*epsilonp*epsilon0).*(betan.^2-
omega.^2*mu0*epsilon2*epsilon0).*sinh(alpha211mn*Y22).^2.*sinh(alphap11mn*Y21
))-
(epsilon2*epsilon0*betan.^2.*alpha211mn.*alphap11mn.*cosh(alpha211mn*Y21)).*b
rack11./(epsilonp*epsilon0*(betan.^2-
omega.^2*mu0*epsilon2*epsilon0).^2.*sinh(alpha211mn*Y22).^2.*cosh(alphap11mn*
Y21)).*brack11.*sinh(alpha211mn*Y22).^2./(sinh(alpha211mn.*Y20).^2*sin(k11m.
*X110).^2);

%Coefficient 11y
G11y =
(epsilon2*epsilon0*alpha211mn.^2.*betan.^2.*cosh(alpha211mn*Y21).*brack11.^2)
./(epsilonp*epsilon0*(betan.^2-
omega.^2*mu0*epsilon2*epsilon0).^2.*cosh(alphap11mn*Y21).*sinh(alpha211mn.*Y2
0).^2.*sin(k11m.*X110).^2);

%Coefficient 11z

```

```
G11z =
sinh(alpha211mn*Y21) ./ (sinh(alpha211mn.*Y20).^2.*sinh(alphap11mn*Y21).*sin(k1
1m.*X110).^2);
```

```
%Coefficient 13x
```

```
brack13 = -1 + (k13m^2*omega.^2*mu0*(epsilon2-
epsilon1)*epsilon0) ./ (alpha213mn.^2.*(betan.^2-
omega.^2*mu0*epsilon1*epsilon0).*(1+(alpha113mn.*(betan.^2-
omega.^2*mu0*epsilon2*epsilon0).*tanh(alpha113mn*Y12)) ./ (alpha213mn.*(betan.^
2-omega.^2*mu0*epsilon1*epsilon0).*tanh(alpha213mn*Y22))));
```

```
G13x = ((k13m^2*betan.*betapn.*(1-
alphap13mn.^2/(k13m^2)).*sinh(alpha213mn*Y21)) ./ ((betapn.^2-
omega.^2*mu0*epsilonp*epsilon0).*(betan.^2-
omega.^2*mu0*epsilon2*epsilon0).*sinh(alpha213mn*Y22).^2.*sinh(alphap13mn*Y21
))-
(epsilon2*epsilon0*betan.^2.*alpha213mn.*alphap13mn.*cosh(alpha213mn*Y21)).*b
rack13 ./ (epsilonp*epsilon0*(betan.^2-
omega.^2*mu0*epsilon2*epsilon0).^2.*sinh(alpha213mn*Y22).^2.*cosh(alphap13mn*
Y21))).*brack13.*sinh(alpha213mn*Y22).^2 ./ (sinh(alpha213mn.*Y20).^2.*sin(k13m.
*X130).^2);
```

```
%Coefficient 13y
```

```
G13y =
(epsilon2*epsilon0*alpha213mn.^2.*betan.^2.*cosh(alpha213mn*Y21).*brack13.^2)
./ (epsilonp*epsilon0*(betan.^2-
omega.^2*mu0*epsilon2*epsilon0).^2.*cosh(alphap13mn*Y21).*sinh(alpha213mn.*Y2
0).^2.*sin(k13m.*X130).^2);
```

```
%Coefficient 13z
```

```
G13z =
sinh(alpha213mn*Y21) ./ (sinh(alpha213mn.*Y20).^2.*sinh(alphap13mn*Y21).*sin(k1
3m.*X130).^2);
```

```
%Coefficient 23x
```

```
brack23 = -1 + (k23m^2*omega.^2*mu0*(epsilon2-
epsilon1)*epsilon0) ./ (alpha223mn.^2.*(betan.^2-
omega.^2*mu0*epsilon1*epsilon0).*(1+(alpha123mn.*(betan.^2-
omega.^2*mu0*epsilon2*epsilon0).*tanh(alpha123mn*Y12)) ./ (alpha223mn.*(betan.^
2-omega.^2*mu0*epsilon1*epsilon0).*tanh(alpha223mn*Y22))));
```

```
G23x = ((k23m^2*betan.*betapn.*(1-
alphap23mn.^2/(k23m^2)).*sinh(alpha223mn*Y21)) ./ ((betapn.^2-
omega.^2*mu0*epsilonp*epsilon0).*(betan.^2-
omega.^2*mu0*epsilon2*epsilon0).*sinh(alpha223mn*Y22).^2.*sinh(alphap23mn*Y21
))-
(epsilon2*epsilon0*betan.^2.*alpha223mn.*alphap23mn.*cosh(alpha223mn*Y21)).*b
rack23 ./ (epsilonp*epsilon0*(betan.^2-
omega.^2*mu0*epsilon2*epsilon0).^2.*sinh(alpha223mn*Y22).^2.*cosh(alphap23mn*
Y21))).*brack23.*sinh(alpha223mn*Y22).^2 ./ (sinh(alpha223mn.*Y20).^2.*sin(k23m.
*X230).^2);
```

```
%Coefficient 23y
```

```
G23y =
(epsilon2*epsilon0*alpha223mn.^2.*betan.^2.*cosh(alpha223mn*Y21).*brack23.^2)
```

```
./ (epsilonp*epsilon0*(betan.^2-
omega.^2*mu0*epsilon2*epsilon0).^2.*cosh(alphap23mn*Y21).*sinh(alpha223mn.*Y2
0).^2.*sin(k23m.*X230).^2);
```

```
%Coefficient 23z
```

```
G23z =
sinh(alpha223mn*Y21) ./ (sinh(alpha223mn.*Y20).^2.*sinh(alphap23mn*Y21).*sin(k2
3m.*X230).^2);
```

```
%Coefficient 33x
```

```
brack33 = -1 + (k33m^2*omega.^2*mu0*(epsilon2-
epsilon1)*epsilon0) ./ (alpha233mn.^2.*(betan.^2-
omega.^2*mu0*epsilon1*epsilon0).* (1+(alpha133mn.*(betan.^2-
omega.^2*mu0*epsilon2*epsilon0).*tanh(alpha133mn*Y12)) ./ (alpha233mn.*(betan.^
2-omega.^2*mu0*epsilon1*epsilon0).*tanh(alpha233mn*Y22))));
```

```
G33x = ((k33m^2*betan.*betapn.*(1-
alphap33mn.^2/(k33m^2)).*sinh(alpha233mn*Y21)) ./ ((betapn.^2-
omega.^2*mu0*epsilonp*epsilon0).(betan.^2-
omega.^2*mu0*epsilon2*epsilon0).*sinh(alpha233mn*Y22).^2.*sinh(alphap33mn*Y21
))-
(epsilon2*epsilon0*betan.^2.*alpha233mn.*alphap33mn.*cosh(alpha233mn*Y21)).*b
rack33 ./ (epsilonp*epsilon0*(betan.^2-
omega.^2*mu0*epsilon2*epsilon0).^2.*sinh(alpha233mn*Y22).^2.*cosh(alphap33mn*
Y21)).*brack33.*sinh(alpha233mn*Y22).^2 ./ (sinh(alpha233mn.*Y20).^2.*sin(k33m.
*X330).^2);
```

```
%Coefficient 33y
```

```
G33y =
(epsilon2*epsilon0*alpha233mn.^2.*betan.^2.*cosh(alpha233mn*Y21).*brack33.^2)
./ (epsilonp*epsilon0*(betan.^2-
omega.^2*mu0*epsilon2*epsilon0).^2.*cosh(alphap33mn*Y21).*sinh(alpha233mn.*Y2
0).^2.*sin(k33m.*X330).^2);
```

```
%Coefficient 33z
```

```
G33z =
sinh(alpha233mn*Y21) ./ (sinh(alpha233mn.*Y20).^2.*sinh(alphap33mn*Y21).*sin(k3
3m.*X330).^2);
```

```
%Coefficient 51x
```

```
brack51 = -1 + (k51m^2*omega.^2*mu0*(epsilon2-
epsilon1)*epsilon0) ./ (alpha251mn.^2.*(betan.^2-
omega.^2*mu0*epsilon1*epsilon0).* (1+(alpha151mn.*(betan.^2-
omega.^2*mu0*epsilon2*epsilon0).*tanh(alpha151mn*Y12)) ./ (alpha251mn.*(betan.^
2-omega.^2*mu0*epsilon1*epsilon0).*tanh(alpha251mn*Y22))));
```

```
G51x = ((k51m^2*betan.*betapn.*(1-
alphap51mn.^2/(k51m^2)).*sinh(alpha251mn*Y21)) ./ ((betapn.^2-
omega.^2*mu0*epsilonp*epsilon0).(betan.^2-
omega.^2*mu0*epsilon2*epsilon0).*sinh(alpha251mn*Y22).^2.*sinh(alphap51mn*Y21
))-
(epsilon2*epsilon0*betan.^2.*alpha251mn.*alphap51mn.*cosh(alpha251mn*Y21)).*b
rack51 ./ (epsilonp*epsilon0*(betan.^2-
omega.^2*mu0*epsilon2*epsilon0).^2.*sinh(alpha251mn*Y22).^2.*cosh(alphap51mn*
```

```

Y21)) .* brack51 .* sinh(alpha251mn*Y22).^2 ./ (sinh(alpha251mn.*Y20).^2 * sin(k51m.*X510).^2);

%Coefficient 51y
G51y =
(epsilon2*epsilon0*alpha251mn.^2.*betan.^2.*cosh(alpha251mn*Y21).*brack51.^2)
./ (epsilonp*epsilon0*(betan.^2-
omega.^2*mu0*epsilon2*epsilon0).^2.*cosh(alphap51mn*Y21).*sinh(alpha251mn.*Y2
0).^2.*sin(k51m.*X510).^2);

%Coefficient 51z
G51z =
sinh(alpha251mn*Y21) ./ (sinh(alpha251mn.*Y20).^2.*sinh(alphap51mn*Y21).*sin(k5
1m.*X510).^2);

%Coefficient 61x
brack61 = -1 + (k61m^2*omega.^2*mu0*(epsilon2-
epsilon1)*epsilon0) ./ (alpha261mn.^2.*(betan.^2-
omega.^2*mu0*epsilon1*epsilon0).*(1+(alpha61mn.*(betan.^2-
omega.^2*mu0*epsilon2*epsilon0).*tanh(alpha61mn*Y12)) ./ (alpha261mn.*(betan.^
2-omega.^2*mu0*epsilon1*epsilon0).*tanh(alpha261mn*Y22))));

G61x = ((k61m^2*betan.*betapn.*(1-
alphap61mn.^2/(k61m^2)).*sinh(alpha261mn*Y21)) ./ ((betapn.^2-
omega.^2*mu0*epsilonp*epsilon0).*(betan.^2-
omega.^2*mu0*epsilon2*epsilon0).*sinh(alpha261mn*Y22).^2.*sinh(alphap61mn*Y21
))-
(epsilon2*epsilon0*betan.^2.*alpha261mn.*alphap61mn.*cosh(alpha261mn*Y21)).*b
rack61 ./ (epsilonp*epsilon0*(betan.^2-
omega.^2*mu0*epsilon2*epsilon0).^2.*sinh(alpha261mn*Y22).^2.*cosh(alphap61mn*
Y21))).*brack61.*sinh(alpha261mn*Y22).^2 ./ (sinh(alpha261mn.*Y20).^2 * sin(k61m.*X610).^2);

%Coefficient 61y
G61y =
(epsilon2*epsilon0*alpha261mn.^2.*betan.^2.*cosh(alpha261mn*Y21).*brack61.^2)
./ (epsilonp*epsilon0*(betan.^2-
omega.^2*mu0*epsilon2*epsilon0).^2.*cosh(alphap61mn*Y21).*sinh(alpha261mn.*Y2
0).^2.*sin(k61m.*X610).^2);

%Coefficient 61z
G61z =
sinh(alpha261mn*Y21) ./ (sinh(alpha261mn.*Y20).^2.*sinh(alphap61mn*Y21).*sin(k6
1m.*X610).^2);

%Full term 11x
T11x = s*G11x.*I11xinx;

%Full term 11y
T11y = s*G11y.*I11yinx;

%Full term 11z
T11z = s*G11z.*I11zinx;

%Full term 13x

```

```

T13x = s*G13x.*I13xinx;

%Full term 13y
T13y = s*G13y.*I13yinx;

%Full term 13z
T13z = s*G13z.*I13zinx;

%Full term 23x
T23x = w*G23x.*I23xinx;

%Full term 23y
T23y = w*G23y.*I23yinx;

%Full term 23z
T23z = w*G23z.*I23zinx;

%Full term 33x
T33x = s*G33x.*I33xinx;

%Full term 33y
T33y = s*G33y.*I33yinx;

%Full term 33z
T33z = s*G33z.*I33zinx;

%Full term 51x
T51x = s*G51x.*I51xinx;

%Full term 51y
T51y = s*G51y.*I51yinx;

%Full term 51z
T51z = s*G51z.*I51zinx;

%Full term 61x
T61x = w*G61x.*I61xinx;

%Full term 61y
T61y = w*G61y.*I61yinx;

%Full term 61z
T61z = w*G61z.*I61zinx;

%Sum of terms
I = T11x + T11y + T11z + T13x + T13y + T13z + T23x + T23y + T23z + T33x +
T33y + T33z + T51x + T51y + T51z + T61x + T61y + T61z;

%Interaction impedance
KNML1 = 2*p*Deltabetan./((epsilonp-epsilon2)*epsilon0*omega.*betan.^2.*I);

```

```

%NML2

%Variable definition
syms x;
syms y;

s = ; %Space between two consecutive metal strips
w = ; %Width of the metallization
l = ; %Length of the metallization
r = ; %Radius of the perturbation
d = ; %Distance from the metallization to the perturbation
t = ; %Thickness of the substrate
a = ; %Length of the enclosure
b = ; %Height of the enclosure
p = ; %Pitch of the meander line
n = ; %Axial mode
m = ; %Transverse mode

Y1 = y;
B1 = t;
Y2 = b-y;
B2 = b-t;

k11m = (2*m-1)*pi/(a/2+l/2-2*w);
X11 = x;
k13m = (2*m-1)*pi/(a/2-l/2);
X13 = a-x;
k21m = (2*m-1)*pi/(a/2-l/2);
X21 = x;
k23m = (2*m-1)*pi/(a/2-l/2);
X23 = a-x;
k31m = (2*m-1)*pi/(a/2-l/2);
X31 = x;
k33m = (2*m-1)*pi/(a/2-l/2);
X33 = a-x;
k34m = (2*m-1)*pi/(l-2*w);
X34 = a/2+l/2-w-x;
k51m = (2*m-1)*pi/(a/2-l/2);
X51 = x;
k53m = (2*m-1)*pi/(a/2+l/2-2*w);
X53 = a-x;

f = ; %Frequency
omega = 2*pi*f; %Angular frequency

mu0 = ; %Vacuum permeability
epsilon0 = ; %Vacuum permittivity
epsilon1 = ; %Permittivity substrate
epsilon2 = ; %Permittivity medium
epsilonop = ; %Permittivity perturbation

betan = ; %Propagation constant
Deltabetan = ; %Propagation constant shift
betapn = Deltabetan + betan;

```

```

alpha111mn = sqrt(k11m^2 + betan.^2 - omega.^2*mu0*epsilon1*epsilon0);
alpha211mn = sqrt(k11m^2 + betan.^2 - omega.^2*mu0*epsilon2*epsilon0);
alpha113mn = sqrt(k13m^2 + betan.^2 - omega.^2*mu0*epsilon1*epsilon0);
alpha213mn = sqrt(k13m^2 + betan.^2 - omega.^2*mu0*epsilon2*epsilon0);
alpha121mn = sqrt(k21m^2 + betan.^2 - omega.^2*mu0*epsilon1*epsilon0);
alpha221mn = sqrt(k21m^2 + betan.^2 - omega.^2*mu0*epsilon2*epsilon0);
alpha123mn = sqrt(k23m^2 + betan.^2 - omega.^2*mu0*epsilon1*epsilon0);
alpha223mn = sqrt(k23m^2 + betan.^2 - omega.^2*mu0*epsilon2*epsilon0);
alpha131mn = sqrt(k31m^2 + betan.^2 - omega.^2*mu0*epsilon1*epsilon0);
alpha231mn = sqrt(k31m^2 + betan.^2 - omega.^2*mu0*epsilon2*epsilon0);
alpha133mn = sqrt(k33m^2 + betan.^2 - omega.^2*mu0*epsilon1*epsilon0);
alpha233mn = sqrt(k33m^2 + betan.^2 - omega.^2*mu0*epsilon2*epsilon0);
alpha134mn = sqrt(k34m^2 + betan.^2 - omega.^2*mu0*epsilon1*epsilon0);
alpha234mn = sqrt(k34m^2 + betan.^2 - omega.^2*mu0*epsilon2*epsilon0);
alpha151mn = sqrt(k51m^2 + betan.^2 - omega.^2*mu0*epsilon1*epsilon0);
alpha251mn = sqrt(k51m^2 + betan.^2 - omega.^2*mu0*epsilon2*epsilon0);
alpha153mn = sqrt(k53m^2 + betan.^2 - omega.^2*mu0*epsilon1*epsilon0);
alpha253mn = sqrt(k53m^2 + betan.^2 - omega.^2*mu0*epsilon2*epsilon0);

alphap11mn = sqrt(k11m^2 + betapn.^2 - omega.^2*mu0*epsilonpn*epsilon0);
alphap13mn = sqrt(k13m^2 + betapn.^2 - omega.^2*mu0*epsilonpn*epsilon0);
alphap21mn = sqrt(k21m^2 + betapn.^2 - omega.^2*mu0*epsilonpn*epsilon0);
alphap23mn = sqrt(k23m^2 + betapn.^2 - omega.^2*mu0*epsilonpn*epsilon0);
alphap31mn = sqrt(k31m^2 + betapn.^2 - omega.^2*mu0*epsilonpn*epsilon0);
alphap33mn = sqrt(k33m^2 + betapn.^2 - omega.^2*mu0*epsilonpn*epsilon0);
alphap34mn = sqrt(k34m^2 + betapn.^2 - omega.^2*mu0*epsilonpn*epsilon0);
alphap51mn = sqrt(k51m^2 + betapn.^2 - omega.^2*mu0*epsilonpn*epsilon0);
alphap53mn = sqrt(k53m^2 + betapn.^2 - omega.^2*mu0*epsilonpn*epsilon0);

%Integral 11x
I11xiny = int(sinh(alphap11mn.*Y2).*sinh(alpha211mn.*Y2),y,t+d+r-sqrt(r^2-(x-
a/2)^2),t+d+r+sqrt(r^2-(x-a/2)^2));

I11xinx = vpa(int(I11xiny.*cos(k11m*X11).^2,x,a/2-r,a/2+r),4);

%Integral 11y
I11yiny = int(cosh(alphap11mn.*Y2).*cosh(alpha211mn.*Y2),y,t+d+r-sqrt(r^2-(x-
a/2)^2),t+d+r+sqrt(r^2-(x-a/2)^2));

I11yinx = vpa(int(I11yiny.*sin(k11m*X11).^2,x,a/2-r,a/2+r),4);

%Integral 11z
I11ziny = int(sinh(alphap11mn.*Y2).*sinh(alpha211mn.*Y2),y,t+d+r-sqrt(r^2-(x-
a/2)^2),t+d+r+sqrt(r^2-(x-a/2)^2));

I11zinx = vpa(int(I11ziny.*sin(k11m*X11).^2,x,a/2-r,a/2+r),4);

%Integral 34x
I34xiny = int(sinh(alphap34mn.*Y2).*sinh(alpha234mn.*Y2),y,t+d+r-sqrt(r^2-(x-
a/2)^2),t+d+r+sqrt(r^2-(x-a/2)^2));

I34xinx = vpa(int(I34xiny.*cos(k34m*X34).^2,x,a/2-r,a/2+r),4);

%Integral 34y

```

```

I34yiny = int(cosh(alphap34mn.*Y2).*cosh(alpha234mn.*Y2),y,t+d+r-sqrt(r^2-(x-
a/2)^2),t+d+r+sqrt(r^2-(x-a/2)^2));

I34yinx = vpa(int(I34yiny.*sin(k34m*X34).^2,x,a/2-r,a/2+r),4);

%Integral 34z
I34ziny = int(sinh(alphap34mn.*Y2).*sinh(alpha234mn.*Y2),y,t+d+r-sqrt(r^2-(x-
a/2)^2),t+d+r+sqrt(r^2-(x-a/2)^2));

I34zinx = vpa(int(I34ziny.*sin(k34m*X34).^2,x,a/2-r,a/2+r),4);

%Integral 53x
I53xiny = int(sinh(alphap53mn.*Y2).*sinh(alpha253mn.*Y2),y,t+d+r-sqrt(r^2-(x-
a/2)^2),t+d+r+sqrt(r^2-(x-a/2)^2));

I53xinx = vpa(int(I53xiny.*cos(k53m*X53).^2,x,a/2-r,a/2+r),4);

%Integral 53y
I53yiny = int(cosh(alphap53mn.*Y2).*cosh(alpha253mn.*Y2),y,t+d+r-sqrt(r^2-(x-
a/2)^2),t+d+r+sqrt(r^2-(x-a/2)^2));

I53yinx = vpa(int(I53yiny.*sin(k53m*X53).^2,x,a/2-r,a/2+r),4);

%Integral 53z
I53ziny = int(sinh(alphap53mn.*Y2).*sinh(alpha253mn.*Y2),y,t+d+r-sqrt(r^2-(x-
a/2)^2),t+d+r+sqrt(r^2-(x-a/2)^2));

I53zinx = vpa(int(I53ziny.*sin(k53m*X53).^2,x,a/2-r,a/2+r),4);

%Point of calculation of K
x0 = ;
y0 = ;
X110 = x0;
X130 = a-x0;
X210 = x0;
X230 = a-x0;
X310 = x0;
X330 = a-x0;
X340 = a/2+1/2-w-x0;
X510 = x0;
X530 = a-x0;
Y10 = y0;
Y20 = b-y0;

%Point of first interface condition perturbation-surrounding medium
x1 = ;
y1 = ;
X111 = x1;
X131 = a-x1;
X211 = x1;
X231 = a-x1;
X311 = x1;
X331 = a-x1;
X341 = a/2+1/2-w-x1;
X511 = x1;

```

```

X531 = a-x1;
Y11 = y1;
Y21 = b-y1;

%Point of second interface condition substrate-surrounding medium
y2 = ;
Y12 = y2;
Y22 = b-y2;

%Coefficient 11x
brack11 = -1 + (k11m^2*omega.^2*mu0*(epsilon2-
epsilon1)*epsilon0)/(alpha211mn.^2.*(betan.^2-
omega.^2*mu0*epsilon1*epsilon0).*(1+(alpha111mn.*(betan.^2-
omega.^2*mu0*epsilon2*epsilon0).*tanh(alpha111mn*Y12)))/(alpha211mn.*(betan.^
2-omega.^2*mu0*epsilon1*epsilon0).*tanh(alpha211mn*Y22))));

G11x = ((k11m^2*betan.*betapn.*(1-
alphap11mn.^2/(k11m^2)).*sinh(alpha211mn*Y21))/(betapn.^2-
omega.^2*mu0*epsilonp*epsilon0).*(betan.^2-
omega.^2*mu0*epsilon2*epsilon0).*sinh(alpha211mn*Y22).^2.*sinh(alphap11mn*Y21
))-
(epsilon2*epsilon0*betan.^2.*alpha211mn.*alphap11mn.*cosh(alpha211mn*Y21)).*b
rack11./(epsilonp*epsilon0*(betan.^2-
omega.^2*mu0*epsilon2*epsilon0).^2.*sinh(alpha211mn*Y22).^2.*cosh(alphap11mn*
Y21)).*brack11.*sinh(alpha211mn*Y22).^2./(sinh(alpha211mn.*Y20).^2*sin(k11m.
*X110).^2);

%Coefficient 11y
G11y =
(epsilon2*epsilon0*alpha211mn.^2.*betan.^2.*cosh(alpha211mn*Y21).*brack11.^2)
./(epsilonp*epsilon0*(betan.^2-
omega.^2*mu0*epsilon2*epsilon0).^2.*cosh(alphap11mn*Y21).*sinh(alpha211mn.*Y2
0).^2.*sin(k11m.*X110).^2);

%Coefficient 11z
G11z =
sinh(alpha211mn*Y21)/(sinh(alpha211mn.*Y20).^2.*sinh(alphap11mn*Y21)).*sin(k1
1m.*X110).^2);

%Coefficient 34x
brack34 = -1 + (k34m^2*omega.^2*mu0*(epsilon2-
epsilon1)*epsilon0)/(alpha234mn.^2.*(betan.^2-
omega.^2*mu0*epsilon1*epsilon0).*(1+(alpha134mn.*(betan.^2-
omega.^2*mu0*epsilon2*epsilon0).*tanh(alpha134mn*Y12)))/(alpha234mn.*(betan.^
2-omega.^2*mu0*epsilon1*epsilon0).*tanh(alpha234mn*Y22))));

G34x = ((k34m^2*betan.*betapn.*(1-
alphap34mn.^2/(k34m^2)).*sinh(alpha234mn*Y21))/(betapn.^2-
omega.^2*mu0*epsilonp*epsilon0).*(betan.^2-
omega.^2*mu0*epsilon2*epsilon0).*sinh(alpha234mn*Y22).^2.*sinh(alphap34mn*Y21
))-
(epsilon2*epsilon0*betan.^2.*alpha234mn.*alphap34mn.*cosh(alpha234mn*Y21)).*b
rack34./(epsilonp*epsilon0*(betan.^2-
omega.^2*mu0*epsilon2*epsilon0).^2.*sinh(alpha234mn*Y22).^2.*cosh(alphap34mn*

```

```

Y21)) .*brack34.*sinh(alpha234mn*Y22).^2./(sinh(alpha234mn.*Y20).^2*sin(k34m.*X340).^2);

%Coefficient 34y
G34y =
(epsilon2*epsilon0*alpha234mn.^2.*betan.^2.*cosh(alpha234mn*Y21).*brack34.^2)
./(epsilonp*epsilon0*(betan.^2-
omega.^2*mu0*epsilon2*epsilon0).^2.*cosh(alphap34mn*Y21).*sinh(alpha234mn.*Y2
0).^2.*sin(k34m.*X340).^2);

%Coefficient 34z
G34z =
sinh(alpha234mn*Y21)/(sinh(alpha234mn.*Y20).^2.*sinh(alphap34mn*Y21).*sin(k3
4m.*X340).^2);

%Coefficient 53x
brack53 = -1 + (k53m^2*omega.^2*mu0*(epsilon2-
epsilon1)*epsilon0)/(alpha253mn.^2.*(betan.^2-
omega.^2*mu0*epsilon1*epsilon0).*(1+(alpha153mn.*(betan.^2-
omega.^2*mu0*epsilon2*epsilon0).*tanh(alpha153mn*Y12))/(alpha253mn.*(betan.^
2-omega.^2*mu0*epsilon1*epsilon0).*tanh(alpha253mn*Y22))));

G53x = ((k53m^2*betan.*betapn.*(1-
alphap53mn.^2/(k53m^2)).*sinh(alpha253mn*Y21))/(betapn.^2-
omega.^2*mu0*epsilonp*epsilon0).*(betan.^2-
omega.^2*mu0*epsilon2*epsilon0).*sinh(alpha253mn*Y22).^2.*sinh(alphap53mn*Y21
))-
(epsilon2*epsilon0*betan.^2.*alpha253mn.*alphap53mn.*cosh(alpha253mn*Y21)).*b
rack53./(epsilonp*epsilon0*(betan.^2-
omega.^2*mu0*epsilon2*epsilon0).^2.*sinh(alpha253mn*Y22).^2.*cosh(alphap53mn*
Y21)).*brack53.*sinh(alpha253mn*Y22).^2./(sinh(alpha253mn.*Y20).^2*sin(k53m.*
X530).^2);

%Coefficient 53y
G53y =
(epsilon2*epsilon0*alpha253mn.^2.*betan.^2.*cosh(alpha253mn*Y21).*brack53.^2)
./(epsilonp*epsilon0*(betan.^2-
omega.^2*mu0*epsilon2*epsilon0).^2.*cosh(alphap53mn*Y21).*sinh(alpha253mn.*Y2
0).^2.*sin(k53m.*X530).^2);

%Coefficient 53z
G53z =
sinh(alpha253mn*Y21)/(sinh(alpha253mn.*Y20).^2.*sinh(alphap53mn*Y21).*sin(k5
3m.*X530).^2);

%Full term 11x
T11x = s*G11x.*I11xinx;

%Full term 11y
T11y = s*G11y.*I11yinx;

%Full term 11z
T11z = s*G11z.*I11zinx;

%Full term 34x

```

```

T34x = 2*s*G34x.*I34xinx;

%Full term 34y
T34y = 2*s*G34y.*I34yinx;

%Full term 34z
T34z = 2*s*G34z.*I34zinx;

%Full term 53x
T53x = s*G53x.*I53xinx;

%Full term 53y
T53y = s*G53y.*I53yinx;

%Full term 53z
T53z = s*G53z.*I53zinx;

%Sum of terms
I = T11x + T11y + T11z + T34x + T34y + T34z + T53x + T53y + T53z;

%Interaction impedance
KNML2 = 2*p*Deltabetan./((epsilonp-epsilon2)*epsilon0*omega.*betan.^2.*I);

```

C. Publications

The following papers have been published in journals and conference proceedings during the PhD and are attached in this appendix:

1. J. M. Socuéllamos, R. Dionisio, R. Letizia and C. Paoloni, "Experimental Validation of Phase Velocity and Interaction Impedance of Meander Line Slow Wave Structures for Space Traveling Wave Tubes", *IEEE Trans. Microw. Theory Tech.*, vol. 69, no. 4, pp. 2148-2154, Apr. 2021.
2. J. M. Socuéllamos, R. Letizia, R. Dionisio and C. Paoloni, "Pillared Meander Line Slow Wave Structure for W-band TWT", in *Proc. 22th Int. Vac. Electron. Conf.*, Rotterdam, The Netherlands: virtual, Apr. 2021.
3. J. M. Socuéllamos, R. Letizia, R. Dionisio and C. Paoloni, "Novel Meander Line Slow Wave Structure for W-band TWT", in *Proc. 45th Int. Conf. Infrared, mm., THz-Wav.*, Buffalo, NY, USA: virtual, Nov. 2020.
4. J. M. Socuéllamos, R. Letizia, R. Dionisio and C. Paoloni, "3D Meander Line Slow Wave Structure for W-band TWT", in *Proc. 21th Int. Vac. Electron. Conf.*, Monterey, CA, USA: virtual, Oct. 2020.
5. J. M. Socuéllamos, R. Letizia, R. Dionisio and C. Paoloni, "Large Signal Analysis of a New Meander Line Topology for W-band TWTs", in *Proc. 12th UK/Europe-China Workshop mm-Wav., THz Tech.*, London, UK, Aug. 2019.
6. J. M. Socuéllamos, R. Letizia, R. Dionisio and C. Paoloni, "Preliminary Study of a New Meander Line for W-band TWT", in *Proc. 20th Int. Vac. Electron. Conf.*, Busan, South Korea, Apr. 2019.

Experimental Validation of Phase Velocity and Interaction Impedance of Meander Line Slow Wave Structures for Space Traveling Wave Tubes

Juan M. Socuéllamos, Roberto Dionisio, Rosa Letizia, *Senior Member, IEEE*, and Claudio Paoloni, *Senior Member, IEEE*

Abstract—Meander lines are promising slow wave structures (SWSs) for millimeter-wave traveling wave tubes (TWTs) due to low-cost manufacture, low-voltage operation and high interaction impedance. However, experimental results on meander lines are rare in literature.

Phase velocity and interaction impedance are the most important parameters for the design and characterization of TWT SWSs. Their experimental determination in meander lines is crucial for validating simulations and developing new topologies.

Based on a new theoretical model, this paper presents an experimental procedure to determine the phase velocity and the interaction impedance. The method is validated on four different Ka-band (33-37 GHz) meander line SWSs, including two of a novel topology.

Index Terms—Interaction impedance, meander line, millimeter wave, phase velocity, satellite communications, slow wave structure (SWS), traveling wave tube (TWT)

I. INTRODUCTION

THE exploitation of the millimeter wave spectrum for satellite communications is growing in interest due to the wide frequency bands available and the short wavelength that permits to reduce size and weight of payload. In particular, the Ka-band (26.5-40 GHz) is opening new perspectives for High Throughput Satellites (HTS) to be integrated in the new 5G networks [1], [2]. Traveling wave tubes (TWTs) are the only devices capable of providing high power over a wide frequency band to enable satellite internet distribution at millimeter waves [3]. Microwave TWTs are mostly based on helix slow wave structures (SWSs). However, above 60 GHz, helix SWSs are either very expensive or unfeasible to fabricate due to manufacture limitations. The need of alternative SWSs feasible at millimeter waves has stimulated the investigation of new full-metal SWSs such as the folded waveguide or the double corrugated waveguide [4], [5].

A different family of SWSs, the meander lines, has also shown promising performance suitable for millimeter-wave space TWTs. Meander line SWSs have some advantages in comparison with full-metal structures such as low-cost

production, lower operation voltage and higher interaction impedance [6].

The interaction impedance of a SWS determines how efficient is the exchange of energy between the RF signal and the electron beam. In space applications, both beam voltage and interaction impedance are important design parameters for saving power and reducing the TWT weight, which has direct implications for the final system and launch costs per satellite [7]. A high interaction impedance ($> 3 \Omega$) is obtained by an enhanced axial electric field intensity and more efficient energy exchange between the RF signal and the electron beam. This increases the gain per period of the SWS and permits to reduce the SWS length to produce more compact and lightweight TWTs. A low beam voltage (< 10 kV) allows to use lightweight and compact high voltage power suppliers with substantial payload reduction.

Despite the interest on meander lines, most of the results in literature are simulations, with experimental validation limited to S-parameters. The interaction impedance is usually derived by 3D electromagnetic simulations. An experimental validation is still missing, but it would be of great importance for a more accurate characterization of meander line SWSs.

The phase velocity and the interaction impedance of helix SWSs can be determined, for instance, by solving the field equations [8] or using resonant or non-resonant perturbation methods [9], [10].

This work aims to provide an experimental procedure to determine the phase velocity and, for the first time, the interaction impedance of meander line SWSs.

The experimental validation of the phase velocity is based on the measurement of the phase difference between the same meander line with two different lengths. This method, already proven to give excellent results applied to metal SWSs [11] and meander line SWSs [12], has been extended, for the first time, to Ka-band meander line SWSs.

The second novelty of this work is the development of a theory to experimentally determine the interaction impedance. A perturbation method, similar to the one presented in [9] for helix SWSs based on the work from [13], has been applied for the purpose. A rigorous analytical method has been developed to compute the electromagnetic fields of meander lines to determine the interaction impedance from measurements of the phase difference between a perturbed and an unperturbed meander line SWS.

In order to experimentally validate the two approaches for

This work was supported by the European Space Agency (ESA) in the framework of ESA's Network Partnering Initiative, contract no. 4000122038. J. M. Socuéllamos, R. Letizia and C. Paoloni are with the Engineering Department, Lancaster University, Lancaster, LA1 4YW, U.K. (e-mail: j.socuellamos@lancaster.ac.uk; r.letizia@lancaster.ac.uk; c.paoloni@lancaster.ac.uk)

R. Dionisio is with the European Space Research and Technology Centre, European Space Agency, 2201 AZ Noordwijk, The Netherlands. (e-mail: roberto.dionisio@esa.int)

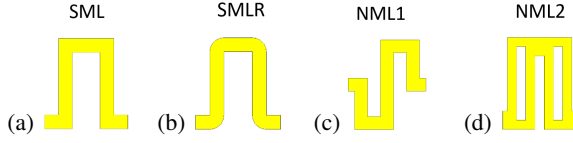


Fig. 1. Single period design of the four meander line topologies studied in this work. SML (a) and SMLR (b) stand for the standard meander line topology with and without round corners and NML1 (c) and NML2 (d) for two novel meander line designs.

measuring both dispersion and interaction impedance, four different meander line topologies have been designed (see Fig. 1) and manufactured at Ka-band. Two novel meander lines (NML1 and NML2) are proposed to improve specific performance depending on the application of the TWT. One, NML1, offers flatter dispersion over a wide band [14], the other, NML2, provides higher interaction impedance but over a narrower band [15]. A standard meander line (SML) (Fig. 1(a)) and the standard meander line with round corners (SMLR) (Fig. 1(b)) are used as reference for comparison with the two novel meander lines, NML1 (Fig. 1(c)) and NML2 (Fig. 1(d)). The experimental results for the phase velocity and the interaction impedance of the four meander line SWSs are discussed and compared with 3D electromagnetic simulations (CST Microwave Studio [16]). Numerical convergence of results in simulations was obtained by modelling the metallization with a local hexahedral mesh with $50 \mu\text{m}^3$ volumetric cells corresponding to one cell every $2 \mu\text{m}$ and $5 \mu\text{m}$ in the vertical and horizontal coordinates, respectively.

II. CALCULATION OF THE PHASE VELOCITY

The phase velocity of a SWS can be experimentally calculated from measurements of the phase difference of two identical SWSs with different lengths (l_1 and l_2) or number of periods (n_1 and n_2). The difference in lengths Δl is a multiple integer $n = n_2 - n_1$ of the pitch length p of the periodic structure, $\Delta l = l_2 - l_1 = np$. The phase delay τ can be defined as the ratio between the variation of phase and frequency $\tau = \Delta\phi/\Delta\omega$. Then, the difference between the phase delay of the SWSs with different lengths is $\Delta\tau = \Delta\phi_2/\Delta\omega - \Delta\phi_1/\Delta\omega$.

The phase velocity $v_p = \Delta l/\Delta\tau$ is, therefore, computed as

$$v_p = \frac{np}{\Delta\phi_2/\Delta\omega - \Delta\phi_1/\Delta\omega}. \quad (1)$$

III. DETERMINATION OF THE INTERACTION IMPEDANCE

A perturbation method is adopted to derive an expression for the interaction impedance K in terms of a measurable quantity such as the propagation constant shift $\Delta\beta$.

The general equation for the calculation of the interaction impedance for the m th transverse and n th axial harmonics at any given point of a particular SWS is given by [17]

$$K_{mn}(x, y, z) = \frac{E_{z,mn}(x, y, z)E_{z,mn}^*(x, y, z)}{2\beta_n^2 P} \quad (2)$$

where $\beta_n = \beta + \frac{2\pi n}{p}$, with β_n being the axial phase constant of the n th space harmonic, β the fundamental axial phase

constant, p the pitch length and m and n integers. $E_{z,mn}$ is the longitudinal electric field magnitude of the n th axial and m th transverse space harmonics, $E_{z,mn}^*$ its complex conjugate and P is the time averaged RF power flow.

When a physical perturbation is introduced in the system under analysis, the propagation constant shift between the perturbed and unperturbed signals can be defined as [13]

$$\Delta\beta_n = \frac{\omega(\epsilon' - \epsilon_2) \int_{\Delta V} \mathbf{E}'_{mn}(x, y, z) \cdot \mathbf{E}_{mn}^*(x, y, z) dV}{4Pp} \quad (3)$$

where \mathbf{E}'_{mn} is the perturbed electric field and \mathbf{E}_{mn}^* is the complex conjugate of the electric field without perturbation. ϵ' and V are the permittivity and the volume of the perturbation, respectively. ϵ_2 is the permittivity of the original medium where the perturbation is applied.

Equation (2) and (3) are valid for any SWS. However, the expressions for the electric fields in these equations need to be derived specifically for the SWS under investigation. In the following, the method will be applied to general meander line SWSs. In particular, expressions for the electromagnetic fields are derived for the four different meander line topologies studied in this work (see Fig. 1). Nevertheless, the procedure permits to obtain the expression of the interaction impedance regardless of the meander line topology.

The model uses a selection of trigonometric functions for computing the electromagnetic fields of meander lines. Even though those functions are considered valid for the purpose, slight differences can be found in literature to describe the fields depending on the approach adopted [18], [19].

The meander line SWS can be assumed made of perfect conductor with infinitesimal thickness placed on a lossless and uniform dielectric substrate. The substrate is surrounded by perfect conductor walls and a ground plane. Following these assumptions, the expressions for the longitudinal components of the electromagnetic field in meander lines can be written as (adapted from [20] for a more general case)

$$E_z(x, y, z) = \sum_{m,n=-\infty}^{\infty} A_{jk,mn} \frac{\sinh(\alpha_{ijk,mn} Y_i)}{\sinh(\alpha_{ijk,mn} B_i)} \sin(k_{jk,m} X_{jk}) e^{-j\beta_n z}, \quad (4)$$

$$H_z(x, y, z) = \sum_{m,n=-\infty}^{\infty} B_{jk,mn} \frac{\cosh(\alpha_{ijk,mn} Y_i)}{\cosh(\alpha_{ijk,mn} B_i)} \cos(k_{jk,m} X_{jk}) e^{-j\beta_n z} \quad (5)$$

where $\alpha_{ijk,mn}^2 = k_{jk,m}^2 + \beta_n^2 - \omega^2 \mu \epsilon_i$.

These expressions contain three indexes i, j and k that vary according to the spatial disposition of the structure and are fundamental to correctly characterize the electromagnetic fields of any meander line topology. Specifically, each index is linked to one spatial dimension; i and k to the transverse vertical and horizontal coordinates, respectively, and j to the longitudinal coordinate.

A standard meander line (SML) enclosed in a rectangular housing, similar to the structure manufactured in this work, is considered as an example to describe the index association.

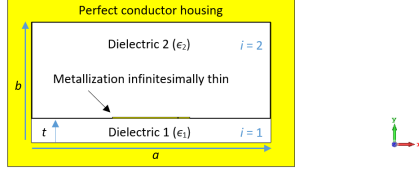


Fig. 2. xy-plane view of the two regions of the meander line to be analyzed. t is the thickness of the substrate, a is the length of the substrate and b is the height of the perfect conductor cavity.

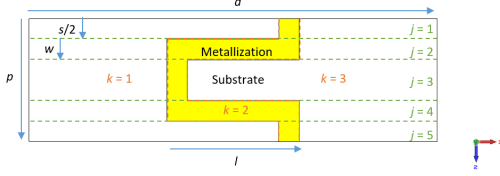


Fig. 3. xz-plane view of the standard meander line. There are five and three regions along the z and x axis, respectively. s is the distance between two consecutive strips, w is the strip width, p is the pitch length, a is the length of the substrate and l is the length of the metallization.

As schematically seen in Fig. 2, the index i (coordinate y) can be either 1 or 2 depending on the region of analysis if the metallization is considered to be infinitesimally thin: the substrate with permittivity ϵ_1 or the medium above with permittivity ϵ_2 . Similarly, the indexes j and k (coordinates z and x , respectively) can be defined taking as a reference the schematic shown in Fig. 3. The index j varies from 1 to 5 in order to consider the five regions with different electromagnetic field. The index k varies from 1 to 3 to define the substrate and metal regions.

As seen in Fig. 2, the expressions for Y_i and B_i in (4) and (5) do not depend on the meander line topology if this is considered infinitesimally thin. However, the other parameters, the field amplitudes A_{jk} and B_{jk} , and X_{jk} and k_{jk} do depend on the meander line shape and vary accordingly.¹

Applying Maxwell's equations to (4) and (5) allows to obtain general expressions for the transverse electric field components as

$$E_x(x, y, x) = \sum_{m,n=-\infty}^{\infty} j \frac{\sinh(\alpha_{ijk,mn} Y_i) \cos(k_{jk,m} X_{jk})}{\beta_n^2 - \omega^2 \mu \epsilon_i} e^{-j\beta_n z} \left(A_{jk,mn} \frac{\partial X_{jk}}{\partial x} \frac{k_{jk,m} \beta_n}{\sinh(\alpha_{ijk,mn} B_i)} + B_{jk,mn} \frac{\partial Y_i}{\partial y} \frac{\alpha_{ijk,mn} \omega \mu}{\cosh(\alpha_{ijk,mn} B_i)} \right), \quad (6)$$

$$E_y(x, y, x) = \sum_{m,n=-\infty}^{\infty} j \frac{\cosh(\alpha_{ijk,mn} Y_i) \sin(k_{jk,m} X_{jk})}{\beta_n^2 - \omega^2 \mu \epsilon_i} e^{-j\beta_n z} \left(A_{jk,mn} \frac{\partial Y_i}{\partial y} \frac{\alpha_{ijk,mn} \beta_n}{\sinh(\alpha_{ijk,mn} B_i)} + B_{jk,mn} \frac{\partial X_{jk}}{\partial x} \frac{k_{jk,m} \omega \mu}{\cosh(\alpha_{ijk,mn} B_i)} \right). \quad (7)$$

Fig. 4 shows the model of a dielectric cylindrical perturbation placed on top of the standard meander line in a similar

¹Expressions for Y_i , B_i , X_{jk} and k_{jk} are derived in App. A for the standard meander line topology (SML) as an example.

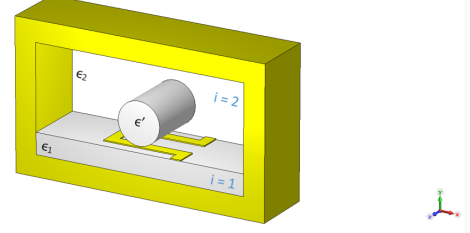


Fig. 4. 3D view of the three regions to be analysed including the perturbation.

configuration to the experimental setup that has been used in this work. The dielectric perturbation with permittivity ϵ' is placed in the region $i = 2$. Three regions are defined: the region within the substrate ($i = 1$), the region above the substrate excluding the perturbation ($i = 2$) and the region within the perturbation.

The fields within the perturbed region are changed in such a way that the field amplitudes A_{jk} and B_{jk} , and the propagation constant β_n are shifted to the equivalent parameters A'_{jk} , B'_{jk} and β'_n , respectively. Setting $i = 2$ in Y_i and B_i as the perturbation is placed in this region, the perturbed field components are then expressed as

$$E'_z(x, y, z) = \sum_{m,n=-\infty}^{\infty} A'_{jk,mn} \frac{\sinh(\alpha'_{jk,mn} Y_2)}{\sinh(\alpha'_{jk,mn} B_2)} \sin(k_{jk,m} X_{jk}) e^{-j\beta'_n z}, \quad (8)$$

$$E'_x(x, y, x) = \sum_{m,n=-\infty}^{\infty} j \frac{\sinh(\alpha'_{jk,mn} Y_2) \cos(k_{jk,m} X_{jk})}{\beta_n'^2 - \omega^2 \mu \epsilon'} e^{-j\beta'_n z} \left(A'_{jk,mn} \frac{\partial X_{jk}}{\partial x} \frac{k_{jk,m} \beta'_n}{\sinh(\alpha'_{jk,mn} B_2)} + B'_{jk,mn} \frac{\partial Y_2}{\partial y} \frac{\alpha'_{jk,mn} \omega \mu}{\cosh(\alpha'_{jk,mn} B_2)} \right), \quad (9)$$

$$E'_y(x, y, x) = \sum_{m,n=-\infty}^{\infty} j \frac{\cosh(\alpha'_{jk,mn} Y_2) \sin(k_{jk,m} X_{jk})}{\beta_n'^2 - \omega^2 \mu \epsilon'} e^{-j\beta'_n z} \left(A'_{jk,mn} \frac{\partial Y_2}{\partial y} \frac{\alpha'_{jk,mn} \beta'_n}{\sinh(\alpha'_{jk,mn} B_2)} + B'_{jk,mn} \frac{\partial X_{jk}}{\partial x} \frac{k_{jk,m} \omega \mu}{\cosh(\alpha'_{jk,mn} B_2)} \right). \quad (10)$$

The interaction impedance can be defined at one arbitrary point (x_0, y_0) according to (2) as

$$K_{mn}(x_0, y_0) = \frac{E_{z,mn}(x_0, y_0) E_{z,mn}^*(x_0, y_0)}{2\beta_n^2 P}. \quad (11)$$

To relate the interaction impedance at this particular point $K_{mn}(x_0, y_0)$ with the measurable quantity $\Delta\beta_n$, it is necessary to find the relation between the product of fields from (11) with that from (3).

The approach to find this relation is based on the application of interface conditions, first, between the dielectric perturbation and its surrounding medium ($i = 2$), and second, between the meander line substrate ($i = 1$) and the medium over it ($i = 2$). For the first case, the perturbation is assumed to be

uniform along the axial direction. Therefore, the continuity of the tangential E_t and normal D_n field components used to relate the perturbed and unperturbed axial field components is valid at any point of the perturbation surface and independent of the z coordinate. Similarly for the second case, at the interface between the substrate ($i = 1$) and the medium ($i = 2$), the tangential E_t and the normal D_n field components are continuous.

Applying all these conditions, the following relationships between the electric fields can be found

$$\begin{aligned} E'_{z,mn}(x, y, z)E_{z,mn}^*(x, y, z) = \\ E_{z,mn}(x_0, y_0)E_{z,mn}^*(x_0, y_0) \cdot \\ G_{jk,z} \sinh(\alpha'_{jk,mn}Y_2) \sinh(\alpha_{2jk,mn}Y_2) \sin^2(k_{jk,m}X_{jk}), \end{aligned} \quad (12)$$

$$\begin{aligned} E'_{x,mn}(x, y, z)E_{x,mn}^*(x, y, z) = \\ E_{z,mn}(x_0, y_0)E_{z,mn}^*(x_0, y_0) \cdot \\ G_{jk,x} \sinh(\alpha'_{jk,mn}Y_2) \sinh(\alpha_{2jk,mn}Y_2) \cos^2(k_{jk,m}X_{jk}), \end{aligned} \quad (13)$$

$$\begin{aligned} E'_{y,mn}(x, y, z)E_{y,mn}^*(x, y, z) = \\ E_{z,mn}(x_0, y_0)E_{z,mn}^*(x_0, y_0) \cdot \\ G_{jk,y} \cosh(\alpha'_{jk,mn}Y_2) \cosh(\alpha_{2jk,mn}Y_2) \sin^2(k_{jk,m}X_{jk}) \end{aligned} \quad (14)$$

with $G_{jk,z}$, $G_{jk,x}$ and $G_{jk,y}$ being the coefficients that contain the particularities of every interface condition.²

Every expression obtained for the product between the perturbed and unperturbed field components (12)-(14) can be then replaced into (3) as

$$\begin{aligned} \Delta\beta_n = \frac{\omega(\epsilon' - \epsilon_2)}{4Pp} E_{z,mn}(x_0, y_0)E_{z,mn}^*(x_0, y_0) \int_{\Delta V} \sum_{j,k} \\ [G_{jk,z} \sinh(\alpha'_{jk,mn}Y_2) \sinh(\alpha_{2jk,mn}Y_2) \sin^2(k_{jk,m}X_{jk}) + \\ G_{jk,x} \sinh(\alpha'_{jk,mn}Y_2) \sinh(\alpha_{2jk,mn}Y_2) \cos^2(k_{jk,m}X_{jk}) + \\ G_{jk,y} \cosh(\alpha'_{jk,mn}Y_2) \cosh(\alpha_{2jk,mn}Y_2) \sin^2(k_{jk,m}X_{jk})] dV. \end{aligned} \quad (15)$$

Finally, solving for the product $E_{z,mn}(x_0, y_0)E_{z,mn}^*(x_0, y_0)$ in (15) and replacing into (11), the interaction impedance at one selected point $K_{mn}(x_0, y_0)$ can be calculated in terms of the measurable quantities β_n and $\Delta\beta_n$ according to

$$K_{mn}(x_0, y_0) = \frac{2p}{\omega(\epsilon' - \epsilon_2)} \frac{\Delta\beta_n}{\beta_n^2} \frac{1}{I_{mn}} \quad (16)$$

where I_{mn} is the numerical result of the integral in (15).

IV. EXPERIMENTAL SETUP

The four meander line SWSs in Fig. 1 have been fabricated with two different number of periods each, $n_1 = 20$ (see Fig. 5) and $n_2 = 40$, in order to be able to measure the phase velocity. The dimensions of the substrate are 21.812 mm x 2.9 mm for the 20-period length and 33.812 mm x 2.9 mm for the 40-period length. The substrate is alumina with relative

²Equation (12) is derived as an example in App. B.

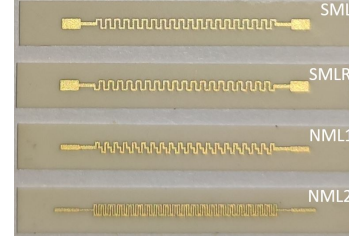


Fig. 5. The four different topologies of the 20-period meander line SWSs manufactured for the experiment.

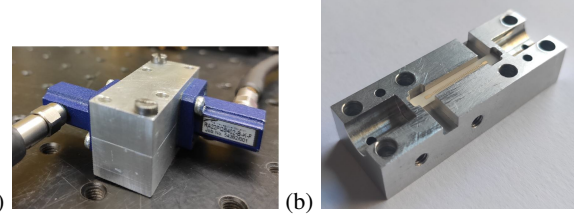


Fig. 6. (a) Measurement setup with the waveguide flanges connected to the housing and (b) bottom half of the housing with one of the meander lines placed inside.

permittivity $\epsilon_1 = 9.9$ and 127 μm thickness. The metallization is made of gold with 10 μm thickness.

Two aluminum housings corresponding to the two different lengths of the meander lines were manufactured. The housings are designed with two WR28 waveguide ports with dimensions 7.112 mm x 3.556 mm, one at each side of the aluminum block, that are connected to the waveguide flanges as seen in the measurement setup in Fig. 6(a). The flanges are then connected to a Vector Network Analyzer to perform the measurements. As shown in Fig. 5, the meander lines are terminated in coupling probes so that the electromagnetic field applied through the waveguide ports can be coupled to the meander line. The final assembly of the meander line inserted into the housing is shown in Fig. 6(b).

The phase velocity measurements for every topology are performed using the same housing and replacing the inner meander line for both 20 and 40-period cases. Then, the phase delay difference is measured for every pair of meander line topologies to obtain the data in (1).

To compute the interaction impedance, the perturbed phase is measured after introducing a nylon ($\epsilon' = 3.4$) rod with radius 120 μm , placed at 450 μm from the metal strip as shown in Fig. 7. The dielectric rod is introduced in the housing by means of two holes that were drilled at both ends of the aluminum holder.

As derived in (16), β and $\Delta\beta$ are the quantities that need to be measured in order to experimentally determine the interaction impedance. The values of β are obtained from the phase velocity measurements as $\beta = \omega/v_p$, and $\Delta\beta$ from the phase difference between the perturbed and unperturbed circuits as $\Delta\beta = \Delta\phi/l$ where l is the length of the circuit.

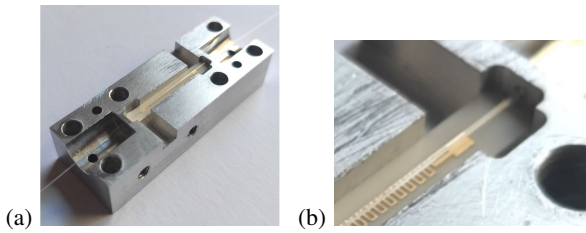


Fig. 7. (a) Bottom half of the housing with the perturbation introduced on top of the meander line. (b) Detail of the perturbation over the meander line.

V. EXPERIMENTAL RESULTS

A. Phase velocity

The measurements of the phase velocity for all the four meander lines are shown in Fig. 8. A measurement error has been added to the results considering that, for a same meander line, different samples were fabricated and measured. In particular, twenty samples were used, two 20-period and 40-period samples of SML and SMLR and three 20-period and 40-period samples of NML1 and NML2. Therefore, to calculate the phase velocity, four curves were computed for SML and SMLR while nine curves were computed for NML1 and NML2. The measurement error, represented by a shadowed area in Fig. 8, is given by the highest and lowest phase velocity measured for the various samples available. The measurement curves, which are drawn with solid lines in Fig. 8, are the mean value of the results obtained from the various samples.

The measurement results for NML1 and NML2 (Fig. 8(c) and 8(d)) show good correlation with the simulated curves. However, the experimental curves for SML and SMLR (Fig. 8(a) and 8(b)) show a correct trend but values slightly higher than the obtained for the simulations at the low-half frequency band. This difference could be due to manufacture tolerances or slight deviations in the position of the meander line inside the housings.

B. Interaction impedance

The experimental curves for the interaction impedance for the four meander lines considered are compared with the simulation results in Fig. 9(a) and 9(b) for SML and SMLR, and Fig. 9(c) and 9(d) for NML1 and NML2. Similar to the measurements of the phase velocity, two samples of SML and SMLR and three samples of NML1 and NML2 have been used for the tests. Therefore, the shadowed areas in Fig. 9, account for the deviation from the mean value considering the different samples of the same meander line. The simulated curves are obtained by two different methods: simulating the equivalent virtual experiment to obtain the data to apply (16) and using the Eigenmode solver in CST-MWS based on (2). The interaction impedance is computed at the centre of the perturbation, corresponding to a distance of $570 \mu\text{m}$ from the metallization ($450 \mu\text{m} + 120 \mu\text{m}$ of the rod radius).

The good agreement between experiment and simulations demonstrates the validity of the method. In meander lines, the longitudinal electric field is concentrated close to the

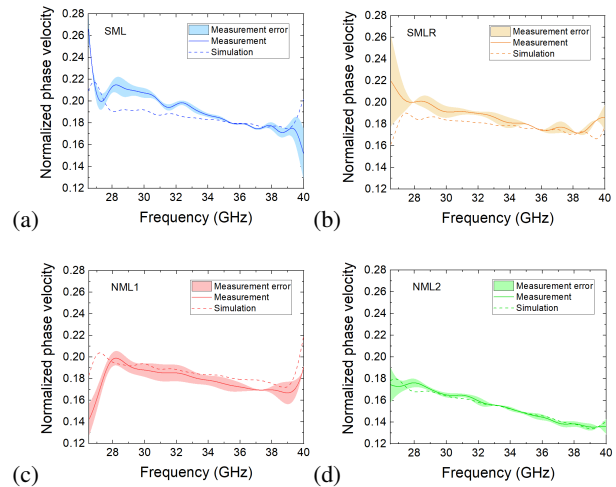


Fig. 8. Comparison of the phase velocity measurements (solid curves plus error) with the simulation curves (dashed curves). (a) SML, (b) SMLR, (c) NML1 and (d) NML2.

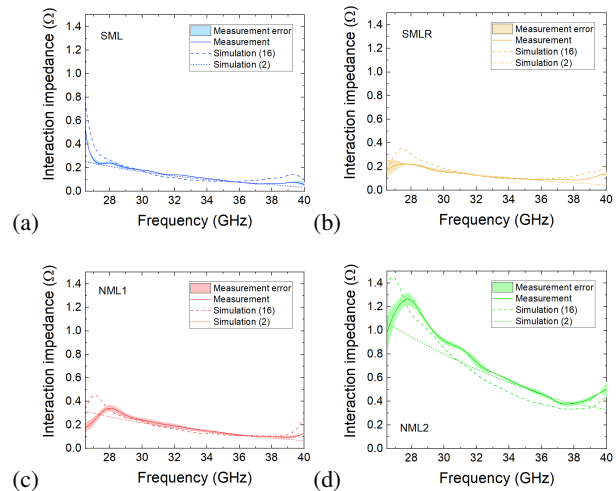


Fig. 9. Comparison of the interaction impedance measurements (solid curves plus error) with the simulation curves using (16) (dashed curves) and using (2) (dotted curves). (a) SML, (b) SMLR, (c) NML1 and (d) NML2.

metallization. Consequently, the interaction impedance grows as the calculation point approaches the meander line. The low interaction impedance measured in Fig. 9 is due to the position of the perturbation far from the metallization. According to simulations, if the perturbation is placed at a distance of $50 \mu\text{m}$ from the metallization, the interaction impedance is over 3Ω for the four meander lines. In future experiments, the perturbation will be placed closer to the meander line to measure higher values of the interaction impedance.

VI. CONCLUSION

The first experimental computation of the phase velocity at Ka-band and a new method for measuring the interaction impedance in meander line SWs for TWTs have been presented. Four Ka-band meander line SWs were manufactured

and tested to validate the theory. In general, the experimental results showed good agreement with 3D electromagnetic simulations.

The presented methods are useful experimental tools for design and test of a new family of meander line SWSs for a new generation of low-cost and lightweight space TWTs for millimeter-wave communications. High interaction impedance and low beam voltage are important meander line features to reduce the size and weight of the TWT and the power supply, with benefits on the mission cost for cost-effective satellite communication systems.

APPENDIX A

DERIVATION OF THE PARAMETERS Y_i , B_i , X_{jk} AND k_{jk}

Assuming an infinitesimal thickness for the metallization, the characterization over the transverse vertical component is not dependent on the meander topology. As seen in Fig. 2, the structure is divided in two regions along the y coordinate ($i = 1, 2$). To obtain the values for Y_i and B_i , these two regions need to satisfy the boundary conditions of the structure, $E_z = 0$ at $y = 0$ and $y = b$. Therefore, expressions for the axial component of the electric field can be obtained depending on the region of analysis as

$0 < y < t$ or $i = 1$

$$E_z(x, y, z) = \sum_{m,n=-\infty}^{\infty} A_{jk,mn} \frac{\sinh(\alpha_{1jk,mn} Y_1)}{\sinh(\alpha_{1jk,mn} B_1)} \sin(k_{jk,m} X_{jk}) e^{-j\beta_n z}$$

with $Y_1 = y$ and $B_1 = t$.

$t < y < b$ or $i = 2$

$$E_z(x, y, z) = \sum_{m,n=-\infty}^{\infty} A_{jk,mn} \frac{\sinh(\alpha_{2jk,mn} Y_2)}{\sinh(\alpha_{2jk,mn} B_2)} \sin(k_{jk,m} X_{jk}) e^{-j\beta_n z}$$

with $Y_2 = b - y$ and $B_2 = b - t$.

The study over the x and z coordinates depends on the particular topology of the meander line. The longitudinal electric field expressions for the standard meander line are derived according to Fig. 3. Five regions can be defined along the z coordinate, $j = 1, 2, 3, 4, 5$, and three regions over the x coordinate, $k = 1, 2, 3$. The regions $k = 1$ and $k = 3$ refer to the left and right hand side of the substrate, respectively, whereas $k = 2$ is the region containing the metallization. Therefore, the limits for the regions along the x coordinate are not fixed and depend on the z position of analysis. For the case of SML, the fields in regions $j = 1$ and $j = 5$ are the same and also those in regions $j = 2$ and $j = 4$. In order to derive expressions for the parameters X_{jk} and k_{jk} , boundary conditions of the structure are applied. Specifically, $E_z = 0$ at $x = 0$ and $x = a$ and also at the areas where the metallization is located. These expressions can be then determined as

$0 < z < s/2, 3s/2 + 2w < z < p$ and $0 < x < a/2 + l/2 - w$ or $j = 1, 5$ and $k = 1$

$$E_z(x, y, z) = \sum_{m,n=-\infty}^{\infty} A_{11,mn} \frac{\sinh(\alpha_{i11,mn} Y_i)}{\sinh(\alpha_{i11,mn} B_i)} \sin(k_{11,m} X_{11}) e^{-j\beta_n z}$$

with $k_{11,m} = \frac{(2m-1)\pi}{a/2+l/2-w}$ and $X_{11} = x$.

$0 < z < s/2, 3s/2 + 2w < z < p$ and $a/2 + l/2 - w < x < a/2 + l/2$ or $j = 1, 5$ and $k = 2$

$$E_z(x, y, z) = 0$$

$0 < z < s/2, 3s/2 + 2w < z < p$ and $a/2 + l/2 < x < a$ or $j = 1, 5$ and $k = 3$

$$E_z(x, y, z) = \sum_{m,n=-\infty}^{\infty} A_{13,mn} \frac{\sinh(\alpha_{i13,mn} Y_i)}{\sinh(\alpha_{i13,mn} B_i)} \sin(k_{13,m} X_{13}) e^{-j\beta_n z}$$

with $k_{13,m} = \frac{(2m-1)\pi}{a/2-l/2}$ and $X_{13} = a - x$.

$s/2 < z < s/2 + w, 3s/2 + w < z < 3s/2 + 2w$ and $0 < x < a/2 - l/2$ or $j = 2, 4$ and $k = 1$

$$E_z(x, y, z) = \sum_{m,n=-\infty}^{\infty} A_{21,mn} \frac{\sinh(\alpha_{i21,mn} Y_i)}{\sinh(\alpha_{i21,mn} B_i)} \sin(k_{21,m} X_{21}) e^{-j\beta_n z}$$

with $k_{21,m} = \frac{(2m-1)\pi}{a/2-l/2}$ and $X_{21} = x$.

$s/2 < z < s/2 + w, 3s/2 + w < z < 3s/2 + 2w$ and $a/2 - l/2 < x < a/2 + l/2$ or $j = 2, 4$ and $k = 2$

$$E_z(x, y, z) = 0$$

$s/2 < z < s/2 + w, 3s/2 + w < z < 3s/2 + 2w$ and $a/2 + l/2 < x < a$ or $j = 2, 4$ and $k = 3$

$$E_z(x, y, z) = \sum_{m,n=-\infty}^{\infty} A_{23,mn} \frac{\sinh(\alpha_{i23,mn} Y_i)}{\sinh(\alpha_{i23,mn} B_i)} \sin(k_{23,m} X_{23}) e^{-j\beta_n z}$$

with $k_{23,m} = \frac{(2m-1)\pi}{a/2-l/2}$ and $X_{23} = a - x$.

$s/2 + w < z < 3s/2 + w$ and $0 < x < a/2 - l/2$ or $j = 3$ and $k = 1$

$$E_z(x, y, z) = \sum_{m,n=-\infty}^{\infty} A_{31,mn} \frac{\sinh(\alpha_{i31,mn} Y_i)}{\sinh(\alpha_{i31,mn} B_i)} \sin(k_{31,m} X_{31}) e^{-j\beta_n z}$$

with $k_{31,m} = \frac{(2m-1)\pi}{a/2-l/2}$ and $X_{31} = x$.

$s/2 + w < z < 3s/2 + w$ and $a/2 - l/2 < x < a/2 - l/2 + w$ or $j = 3$ and $k = 2$

$$E_z(x, y, z) = 0$$

$s/2 + w < z < 3s/2 + w$ and $a/2 - l/2 + w < x < a$ or $j = 3$ and $k = 3$

$$E_z(x, y, z) = \sum_{m,n=-\infty}^{\infty} A_{33,mn} \frac{\sinh(\alpha_{i33,mn} Y_i)}{\sinh(\alpha_{i33,mn} B_i)} \sin(k_{33,m} X_{33}) e^{-j\beta_n z}$$

with $k_{33,m} = \frac{(2m-1)\pi}{a/2+l/2-w}$ and $X_{33} = a - x$.

APPENDIX B DERIVATION OF (12)

The product between the axial components of the perturbed and the complex unperturbed fields, (8) and the conjugate equivalent of (4), can be written as

$$E'_{z,mn}(x, y, z) E_{z,mn}^*(x, y, z) = \frac{A'_{jk,mn}}{A_{jk,mn}} A_{jk,mn}^* A_{jk,mn} \frac{\sinh(\alpha'_{jk,mn} Y_2) \sinh(\alpha_{ijk,mn} Y_i)}{\sinh(\alpha'_{jk,mn} B_2) \sinh(\alpha_{ijk,mn} B_i)} \sin^2(k_{jk,m} X_{jk}) e^{-j(\beta'_n - \beta_n)z}. \quad (17)$$

The unperturbed axial field component at one given point (x_0, y_0) within the region of perturbation is defined, according to (4), as

$$E_{z,mn}(x_0, y_0, z) = A_{jk,mn} \frac{\sinh(\alpha_{2jk,mn} Y_2^0)}{\sinh(\alpha_{2jk,mn} B_2)} \sin(k_{jk,m} X_{jk}^0) e^{-j\beta_n z}, \quad (18)$$

and multiplying with its complex conjugate gives

$$E_{z,mn}(x_0, y_0) E_{z,mn}^*(x_0, y_0) = A_{jk,mn} A_{jk,mn}^* \frac{\sinh^2(\alpha_{2jk,mn} Y_2^0)}{\sinh^2(\alpha_{2jk,mn} B_2)} \sin^2(k_{jk,m} X_{jk}^0). \quad (19)$$

Solving for the product between the field amplitudes gives

$$A_{jk,mn} A_{jk,mn}^* = E_{z,mn}(x_0, y_0) E_{z,mn}^*(x_0, y_0) \frac{\sinh^2(\alpha_{2jk,mn} B_2)}{\sinh^2(\alpha_{2jk,mn} Y_2^0) \sin^2(k_{jk,m} X_{jk}^0)}. \quad (20)$$

The continuity of the tangential axial field component at the perturbation surface implies that at one given point (x_1, y_1) of the surface, $E'_z(x_1, y_1, z) = E_z(x_1, y_1, z)$. By using this relation, a relationship between the unperturbed and perturbed field coefficients can be found

$$\frac{A'_{jk,mn}}{A_{jk,mn}} e^{-j(\beta'_n - \beta_n)z} = \frac{\sinh(\alpha_{2jk,mn} Y_2^1) \sinh(\alpha'_{jk,mn} B_2)}{\sinh(\alpha'_{jk,mn} Y_2^1) \sinh(\alpha_{2jk,mn} B_2)}. \quad (21)$$

Finally, replacing the expressions from (20) and (21) into (17), the product of the perturbed and unperturbed fields can be rewritten in terms of the product between the original and complex unperturbed axial field components as

$$E'_{z,mn}(x, y, z) E_{z,mn}^*(x, y, z) = E_{z,mn}(x_0, y_0) E_{z,mn}^*(x_0, y_0) \frac{G'_{jk,z} \sinh(\alpha'_{jk,mn} Y_2) \sinh(\alpha_{2jk,mn} Y_2) \sin^2(k_{jk,m} X_{jk})}{\sinh^2(\alpha_{2jk,mn} Y_2^0) \sin^2(k_{jk,m} X_{jk}^0)}, \quad (22)$$

with

$$G'_{jk,z} = \frac{\sinh(\alpha_{2jk,mn} Y_2^1)}{\sinh(\alpha'_{jk,mn} Y_2^1) \sinh^2(\alpha_{2jk,mn} Y_2^0) \sin^2(k_{jk,m} X_{jk}^0)}.$$

Equation (13) and (14) can be derived in a similar fashion applying the interface conditions that correspond to each field component.

REFERENCES

- [1] G. Giambene, S. Kota and P. Pillai, "Satellite-5G Integration: A Network Perspective", *IEEE Netw.*, Vol. 32, No. 5, pp. 25-31, Sep/Oct. 2018.
- [2] A. I. Perez-Neira, M. A. Vazquez, M. R. Bhavani Shankar, S. Maleki and S. Chatzinotas, "Signal Processing for High-Throughput Satellites: Challenges in New Interference-Limited Scenarios", *IEEE Signal Process. Mag.*, Vol. 36, No. 4, pp. 112-131, Jul. 2019.
- [3] N. Ayllon, P. Angeletti, M. Ludwig and R. Dionisio, "An overview of European Spaceborne Vacuum Tube Amplifiers and System Needs", in *Proc. 18th Int. Vac. Electron. Conf.*, London, UK, Apr. 2017.
- [4] C. W. Robertson, A. W. Cross, C. Gilmour, D. Dyson, P. G. Huggard, F. Cahill, M. Beardsley, R. Dionisio and K. Ronald, "71-76 GHz Folded Waveguide TWT for Satellite Communications", in *Proc. 20th Int. Vac. Electron. Conf.*, Busan, South Korea, Apr. 2019.
- [5] X. Li, X. Huang, S. Mathisen, R. Letizia and C. Paoloni, "Design of 71-76 GHz Double-Corrugated Waveguide Traveling-Wave Tube for Satellite Downlink", *IEEE Trans. Electron Devices*, Vol. 65, No. 6, pp. 2195-2200, Jun. 2018.
- [6] G. Ulisse, V. Krozer, N. Ryskin, A. Starodubov, A. Serdobintsev, A. Pavlov, V. Galushka and M. Samarskiy, "Fabrication and Measurements of a Planar Slow Wave Structure Operating in V-band", in *Proc. 20th Int. Vac. Electron. Conf.*, Busan, South Korea, Apr. 2019.
- [7] G. Kornfeld and E. Bosch, "From History to Future of Satellite TWT Amplifiers", *Frequenz*, Vol. 55, No. 9-10, pp. 258-262, Sep. 2001.
- [8] S. D'Agostino, F. Emma and C. Paoloni, "Accurate Analysis of Helix Slow-Wave Structures", *IEEE Trans. Electron Devices*, Vol. 45, No. 7, pp. 1605-1613, Jul. 1998.
- [9] C. L. Kory and J. A. Dayton, "Computational Investigation of Experimental Interaction Impedance Obtained by Perturbation for Helical Traveling-Wave Tube Structures", *IEEE Trans. Electron Devices*, Vol. 45, No. 9, pp. 2063-2071, Dec. 1998.
- [10] S. J. Rao, S. Ghosh, P. K. Jain and B. N. Basu, "Nonresonant Perturbation Measurements on Dispersion and Interaction Impedance Characteristics of Helical Slow-Wave Structures", *IEEE Trans. Microw. Theory Techn.*, Vol. 45, No. 9, pp. 1585-1593, Sep. 1997.
- [11] C. Paoloni, M. Mineo, M. Henry and P. G. Huggard, "Double Corrugated Waveguide for Ka-band Traveling Wave Tube", *IEEE Trans. Electron Devices*, Vol. 62, No. 11, pp. 3851-3856, Nov. 2015.
- [12] C. Chua and S. Aditya, "A 3-D U-Shaped Meander-Line Slow-Wave Structure for Traveling-Wave-tube Applications", *IEEE Trans. Electron Devices*, Vol. 60, No. 3, pp. 1251-1256, Mar. 2013.
- [13] R. P. Lagerstrom, "Interaction impedance measurements by perturbation of traveling waves", Tech. Rep. no. 7, Stanford Electronics Laboratories, Stanford Univ., Stanford, CA, USA, Feb. 1957.
- [14] J. M. Socu llamos, R. Letizia, R. Dionisio and C. Paoloni, "Large Signal Analysis of a New Meander Line Topology for W-band TWTs", in *Proc. 12th UK/Europe-China Workshop mm-Wav., THz Tech.*, London, UK, Aug. 2019.
- [15] J. M. Socu llamos, R. Letizia, R. Dionisio and C. Paoloni, "Novel Meander Line Slow Wave Structure for W-band TWT", in *Proc. 45th Int. Conf. Infrared, mm., THz-Wav.*, virtual, Nov. 2020.
- [16] CST-MWS. [Online]. Available: <https://www.cst.com/products/csts2>
- [17] A. S. Gilmour, "Principles of Traveling Wave Tubes", Artech House Radar Library, Michigan Univ., Boston, MA, USA, Dec. 1994.
- [18] T. Itoh and R. Mittra, "Spectral-Domain Approach for Calculating the Dispersion Characteristics of Microstrip Lines", *IEEE Trans. Microw. Theory Techn.*, Vol. 21, No. 7, pp. 496-499, Jul. 1973.
- [19] J. A. Weiss, "Dispersion and Field Analysis of a Microstrip Meander-Line Slow-Wave Structure", *IEEE Trans. Microw. Theory Techn.*, Vol. 22, No. 12, pp. 1194-1201, Dec. 1974.
- [20] D. G. Zhang, Edward K. N. Yung and H. Y. Ding, "Dispersion characteristics of a novel shielded periodic meander line", *Microw. Opt. Techn. Lett.*, Vol. 12, No. 1, pp. 1-5, May 1996.

Pillared Meander Line Slow Wave Structure for W-band Traveling Wave Tube

Juan M. Socuéllamos
Engineering Department
Lancaster University
Lancaster, United Kingdom
j.socuellamos@lancaster.ac.uk

Rosa Letizia
Engineering Department
Lancaster University
Lancaster, United Kingdom
r.letizia@lancaster.ac.uk

Roberto Dionisio
European Space Technology
and Research Center
European Space Agency
Noordwijk, The Netherlands
roberto.dionisio@esa.int

Claudio Paoloni
Engineering Department
Lancaster University
Lancaster, United Kingdom
c.paoloni@lancaster.ac

Abstract—The low beam voltage operation and the simple fabrication of meander lines make them a promising slow wave structure for the production of novel and low-cost traveling wave tubes for W-band satellite communications. However, the poor interaction of planar structures with a cylindrical beam has led to the investigation of alternative meander line configurations that could improve their performance. A novel slow wave structure based on adding pillars to a meander line for improving the interaction with a cylindrical electron beam is described. Cold parameter and large signal results are presented in the paper.

Keywords—Meander line; Traveling wave tube (TWT); Slow wave structure (SWS); W-band.

I. INTRODUCTION

The increasing demand of communication services such as high definition streaming, video conferencing or online video games is pushing to explore higher frequency bands in order to increase the available bandwidth and the channel capacity to permit high data rate transmission.

Even though the free space path loss and the atmospheric attenuation become more important as frequency is increased, the W-band (71-76 GHz for satellite downlink) offers a relatively low attenuation window [1].

Given the high atmospheric attenuation and the bandwidth required for telecommunication services, the traveling wave tube (TWT) is the only amplifier able to provide adequate power level. However, the impossibility of using the helix slow wave structure (SWS) for the interaction beam-RF signal due to its unfeasible manufacture at high frequencies, has made necessary to explore novel and alternative SWSs [2-4].

Meander lines represent a promising family of SWSs for the new generation of millimetre-wave TWTs [5,6]. The potential use of low-voltage electron beams, the high interaction impedance and the simple fabrication of the meander line, are some of the advantages of this kind of SWS that could lead to the realization of novel low-cost TWTs.

The interaction of planar meander lines with cylindrical beams is not efficient and the sheet beam is more effective to obtain high output levels [7]. Nevertheless, while the experimental knowledge on sheet beams is limited, the cylindrical beam has been extensively studied and is commonly used in space TWTs. The simple and low magnetic field required to confine a cylindrical beam is also advantageous to manufacture lightweight and cost-effective TWTs.

With the purpose of benefiting from the meander line properties and the use of a cylindrical electron beam, this work presents a novel pillared meander line (PML), whose schematic is shown in Fig. 1, that works with a low beam voltage and offers a substantial increase of the interaction impedance with consequent improvement of the TWT output power at W-band.

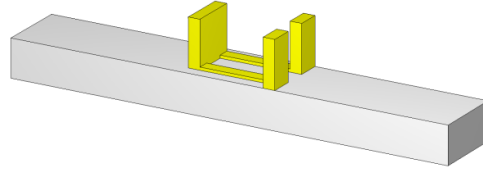


Fig. 1. Schematic of one period of the pillared meander line (PML).

II. COLD PARAMETER SIMULATIONS

The cold parameter simulations are performed by using CST Microwave Studio [8]. Alumina with relative permittivity $\epsilon_r = 9.9$ and gold with conductivity $\sigma = 4.56 \times 10^7$ S/m are used for the substrate and metal, respectively.

The cold parameters for PML, including dispersion and interaction impedance, are shown in Fig. 2 and Fig. 3, respectively. The pillared meander line is designed to interact with an electron beam of 6.5 kV within the 71-76 GHz band. The interaction impedance within than range is over 10Ω .

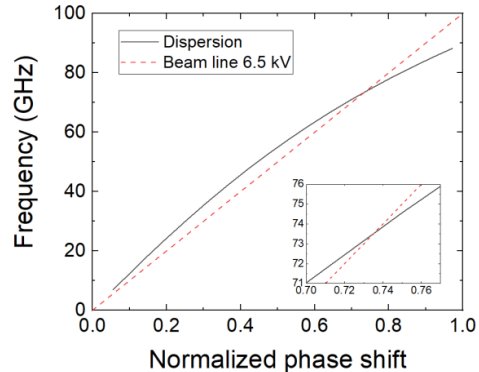


Fig. 2. Dispersion curve for the PML.

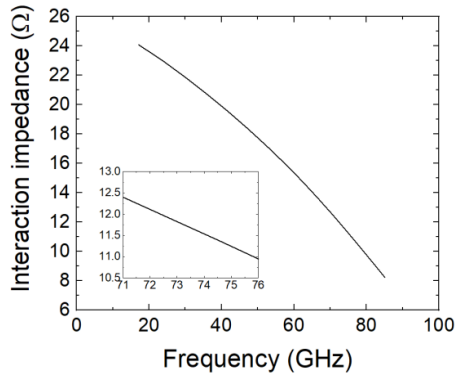


Fig. 3. Interaction impedance curve for the PML.

III. LARGE SIGNAL SIMULATIONS

The coupling transition between the pillared meander line and the waveguide is very similar to the one for planar meander lines [7]. The bottom metallization of the structure is extended at both ends to serve as a probe to couple the electromagnetic wave coming from the waveguide.

Gain and output power of the PML are simulated using a cylindrical beam with radius 80 μm , 6.5 kV voltage, 40 mA current (current density of 200 A/cm^2) and focused with 0.6 T magnetic field. A RF signal with 50 mW input power is applied. The results are shown in Fig. 6. Gain over 25 dB and output power over 18 W are obtained at W-band.

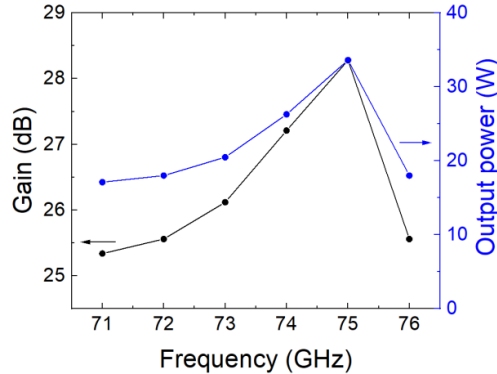


Fig. 4. Gain and output power for the PML at W-band.

IV. FABRICATION PROCESS

The pillared meander line can be fabricated following the schematic proposed in Fig. 7. After preparation of the alumina substrate, it needs to be metallized in order to improve adhesion with low-reactivity metals. This first layer can be deposited via a sputtering process. Once the substrate is metallized, a photoresist is applied and exposed to UV-

light to pattern the meander line design using a photomask. After the photoresist is developed, the meander line can be grown by electroplating. A subsequent photoresist application and electroplating process can be performed in order to grow the pillars. Once the full structure is created, the photoresist is removed and the first metallized layer etched.

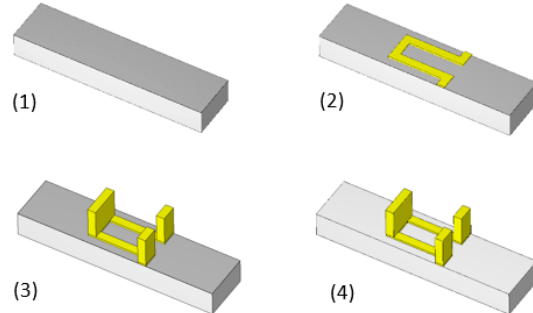


Fig. 5. Schematic of the fabrication of the PML divided in four steps.

V. CONCLUSION

A novel pillared meander line SWS has been proposed showing improved performance in comparison with planar meander lines for interaction with a cylindrical beam. The PML can provide the output power estimated for W-band satellite communications while also benefiting from the advantages of planar meander lines and the use of a cylindrical electron beam.

REFERENCES

- [1] N. Ayllon, P. Angeletti, M. Ludwig and R. Dionisio, "An overview of European Spaceborne Vacuum Tube Amplifiers and System Needs", in *Proc. IEEE 18th Int. Vac. Electron. Conf.*, London, UK, Apr. 2017.
- [2] X. Li, X. Huang, S. Mathisen, R. Letizia, C. Paoloni, "Design of 71-76 GHz Double-Corrugated Waveguide Traveling-Wave Tube for Satellite Downlink", *IEEE Trans. on Electron Devices*, vol. 65, no. 6, pp. 2195-2200, Jun. 2018.
- [3] C. W. Robertson, A. W. Cross, C. Gilmour, D. Dyson, P. G. Huggard, F. Cahill, M. Beardsley, R. Dionisio and K. Donald, "71-76 GHz Folded Waveguide TWT for Satellite Communications", in *Proc. 20th Int. Vac. Electron. Conf.*, Busan, South Korea, Apr. 2019.
- [4] C. Paoloni, D. Gamzina, R. Letizia, Y. Zheng and N. C. Luhmann Jr., "Millimeter Wave Traveling Wave Tubes for the 21st Century", *J. Electromagn. Wav. Appl.*, Dec. 2020.
- [5] J. M. Socu llamos, R. Letizia, R. Dionisio, C. Paoloni, "Large Signal Analysis of a New Meander Line Topology for W-band TWTs", in *Proc. 12th UK/Europe-China Works. on mm-Wav. and Ter. Tech.*, London, UK, Aug. 2019.
- [6] J. M. Socu llamos, R. Letizia, R. Dionisio, C. Paoloni, "Novel Meander Line Slow Wave Structure for W-band TWT", in *Proc. 45th Int. Conf. Infrared, mm., THz-wav.*, virtual, Nov. 2020.
- [7] J. M. Socu llamos, R. Letizia, R. Dionisio, C. Paoloni, "3D Meander Line Slow Wave Structure for W-band TWT", in *Proc. 21st Int. Vac. Electron. Conf.*, virtual, Oct. 2020.
- [8] CST-MWS. [Online]. Available: <https://www.cst.com/products/csts2>

Novel Meander Line Slow Wave Structure for W-band TWT

Juan M. Socuéllamos¹, Rosa Letizia¹, Roberto Dionisio² and Claudio Paoloni¹

¹Engineering Department, Lancaster University, Lancaster, United Kingdom

²European Space Technology and Research Centre, European Space Agency, Noordwijk, The Netherlands

Abstract—The unfeasible fabrication of helix slow wave structures in W-band traveling wave tubes makes necessary to find alternative slow wave structures in order to amplify the RF signal to the output levels required to overcome atmospheric attenuation in satellite communications. Meander lines are nowadays being studied as slow wave structures for W-band traveling wave tubes due to their favorable properties compared to full metal alternatives. A novel meander line topology is introduced in this work, showing that high gain and output power can be achieved using a low-voltage electron beam. Cold and large signal simulations are presented in this work.

I. INTRODUCTION

W-BAND (71-76 GHz) may offer a suitable transmission window with relatively low atmospheric attenuation that will provide both high channel capacity and data transfer rate [1]. Yet the use of this band for satellite communications is so far prevented by the lack of power amplifiers. Traveling wave tubes (TWTs) are extensively used for satellite communications at microwaves and are able to provide tens or hundreds of watt. However, space TWTs are based on helix slow wave structures (SWSs) for the interaction beam-radiofrequency signal. Helix SWSs are not feasible at W-band due to the small dimensions. This has made necessary to find alternative slow wave structures for space TWTs [2, 3]. Meander lines are theoretically capable of providing similar gain and output power as full-metal SWSs while needing a much lower beam voltage [4, 5]. This benefit, along with the suitability for low-cost and high-volume production, makes meander lines a promising SWS for W-band TWT.

This paper presents a novel meander line topology that provides peak gain and output power of 37 dB and 25 W, respectively, while using a beam voltage of only 8 kV.

II. RESULTS

A. Cold simulations

The proposed new meander line (NML) is presented in Fig. 1. The novel meander line has been designed on alumina substrate with thickness 127 μm and relative permittivity $\epsilon_r = 9.9$, and gold metallization with thickness 10 μm and electric conductivity $\sigma = 4.56 \times 10^7$ S/m. The simulations have been performed using the electromagnetic analysis software CST Microwave Studio [6].

The normalized phase velocity curve of the new meander line is presented in Fig. 2. The novel meander line is designed to interact with a sheet electron beam with voltage of 8 kV.

The interaction impedance curve for the new meander line is shown in Fig. 3. Within the 71-76 GHz bandwidth, the new meander line offers an average interaction impedance of 2.6 Ω .

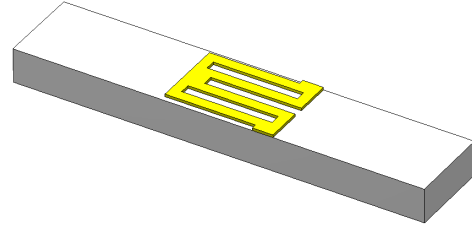


Fig. 1. Design of one period of the new meander line.

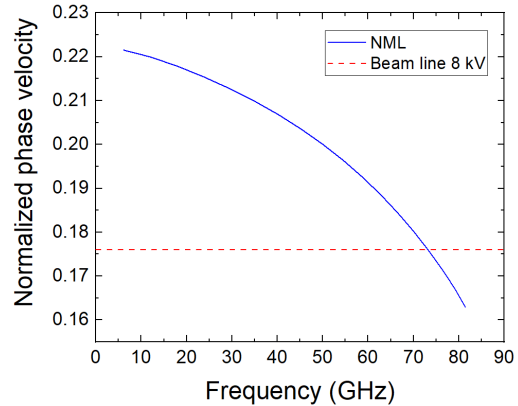


Fig. 2. Normalized phase velocity of the new meander line (blue solid curve) and beam line for 8 kV (red dashed curve).

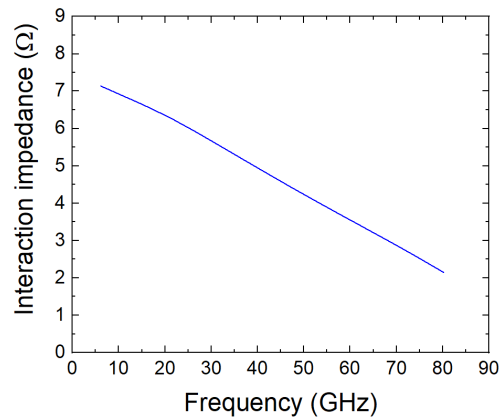


Fig. 3. Interaction impedance of the new meander line.

B. Full SWS simulations

Large signal simulations are performed using a sheet electron beam with relatively low aspect ratio 2:1 where the greatest dimension equals the length of the novel meander line. The sheet beam is computed at a distance of 50 μm from the metallization. The beam is focused with 1 T magnetic field for a current density of 160 A/cm². An input RF signal of 5 mW is applied.

Gain and output power results at W-band (71-76 GHz) are presented in Fig. 4. Gain and output power over 31 dB and 5 W, respectively, are obtained for the whole 71-76 GHz band. Peak gain and output power reach 37 dB and 25 W at 75 GHz.

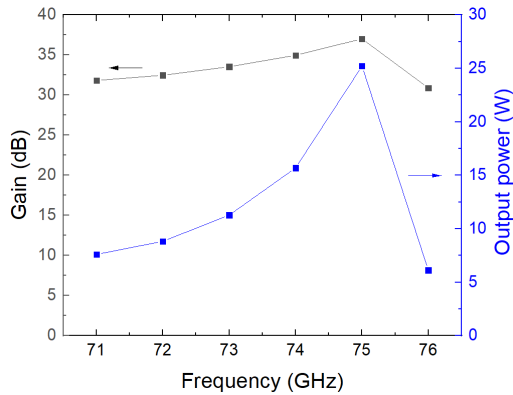


Fig. 4. Gain (black curve) and output power (blue curve) of the new meander line.

III. SUMMARY

A novel meander line topology has been designed and simulated at W-band. Cold results have shown that the novel meander line can operate with a beam voltage around 8 kV. The new meander line is capable of providing high levels of gain and output power while operating with a low beam voltage. The novel meander line represents a feasible alternative to helix slow wave structures and other full-metal slow wave structures for the production of low-cost, low-voltage W-band traveling wave tubes.

REFERENCES

- [1] N. Ayllon, P. Angeletti, M. Ludwig and R. Dionisio, "An overview of European Spaceborne Vacuum Tube Amplifiers and System Needs", in *Proc. IEEE 18th Int. Vac. Electron. Conf.*, London, UK, April 2017.
- [2] X. Li, X. Huang, S. Mathisen, R. Letizia, C. Paoloni, "Design of 71-76 GHz Double-Corrugated Waveguide Traveling-Wave Tube for Satellite Downlink", *IEEE Trans. on Electron Devices*, vol. 65, no. 6, pp. 2195-2200, June 2018.
- [3] C. W. Robertson, A. W. Cross, C. Gilmour, D. Dyson, P. G. Huggard, F. Cahill, M. Beardsley, R. Dionisio and K. Donald, "71-76 GHz Folded Waveguide TWT for Satellite Communications", in *Proc. 20th Int. Vac. Electron. Conf.*, Busan, South Korea, April 2019.
- [4] J. M. Socuéllamos, R. Letizia, R. Dionisio, C. Paoloni, "Large Signal Analysis of a New Meander Line Topology for W-band TWTs", in *Proc. 12th UK/Europe-China Works. on mm-Wav. and Ter. Tech.*, London, UK, Aug. 2019.
- [5] F. Shen, Y. Wei, H. Yin, Y. Gong, X. Xu, S. Wang, W. Wang and J. Feng, "A Novel V-Shaped Microstrip Meander-Line Slow Wave Structure for W-band MMPM", *IEEE Trans. on Plasma Science*, vol. 40, no. 2, pp. 463-469, Feb. 2012.
- [6] CST-MWS. [Online]. Available: <https://www.cst.com/products/cst>.

3D Meander Line Slow Wave Structure for W-band TWT

Juan M. Socuéllamos¹, Rosa Letizia¹, Roberto Dionisio² and Claudio Paoloni¹

¹Engineering Department, Lancaster University, Lancaster, United Kingdom

²European Space Technology and Research Centre, European Space Agency, Noordwijk, The Netherlands

Abstract: Planar meander lines have been recently studied in detail due to their favorable properties as slow wave structures for traveling wave tubes. However, the interaction of a cylindrical electron beam with this kind of structures is not efficient enough in order to achieve the output power levels required for space applications at W-band. A new design, suitable and optimized for the cylindrical beam geometry, is introduced in this work. Cold and large signal results are presented in the paper.

Keywords: Traveling wave tube (TWT); Slow wave structure (SWS); Meander line; W-band.

Introduction

The exploitation of W-band for the feeder downlink (71-76 GHz) between satellites and ground stations could offer a suitable transmission window for high data transfer rate [1]. The bandwidth and transmission power required to overcome atmospheric attenuation at W-band can be provided only by TWTs. Given the infeasibility of helix-type slow wave structures at high frequencies, different full-metal topologies have been tested as alternative SWSs [2, 3].

Meander lines represent a promising alternative to the full-metal designs as they are potentially capable to provide similar gain and output power levels while offering higher interaction impedance and lower operation voltage. However, due to the intrinsic planar design of meander lines, high output levels are only obtained when the structure interacts with planar electron beam geometries, for instance sheet beams [4]. The use of sheet electron beams as particle sources in traveling wave tubes is not desirable due to the instability that the beam suffers as the electrons travel along the tube [5]. Cylindrical geometries are typically much more stable and can be easily controlled by means of conventional periodic permanent magnets, but the results for gain and output power are very discrete [6]. Even though different efforts have been made in order to increase the output levels using cylindrical electron beams [7, 8], the results are not yet satisfactory for satellite applications at W-band and better configurations are necessary.

This paper presents a three-dimensional meander line structure which has been shown to provide much better results than a planar meander line of the same characteristics. Cold and large signal simulations, and a possible fabrication process, are presented in the following sections.

Planar-3D meander

The typical planar meander line and the proposed three-dimensional (3D) meander line designs are shown in Fig. 1. The 3D structure can be understood as a projection in height of the conventional planar meander line. The beam tunnel is obtained in the centre of the metal structure.

The electric field distribution in the transmission direction for the planar and 3D meanders is plotted in Fig. 2, where a lateral cut-plane of the structures is presented. The electric

field of the planar meander line is concentrated close to the metal line; this implies that a cylindrical beam with certain realistic radius traveling on top of the metal line will not interact uniformly with the electric field. It is expected that the bottom side of the cylindrical beam will present a better interaction with the electric field than the top part of the beam, thus lowering the overall efficiency. Instead, the electric field profile of the 3D meander is more suitable in order to accommodate a cylindrical beam as the whole electron beam is immersed in the electric field and a more uniform interaction should be achieved.

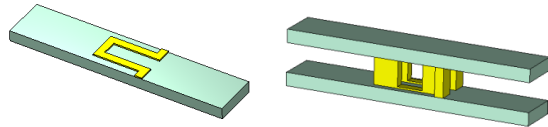


Fig. 1. Design of one period of the planar (left) and the 3D (right) meander lines.

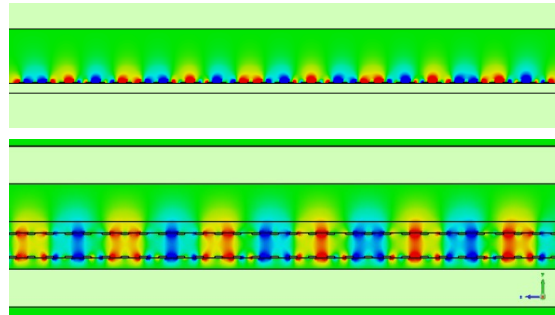


Fig. 2. Electric field profile for the full planar (top plot) and 3D (bottom plot) meander lines.

3D meander simulations

A preliminary simulation is performed in order to roughly compare the performance of the planar and 3D meander lines using the same dimensions and parameters. The results are shown in Tab. 1. As expected, considering the more favourable electric field distribution, the 3D meander slow wave structure shows much better performance than the conventional planar meander line.

Tab. 1. Results obtained after cold and large signal analysis of the planar and 3D meander line. The values show the average improvement in percentage of the 3D structure in comparison with the planar meander line.

	Interaction impedance	Gain	Output power	Electronic efficiency
Planar line	--	--	--	--
3D meander	+220%	+30%	+400%	+150%

The simulations are performed using CST Microwave Studio [9]. Alumina with relative permittivity $\epsilon_r = 9.9$ and copper with reduced conductivity $\sigma = 2.25 \times 10^7$ S/m are used for the substrate and metal, respectively.

The cold results for the 3D structure, computed for an operation voltage of 6.5 kV, are presented in Fig. 3. An average interaction impedance of about 13.5Ω in the frequency range 71-76 GHz is obtained.

The coupling transition design between the 3D meander and waveguides is similar to the one for planar meanders [6]. The bottom planar meander line is extended at both ends acting as a probe for the electric field coming from and leaving the waveguide (Fig. 4). The S-parameters of the SWS with this coupler are provided in Fig. 5. Good transmission is achieved in the 71-76 GHz frequency range.

For the large signal simulations, a cylindrical electron beam with radius $80 \mu\text{m}$ and current 40 mA (current density 200 A/cm^2) is chosen. The beam is focused with 0.5 T magnetic field. An input signal of 50 mW is applied. Gain and output power at W-band are presented in Fig. 5, providing peak values close to 30 dB and 50 W, respectively.

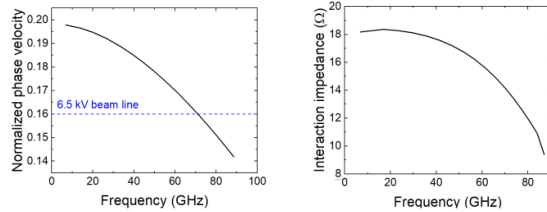


Fig. 3. Normalized phase velocity (left) and interaction impedance (right) for the 3D meander line.

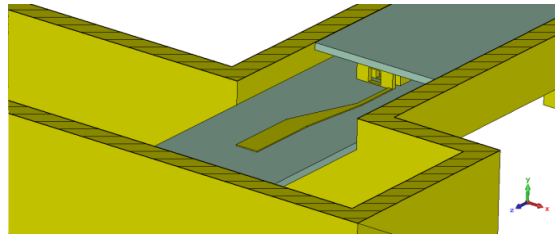


Fig. 4. Cut-plane view of the coupling transition between the meander line and the waveguide ports.

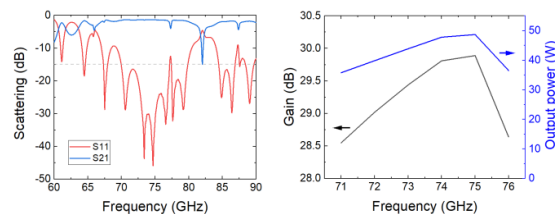


Fig. 5. Scattering parameters (left) and gain and output power (right) for the 3D meander line.

Fabrication of the 3D meander

The fabrication of a three-dimensional structure at W-band is a more demanding task in comparison with planar

configurations which can be easily built using lithography. Nevertheless, a possible fabrication approach would consist of splitting the structure into two parts which could be fabricated using, for example, LIGA process: one substrate would contain the 3D part of the structure whereas on the other one, a planar meander would be grown. Fig. 6 shows schematically the design.

The final step would be to join both structures placing the planar meander on top of the other part. However, a method to bond the two parts is under investigation.

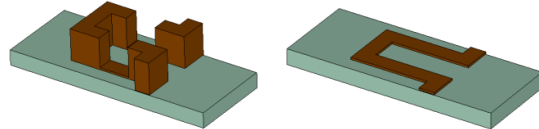


Fig. 6. Schematic of the parts of the 3D meander line.

Conclusion

A 3D meander line has been designed and compared with a conventional planar line with the same characteristics showing enhanced overall performance. The SWS is able to provide the output power level suitable for space applications at W-band with the advantages of lower operation voltage and higher interaction impedance in comparison with other full-metal SWSs. Further work will be focus on finding a suitable joining method between both parts of the structure and investigating the most suitable materials in order to facilitate the fabrication process.

References

- [1] N. Ayllon, P. Angeletti, M. Ludwig and R. Dionisio, "An overview of European Spaceborne Vacuum Tube Amplifiers and System Needs", in *Proc. IEEE 18th Int. Vac. Electron. Conf.*, London, UK, April 2017.
- [2] X. Li, X. Huang, S. Mathisen, R. Letizia, C. Paoloni, "Design of 71-76 GHz Double-Corrugated Waveguide Traveling-Wave Tube for Satellite Downlink", *IEEE Trans. on Electron Devices*. vol. 65, no. 6, pp. 2195-2200, June 2018.
- [3] C. W. Robertson, A. W. Cross, C. Gilmour, D. Dyson, P. G. Huggard, F. Cahill, M. Beardsley, R. Dionisio and K. Donald, "71-76 GHz Folded Waveguide TWT for Satellite Communications", in *Proc. 20th Int. Vac. Electron. Conf.*, Busan, South Korea, April 2019.
- [4] F. Shen, Y. Wei, H. Yin, Y. Gong, X. Xu, S. Wang, W. Wang and J. Feng, "A Novel V-Shaped Microstrip Meander-Line Slow-Wave Structure for W-band MMPM", *IEEE Trans. on Plas. Sci.*, vol. 40, no. 2, Feb. 2012.
- [5] X. Shi, Z. Wang, T. Tang, H. Gong, Y. Wei, Z. Duan, X. Tang, Y. Wang, J. Feng and Y. Gong, "Theoretical and Experimental Research on a Novel Small Tunable PCM System in Staggered Double Vane TWT", *IEEE Trans. on Electron Devices*. vol. 62, no. 12, Dec. 2015.
- [6] J. M. Socuéllamos, R. Letizia, R. Dionisio, C. Paoloni, "Large Signal Analysis of a New Meander Line Topology for W-band TWTs", in *Proc. 12th UK/Europe-China Works. on mm-Wav. and Ter. Tech.*, London, UK, Aug. 2019.
- [7] S. Sengele, H. Jiang, J. H. Booske, C. L. Kory, D. W. van der Weide and R. L. Ives, "Microfabrication and Characterization of a Selectively Metallized W-band Meander-Line TWT Circuit", *IEEE Trans. on Electron Devices*. vol. 56, no. 5, May 2009.
- [8] A. Starodubov, N. Ryskin, A. Rozhnev, A. Pavlov, A. Serdobintsev, R. Torgashov, V. Galushka, I. Kozhevnikov, I. Bahteev, G. Ulisse and V. Krozer, "Microfabrication and Study of Planar Slow-Wave Structures for Low-Voltage V-band and W-band Vacuum Tubes", in *Proc. 44th Int. Conf. on Infr., mm and Ter. Waves*, Paris, France, Sept. 2019.
- [9] CST-MWS. [Online]. Available: <https://www.cst.com/products/cst2>

Large Signal Analysis of a New Meander Line Topology for W-band Traveling Wave Tubes

Juan M. Socuéllamos¹, Rosa Letizia¹, Roberto Dionisio² and Claudio Paoloni¹

¹Engineering Department, Lancaster University, Lancaster, United Kingdom

²European Space Technology and Research Centre, European Space Agency, Noordwijk, The Netherlands

Abstract—Satellite distribution of high data rate needs wide frequency band. The millimeter waves, in particular the W-band, provide wide bandwidth and relatively low attenuation. The link transmission power can be provided only by Traveling Wave Tubes (TWTs). A new meander line topology to be used as slow wave structure for 71-76 GHz TWTs, with improved performance in comparison to the conventional one, is proposed. The new meander line compared to a standard meander line shows flatter gain and higher output power.

Keywords—Traveling wave tube, Slow wave structure, Meander line, W-band

I. INTRODUCTION

The allocated W-band (71-76 GHz) for satellite downlink aims to provide a suitable transmission window for high data transfer rate [1]. The wideband transmission power for the link can be only provided by TWTs. The traditional use of helix-type slow wave structures is not realizable at high frequencies due to manufacturing limitations. Different topologies of slow wave structures must be found [2, 3].

Meander lines have been studied in detail as slow wave structures for traveling wave tubes due to their favourable properties. This sort of structures is simple to fabricate using microfabrication techniques, with easy assembly and suitable for large scale production [4]. Moreover, meander structures are potentially capable of working with lower operation voltage as well as higher interaction impedance while providing similar performance as three-dimensional full metal structures [5, 6].

However, a remarkable drawback of meander lines is the narrow region of synchronism between the electromagnetic wave and the electron beam which limits the effective bandwidth. This issue is greatly influenced by the shape of the metal line and can also be moderately controlled modifying the dimensions of the metal strip as well as the size of the substrate where the metal line is placed. In this paper, a new meander line topology is studied aiming to improve the gain and output power flatness of this kind of structures.

The new structure was previously analysed and compared with a standard meander line of exactly the same dimensions by means of cold simulations. It was found that the dispersion slope of the new meander line was reduced by 32% while the interaction impedance was increased by 6% in comparison with the standard line [7]. Now, in this work, both structures are compared for large signal simulations obtaining results for the gain and output power within the frequency range of interest.

II. RESULTS

The proposed new topology and the standard meander line are designed using the same dimensions as shown in Fig.

1. The copper line, assumed with reduced conductivity $\sigma = 2.25 \times 10^7$ S/m to account for the metal loss at W-band [8], is placed on top of an alumina substrate with relative permittivity $\epsilon_r = 9.9$. Both the cold and hot simulations have been performed using CST Microwave Studio [9].

The dispersion curves of the new and standard meander lines are compared in Fig. 2. The dispersion of the standard line presents a more pronounced slope than the one of the new line, so it is to be expected that the new meander will be benefited from a flatter gain and output power within the 71-76 GHz range. In order to approximately obtain the operational voltage that will be used for the large signal simulations, different beam lines are plotted along the dispersion curves. The 4.4 kV beam line is the one that better matches the dispersion relation of the new meander so that the maximum output is centered within the frequency range of interest. As the standard structure presents a different dispersion curve, the suitable beam line for that structure has also a different value. For this case, the selected voltage is 3.2 kV as shown in Fig. 2.

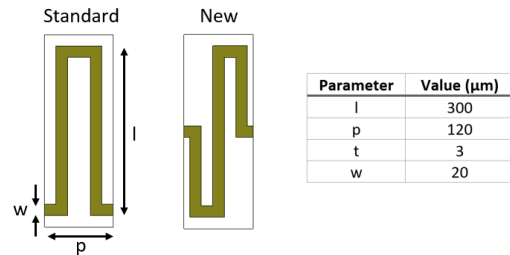


Fig. 1. Shape of the standard and new meander lines as well as the dimensions of both structures. The metal strips are designed with length l , thickness t and width w . The period of the structure is denoted with p .

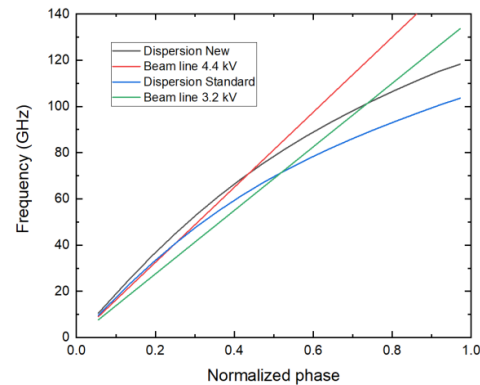


Fig. 2. Dispersion curve for the new (black curve) and standard (blue curve) meander lines as well as their corresponding beam lines of 4.4 kV (red line) and 3.2 kV (green line).

Once the beam voltage has been determined, the large signal performance of the new structure can be analysed. The new meander and the standard line are compared using the same hot parameters.

A cylindrical electron beam with a radius of $80\ \mu\text{m}$ is placed at a distance of $25\ \mu\text{m}$ from the metal strip. The current of the electron beam is $50\ \text{mA}$, equivalent to a current density of $250\ \text{A}/\text{cm}^2$. A radiofrequency signal with $4\ \text{mW}$ input power is introduced into the structure by the input ports. The waveguides and the meander line are connected following an E-field probe coupling transition [8], which was shown to provide adequate transmission and low losses when applied to the new meander line [7]. Finally, a magnetic field of $0.6\ \text{T}$ is selected to focus the electron beam. The only difference between both simulations is the value of the voltage as shown in Fig. 2.

In order to analyse the large signal performance of the structure, both the gain and output power of the new meander are compared with the results for the standard line. The gain for both structures within the 71-76 GHz frequency range is represented in Fig. 3. The new design presents a lower variation between the different points in the curve. Moreover, the gain for the standard line drops dramatically as the frequency approaches the edges of the band. The maximum gain for the new design is $23.8\ \text{dB}$, a higher value in comparison with $22.8\ \text{dB}$ of the standard line.

Similarly, Fig. 4 shows the comparison of the output power between both structures within the bandwidth of interest. The output power presents a smaller variation among the different frequencies for the case of the new meander line. The maximum output power of the new topology is $1\ \text{W}$, an increased value compared to the $0.8\ \text{W}$ that the standard line provides.

The low levels of output power can be explained considering the low input power and current used for the simulations. Moreover, only a single section is analysed. The complete structure can be designed to have two or more sections in order to increase the gain and meet the requirements of traveling wave tubes for space applications.

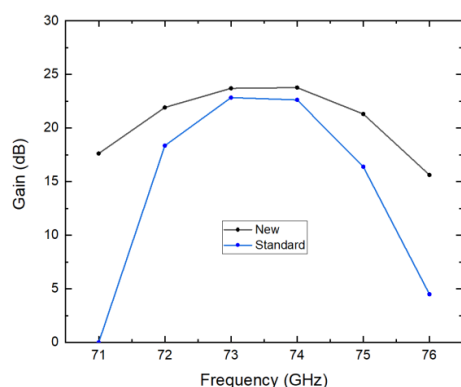


Fig. 3. Gain of the new (black line) and standard (blue line) meanders from 71 to 76 GHz.

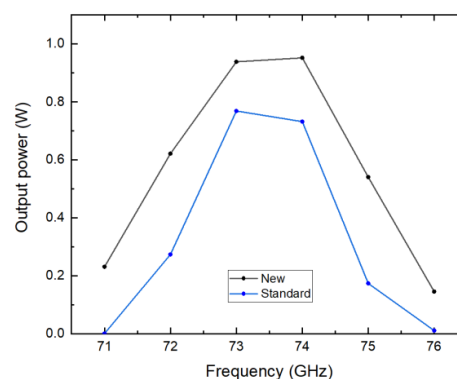


Fig. 4. Output power of the new (black line) and standard (blue line) meanders from 71 to 76 GHz.

III. CONCLUSION

A new meander line topology has been proposed to improve the gain and output power flatness of this kind of slow wave structures. Cold results revealed a gentler dispersion curve and higher interaction impedance in comparison with the standard meander line shape. These results have been transferred to the large signal analysis of the structure showing that the new design offers flatter gain and higher output power within the 71-76 GHz frequency range. Further work will be focus on improving the output power and gain of the structure.

REFERENCES

- [1] N. Ayllon, P. Angeletti, M. Ludwig and R. Dionisio, "An overview of European Spaceborne Vacuum Tube Amplifiers and System Needs", in *Proc. IEEE 18th Int. Vac. Electron. Conf.*, London, UK, April 2017.
- [2] M. Mineo and C. Paoloni, "Double Corrugation Rectangular Waveguide Slow-wave Structure for THz Vacuum Devices", *IEEE Trans. on Electron Devices*, vol. 57, no. 11, pp.3169-3175, November 2010
- [3] X. Li, X. Huang, S. Mathisen, R. Letizia, C. Paoloni, "Desing of 71-76 GHz Double-Corrugated Waveguide Traveling-Wave Tube for Satellite Downlink", *IEEE Trans. on Electron Devices*. vol. 65, no. 6, pp. 2195-2200, June 2018.
- [4] S. Wang, S. Aditya, X. Xia, Z. Ali and J. Miao, "On-Wafer Microstrip Meander Line Slow Wave Structure at Ka-Band", *IEEE Trans. on Electron Devices*. vol. 65, no. 6, pp. 2142-2148, June 2018.
- [5] F. Shen, Y. Wei, H. Yin, Y. Gong, X. Xu, S. Wang, W. Wang and J. Feng, "A Novel V-shaped Microstrip Meander Line Slow Wave Structure for W-band MMPM", *IEEE Trans. on Plasma Sci.*, vol. 40, no. 2, pp. 463-469, February 2012.
- [6] W. Zhang, Y. Wang, B. Qu, "Design of Folded Double-Ridged Waveguide Slow-Wave Structure", in *Proc. 19th Int. Vac. Electron. Conf.*, Monterey, USA, April 2018.
- [7] J. M. Socuélamos, R. Letizia, R. Dionisio, C. Paoloni, "Preliminary Study of a New Meander Line for W-band TWT", in *Proc. 20th Int. Vac. Electron. Conf.*, Busan, South Korea, April 2019.
- [8] C. Kory, R. L. Ives, M. Read, J. Booske, H. Jiang, D. van der Weide, S-J Ho, S. Sengele and P. Phillips "Overview of W-band Travelling Wave Tube Programs", in *Proc. 7th Int. Vac. Electron. Conf.*, Monterey, USA, April. 2006.
- [9] CST-MWS. [Online]. Available: <https://www.cst.com/products/csts2>

Preliminary Study of a New Meander Line for W-band TWT

Juan M. Socuélamos¹, Rosa Letizia¹, Roberto Dionisio² and Claudio Paoloni¹

¹Engineering Department, Lancaster University, Lancaster, United Kingdom

²European Space Technology and Research Centre, European Space Agency, Noordwijk, The Netherlands

Abstract—A new meander line topology for 71-76 GHz Traveling Wave Tubes is proposed. This new shape offers flatter dispersion relation and enhanced interaction impedance in comparison with the standard meander line. Results of the interaction impedance over the beam cross section and the effect of a meander line-to-waveguide coupler are also analyzed in this work.

Keywords—Traveling wave tube, W-band, meander line, coupler

I. INTRODUCTION

The exploitation of the W-band (71-76 GHz) for space communications to provide broadband for high data transfer rate with a reduced size of payload, has recently gained the interest [1]. The system specifications in terms of transmission power, operating bandwidth and efficiency require the use of traveling wave tube amplifiers. The traditional helix slow wave structures (SWS) are not feasible for frequencies over 50-60 GHz due to manufacturing limitations and high cost. Novel structures have been proposed as an alternative such as the double corrugated or the folded waveguide. Their performance are quite good, but they are usually operating at beam voltage higher than 10 kV [2,3]. For satellite communications, a lower beam voltage would reduce the impact of the power supply on payload. Meander lines are potentially able to offer similar performance as the 3D metal structures but working at a much lower voltage [4]. In addition, meander lines seem to offer also a relatively higher interaction impedance.

One of the disadvantages of conventional meander lines is the narrow region of synchronism between the electromagnetic wave and the electron beam, which limits the frequency band. A new topology is reported in this paper in order to increase the bandwidth of meander lines. The interaction impedance was well defined for helix structures that have cylindrical symmetry but it is not yet fully defined when is applied to slow wave structures with arbitrary symmetry like the meander lines [5]. A study of the interaction impedance profile over the beam cross section presented in this work is performed to better understand its distribution over the beam cross section. A simulation of the new meander line including the input and output couplers to the waveguide flanges is presented. The large signal simulations are in progress to compare the performance with conventional meander line SWSs.

II. COLD PARAMETERS

The proposed new meander line is shown in Fig. 1. The copper line, assumed with reduced conductivity $\sigma = 2.25 \times 10^7$ S/m to account for the metal loss at W-band [6], is placed on top of an alumina substrate (relative permittivity $\epsilon_r = 9.9$).

This new structure is compared to a standard meander line designed with exactly the same overall dimensions (Fig. 1) in order to evaluate the advantages of this new design in terms

of dispersion and interaction impedance. All the simulations have been performed using CST Microwave Studio [7].

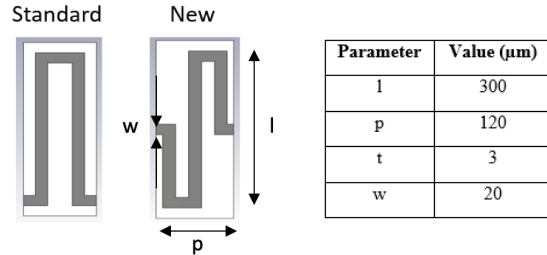


Fig. 1. Shape of the standard line and the new meander line as well as the dimensions of both structures: l is the length of the line, p is the period of the structure and t and w are the thickness and width of the strip.

A. Dispersion

The dispersion of the new meander line is compared to the standard meander line in Fig. 2. The inset shows that the dispersion slope in the frequency range of interest is better for the new design. The phase velocity flatness is improved from a 3.48% for the standard line to a 2.38% for the new design; with a relative improvement of 32%. This value should improve the gain flatness over the 71-76 GHz frequency band.

B. Interaction impedance

The interaction impedance of the new and standard meander lines are compared in Fig. 3. The inset shows that the new design presents an enhanced interaction impedance for the frequencies of interest in comparison with the standard line. Specifically, the new meander line has an average value of 5.92Ω whereas the standard line has 5.58Ω from 71 to 76 GHz; an increase of about 6% in the interaction impedance value of the structure. A higher interaction impedance improves the overall performance.

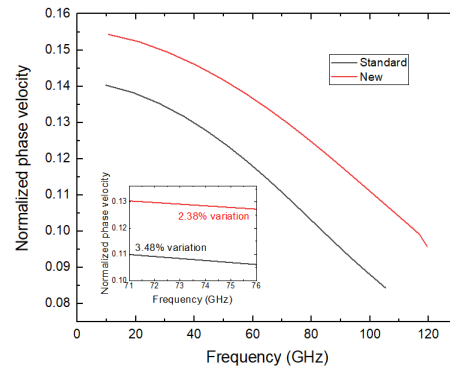


Fig. 2. Phase velocity curve of the new (red line) and standard (black line) meander line. The inset presents a zoom-in view from 71 to 76 GHz.

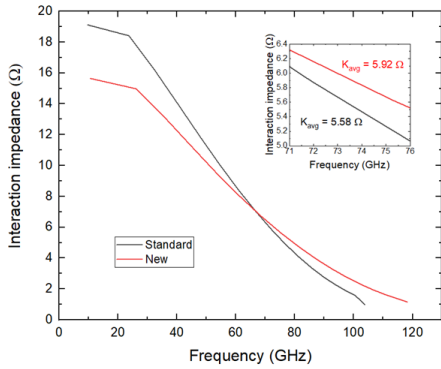


Fig. 3. Interaction impedance of the new (red line) and standard (black line) meander line. The inset presents a zoom-in view from 71 to 76 GHz.

A further study on the interaction impedance is presented in Fig. 4 to evaluate its distribution over the beam cross section for the two meander lines. A cylindrical beam of radius 80 μm placed at 25 μm from the metal strip line is assumed. The coordinate point $(x,y) = (0,0)$ indicates the beam axis position.

The interaction impedance profile along the x-coordinate of the beam for $y = 0$ shows that this value is higher on the center of the structure regardless of the shape of the line. It can be also appreciated that the pattern is approximately symmetrical and the interaction impedance decreases towards the edges of the meander line. The interaction impedance of the new line is higher than that of the standard line as expected, considering the higher average value obtained in Fig. 3. Sweeping the y-coordinate for $x = 0$ indicates that the interaction impedance is higher as the position of the beam is closer to the meander line. As expected, to maximize the interaction between wave and beam, the latter should be positioned as close as possible to the structure and centered over the meander line.

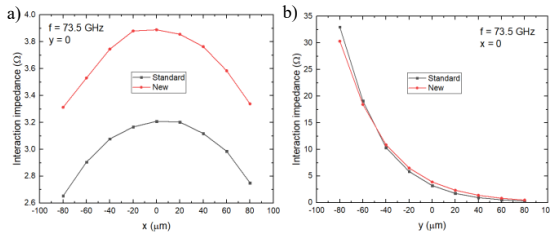


Fig. 4. Interaction impedance of the new (red line) and standard (black line) meander line over the circular beam cross section at 73.5 GHz. a) For a fixed $y = 0$ point, the x-coordinate is swept over the beam diameter and b) for $x = 0$, the y-coordinate is swept over the beam diameter. The beam radius is 80 μm .

III. FULL SWS SIMULATIONS

A suitable transition between the meander line and a waveguide is fundamental to properly couple the input/output signal, and its design plays an important role on the final performance of the device. The E-field probe approach has been already tested with meander lines [6] providing adequate transmission within a broad bandwidth. The meander line is extended at both ends with a tapered probe that is inserted into a waveguide connected with

flanges. The performance of the proposed meander line with and without an ideal port matching, as well as the comparison with the standard line are presented in Fig. 5. The simulation without couplers is performed placing virtual ports at both endings of the meander line structure.

The design with the coupler provides a reflection coefficient below -15 dB (point of reference for comparison) from 69 to 81 GHz whereas the design without the coupler gives a result with the coefficient below that value for the whole frequency range analysed. The transmission coefficient is similar for both designs. The difference of the scattering parameters between both structures is higher as the frequency approaches the edges of the band. The comparison with the standard meander line shows that the new meander line offers a slightly better value for the transmission coefficient and a broader frequency range with the reflection coefficient below -15 dB.

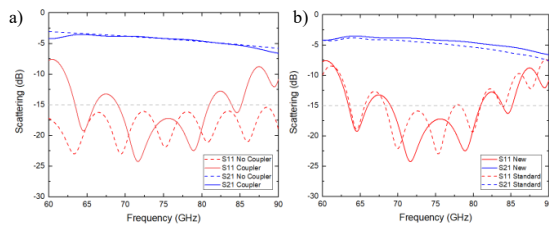


Fig. 5. a) Scattering parameters of the new meander line with coupler (solid line) and without coupler (dashed line) and b) comparison of the new meander (solid line) with the standard meander (dashed line), both with couplers.

IV. CONCLUSION

A new meander line design has been proposed to achieve better dispersion and interaction impedance than the conventional design. The study of the interaction impedance profile has shown an approximate symmetrical result with higher interaction impedance over the beam center position. Further investigation is in progress to optimize the performance and evaluate the large signal performance of TWTs using the proposed meander line.

REFERENCES

- [1] N. Ayllon, P. Angeletti, M. Ludwig and R. Dionisio, "An overview of European Spaceborne Vacuum Tube Amplifiers and System Needs," 2017 International Vacuum Electronics Conference (IVEC).
- [2] X. Li, X. Huang, S. Mathisen, R. Letizia and C. Paoloni, "Design of 71-76 GHz Double-Corrugated Waveguide Traveling-Wave Tube for Satellite Downlink", IEEE Transactions on Electron Devices, vol. 65, pp. 2195-2200, June 2018.
- [3] J. Cai, X. Wu and J. Feng, "A Cosine-Shaped Vane-Folded Waveguide and Ridge Waveguide Coupler", IEEE Transactions on Electron Devices, vol. 63, pp. 2544-2549, June 2016.
- [4] F. Shen, Y. Wei, H. Yin, Y. Gong, X. Xu, S. Wang, W. Wang and J. Feng, "A Novel V-shaped Microstrip Meander Line Slow Wave Structure for W-band MPPM", IEEE Transactions on Plasma Science, vol. 40, pp. 463-469, February 2012.
- [5] R. Waring, C. Paoloni, "Lagrangian Simulator for Millimetre Wave TWT based on Non-Rotationally Symmetric Slow-Wave Structure", Journal of Electromagnetic Waves and Applications, 31, 17, pp. 1902-1913, September 2017.
- [6] C. Kory, R. L. Ives, M. Read, J. Booske, H. Jiang, D. van der Weide, S-J Ho, S. Sengele and P. Phillips "Overview of W-band Travelling Wave Tube Programs", 2006 International Vacuum Electronics Conference (IVEC).
- [7] CST-MWS. [Online]. Available: <https://www.cst.com/products/csts2>